University of Bremen — Institute of Remote Sensing

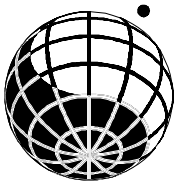

Atmospheric Parameter Retrieval from UV-vis-NIR Limb Scattering Measurements

Johannes W. Kaiser

Atmospheric Parameter Retrieval from UV-vis-NIR Limb Scattering Measurements

A dissertation
submitted in partial fulfilment of the requirements for the degree of
Dr. rer. nat.
in the University of Bremen, Fachbereich 1,
by

Dipl. Phys. Johannes W. Kaiser

July 2, 2001

affiliation	Institute of Environmental Physics / Institute of Remote Sensing, University of Bremen
homepage	www.uni-bremen.de/∼johannes
email	johannes@uni-bremen.de

date of the colloquium	August 29, 2001
1. reviewer	Prof. Dr. J.P. Burrows
2. reviewer	Prof. Dr. K. Künzi
further examiners	Prof. Dr. J. Bleck-Neuhaus Prof. Dr. G. Czycholl

Abstract

A new, fast radiative transfer model has been developed for retrievals from the future limb measurements of SCIAMACHY. It has been used to characterise UV-vis-NIR limb measurements.

The hyperspectral spectrometer SCIAMACHY will be launched aboard the European satellite Envisat in October 2001. It will measure atmospheric radiance spectra extending from the UV to the NIR spectral region, i.e., 240–$2380\,\mathrm{nm}$, with a moderate resolution of 0.24–$1.5\,\mathrm{nm}$. SCIAMACHY will operate in three measurement geometries: nadir, limb and occultation.

SCIAMACHY's hyperspectral capabilities will enable the simultaneous retrieval of a large set of atmospheric parameters from each individual measurement. Among the retrieval targets are the trace gases O_3, NO_2, OClO, BrO, SO_2, HCHO, H_2O, CH_4, CO_2, CO, and N_2O. Additionally, temperature, aerosol and cloud parameters will be determined.

SCIAMACHY's measurements in limb geometry will provide vertically resolved profiles of the retrieval parameters. Since the limb measurements are conceptually new, no retrieval algorithms and radiative transfer models have been established for them yet.

In this thesis, a new, fast radiative transfer model for UV-vis-NIR limb radiances has been developed, implemented, and validated. It takes into account the sphericity of the atmosphere and up to two orders of scattering and surface reflection. Since the radiance and weighting functions for all atmospheric parameters are calculated from analytical formulae, the model is fast. Due to the combination of these properties, the model is a unique tool for retrievals from UV-vis-NIR limb measurements.

An instrument model with field-of-view integration and signal-to-noise computation has been developed. It models SCIAMACHY's real characteristics as measured in the laboratory.

Retrieval algorithms based on the optimal estimation technique have also been implemented. They have been combined with the new radiative transfer and instrument models in the new program package *SCIARAYS*.

The program package *SCIARAYS* has been applied for the characterisation of UV-vis-NIR limb measurements in several ways:

The radiances and weighting functions calculated with *SCIARAYS* have been compared to those calculated with the radiative transfer model CDIPI, which accounts for full multiple scattering, but is much much slower. The second order of scattering and reflection modelled by *SCIARAYS* yields 60–$95\,\%$ of the full multiply scattered radiance, depending on wavelength and solar coordinates.

The simulated weighting functions agree within $10\,\%$. Their feature at the tangent height is particularly well reproduced. Therefore, *SCIARAYS*' weighting functions

can be used to calculate theoretical precision estimates and averaging kernels. In conformance with this, test retrievals with approximate weighting functions converge correctly. Thus the approximate weighting functions of *SCIARAYS* are well suited for retrievals from SCIAMACHY's limb measurements.

Detailed theoretical retrieval precisions have been calculated depending on profile altitude for SCIAMACHY's trace gas targets. Generally, the measurements of trace gases with absorption signatures in the UV-vis spectral region will exhibit the best precisions in the lower and middle stratosphere, while those of trace gases with absorption signatures in the NIR have better precisions for lower profile heights. The conclusion is that a UV-vis-NIR limb sensor like SCIAMACHY is well suited for studying the vertical structure of the stratosphere, especially the lower stratosphere, and also the upper troposphere above cloud top.

For instance, O_3 profiles with the nominal vertical resolution ($3\,\mathrm{km}$ for SCIAMACHY) can be measured with $1\,\%$ theoretical precision. Retrieved H_2O profiles have a theoretical precision of 1–$2\,\%$ in the upper troposphere and lower stratosphere. The dynamical behaviour in the tropopause region can be studied using these tracers for stratospheric and tropospheric air.

NO_2 profiles can be measured with 1–$10\,\%$ theoretical precison in the lower and middle stratosphere. These measurements will provide further insight in the stratospheric chemistry, especially the denoxification and ozone depletion.

Further investigations show that the vertical resolution of retrievals from SCIAMACHY's limb measurements can be improved beyond its geometrical limits. Even though SCIAMACHY operates with a tangent step size of $3\,\mathrm{km}$ and a field-of-view with $2.6\,\mathrm{km}$ vertical extent at the tangent height, retrievals with a finer vertical profile resolution can be performed. As a trade-off for better vertical resolution, the retrieval precision gets worse. Thus O_3 profile features with $1\,\mathrm{km}$ vertical extent are detectable with a precision of 20–$30\,\%$.

The trade-off between vertical resolution and retrieval precision implies that the choice of retrieval parameters needs to be adapted to the investigated atmospheric phenomenon. For instance, studying tropopause folds requires a good vertical resolution, while excellent retrieval precisions might be more important for studying the stratospheric chemistry.

Contents

List of Figures x

List of Tables xiii

Outline of this Thesis xiv

I INTRODUCTION 1

1 (Pre-)Historical Introduction 3

2 Stratospheric Chemistry & Anthropogenic Influences 6
2.1 The General Structure of the Atmosphere 6
2.2 Stratospheric Ozone Chemistry 8
2.2.1 The Natural State 8
2.2.2 Perturbed Gas Phase Chemistry 9
2.2.3 Heterogeneous Chemistry 10
2.3 Human Activities 12
2.3.1 Stratospheric Ozone Depletion 12
2.3.2 Global Warming 14
2.3.3 How to deal with it? 19

3 SCIAMACHY 20
3.1 Optical Characteristics 20
3.2 Measurement Geometries 22
3.3 Spacial Characteristics 24
3.4 Other Space-Borne Limb Scattering Measurements 25
3.5 Retrieval Considerations 27

II THEORY 29

Outline of the Theory 31

4 Radiative Processes in the Atmosphere **32**
4.1 Rayleigh Scattering . . . 32
4.2 Trace Gas Absorption . . . 34
4.3 Aerosol Scattering and Absorption . . . 38
4.4 Surface Reflection . . . 39
4.5 Clouds, Thermal Emission and Raman Scattering . . . 40
4.6 Refraction . . . 40
4.6.1 Snell's Law . . . 41
4.6.2 Parametrisations . . . 41

5 Radiative Transfer **44**
5.1 Definitions of Radiative Quantities . . . 44
5.1.1 Characteristics of the Atmosphere . . . 44
5.1.2 Path Coordinates . . . 45
5.1.3 Characteristics of the Radiation Field . . . 47
5.2 Two Forms of the Radiative Transfer Equation . . . 49
5.2.1 General Formulation . . . 49
5.2.2 UV-vis Measurements of the Terrestrial Atmosphere . . . 50
5.3 Model Types . . . 52
5.3.1 Integro-Differential Equation . . . 52
5.3.2 Integral Equation . . . 53
5.3.3 Orders of Scattering . . . 54
5.3.4 Combination . . . 54
5.3.5 Monte Carlo . . . 55

6 The Radiative Transfer Model in *SCIARAYS* **57**
6.1 Overview . . . 57
6.2 The Rays in *SCIARAYS* . . . 60
6.2.1 Naming Conventions . . . 60
6.2.2 Ray Paths in *SCIARAYS* . . . 60
6.2.3 Observational Geometries in *SCIARAYS* . . . 63
6.3 Discretisation . . . 64
6.3.1 General Approach . . . 65
6.3.2 Application to the Ray Paths . . . 67
6.4 Validation . . . 69
6.4.1 Comparison to MODTRAN . . . 69
6.4.2 Comparison to SIRO . . . 70
6.4.3 Comparison to GOMETRAN . . . 74
6.5 Weighting Functions . . . 75
6.5.1 Introduction . . . 75
6.5.2 Implemented Analytical Expressions . . . 77
6.5.3 Consistency Checks . . . 79

7 The Instrument Simulator in *SCIARAYS* 83
7.1 Introduction . . . 83
7.2 Measurement Noise . . . 84
7.3 Field of View . . . 88
7.4 Implementation . . . 88

8 Inversion with Optimal Estimation 90
8.1 Formulating the Inverse Problem . . . 90
8.1.1 A Linear, Discrete World . . . 91
8.1.2 Statistical Properties . . . 92
8.1.3 The Inverse Problem . . . 93
8.2 The Optimal Retrieval . . . 93
8.3 Characterisation . . . 94
8.4 Nonlinear Problems . . . 95

III APPLICATIONS 97

Outline of the Applications 99

9 Properties of Limb Scattering Measurements 100
9.1 Radiance and Noise . . . 100
9.2 Weighting Functions . . . 102
9.3 Averaging Kernels . . . 112

10 Vertical Resolution vs. Retrieval Error 115
10.1 Introduction . . . 115
10.2 Averaging Kernels . . . 115
10.3 Retrieval Tests . . . 119
10.4 Conclusions . . . 122

11 Sensitivities of a Limb Sensor 123
11.1 Introduction . . . 123
11.2 Method . . . 123
11.2.1 Radiative Transfer Model *SCIARAYS* . . . 124
11.2.2 Inversion Formalism . . . 124
11.2.3 Diagnostics Output (number density — VMR) . . . 125
11.3 Measurement Scenarios . . . 125
11.3.1 Measurement Geometry . . . 125
11.3.2 Atmospheric Profiles and Albedo . . . 126
11.3.3 Retrieval Parameter Grouping and Spectral Points . . . 126
11.3.4 Cross Sections . . . 126
11.3.5 *A Priori* . . . 128
11.4 Results . . . 128

11.5 Further Error Sources . . . 143
11.5.1 Multiple Scattering . . . 143
11.5.2 Refraction . . . 144
11.5.3 Retrieval Algorithm . . . 144
11.5.4 Temperature–Pressure–Aerosols–Albedo–Pointing . . . 147
11.5.5 Horizontal Inhomogeneities . . . 150
11.5.6 Spectral Uncertainties . . . 150
11.5.7 Clouds . . . 150
11.5.8 Forward Model IR Approximation . . . 151
11.6 Conclusions . . . 151

12 Comparison to Multiple Scattering **153**
12.1 Model Assumptions . . . 153
12.2 Model Comparisons . . . 154
12.2.1 Dependence on Wavelength . . . 154
12.2.2 Dependence on Solar Coordinates . . . 156
12.2.3 Ozone Weighting Functions . . . 156
12.3 Test Retrievals . . . 158
12.4 Summary . . . 165

IV EPITOME **167**

13 Summary, Conclusions, and Outlook **169**
13.1 Summary and Conclusions . . . 169
13.2 Outlook . . . 173

V APPENDICES **175**

A Ray Tracing **177**
A.1 Representing a Ray . . . 177
A.2 Geometric Ray Tracing . . . 178
A.2.1 Plane-Parallel Atmosphere . . . 178
A.2.2 Spherical Atmosphere . . . 179
A.3 Refractive Spherical Ray Tracing . . . 184
A.3.1 General Considerations . . . 184
A.3.2 Tangent Radius . . . 185
A.3.3 Radius Levels . . . 185
A.3.4 Zenith Angles . . . 185
A.3.5 Polar Coordinates and Path Lengths . . . 186
A.4 Solar Coordinates . . . 188
A.4.1 Solar Coordinate System . . . 188

A.4.2 Statement of the Problem 188
A.4.3 Solution 189

B Detailed Weighting Functions **193**

C Curriculum Vitae **206**

D List of Publications **208**

E I Declare ... **211**

Acknowledgements **212**

Bibliography **213**

Index **225**

List of Figures

2.1 Atmospheric temperature and ozone profiles. 7
2.2 Variations of Earth's surface temperature over the last millennium. 15
2.3 Estimated contributions to external climate forcing. 16
2.4 Estimated mean surface temperature change for the 21st century. 18

3.1 SCIAMACHY's three measurement geometries. 23
3.2 Details of SCIAMACHY's nadir and limb measurement geometries. 24
3.3 Matching of SCIAMACHY's nadir and limb measurements. 27

4.1 Absorption cross section of trace gases in the UV-vis spectral region. . . . 35
4.2 Absorption cross sections of trace gases in SCIAMACHY's channels 3–6. . 36
4.3 Absorption cross sections of trace gases in SCIAMACHY's channels 7, 8. . 37

5.1 Path coordinate s and optical depth τ. 46
5.2 Pseudo-spherical solution of the integro-differential RTE. 52
5.3 Single-scattering solution of the integral form of the RTE. 53
5.4 Orders of Scattering: the first two orders. 54
5.5 Combination of integral and integro-differential equations. 55
5.6 Simulation of photon paths for Monte Carlo modelling. 55

6.1 Ray paths modelled by *SCIARAYS*. 61
6.2 Relative difference of the radiance computed by *SCIARAYS* as compared to output from MODTRAN. 70
6.3 Comparison between *SCIARAYS* and the Monte Carlo (MC) model SIRO for scenario A. 72
6.4 Comparison between *SCIARAYS* and the Monte Carlo (MC) model SIRO for scenarios B (albedo 0) and C (albedo 1). 73
6.5 Relative difference of the radiance computed by *SCIARAYS* as compared to output from GOMETRAN. 75
6.6 Relative-absolute weighting functions for O_3 and NO_2 computed with *SCIARAYS*. Quasi-analytical and numerical computations. 81
6.7 Relative-absolute weighting functions for pressure and temperature computed with *SCIARAYS*. Quasi-analytical and numerical computations. . . 82

7.1 Throughput of SCIAMACHY measured during OPTEC 5. 86

7.2 *SCIARAYS'* throughput parametrisation of SCIAMACHY. 86
7.3 *SCIARAYS'* throughput parametrisation for ACE. 86
7.4 Readout noise of SCIAMACHY measured during OPTEC 5. 87
7.5 *SCIARAYS'* readout noise parametrisation of SCIAMACHY. 87

9.1 Radiance values and signal/noise values for SCIAMACHY. 101
9.2 Ozone profile weighting functions as functions of the profile altitude level. 103
9.3 Ozone weighting functions as functions of tangent altitude. 104
9.4 Ozone profile weighting functions for $790\,\mathrm{nm}$. 107
9.5 Relative-relative weighting function of the $15\,\mathrm{km}$-level of the O_3 profile (top) and SCIAMACHY's relative noise (bottom). 109
9.6 Relative-relative weighting function of the $15\,\mathrm{km}$-level of the BrO profile (top) and SCIAMACHY's relative noise (bottom). 110
9.7 Relative-relative weighting function of the $15\,\mathrm{km}$-level of the CH_4 profile (top) and SCIAMACHY's relative noise (bottom). 111
9.8 Averaging kernels of O_3 and BrO for a retrieval from 300–$370\,\mathrm{nm}$. 113

10.1 O_3 averaging kernels for a retrieval with $1\,\mathrm{km}$ retrieval grid spacing. . . . 116
10.2 O_3 averaging kernels for retrievals from different spectral ranges. 118
10.3 Ensemble statistics of O_3 retrieval with $3\,\mathrm{km}$ vertical resolution. 120
10.4 Ensemble statistics of O_3 retrieval with $1\,\mathrm{km}$ vertical resolution. 120
10.5 Ensemble statistics of O_3 retrieval with $3\,\mathrm{km}$ vertical resolution. 121
10.6 Ensemble statistics of O_3 retrieval with $1\,\mathrm{km}$ vertical resolution. 121

11.1 Theoretical precision results for O_3. 130
11.2 Theoretical precision results for NO_2. 131
11.3 Theoretical precision results for BrO. 132
11.4 Theoretical precision results for OClO. 133
11.5 Theoretical precision results for ClO. 134
11.6 Theoretical precision results for temperature. 135
11.7 Theoretical precision results for pressure. 136
11.8 Theoretical precision results for albedo. 137
11.9 Theoretical precision results for H_2O. 138
11.10 Theoretical precision results for CH_4. 139
11.11 Theoretical precision results for CO_2. 140
11.12 Theoretical precision results for CO. 141
11.13 Theoretical precision results for N_2O. 142
11.14 Theoretical precision results for BrO calculated with only one order of scattering and reflection and with two orders of scattering and reflection. . 143
11.15 Theoretical precision results for NO_2 calculated for a simplified scenario with refractive and with geometrical ray tracing. 145
11.16 Theoretical precision results for NO_2 retrieved with the differential retrieval approach compared retrieved with the absolute approach. 146

11.17 O_3, temperature and pressure profile precisions derived in the 240–550 nm range. 149

12.1 Sun-normalised limb radiance spectra computed with several ray paths. . 155
12.2 Fractions of the reference spectrum covered by several ray paths. 155
12.3 Solar zenith dependence of modelled fraction of radiance for $0\,^\circ$ azimuth angle. 157
12.4 Solar zenith dependence of modelled fraction of radiance for $90\,^\circ$ azimuth angle. 157
12.5 Solar zenith dependence of modelled fraction of radiance for $180\,^\circ$ azimuth angle. 157
12.6 Weighting functions of the O_3 profile for 330 nm wavelength and 18 km tangent height 158
12.7 Individual test retrieval of NO_2 with approximated weighting functions. . 160
12.8 Individual test retrieval of O_3 from the UV spectral region with approximated weighting functions. 161
12.9 Individual test retrieval of O_3 from the NIR spectral region with approximated weighting functions. 161
12.10 Ensemble of test retrievals of NO_2 with approximated weighting functions. 162
12.11 Ensemble of test retrievals of O_3 from the UV spectral region with approximated weighting functions. 164
12.12 Ensemble of test retrievals of O_3 from the NIR spectral region with approximated weighting functions. 164

A.1 Geometry of a sky-bound ray (without refraction) 180
A.2 Geometry of a ground-bound ray (without refraction) 181
A.3 Change of properties along a ray: (a) near ground-bound points, (b) near sky-bound points 187
A.4 Ray points in the solar coordinate system. 190

B.1 Relative-relative weighting function of the 15 km-level of the O_3 profile. . . 194
B.2 Relative-relative weighting function of the 15 km-level of the NO_2 profile. . 195
B.3 Relative-relative weighting function of the 15 km-level of the BrO profile. . 196
B.4 Relative-relative weighting function of the 15 km-level of the OClO profile. 197
B.5 Relative-relative weighting function of the 15 km-level of the ClO profile. . 198
B.6 Relative-relative weighting function of the 15 km-level of the HCHO profile. 199
B.7 Relative-relative weighting function of the 15 km-level of the SO_2 profile . 200
B.8 Relative-relative weighting function of the 15 km-level of the H_2O profile. . 201
B.9 Relative-relative weighting function of the 15 km-level of the CH_4 profile. . 202
B.10 Relative-relative weighting function of the 15 km-level of the CO_2 profile. . 203
B.11 Relative-relative weighting function of the 15 km-level of the CO profile. . 204
B.12 Relative-relative weighting function of the 15 km-level of the N_2O profile. . 205

List of Tables

3.1 Optical Parameters of SCIAMACHY's Spectrometer 21

6.1 Units of the Atmospheric Input and Output of *SCIARAYS* 59
6.2 Scenarios for Comparison to SIRO 71

7.1 Variable Definitions of this Chapter 85
7.2 Input and Output of the Instrument Simulator 89

11.1 Retrieval parameter grouping: The set of retrieval parameters is divided into two groups and retrieved from separate spectral regions. 127
11.2 Anticipated Theoretical Precisions. 152

12.1 Radiative Transfer Models for Approximation Comparisons 154
12.2 Atmospheric Model for Approximation Comparisons 154
12.3 Measurement Scenario and Retrieval Setup 159

Outline of this Thesis

This thesis is structured in five main parts. They are not completely stand-alone, but it should be possible to start reading in the middle as cross references to the relevant earlier chapters are included.

- Part I introduces the scientific background, the global anthropogenic influence on the atmosphere and SCIAMACHY's observations of it, upon which the current work is set.
- Part II describes the radiative transfer modelling in general, the physical processes which are modelled and their implementation in the new program package *SCIARAYS* in particular. The new instrument model and the retrieval formalism implemented in *SCIARAYS* are also introduced.
- Part III comprises applications of *SCIARAYS* to characterise UV-vis-NIR limb measurements and feasible retrieval strategies.
- Part IV summarises the findings and suggests a strategy for future investigations.
- Part V contains the appendixes. Appendix A details the geometrical and refractive ray tracing formulae used in *SCIARAYS*. Detailed weighting functions for many trace gases can be found in appendix B.

Conventions

- Equations are referenced in the text by giving their number in brackets, e.g., (4.18) is stating Snell's law.
- Physical quantities consist of a number and a unit, e.g., room temperature $T = 20\ ^\circ\mathrm{C} \approx 293$ K. Square brackets $[.]$ behind a variable name are used to denote the number of the quantity in the specified unit: $T[^\circ\mathrm{C}] = 20$. [-] is used for dimensionless quantities.
- Citations are labelled with the author's name(s) and the year of the publication. These labels are marked with square brackets [.]. The detailed bibliographical data are listed in the bibliography starting on page 213.

- The definitions of all symbols and most technical terms used in this report can be found using the index starting on page 225. Entries of the index are typeset in *emphasised font* at their referenced point in the text.

Further Formats

The whole thesis is available in *pdf* format for printing as well as on-screen viewing with clickable links, searchable text, zoomable colour plots, bookmarks, and thumbnails at the URL `http://www.uni-bremen.de/~johannes/diss` .

Part I

INTRODUCTION

Chapter 1

(Pre-)Historical Introduction

15 billion years ago, our universe was created in the Big Bang. Physical laws permit to reconstruct its evolution from the Heisenberg time, 10^{-43} seconds after the Big Bang, to the present [Shu, 1982, Bublath, 1999].

After 10^{-10} seconds protons and neutrons condensed. 3 Minutes later some helium and lithium nuclei became stable. After 300 thousand years, the nuclei formed atoms with electronic shells: mostly hydrogen, but also some helium and lithium.

After one billion years, astronomical hydrogen clouds with a very small density[1] collapsed under their own gravitational pull. Thus (population II) stars were formed in the core of which nuclear fusion transformed hydrogen nuclei (protons) to helium nuclei (alpha particles). After the hydrogen in the core was exhausted, the internal energy source stopped and the core contracted under its own gravitational pull. Thus the density and temperature became large enough to start fusion of the helium nuclei to carbon nuclei[2]. After the helium nuclei had been used up in the inner core, further contraction started the fusion of carbon nuclei to those of heavier elements, amongst them oxygen.

If the total mass of the star is larger than six times the mass of our sun, successive fusion to heavier elements continues up to iron, the nucleus of which has the lowest energy per nucleon. Since no further energy source is available to balance the gravitational pull of the star, its core collapses. The resultant close packing of the nuclei suddenly releases such a huge amount of energy that the whole star explodes in a *Super Nova* (of Type II). The collapsed core may be left over as a *Black Hole*. During the Super Nova explosion many neutrons are emitted. All elements heavier than iron are formed by capture of neutrons and subsequent beta decay.

Thus the material ejected by Super Novae contains all heavy elements besides large amounts of hydrogen. Our sun was formed by contraction of a cloud of such material. Since the conservation of rotational momentum prevents some of the material from falling further toward the centre, i.e., the sun, loose matter forms a plane around the sun. Coagulation leads to the known planets, among them Earth. At the given thermal

[1] vacuum to any terrestrial laboratory standard

[2] In intermediate steps, beryllium and excited carbon are formed.

energies, light molecules reached the escape velocity. Nevertheless, Earth has enough mass to hold a gaseous atmosphere. It also was warm (and cold) enough to produce liquid oceans.

About four billion years ago, Earth had solidified. In the beginning, its atmosphere contained only small amounts of molecular oxygen. After life had started[3], the early evolution led to plants, especially algae, which produced oxygen by photosynthesis. Following the spread of plants in the oceans the abundances of molecular oxygen slowly build up in the oceans and the atmosphere. The plants had evolved inside the ocean since the solar ultraviolet (*UV*) radiation above the water would have destroy their molecular structure, in particular the proteins of their DNA, which holds a species' identity.

About 1.5 billion years ago, oxygen-producing green-blue algea spread widely. Thus the atmosphere's composition was shifted from a reducing to an oxidising atmosphere. Ever since, roughly one fifth of the atmosphere consists of molecular oxygen. Abundant oxygen is a prerequisite for the evolution and existence of mankind for all animals and humans draw their energy from oxidation.

In the higher parts of the atmosphere the solar radiation induces a photo-chemistry in which molecular oxygen is split and ozone is formed. Thus the stratospheric *ozone layer* is formed at an altitude of 20–$25\,\mathrm{km}$. It shields Earth's surface from UV radiation since ozone absorbs this radiation in its *Hartley-Huggins bands*.

The absorbed energy is transformed to thermal energy by *collisional quenching*. This causes a temperature inversion, which stabilises the dynamics leading to a horizontal *stratification* of the atmosphere in this height regime, which is therefore called the *stratosphere*. Due to this stratification, the shielding of UV radiation is relatively stable on the whole surface. Only due to the secure UV shield, plants and animals living on land were able to evolve.

About forty thousand years ago, our own species, homo sapiens sapiens, appeared. About fifty years ago, we started to produce large amounts of chloro-fluoro-carbons (CFCs) and to release them into the atmosphere. About twenty years ago, the CFCs started to induce a massive ozone depletion in springtime over Antarctica, the *antarctic ozone hole*. Sixteen years ago, this was discovered by the British Antarctic Survey. The ozone hole was a clearly visible reminder that mankind is influencing Earth's atmosphere on a global scale. It was followed by the public realisation that the influence needs to be controlled. Therefore, scientific monitoring, understanding, and forecasting is necessary, as well as political (re)action.

Thus intense scientific research has been undertaken. In the course of increased scientific interest in the atmosphere the satellite spectrometer SCIAMACHY (see Chapter 3) has been build. Its launch is planned for October 2001 and it will record UV-vis-NIR limb spectra of the atmosphere. Since such measurements are a novelty, new computer algorithms are needed to extract the knowledge on Earth's atmosphere from SCIAMACHY's measurements.

[3] "been created?"

This thesis deals with the development of radiative transfer and retrieval algorithms for SCIAMACHY's limb measurements.

Chapter 2

Stratospheric Chemistry & Anthropogenic Influences

2.1 The General Structure of the Atmosphere

Typical profiles of three key parameters of Earth's atmosphere are shown in Figure 2.1: temperature, ozone partial pressure and total pressure.

The temperature profile displays a minimum between $10\,\mathrm{km}$ and $20\,\mathrm{km}$ and a maximum near $50\,\mathrm{km}$. These extrema, called *tropopause*[1] and *stratopause*, divide the atmosphere into height regimes with distinct physical behaviour: the *troposphere* below the tropopause, the *stratosphere* between the tropopause and the stratopause, and the *mesosphere* above the stratopause.

Due to the temperature gradient, the stratosphere[2] has a stable layering with little vertical mixing, while the troposphere[3] is well-mixed by the processes of ordinary *weather*.

The ozone profile has a pronounced maximum in the stratosphere, small values in the troposphere, and even smaller values in the mesosphere. The maximum near 20–$25\,\mathrm{km}$ is called the stratospheric *ozone layer* or, more colloquial, the *ozone shield*, as it shields Earth's surface from solar ultraviolet (UV) radiation. The radiation is absorbed by the ozone molecules and transformed into thermal energy by collisional quenching. This source of thermal energy is the main cause of the temperature rise in the stratosphere. The higher temperatures in the troposphere are explained by the heating of the sunlit surface.

The right y-axis in Figure 2.1 shows the total atmospheric pressure. It decreases exponentially with a scale height of about $8\,\mathrm{km}$. The exponential character reflects the fact that the atmosphere is close to hydrostatic equilibrium. Since the gravitational pull of

[1] It is also common to define the tropopause as a vertical transport barrier. This definition is more consistent with its role in the description of atmospheric processes, but it makes measuring the tropopause height much difficult.

[2] "Stratus" is Latin for "layered".

[3] "Tropos" is Greek for "turning".

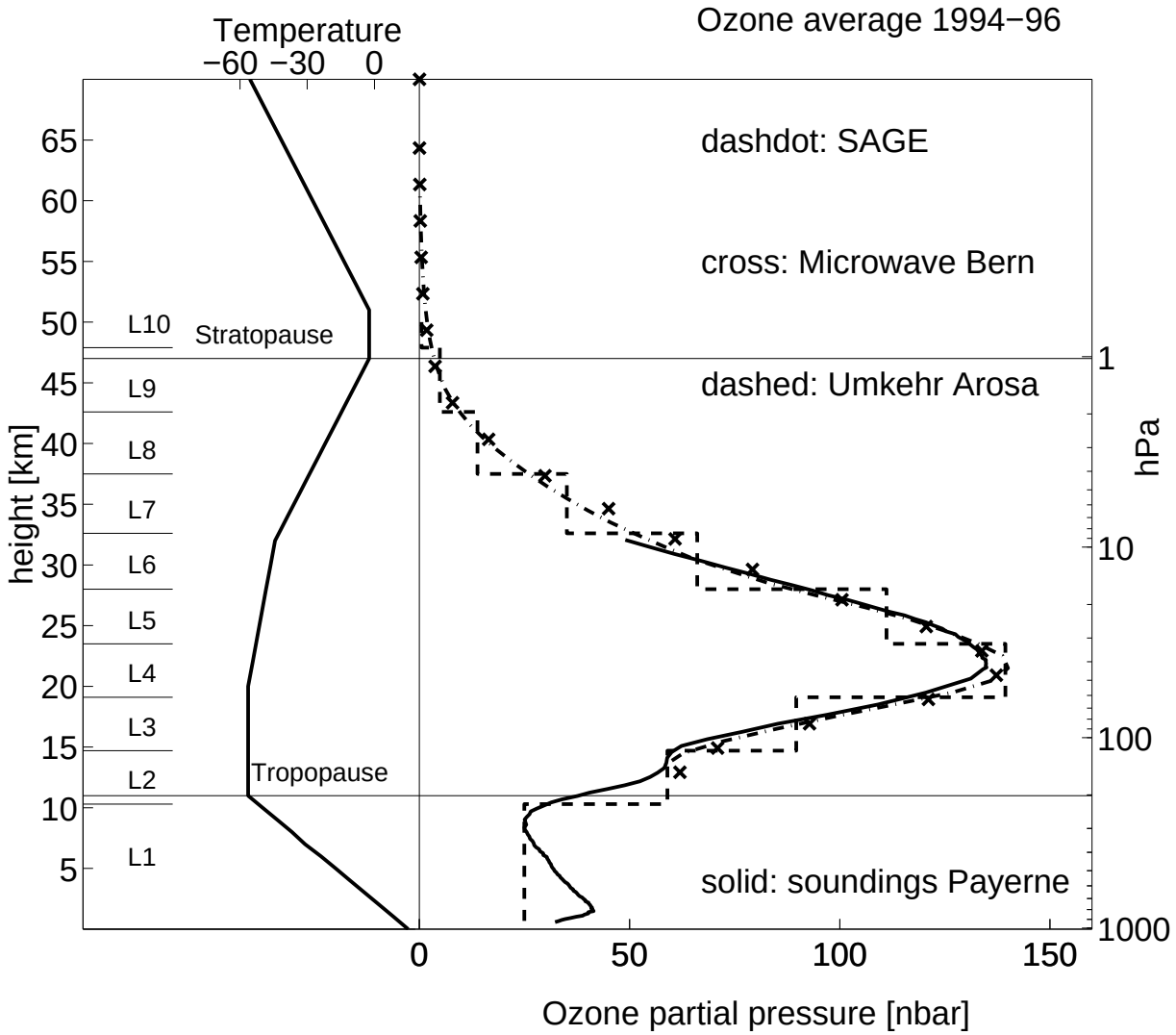

Figure 2.1: Atmospheric temperature $[^\circ\mathrm{C}]$ and ozone partial pressure $[\mathrm{nbar}] \equiv [10^{-6}\,\mathrm{hPa}]$ profiles for mid-latitudes. Data sources: US Standard Atmosphere 1976, Payerne balloon sounds, Arosa Umkehr measurements, Bern ground-based microwave measurements, and SAGE satellite occultation measurements. [Weiss, 2000, fig. 2.1]

Earth is nearly constant throughout the atmosphere, the pressure at a given height is proportional to the total atmospheric mass above this height. Thus about $80\,\%$ of the atmospheric mass is located in the troposphere and about $20\,\%$ in the stratosphere (in mid-latitudes). Globally, the ratio between tropospheric and stratospheric air mass is even larger due to the higher tropical tropopause [Solomon, 1999]: $90\,\%$ in the troposphere, $10\,\%$ in the stratosphere, and only $0.1\,\%$ above.

2.2 Stratospheric Ozone Chemistry

2.2.1 The Natural State

Chapman [1930] was the first to realise that ozone O_3 would be formed by stratospheric photochemistry: Short wave solar radiation splits oxygen molecules O_2 into oxygen radicals O which quickly form ozone with molecular oxygen if a collision partner M is available to carry away excess energy. The ozone production reactions are:

$$O_2 + h\nu\ (\lambda < 242\,\mathrm{nm}) \longrightarrow O + O \tag{2.1}$$
$$O + O_2 + M \longrightarrow O_3 + M\ . \tag{2.2}$$

The ozone molecule can also be photolysed. If the radiative energy is large enough, activated $O(^1D)$ is produced, which may subsequently dissipate its energy by *collisional quenching* (2.5). The oxygen radical in its ground state can also produce molecular oxygen through reactions with ozone or another oxygen radical. The ozone destruction reactions are:

$$O_3 + h\nu\ (\lambda < 1200\,\mathrm{nm}) \longrightarrow O_2 + O \tag{2.3}$$
$$O_3 + h\nu\ (\lambda < 310\,\mathrm{nm}) \longrightarrow O_2 + O(^1D) \tag{2.4}$$
$$O(^1D) + M \longrightarrow O + M \tag{2.5}$$
$$O + O_3 \longrightarrow O_2 + O_2 \tag{2.6}$$
$$O + O + M \longrightarrow O_2 + M \tag{2.7}$$

Assuming chemical equilibrium, i.e., balancing the ozone production and destruction rates, qualitatively explains the upper stratospheric ozone layer[4]. However, Chapman's reaction scheme overestimates the ozone equilibrium concentration. The natural ozone profile can only be modelled quantitatively by adding the catalytic destruction mechanisms involving the hydrogen [Bates and Nicolet, 1950, Hampson, 1964] and nitrogen [Crutzen, 1970, 1971, Johnston, 1971] oxides. The catalytic odd ozone[5] destruction cycles are of the form

[4] The higher in the atmosphere, the fewer collisions occur, the slower is the ozone producing reaction. On the other hand, oxygen is not photolysed in the lower atmosphere since the shortwave radiation does not penetrate deep enough. Therefore, substantial ozone production occurs only in a limited height range. This is the reason why ozone is not distributed homogeneously but forms a layer.

[5] *Odd ozone* is the sum of the oxygen radical O and ozone O_3.

$$XO^\bullet + O \longrightarrow X^\bullet + O_2 \quad (2.8)$$
$$X^\bullet + O_3 \longrightarrow O_2 + XO^\bullet \quad (2.9)$$
$$(\text{net:} \quad O + O_3 \longrightarrow O_2 + O_2 \quad), \quad (2.10)$$

where radicals are identified by a bullet, e.g., $X^\bullet$, and X denotes either hydrogen H or nitrogen N. Since the initial radicals ($HO^\bullet$ and $NO^\bullet$) are reproduced, the reactions are *catalytic* and already small amounts of these radicals can influence the much larger ozone abundance. The photochemistry determines the ozone concentration in the upper stratosphere.

The lower stratosphere is dominated by transport processes as the solar short-wave radiation is blocked out by the ozone above. The altitude range of 25–$35\,\mathrm{km}$ represents a transition region between photochemical and dynamical control in the stratosphere [WMO, 1999b]. The bulk of stratospheric ozone is formed in the tropics. Ozone is supplied in the middle and higher latitudes through a net ozone transport from the tropics to the poles. Thus ozone is permanently transported from its photochemical production region over the tropics into the extra-tropical lower stratosphere [Dobson, 1930, Brewer, 1949]. This circulation, historically referred to as *Brewer-Dobson circulation*, revolves with a timescale of approximately five years. It generates the pronounced ozone maximum at 20–$25\,\mathrm{km}$ height over mid-latitudes (see Figure 2.1). For a recent review of the dynamical processes refer to Holton et al. [1995].

For the ozone *column density*[6], the height of the tropopause, which separates ozone-rich stratospheric air from ozone-poor tropospheric air, is of importance. Thus the question of how much of the atmospheric column is tropospheric and how much is stratospheric strongly influences the ozone column density at a given longitude and latitude. Therefore, it determines the global ozone distribution. In the tropics, the tropopause is at a height of about $16\,\mathrm{km}$, over the poles at about $8\,\mathrm{km}$. Hence, the ozone column density maximum is located at the poles, while highest ozone *volume mixing ratios*[7] occur in the ozone source region over the tropics.

2.2.2 Perturbed Gas Phase Chemistry

Stolarski and Cicerone [1974] pointed out that chlorine Cl could also destroy ozone in a catalytic cycle (2.8–2.10) with $X \equiv Cl$. Molina and Rowland [1974], Rowland and Molina [1975] showed that the major source for such ozone-depleting stratospheric chlorine would be man-made chlorofluorocarbons (*CFC*s), which have so long atmospheric residence times that they are transported to the stratosphere and photolysed there by solar UV radiation. Owing to the slow transport across the tropopause into the stratosphere,

[6] The height-integrated concentration in $[\mathrm{molec/cm^2}]$ or *Dobson Units* [DU]. Also called *column* or, e.g., for ozone, *total ozone*.

[7] The ratio of trace gas number density $[\mathrm{cm^{-3}}]$ and total number density $[\mathrm{cm^{-3}}]$. It is dimensionless [-], but common units, e.g. $[\mathrm{ppb}] \equiv [10^{-9}]$ (parts per billion), transform to convenient orders of magnitude.

chlorine is destroying stratospheric ozone for many decades after its release in CFCs into the troposphere.

Chlorine also reacts with further stratospheric constituents in a complex way. Two example reactions, which transform the *active radicals* of chlorine into non-ozone-destroying *reservoir gases*, are:

$$\mathrm{Cl} + \mathrm{CH_4} \longrightarrow \mathrm{HCl} + \mathrm{CH_3} \tag{2.11}$$

$$\mathrm{ClO} + \mathrm{NO_2} + \mathrm{M} \longrightarrow \mathrm{ClONO_2} + \mathrm{M} \quad . \tag{2.12}$$

The *partitioning* between active radicals and reservoir gases is controlled by the rates of all reservoir forming and destroying reactions. Together with the total load of chlorine, the partitioning determines the amount of radicals, which is available for the ozone-destroying catalytic cycle. Therefore, it is critical for the ozone destruction rate.

The other *halogens* fluoride F and bromine Br theoretically also have ozone destruction capabilities in a catalytic cycle like (2.8–2.10). However, fluoride is partitioned in such a way that it is nearly completely in the reservoir HF. A relatively large fraction of the stratospheric bromine resides in active radicals, but its total stratospheric abundance is small[8]. Therefore, the ozone destruction by halogens is currently dominated by the chlorine cycle [Solomon, 1999].

In the higher stratosphere near $40\,\mathrm{km}$ altitude, an ozone trend of $-8\,\%/\mathrm{decade}$ has been observed since 1970. It can be attributed to the catalytic ozone destruction involving chlorine from man-made CFCs [Crutzen, 1974, Solomon, 1999].

2.2.3 Heterogeneous Chemistry

Over Antarctica, a special situation is encountered. In the polar night, a cold circumpolar vortex builds up and prevents air exchange with mid-latitudes. The temperature within the vortex drops below $-70\,^{\circ}\mathrm{C}$, and *polar stratospheric clouds* (*PSC*s) form. Solomon et al. [1986] suggested that reservoir gases are destroyed on the surface of the PSCs:

$$\mathrm{HCl} + \mathrm{ClONO_2} \xrightarrow{\mathrm{PSC}} \mathrm{HNO_3} + \mathrm{Cl_2} \quad . \tag{2.13}$$

As soon as the first sun light arrives in polar spring, the molecular chlorine $\mathrm{Cl_2}$ is photolysed and forms Cl radicals. Thus the partitioning of chlorine is changed toward the active radicals, which efficiently destroy ozone in catalytic cycles similar to (2.8–2.10).

An important condition for sustained ozone destruction is the effect that the reservoir $\mathrm{ClONO_2}$ is not readily formed again via (2.12) since the nitrogen is bound in $\mathrm{HNO_3}$ instead of $\mathrm{NO_2}$. This state of suppressed $\mathrm{NO_2}$ is called *denoxification*. It is reversible through the photolysis of $\mathrm{HNO_3}$. When nitrogen is bound in particles[9] which are subsequently deposited, it is irreversibly removed from some stratospheric layers. This

[8] 200 times less than chlorine.

[9] For instance, $\mathrm{HNO_3}$ may be solved in liquid water.

process, called *denitrification*, pushes the chlorine partitioning permanently toward the ozone-destroying radicals.

Like in the perturbed gas phase chemistry, the ozone is depleted in the Antarctic spring by catalytic cycles with halogen radicals. However, the cycles are more complex than (2.8–2.10). Molina and Molina [1987] discovered an ozone-destroying catalytic cycle involving the formation and photolysis of the ClO-*dimer*, Cl_2O_2:

$$2\,[\,Cl + O_3 \longrightarrow ClO + O_2\,] \tag{2.14}$$
$$ClO + ClO + M \longrightarrow Cl_2O_2 + M \tag{2.15}$$
$$Cl_2O_2 + h\nu \longrightarrow Cl + ClO_2 \tag{2.16}$$
$$ClO_2 + M \longrightarrow Cl + O_2 + M \tag{2.17}$$
$$(\text{net:}\quad 2\,O_3 \longrightarrow 3\,O_2) \tag{2.18}$$

Another catalytic cycle was proposed by McElroy et al. [1986] and Tung et al. [1986]. It involves both bromine and chlorine radicals simultaneously:

$$Cl + O_3 \longrightarrow ClO + O_2 \tag{2.19}$$
$$Br + O_3 \longrightarrow BrO + O_2 \tag{2.20}$$
$$ClO + BrO \longrightarrow Br + ClO_2 \tag{2.21}$$
$$ClO_2 + M \longrightarrow Cl + O_2 + M \tag{2.22}$$
$$(\text{net:}\quad 2\,O_3 \longrightarrow 3\,O_2) \tag{2.23}$$

The ozone hole over Antarctica, which was discovered by Farman et al. [1985], is caused by heterogeneous chlorine activation and nitrogen deactivation on PSCs. The catalytic cycle (2.14–2.18) involving the ClO-dimer is now recognised to be responsible for $75\,\%$ of the ozone removal in the ozone hole, another $20\,\%$ are attributed to the combined chlorine-bromine cycle (2.19–2.23) [Solomon, 1999] .

In the Arctic, the heterogeneous chemistry is the same, but the dynamical conditions differ from those over Antarctica. Less PSCs form in the Arctic as it is warmer because the polar vortex is less stable[10]. Therefore the ozone loss is much weaker than in the Antarctic. Nevertheless, denitrification has also been observed in some years. If the stratosphere cools due to the greenhouse effect, more denitrification and more ozone loss must be expected in future in the Arctic [Waibel et al., 1999].

Heterogeneous chemistry on volcanic aerosols was demonstrated by Fahey et al. [1993] to play a role in mid-latitudinal ozone destruction. On sulfate aerosol surfaces, nitrogen is transformed to inert compounds, thereby being no longer available for chlorine deactivation. In addition, chlorine is activated on aerosol surfaces. The ozone destruction associated with aerosols is considerably smaller than the one due to PSCs as the mass and efficiency of aerosols are much smaller than those of the PSCs. However, since about 1980 significant ozone loss has been observed after major volcanic eruptions [Hofmann and Solomon, 1989, WMO, 1995].

[10]The underlying reason is the irregular land–sea distribution in the northern hemisphere

2.3 Human Activities

2.3.1 Stratospheric Ozone Depletion

The discovery of the Antarctic Ozone Hole by the British Antarctic Survey brought the global dimension of the anthropogenic impact on the Earth's atmosphere to the world-wide public consciousness in 1985. Since then, many measurement campaigns and theoretical investigations have led to a much more detailed picture of the trends of stratospheric ozone and a qualitatively good understanding of the controlling chemical and physical processes.

Observations of Ozone Depletion at Mid-Latitudes

Ground-based measurements of the ozone column density generally exhibit a negative trend in mid-latitudes since about 1970. For instance, the time series of Arosa, Switzerland, documents a decadal decrease of about $3\,\%$ [Staehelin et al., 1998]. Assessing the vertical distribution of the ozone trend, SPARC [1998, p. 289] finds that the trend is the strongest near 40 and $15\,\mathrm{km}$.

Observations of the Antarctic Ozone Hole

Farman et al. [1985] were the first to document a measurable ozone depletion which had occurred in spring over Halley, Antarctica. The observation was soon confirmed by other stations and satellite-based measurements [e.g., Stolarski et al., 1986]. Every austral spring, the ozone concentration in the height regime of 12–$25\,\mathrm{km}$ is severely reduced inside the polar vortex over Antarctica. When the vortex breaks up, ozone-rich air from higher latitudes is mixed in and the ozone layer recovers. On the other hand, large areas in New Zealand, Australia and Southern America experience low ozone column densities in summer owing to the mixing with ozone-reduced air from the Antarctic vortex.

Re-analysis of older measurements revealed that the Antarctic ozone hole had started to develop in the late 1970s. It has become more and more severe until the mid-1990s. Since then, nearly all ozone between 15 and $20\,\mathrm{km}$ height is regularly destroyed in the Antarctic ozone hole. Thus the ozone column density is reduced by up to $75\,\%$ [Solomon, 1999].

Several measurement campaigns have shown that PSCs and increased abundances of ClO and OClO are spatially and temporally correlated with the ozone loss over Antarctica [Solomon, 1999, and references therein]. These measurements among others have lead to the presently accepted theorectical explanation of the phenomenon.

Explanation

The current understanding of stratospheric ozone chemistry is summarised in Section 2.2. The Antarctic ozone hole can be attributed to the increased stratospheric abundance of halogen radicals via the heterogeneous re-partitioning (see Section 2.2.3). The mid-latitudinal ozone trend in the upper stratosphere is caused by the catalytic ClO cycle in the gas phase chemistry (see Section 2.2.2), while the trend in the lower stratosphere is explained by heterogeneous chemistry and additional dynamical influences [Appenzeller et al., 2000].

The increased stratospheric abundance of halogens is caused by the anthropogenic emission of CFCs into the troposphere and their subsequent transport across the tropopause and photolysis by solar short-wave radiation in the stratosphere. The CFCs are mainly *CFC-12* (CF_2Cl_2) and *CFC-11* ($CFCl_3$), but also include a large list of other industrial compounds [WMO, 1995]. The natural stratospheric background of chlorine compounds as originating from volcanoes, sea spray and gas production by sea algae is much smaller [Solomon, 1999].

Political Action

In 1987, soon after the scientific community had identified the man-made CFCs as the primary cause of the stratospheric ozone depletion, political action was taken with the *Montreal Protocol*, in which 21 nations agreed to halve their production of CFCs. More states joined the effort and in 1990 and 1992 it was agreed to take more drastic steps: Since 1996 the production of CFCs is prohibited in the industrial countries. The developing countries agreed to stop their production by 2006. Further restrictions regarding the so-called halones and H-CFCs, which also transport halogens to the stratosphere, are in effect.

Since the threat to the stratospheric ozone layer and the Montreal Protocol have been widely acknowledged, the worldwide use of CFCs had decreased by $85\,\%$ in 1997 [BMU, 2000] and the total tropospheric chlorine content is decreasing measurably [Solomon, 1999].

Future Development

Studies of the lifetime of the chlorine-containing atmospheric compounds reveal that the total chlorine content will reach about $2\,\mathrm{ppb}$ again in 40–50 years. This is the level at which the rapid stratospheric ozone depletion started in the late 1970s. Therefore, the stratospheric ozone layer is anticipated to recover to its late 1970s state around 2040–2050: By this time the phenomenon of the Antarctic ozone hole is anticipated to stop [WMO, 1999a].

Of course, this prediction only holds if the Montreal Protocol is respected by all countries worldwide. Furthermore, other atmospheric changes may alter the numbers: For instance, Shindell et al. [1998] suggested that the global warming would enhance

the Arctic ozone depletion by heterogeneous chemistry as it implies more PSCs due to stratospheric cooling. This coupling might well slow down the recovery of the ozone layer by several decades.

Owing to such uncertainties, the future development of the stratospheric ozone layer needs to be monitored closely on a global scale.

The actual exchange mechanisms across the tropopause are still subject to intense scientific research [see, e.g., Holton et al., 1995]. Since the educts for the stratospheric chemistry originally come from the troposphere, a quantitative understanding of these exchange mechanisms is essential for a quantified prediction of the stratospheric chemistry.

2.3.2 Global Warming

Since the 19th century, mankind is increasing the atmospheric abundance of carbon dioxide, CO_2, by burning the fossil fuels coal, oil and gas. The increase of carbon dioxide and other gases, which absorb infrared radiation, change Earth's radiative budget and lead to *global warming*. The effect was also named *greenhouse effect* and the gases are called *greenhouse gases*.

Observations

The global warming is difficult to verify observationally as the Earth's surface temperature has a relatively large natural variation. Additionally, the effect has a spacial *footprint*, e.g., it is strong in some locations and weak or even negative in others. Figure 2.2 shows a compilation of surface temperature measurements during the last millennium.

During the last decade, the surface temperature has risen significantly above the variations encountered in the thousand years before. Other changes, which are connected to rising temperatures, have been observed on a global scale, too [IPCC, 2001c]. The most striking ones are:

- The snow cover and ice extent have decreased.
- The global average sea level has risen by about 10–$20\,\mathrm{cm}$ during the 20th century.
- The precipitation has increased over most northern high and mid latitudes, while it has decreased over most northern sub-tropics. (A clear example of a *footprint*.)

Explanation

The basic principles of the greenhouse effect are well understood, for a detailed explanation see, e.g., Wayne [1991]. It is based on the fact that the incoming solar short-wave radiation energy flux is balanced by the outgoing thermal long-wave radiation energy

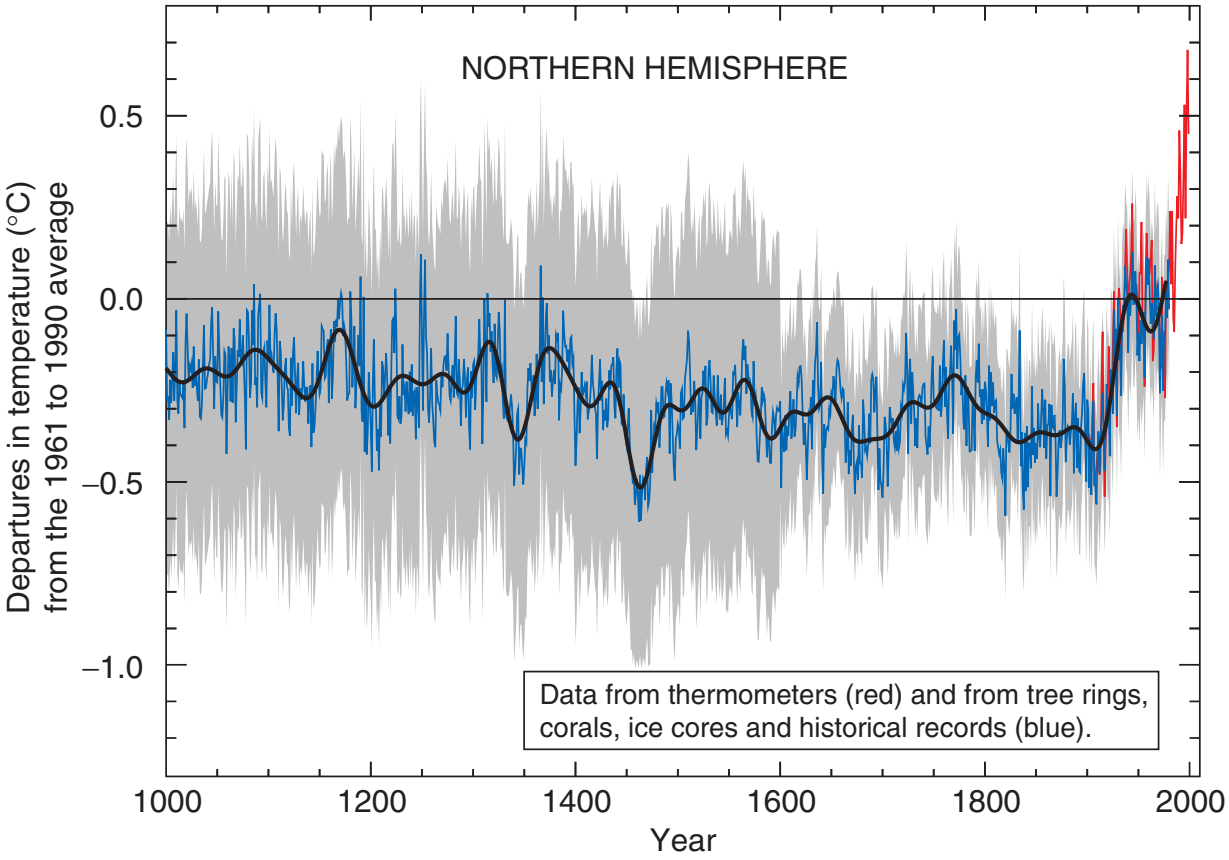

Figure 2.2: Variations of Earth's surface temperature over the last millennium. Year by year (blue and red) and 50 year average (black) variations of the average surface temperature of the Norther Hemisphere along with the annual 95 % confidence range (grey). [IPCC, 2001c, fig. 1]

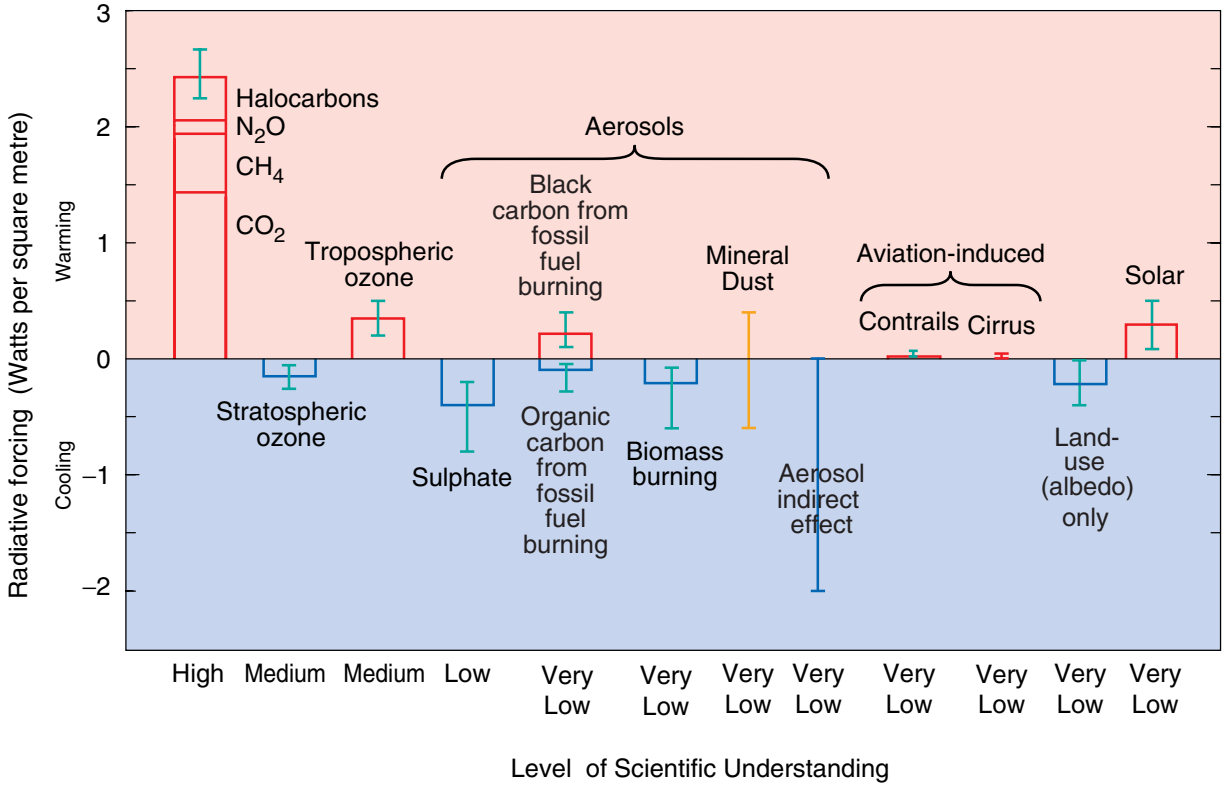

Figure 2.3: Estimated contributions to external climate forcing. [IPCC, 2001c, fig. 3]

flux. Atmospheric constituents with absorption bands in the infrared disturb this balance by partially blocking the outgoing radiation. Thus the average surface temperature is altered depending on the abundance of the greenhouse gases.

Even though global warming has been predicted long before its observational verification, quantifications are difficult to obtain, owing to the complexity of the atmosphere. The effect $[\mathrm{W/m^2}]$ on Earth's energy balance is called *radiative forcing*. Figure 2.3 summarises the current knowledge of the radiative forcing due to the most important alterations of Earth's state, all of which are linked in some form to human activity. The forcing due to solar variability is also shown.

In addition to the directly emitted pollutants, the distribution and abundance of the highly variable natural water vapour and clouds have a significant influence on the radiative budget of the Earth[11]. Since global warming changes the dynamical behaviour of the atmosphere, it might feedback by redistributing water in the atmosphere. The abundance in the region around the tropopause (the *UT/LS*[12] region) is particularly important for Earth's radiative budget due to the low temperatures in this region.

A concise presentation of the established scientific knowledge on the global warming can be found in IPCC [2001c]. The anticipated impacts and their possible mitigation

[11] Water vapour contributes about $1/3$ of the natural radiative forcing [Wayne, 1991, Table 2.2].
[12] upper troposphere / lower stratosphere

are discussed in IPCC [2001a] and IPCC [2001b].

Political Action

In 1992, the United Nations hosted the *United Nations Conference on Environment and Development* (*UNCED*) in Rio de Janeiro. During the conference, a framework for the protection of Earth's climate against too strong anthropogenic influence was set and the industrial nations promised to reduce their emissions of greenhouse gases to the values of 1990. Unfortunately, this goal was not met.

In 1997, the *Kyoto protocol* was signed in the framework set by UNCED. In it, the industrialised countries agreed to decrease their emission of greenhouse gases until 2012 by about $5\,\%$ as compared to 1990. However, the Kyoto protocol has not been ratified by any of these countries yet.

Future Development

The prediction of future surface temperatures is very difficult for two reasons:

- It is unclear how much anthropogenic emission of greenhouse gases will occur. This appears unpredictable especially since the political promises made in the early 1990s were not fulfilled. The reasons behind this failure are the enormous economical implications of the emission control.

- The required numerical model is extremely complex: It needs to account for atmospheric dynamics, atmospheric chemistry, the oceanic system and their coupling.

Predictions of the mean surface temperature during the 21st century are shown in Figure 2.4. The predictions for several emission scenarios are plotted in coloured lines and the range of calculations with different models is given in grey.

It can be concluded that a temperature rise of 2–$4^\circ\mathrm{C}$ is very likely to occur during our century. More precise predictions for each given emission scenario require better models, i.e., better understanding of the complex global system. This, in turn, requires more precise measurements, especially of the "greenhouse-active" UT/LS region.

The control of the Kyoto protocol would require that the tropospheric emissions are measured with global coverage. This can only by done by satellite measurements.

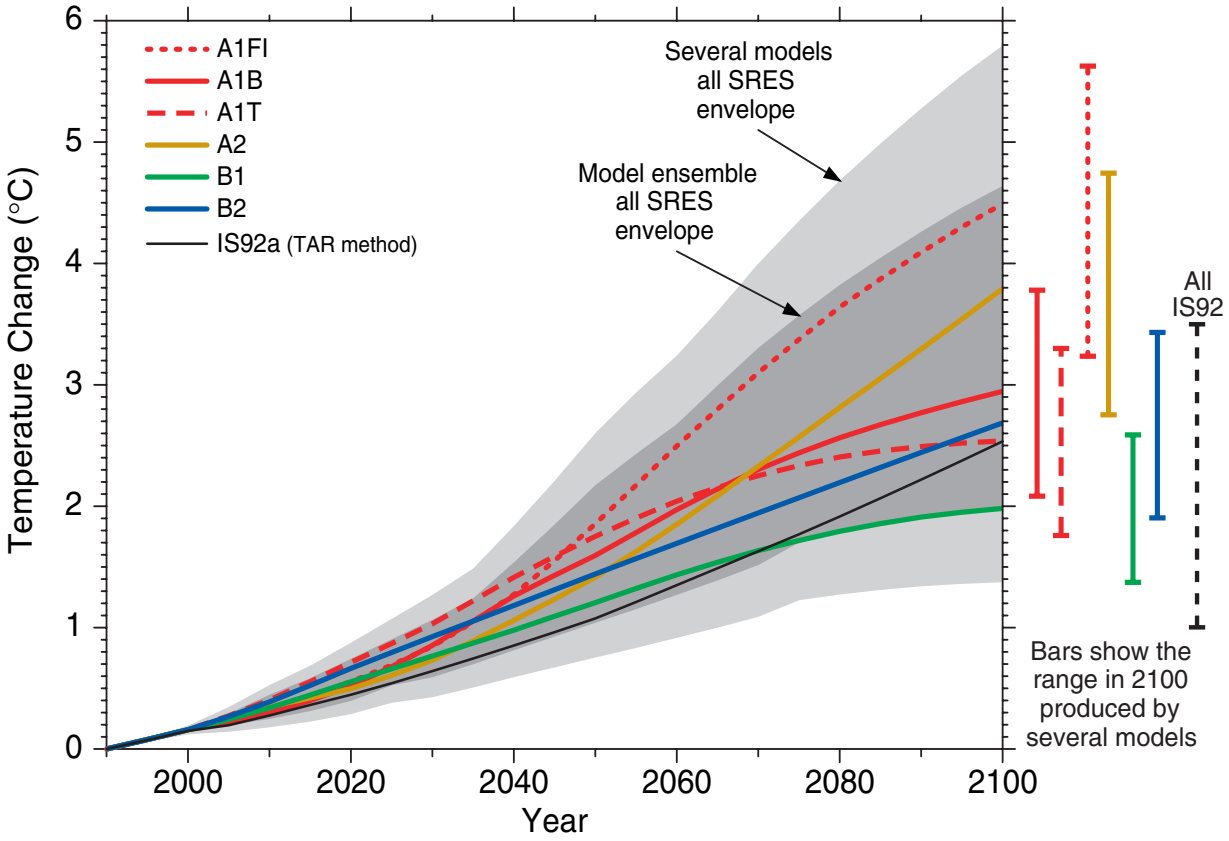

Figure 2.4: Estimated mean surface temperature change for the 21st century. [IPCC, 2001c, fig. 5]

2.3.3 How to deal with it?

The Antarctic ozone hole and the Montreal Protocol are a good example of how the anthropogenic influences on our environment can be dealt with[13]:

1. The monitoring of the atmospheric state led to the relatively early discovery of unforeseen changes, i.e., the ozone hole.
2. Through focused observations and theoretical investigations the phenomenon was understood and the CFCs were identified as the primary cause.
3. On the basis of the newly understood mechanisms, fast political action was taken with the Montreal Protocol.
4. Further quantitative understanding enabled more realistic predictions with improved numerical models. These served for an enhancement of the political action.
5. Finally, the success of the political action is controlled by sustained monitoring. At the same time, this may lead to new discoveries, which imply a return to step 1.

Measurements are important for this process in three different respects:

- monitoring (step 1, 5)
- New mechanisms may by discovered and validated by comparison of models with past measurements. (step 2)
- The prediction of the future requires a detailed knowledge of the current state. (step 4)

The political reaction toward controlling global warming due to the emission of greenhouse gases will hopefully become effective in the near future. More accurate predictions still require substantial scientific progress, i.e., theoretical and observational work. In addition to the points mentioned above, the

- monitoring of each country's total emission of greenhouse gases

will become important for the success of our effort to control the impact of human activities.

Satellite-based measurements are particularly useful as they yield data sets with full global and temporal coverage. Modern instruments observe a large set of atmospheric parameters, e.g., different trace gases. Spectrometers for the UV-vis-NIR spectral region constitute an important class of such instruments. They are discussed in the next chapter.

[13]The whole process reflects the interaction between observations and theory which is typical for empirical sciences.

Chapter 3

SCIAMACHY

The ESA satellite *Envisat*[1] is scheduled for launch in October 2001. It will fly on a sun-synchronous polar orbit[2] with 10 a.m. descending node and carry a large range of instruments for probing Earth. Among these instruments is the spectrometer *SCIAMACHY* (**SC**anning **I**maging **A**bsorption Spectro**M**eter for **A**tmospheric **CH**artograph**Y**) which has been designed for the observation of the atmospheric composition.

SCIAMACHY is a passive remote sensing instrument operating in a wavelength range from the ultraviolet through the visible to the near infrared (UV-vis-NIR) with a moderate spectral resolution. It represents a new generation of atmospheric measurement devices in two respects: It combines a novel measurement geometry with well established geometries and it is *hyperspectral*, i.e., it simultaneously covers a relatively wide wavelength range with many spectral points. SCIAMACHY will measure a large set of atmospheric parameters simultaneously and therefore self-consistently. Among the retrieval targets are the trace gases O_3, NO_2, OClO, BrO, SO_2, HCHO, H_2O, CH_4, CO_2, CO, and N_2O. Additionally, temperature, aerosol and cloud parameters will be determined. A concise description of the major aspects of the SCIAMACHY mission has been compiled by Bovensmann et al. [1999].

The next three sections illuminate the two new aspects of SCIAMACHY's measurements. Section 3.4 describes other flown, flying and seriously projected limb scattering sensors in the UV-vis. Finally, requirements for the retrieval of atmospheric parameters from such measurements are pointed out in Section 3.5.

3.1 Optical Characteristics

SCIAMACHY is recording atmospheric radiance spectra in the UV-vis-NIR range 240–2380 nm. The radiation in this spectral range originates almost completely from

[1] URL http://envisat.esa.int

[2] *polar*: The poles are (approximately) passed by. *sun-synchronous*: The local time underneath the satellite is the same for all orbits. *descending node*: The equator crossing on the satellite's way southwards. Its local time roughly equals the local times of all dayside positions.

the sun and is scattered in the atmosphere. Shorter wavelength radiation is not suitable for atmospheric remote sensing as it does not penetrate the atmosphere. Longer wavelength radiation is used by other instruments, e.g., MIPAS [Endemann, 1999]. These instruments measure (mostly) the thermal emission of the atmosphere itself, while scattering is a secondary effect.

The UV-vis-NIR spectral range has the advantage that high signal/noise (*S/N*) ratios can be achieved due to the relatively high energy of the photons and the large intensity of the solar radiation. (Typical S/N values of SCIAMACHY are shown in Figure 9.1.) Disadvantages of this spectral range are that the nightside cannot be observed[3] and that clouds interfere with the radiative transfer. Cloud-free radiative transfer modelling alone is very demanding.

The cross sections associated with the ozone absorption and the Rayleigh and aerosol scattering vary extremely within the spectral range of SCIAMACHY. Generally, the atmosphere becomes more opaque for shorter wavelengths[4]. Therefore, different spectral regions of each individual measurement are sensitive to different height regions of the atmosphere. This *hyperspectral* advantage enhances SCIAMACHY's spacial resolution even further (see Chapter 10).

SCIAMACHY has been designed as a double spectrometer: The whole spectral range is separated by a predisperser prism and dichroic mirrors into eight spectral channels. In the channels, the spectra are observed with eight individual gratings and photo diode arrays with 1024 pixels each. Thus approximately 8000 spectral points are recorded simultaneously. The spectral ranges of the eight channels and their spectral resolution are listed in Table 3.1.

Table 3.1: Optical Parameters of SCIAMACHY's Spectrometer

channel no.	spectral range [nm]	resolution [nm]
1	240–314	0.24
2	309–405	0.26
3	394–620	0.44
4	604–805	0.48
5	785–1050	0.54
6	1000–1750	1.48
7	1940–2040	0.22
8	2265–2380	0.26

[3] It is obviously dark.

[4] Below about 300 nm, the ozone absorption is so strong that virtually no radiation can penetrate the stratospheric ozone layer. Up to about 400 nm the scattering is so strong that multiple scattering strongly influences the radiance. For larger wavelengths, the relative contribution of multiple scattering becomes weaker and weaker.

3.2 Measurement Geometries

The three observational measurement modes of SCIAMACHY are depicted in Figure 3.1.

The *nadir* measurement mode is well-known from instruments like TOMS, SBUV and GOME. The instrument is facing straightly downward to measure the radiance from underneath the satellite. Thus solar radiation, which has been scattered in the atmosphere and/or reflected on the surface, is recorded. These measurements are performed on the whole dayside of Earth.

An advantage of the nadir measurements is the fact that global coverage[5] can be achieved in three days as Envisat is flying in a sun-synchronous polar orbit and Earth is rotating underneath. Furthermore, retrieval from this measurement geometry can be performed with a good horizontal resolution.

Its main disadvantage is the fact that very little information on the vertical structure of the atmosphere is obtained. The shapes of most trace gas profiles are even need as *a priori* information for the retrieval of their column densities.

The *occultation* measurement mode is also well-established by instruments like POAM and SAGE [e.g., Chu et al., 1989, Tsou et al., 1995]. The instrument is tracking the sun (or the moon) during its rise or set behind Earth. Thus mainly directly transmitted solar (or lunar) radiation is recorded for different tangent altitudes.

Occultation measurements yield highly accurate information on the vertical structure of the atmosphere, but they have a bad horizontal resolution owing to the averaging over long paths. They are not suitable to obtain measurements with global coverage since only one sunrise[6] can be measured per satellite orbit.

The *limb* measurement mode of SCIAMACHY is a combination of the nadir and occultation geometries: The instrument is scanning the Earth's limb like in occultation mode, while the sun is illuminating the atmosphere from above like in nadir mode. Thus atmospheric radiance spectra can be obtained for different tangent altitudes at any location on Earth's dayside.

By that means, limb measurements of scattered solar radiation combine the advantages of nadir and occultation measurements: Vertically resolved information on the atmospheric composition is obtained with global coverage. The price for this combination of advantages is the relatively bad horizontal resolution of the occultation mode.

The retrieval algorithms required for limb measurements in the UV-vis-NIR spectral range of the whole stratosphere are very demanding, see Section 3.5. This is a major reason why such measurements have never been performed operationally. Only very few individual measurements exist so far, see Section 3.4.

[5] except for the polar winter

[6] SCIAMACHY is looking forward, i.e., in the flight direction. Therefore, the sunrise over the Arctic is recorded, but no sunset. The lunar rises are all in the Southern Hemisphere, but they occur less frequently.

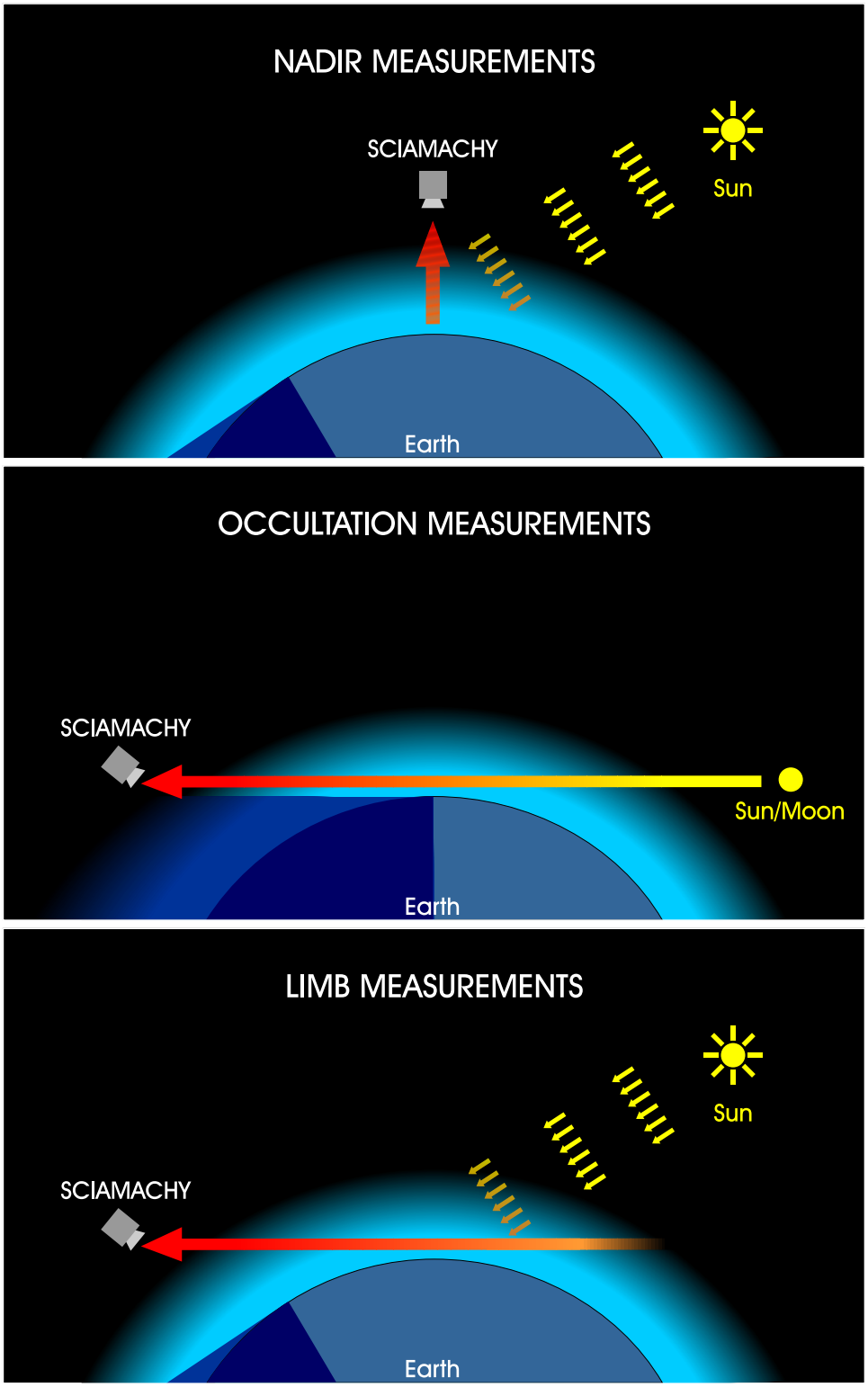

Figure 3.1: SCIAMACHY's three measurement geometries. (graphics by S. Noël)

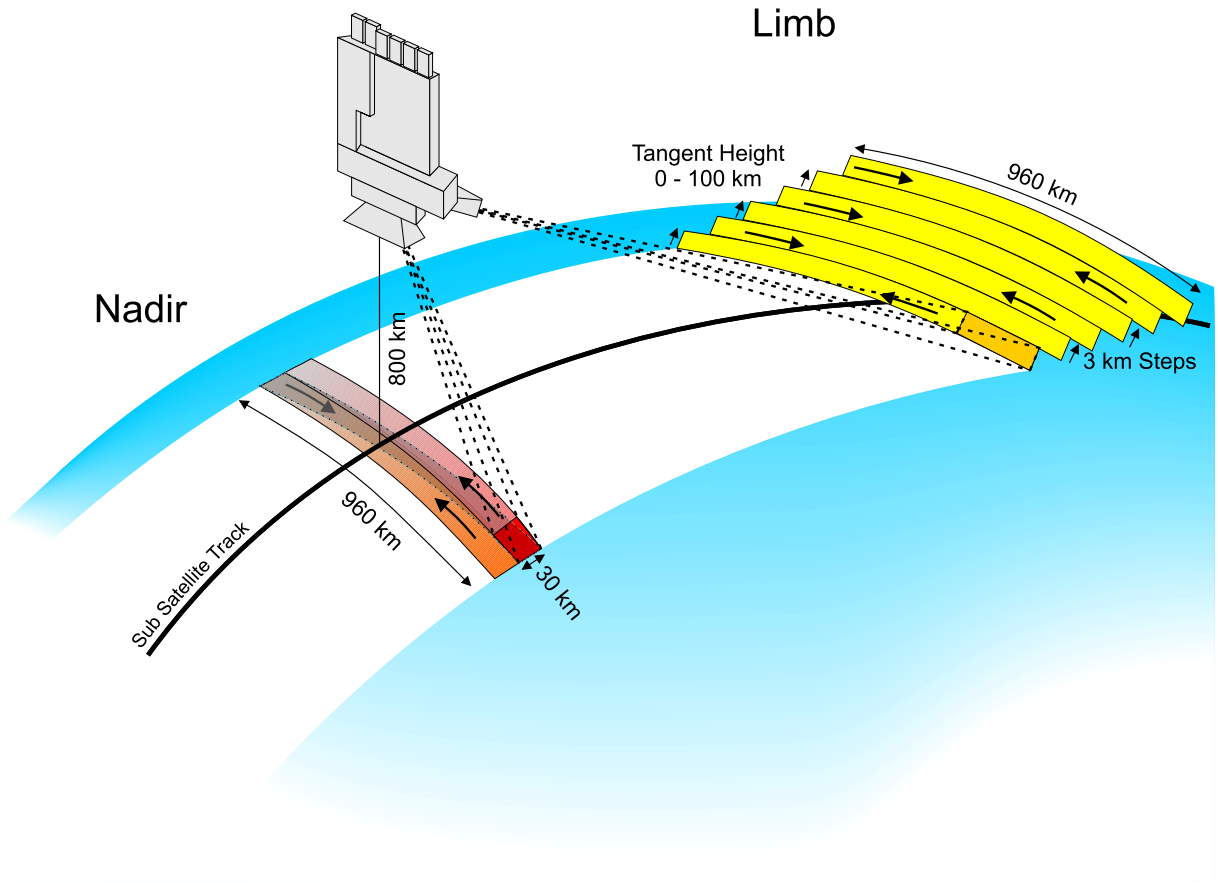

Figure 3.2: Details of SCIAMACHY's nadir and limb measurement geometries. (graphics by S. Noël)

3.3 Spacial Characteristics

Details of SCIAMACHY's spatial resolution and scan sequence are shown in Figure 3.2.

Nadir Mode

In nadir mode, the nadir mirror scans across the satellite track and returns to its original position for the next scan. Each scan covers an area on the ground of approximately $30\,\mathrm{km}$ along track (mostly North–South) and $960\,\mathrm{km}$ across track (mostly East–West). Therefore, the spatial resolution along track is $30\,\mathrm{km}$. Across track, it is determined by the number of readouts per scan, which is determined by the scan speed of the mirror ($240\,\mathrm{km/s}$), the integration time of the detector, and the number of on-board coadditions of successive integration periods. The latter two are optimised to meet requirements set by signal/noise, saturation of the detector, and the available data rate to the ground station.

Depending on the integration periods and numbers of coadditions, the spatial res-

olution across track varies for different parts of the measurement spectrum: A typical upper limit for all pixels is $240\,\mathrm{km}$. A better resolution of $60\,\mathrm{km}$ across track will be achieved for the important constituents O_3, NO_2, H_2O, and aerosols in mid and high latitudes. The seven broad-band *polarisation measurement devices* (*PMD*s) will even perform with $15\,\mathrm{km}$ resolution across track for cloud characterisation.

Limb Mode

In limb mode, SCIAMACHY is looking forward in flight direction. Horizontal scans (analogous to across track) are embedded in each vertical scan of Earth's limb: Starting with approximately zero tangent height, a horizontal scan of $960\,\mathrm{km}$ at the tangent point is performed. Then the tangent height is stepped up by $3\,\mathrm{km}$ and another horizontal scan back is done. This procedure is repeated, until typically 34 horizontal scans with tangent heights between 0 and $100\,\mathrm{km}$ are obtained[7]. This cycle imposes limits on the spacial resolution of the limb measurements.

The *instantaneous field of view* (*IFOV*) limits the spacial resolution, too. In order to achieve a good vertical resolution, the spectrometer's slit is projected horizontally. Thus the IFOV opens with $0.045\,^\circ$ vertically and $1.8\,^\circ$ horizontally. At the tangent points, these values roughly correspond to $2.6\,\mathrm{km}$ vertically and $110\,\mathrm{km}$ horizontally.

The vertical resolution is limited by the IFOV and the tangent height stepping size. Therefore, it is effectively $3\,\mathrm{km}$ (for parameters with strong signature). The horizontal resolution across track is limited by the IFOV and the number of readouts during the horizontal scan. With typically four readouts, a value of roughly $240\,\mathrm{km}$ will be achieved. It can by no means be improved to $110\,\mathrm{km}$ or less.

The horizontal resolution along track is determined by the nearly horizontal paths with lengths of the order of several, say four, hundred kilometres.

In-Flight Flexibility

It shall be noted that the integration times and numbers of on-board coadditions of the various spectral windows (*clusters*) within the whole measured spectrum can still be optimised in-flight in order to find the best compromise between retrieval precision and spacial resolution.

3.4 Other Space-Borne Limb Scattering Measurements

A complete overview over passive remote sensing instruments for atmospheric applications has been given by Burrows [1999]. In this section, an updated list of space-borne limb scattering measurements is discussed briefly.

[7] The whole cycle has a typical duration of $60\,\mathrm{s}$, during which the spacecraft moves roughly $400\,\mathrm{km}$ forward.

SME

The *Solar Mesosphere Explorer* (*SME*) was the first space-borne UV-vis-NIR spectrometer operating in limb mode [Thomas et al., 1980, Barth et al., 1983]. It measured the scattered limb radiance for tangent height from 20 to $120\,\mathrm{km}$ between the Decembers of 1981 and 1986.

The scattered solar radiation was recorded at two wavelengths in the UV ($265\,\mathrm{nm}$ and $296\,\mathrm{nm}$) and a pair of wavelengths in the visible (around $440\,\mathrm{nm}$). Additionally, emission lines at $1.27\,\mu\mathrm{m}$ and $1.87\,\mu\mathrm{m}$ were observed. From the UV and visible wavelengths, retrievals were successfully and operationally performed for ozone and NO_2 in the height ranges 45–$70\,\mathrm{km}$ and 28–$40\,\mathrm{km}$, respectively. The retrieval's altitude ranges had to be limited as the retrieval algorithms employed the single scattering approximation [Mount and Rusch, 1984, Rusch et al., 1983, 1884, Thomas et al., 1984].

SOLSE/LORE

The instrument pair *SOLSE/LORE* was flown by NASA as a proof-of-concept mission on the Space Shuttle in December 1997. It operated in the 260–$350\,\mathrm{nm}$ spectral region with a resolution of $0.5\,\mathrm{nm}$ and had additional filters at 345, 525, 603, 677, and $1000\,\mathrm{nm}$. One ozone profile for 15–$50\,\mathrm{km}$ height has successfully been retrieved and validated from SOLSE/LORE's measurements [McPeters et al., 2000]. In order to compensate for unknown aerosol, cloud and surface reflection effects, all radiances are divided by those of one reference tangent height and used in pairs of strong/weak O_3 absorptions [Flittner et al., 2000].

OSIRIS

The spectrometer *OSIRIS* has been launched aboard the Swedish satellite *ODIN* in February 2001. It records the spectral range 280–$800\,\mathrm{nm}$ with a resolution of 1–$2\,\mathrm{nm}$ and an additional band at $1270\,\mathrm{nm}$ [Llewellyn et al., 1997]. Thus about 500 spectral points are obtained simultaneously for each tangent height. The satellite is flying in a sun-synchronous orbit over the *terminator* ($90\,^\circ$ solar zenith angle). The first spectra have been recorded successfully, but no retrieval has been published by June 2001.

GOMOS

The spectrometer *GOMOS* was designed for the measurement of stellar occultations in the UV-vis spectral range 250–$675\,\mathrm{nm}$ with a resolution of $0.6\,\mathrm{nm}$ [Bertaux et al., 1991]. Two additional NIR channels exist at 753–$773\,\mathrm{nm}$ and 926–$952\,\mathrm{nm}$. Like SCIAMACHY, it belongs to the payload of Envisat, which is schedule for launch in October 2001. Since GOMOS measurements need to be corrected for the background of solar radiation scattered in the atmosphere, this correction term is observed, too. In theory, the correction

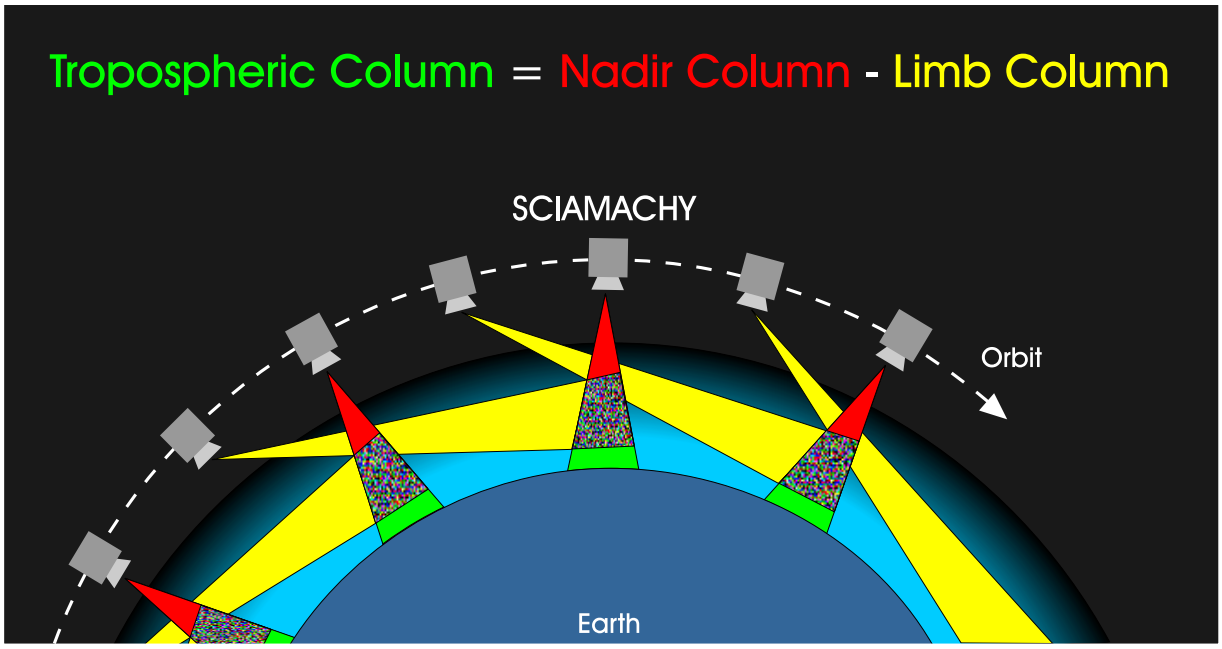

Figure 3.3: Matching of SCIAMACHY's nadir and limb measurements. (graphics by S. Noël)

term can be used for retrievals itself, but its spectral resolution of $5\,\mathrm{nm}$ is relatively poor[8].

3.5 Retrieval Considerations

Limb-Nadir Matching

A speciality of SCIAMACHY is depicted in Figure 3.3: The timeline of operations is designed in a way that each limb measurement is followed after 7 minutes by a nadir measurement of the same atmospheric volume. Since the stratospheric profile of a trace gas is determined from the limb measurement, the stratospheric column is known. Subtracting this from the total column, which is measured in nadir, yields the tropospheric column. Therefore SCIAMACHY is capable of measurements of the troposphere.

Future advanced retrieval algorithms will exploit SCIAMACHY's limb-nadir matching even more efficiently by retrieving from the matching limb and nadir measurements simultaneously, i.e., in a *tomographic* fashion. This approach is expected to yield improved tropospheric parameters as well as vertically and horizontally resolved parameter fields.

[8]The spectral resolution of the transmitted stellar spectra is much better since the tiny apparent size of the stars is employed in a clever way to substitute the spectrometer's entrance slit.

Limb Measurements

Up to date, the only published retrievals from space-borne UV-vis limb measurements are those of SME and SOLSE/LORE. Compared to these instruments, SCIAMACHY is covering a wider spectral range with better spectral resolution and aiming at retrievals of a more complete set of atmospheric parameters. This requires more generally applicable retrieval algorithms.

Since the retrieval from UV-vis-NIR limb measurements of the stratosphere is a new technique, existing radiative transfer models (RTM) and retrieval strategies have to be adapted and extended or replaced for the accurate inversion of these observations. The most demanding requirements for the RTM are:

- Earth's sphericity must be fully accounted for.
- Multiple scattering and surface reflection have to be modelled.
- Weighting functions[9] must be calculated in a computationally efficient way along with the radiances. This can only be achieved by evaluating the weighting functions from analytical formulae, i.e., with so-called *quasi-analytical* computations.

Up to date, no published RTM fulfils all three requirements.

In order to process the large amounts of data produced by SCIAMACHY (6 CDs of highly compressed data daily), it will be necessary to speed up the RTM by introducing reasonable approximations.

Goal of this Thesis

The goal of this thesis is the development of the basis of an RTM and retrieval algorithms for SCIAMACHY's limb measurements and their application for the characterisation of UV-vis-NIR limb measurements in general and those SCIAMACHY in particular.

[9] See page 75 for a definition.

Part II

THEORY

Outline of the Theory

This part introduces the new program package *SCIARAYS*, which has been developed and implemented for this thesis. It consists of new radiative transfer and instrument models and algorithms for retrievals from UV-vis-NIR limb measurements.

The physical processes which determine the optical properties of the Earth's atmosphere are described in Chapter 4.

Given the atmosphere's optical properties, the radiative transfer equation has to be solved: Chapter 5 introduces the equation and discusses several approaches to solving it, partially by making approximations.

The actual implementation of the new radiative transfer model in *SCIARAYS* is described in Chapter 6. Besides computing the atmospheric radiance, the model calculates the weighting functions for all atmospheric model parameters efficiently from analytical formulae.

The newly developed instrument model performs the field-of-view integration and computes signal-to-noise ratios depending on the simulated radiances. It's implementation in *SCIARAYS* is described in Chapter 7. The parametrisation is chosen to represent the real SCIAMACHY instrument.

Both the RTM and the instrument model are used by the retrieval algorithms implemented in *SCIARAYS*. They are briefly described in Chapter 8.

Note: The spherical geometry of the radiative transfer problem requires a careful parametrisation of the light ray paths. The necessary formulae are derived with and without refraction in appendix A.

Chapter 4

Radiative Processes in the Atmosphere

4.1 Rayleigh Scattering

The elastic scattering of light by the molecules of a gas is called *Rayleigh scattering*, *molecular scattering* or *Cabannes scattering*. It is an elastic, incoherent process: No energy is absorbed, so that the frequency of the light remains unchanged, and there is no phase correlation between incident and scattered light. Since the scattered light is partially polarised, a complete description needs to take into account the 4-dimensional Stokes vectors [e.g., Coulson, 1988]. The present work is limited to the intensities of the radiation. Therefore, the 2^{nd}–4^{th} components of the Stokes vectors, which describe the polarisation effects, are neglected.

Leonardo da Vinci was the first to investigate the scattering of solar light by small particles [Richter, 1970, p. 237 ff.]. John William Strutt, who became the Lord Rayleigh later on, published the first quantitative description and applied it for an explanation of the blue colour of the sky [Strutt, 1871]. King [1923] derived a correction factor taking into account the non-isotropy of the polarisability of the air's molecules.

The intensity of Rayleigh scattering is described by the *Rayleigh scattering cross section* χ_r and the angular distribution of the scattered light by the dimensionless *Rayleigh scattering phase function* ϕ. The unit of χ_r is that of a surface, commonly $[cm^2]$.

The Rayleigh scattering cross section $\chi_r(X)$ of a species X is given by [cf. Dalgarno and Williams, 1962, Chandrasekhar, 1960, (256)]

$$\chi_r(X) \quad = \quad \frac{8\pi^3}{3N_A^2} \frac{(n^2(X)-1)^2}{\lambda^4} F_{King}(X) \quad , \tag{4.1}$$

where N_A denotes *Avogadro's number*[1], and $n(X)$ is the *refractive index* at this density (see Section 4.6). The *King factor* $F_{King}(X)$ is commonly expressed in terms of the *depolarisa-*

[1] $N_A = 2.686763 \cdot 10^{19}\,\mathrm{molec/cm^{-3}}$ is the air number density at standard conditions. It is also called *Loschmidt number* in older literature and should not be confused with Avogadro's constant $6.022 \cdot 10^{23}\,\mathrm{molec/mol}$. [Falbe and Regitz, 1995]

tion factor $d(X)$ of species X [King, 1923]:

$$F_{King}(X) = \frac{6 + 3\,d(X)}{6 - 7\,d(X)} \quad . \tag{4.2}$$

The Rayleigh scattering cross section χ_r of air is the weighted mean value of all constituent's cross sections:

$$\chi_r = \sum_X f(X)\chi_r(X) \quad , \tag{4.3}$$

with $f(X)$ being the volume mixing ratio[2] of constituent X. In analogy to (4.1) an *effective King correction factor*[3] F_{King} for air can be defined such that:

$$\chi_r = \frac{8\pi^3}{3N_A^2}\frac{(n^2-1)^2}{\lambda^4}F_{King} \quad . \tag{4.4}$$

Sometimes this expression is modified by the approximation $n^2 - 1 \approx 2\,(n-1)$, which holds for $n \approx 1$. The following formula also adjusts the units to those used in GOMETRAN and *SCIARAYS*:

$$\chi_r[\mathrm{cm}^2] = \frac{32\pi^3}{3}\left(10^{14}\frac{n[\text{-}]-1}{N_A[\mathrm{cm}^{-3}]}\right)^2\frac{F_{King}[\text{-}]}{\lambda^4[\mathrm{nm}^4]} \quad . \tag{4.5}$$

The effective King factor can either be computed by interpolating the table by Bates [1984] or by evaluating (4.2) with a prescribed depolarisation factor d, e.g., by Young [1980]. The latter is implemented in GOMETRAN, *SCIARAYS* and MODTRAN3.7 with $d = 0.0295$ and 0.0279. The value of the refractive index can be calculated, for instance, with Edlén's parametrisation (4.20).

The *Rayleigh scattering coefficient* σ_r is obtained by multiplication with the *neutral density* n, which can be obtained from the ideal gas law[4]:

$$\sigma_r = \chi_r\, n \tag{4.6}$$

$$n = \frac{p}{k_B\,T} \quad , \tag{4.7}$$

where $k_B = 1.3806 \cdot 10^{-23}\mathrm{J/K}$ is *Boltzmann's constant*.

The *Rayleigh scattering phase function* ϕ is given by [cf. Lenoble, 1993, (12.28)]

$$\phi(\gamma) = \frac{1}{4\pi}\,\frac{3}{2}\,\frac{1}{2+d}\,\left[(1+d) + (1-d)\cos^2(\gamma)\right] \quad , \tag{4.8}$$

where γ denotes the scattering angle. It is normalised to unity.

[2] also known as *fractional volume abundance*

[3] The concept of an effective King factor is necessary since the cross section depends non-linearly on the refractive index of the constituents.

[4] In the common units of GOMETRAN and *SCIARAYS*, (4.6) and (4.7) become:
$\sigma_r[\mathrm{km}^{-1}] = \chi_r[\mathrm{cm}^2]\,n[\mathrm{cm}^{-2}\mathrm{km}^{-1}]$
$n[\mathrm{cm}^{-2}\mathrm{km}^{-1}] = 10^{-1}\,n[\mathrm{m}^{-3}] = 10^{-1}\,\frac{p[\mathrm{Pa}]}{k_B[\mathrm{J/K}]\,T[\mathrm{K}]} = 10\,\frac{p[\mathrm{hPa}]}{k_B[\mathrm{J/K}]\,T[\mathrm{K}]}$.

4.2 Trace Gas Absorption

Gaseous molecules absorb photons with energies corresponding to their quantum-mechanical transitions. Electronical, vibrational and rotational transitions cause absorption lines in the spectrum of transmitted radiation, while ionisation and dissociation processes lead to absorption continua.

The strength of the absorption is quantified with the *molecular absorption cross section* χ_i of the species i, which has the units of a surface, commonly $[\mathrm{cm}^2]$. It is strongly wavelength-dependent and often varies with temperature (Doppler broadening with Gaussian shape), pressure (broadening with Lorentian shape), and the occupation numbers of the quantum-mechanical states. The variations are generally more pronounced in the near infrared (*NIR*) wavelength region than in the ultraviolet (*UV*) and visible (*vis*).

During molecule collisions the excitation energy can be transformed to thermal energy which is distributed among the molecules. The final effect is a heating of the whole absorbing gas. This process of *thermalisation* is called *collisional quenching*. If it is fast enough to make the occupation numbers of the quantum-mechanical states conform to the Boltzmann distribution with a temperature equal to the thermal temperature at each location, then the system is in the *local thermodynamic equilibrium* (*LTE*). This is given for Earth's troposphere and most parts of its stratosphere.

Molecular absorption cross sections χ_i are available from data bases of several types:

1. Files containing $\chi_i(\lambda)$, possibly for several temperatures, are obtained from spectroscopic laboratory measurements of the species i at the specified temperature(s).

2. The coefficients of the *Bass-Paur-parametrisation* as obtained from a fit to laboratory measurements can be used to model the wavelength and temperature dependent ozone absorption cross section in the UV.

3. The *HITRAN* data base contains parameters of many individual absorption lines which are derived from laboratory measurements and theoretical considerations. They are used to calculate the molecular absorption cross sections depending on given temperatures and pressures with high spectral resolution in the NIR wavelength range.

4. An ESFT data base can be created for predefined spectral grid and resolution from the HITRAN data base. The ESFT method allows to significantly speed up so-called line-by-line radiative transfer calculations [Buchwitz et al., 1998, Buchwitz, 2000].

The most important atmospheric trace gas absorption cross sections in SCIAMACHY's spectral range are plotted in the Figures 4.1–4.3.

Figure 4.1 shows the absorption cross sections of absorbers, which do not vary pressure. They are generally measured in the laboratory for several temperatures, stored in files and interpolated for radiative transfer calculations. O_3 has been measured in

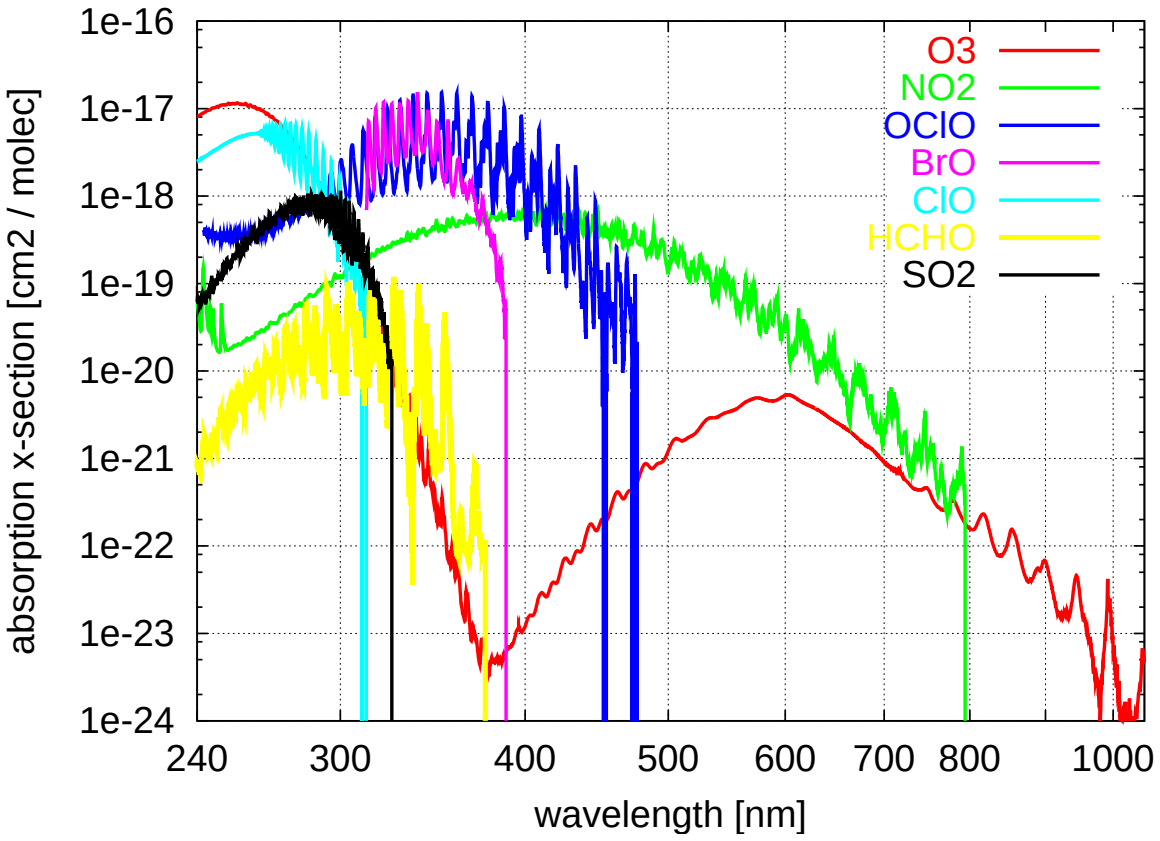

Figure 4.1: Absorption cross section of trace gases in the UV-vis spectral region. O_2 and H_2O are shown in Figure 4.2. Note that both axes are logarithmic.

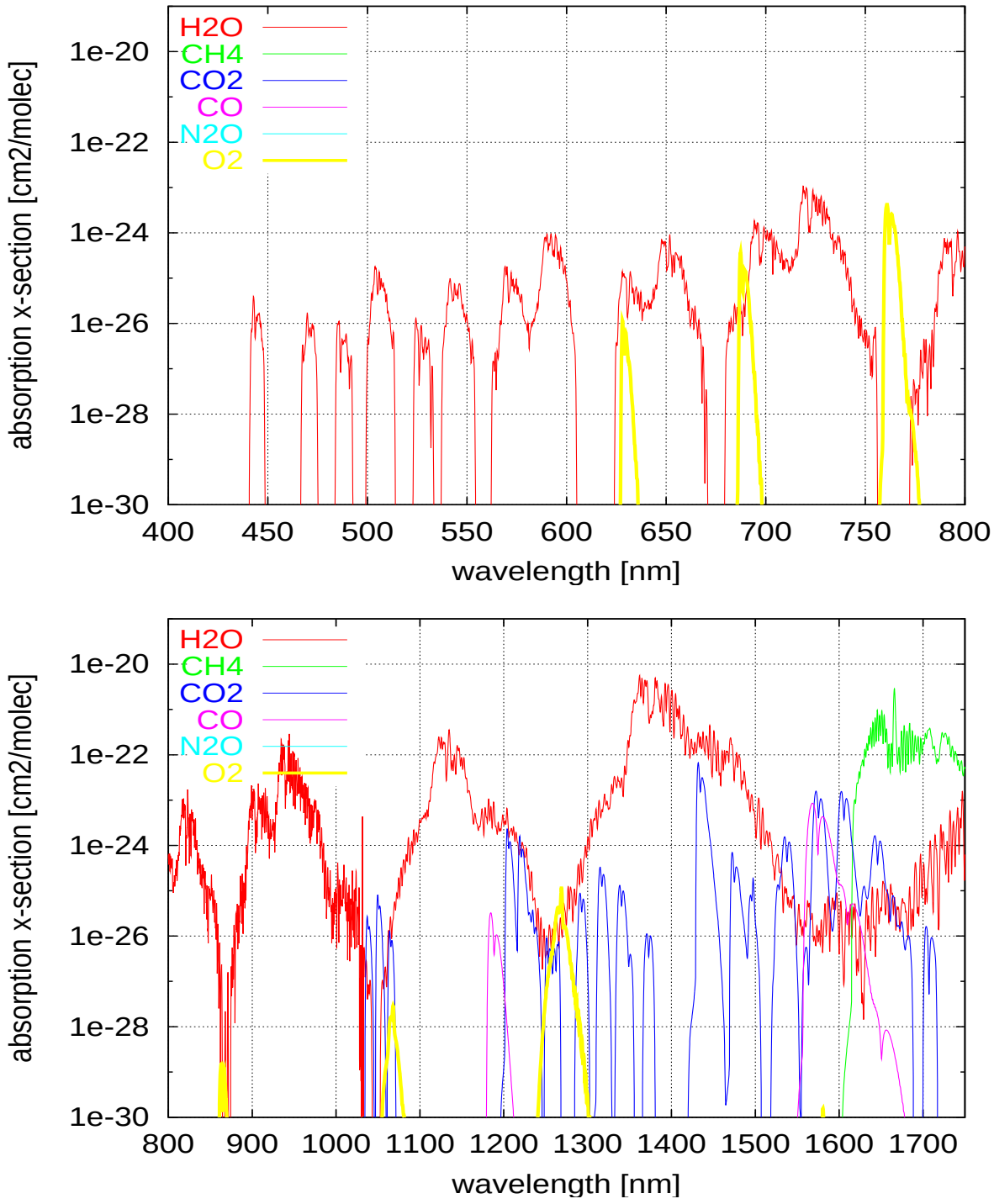

Figure 4.2: Absorption cross sections of trace gases in SCIAMACHY's channels 3–6. In the visible range, the molecules shown in Figure 4.1 are omitted. The yellow curves represent O_2.

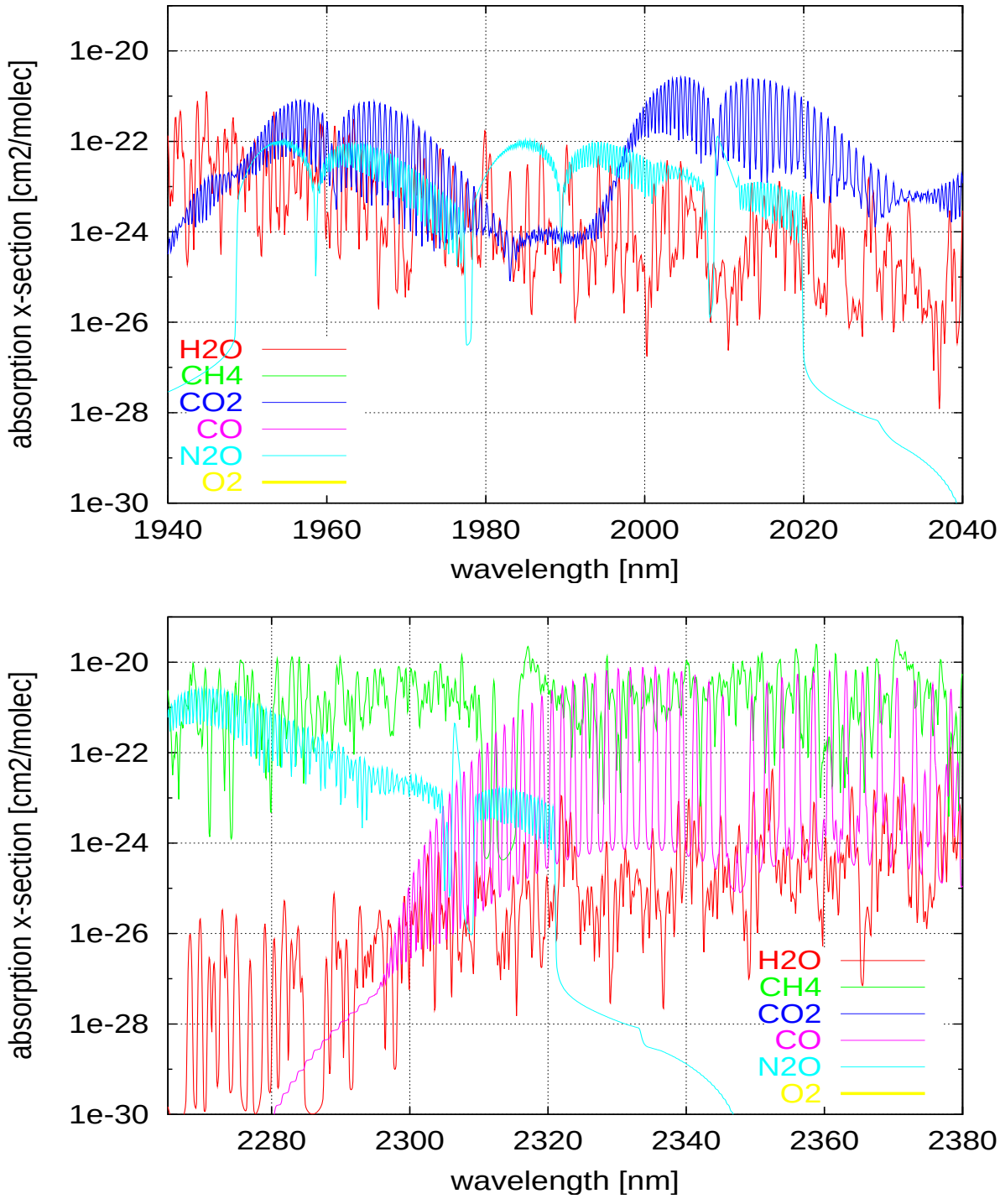

Figure 4.3: Absorption cross sections of trace gases in SCIAMACHY's channels 7 (top) and 8 (bottom).

the laboratory with SCIAMACHY and provided by Bogumil et al. [1999]. NO_2 cross sections have been recorded using the GOME spectrometer by Burrows et al. [1998]. Thus the cross sections themselves have the spectral resolution of SCIAMACHY. The cross sections of BrO, OClO, ClO and SO_2 are taken from Wahner et al. [1988], Wahner et al. [1987], Simon et al. [1990] and Hearn and Joenst [1991], respectively. For the cross sections of HCHO consult Moortgat et al. [1980] and Meller and Moortgat [2000].

Figures 4.2–4.3 show the absorption cross sections of H_2O, CH_4, CO_2, CO, N_2O and O_2, which vary with temperature and pressure. They have been extracted from the HITRAN data base and convolved with SCIAMACHY's slit function. The assumed temperature and pressure are $229\,\mathrm{K}$ and $9\,\mathrm{hPa}$. The cross sections of molecules, for which no curves are visible, are smaller than $10^{-30}\,\mathrm{cm}^2$.

4.3 Aerosol Scattering and Absorption

Aerosols scatter and absorb light. The sum of the *aerosol scattering coefficient* σ_{ai} and the *aerosol absorption coefficient* α_{ai} yields the *aerosol extinction coefficient* κ_{ai} for each aerosol type i. All three coefficients have the unit of an inverse length, e.g., $[\mathrm{km}^{-1}]$. The angular distribution of the scattered light is modelled with the dimensionless *aerosol scattering phase function* ξ_i. Generally, it has a strong peak in the forward scattering direction and is very complex otherwise. A widely used parametrisation is the *Henyey-Greenstein* phase function [e.g., Sobolev, 1975, (1.16)]:

$$\xi_i(\gamma) \;=\; \frac{1-g^2}{(1+g^2-2g\cos\gamma)^{3/2}} \quad , \tag{4.9}$$

with the *asymmetry factor* g in the range $[-1,1]$. The Henyey-Greenstein phase function is normalised to 4π.

For stratospheric background aerosol the absorption is much weaker than the scattering ($\alpha_{ai} \leq 0.95\,\sigma_{ai}$). In this case the extinction coefficient can be approximated by the scattering coefficient alone:

$$\kappa_{ai} \approx \sigma_{ai} \quad . \tag{4.10}$$

Like Rayleigh scattering, the aerosol extinction is a broadband effect. Its wavelength dependence normally is weaker than that of Rayleigh scattering. It can be modelled with the *Ångström parametrisation* [e.g., Hess et al., 1998, (4j)]:

$$\kappa_{ai}(\lambda) = \beta_i\,\lambda^{-\alpha_i} \quad , \tag{4.11}$$

where $\alpha_i \in [-0.5,\,2]$ are typical values. The wavelength λ usually is specified in $[\mu\mathrm{m}]$ and β_i is the aerosol extinction at $\lambda = 1\,\mu\mathrm{m}$.

Unlike trace gas molecules, the individual particles of an aerosol type are microscopically not alike. Therefore, optical properties can only be effective values which describe the whole ensemble of individual particles of an aerosol type in an approximating way.

Thus the extinction coefficient is modelled directly instead of calculating it as product of cross section and number density.

More complex parametrisations of the optical properties of aerosols are employed for the database used in GOMETRAN [Hoogen, 1995].

One of the techniques employed for creating a more complex aerosol model is to describe an atmospheric aerosol scenario with a mixture of several, say N, aerosol types. Then the *aerosol extinction coefficient* κ_a is the sum of the individual extinction coefficients:

$$\kappa_a = \sum_{i=1}^{N} \kappa_{ai} \quad , \tag{4.12}$$

and the *effictive aerosol scattering phase function* ξ is the average of all indivial aerosol scattering phase functions ξ_i weighted with their correspondig scattering coefficients σ_{ai}:

$$\xi = \sum_{i=1}^{N} \sigma_{ai}\, \xi_i \quad . \tag{4.13}$$

4.4 Surface Reflection

At the lower boundary of the atmosphere, Earth's surface partially absorbs the down-welling radiation. The remaining radiation is reflected back into the atmosphere. Since many processes which depend on the surface type (water, vegetation, settlement,...) and the physical conditions (weather,...) are involved, it is impossible to model the reflection *en detail*. Instead, the average properties are parametrised.

Most generally speaking, the reflection is described for every direction $\vec{\Omega}$ by a *bi-directional reflection distribution function* (*BRDF*) $\hat{\rho}(\vec{r}, \vec{\Omega}', \vec{\Omega})$ depending on the location $\vec{r}$ on the surface and the direction of the incoming radiation $\vec{\Omega}'$. The BRDF also depends on the wavelength of the radiation.

The dimensionless *albedo* $A \in [0,\, 1]$ is defined as the ratio of the fluxes of reflected (up-welling) and incident (down-welling) radition:

$$A \;=\; \frac{F^{\uparrow}}{F^{\downarrow}} \quad . \tag{4.14}$$

The approximation of *Lambertian surface reflection* assumes that the reflected light is redistributed isotropically in the upper half sphere. On a homogeneous surface, the reflection does not depend on the location $\vec{r}$. Equating the up-welling flux and the down-welling flux weighted with the albedo yields:

$$\hat{\rho}(\vec{r}, \vec{\Omega}', \vec{\Omega}) \;=\; A\, \rho(\vec{\Omega}') \tag{4.15}$$

$$\text{with:} \quad \rho(\vec{\Omega}') \;=\; \frac{\cos(\psi(\vec{\Omega}'))}{\pi} \quad . \tag{4.16}$$

The factor of angular dependence, ρ, is called *reflection phase function* in this report. It only depends on the zenith angle $\psi(\vec{\Omega}')$ of the incoming radiation, while the albedo A may depend on the wavelength of the radiation.

4.5 Clouds, Thermal Emission and Raman Scattering

Clouds, where present, are the strongest cause of scattering of visible light in Earth's atmosphere. Additionally, their distribution is only in special situations horizontally homogeneous. Therefore, clouds constitute one of the hardest problems in radiative transfer modelling.

An optically thick cloud layer can be modelled as an reflecting surface with bi-directional redistribution function which is characteristic for each cloud type. See Kurosu [1997] and the references therein for a description of calculations using this type of cloud modelling and for a general discussion of the optical properties of clouds.

Thermal emission is much weaker than scattering of solar light in the UV-vis-NIR spectral region. It can be completely neglected in the UV-vis range and only is a minor effect in the NIR range.

Molecules of a gas also scatter light in an inelastic process in which a rotational transition is involved. This process is called *Raman scattering*. Since it is inelastic, it leads to a filling in of strong solar and terrestrial absorption lines. For a detailed description and simulations see Vountas [1999a].

Raman scattering is unique among the effects introduced in this chapter since it couples the radiation fields of different wavelengths. Thus it cannot be modelled with a strictly monochromatic radiative transfer model. Since lines of the solar spectrum are filled in, the scattered radiation is not proportional to the incoming (solar) radiation.

4.6 Refraction

Light rays in Earth's atmosphere are bend up to about 1° by gradients in the atmospheric refractive index. This can cause dramatic (up to 30%) changes in the path lengths in some of the atmospheric layers. It also changes the tangent height of the line-of-sight significantly. Ray tracing calculations must take this into account. The refractive index of air varies with wavelength λ, pressure p, and temperature T.

Electromagnetic radiation of a given frequency ν has variable wavelength λ_i and speed $c_i = \lambda_i \, \nu$ depending on the material, i, in which it propagates. For monochromatic radiation, (fixed frequency), the ratio of the vacuum wavelength λ_{vac} to the wavelength λ_i in a certain material is called the *refractive index* n_i of the material i:

$$n_i \equiv \frac{\lambda_{vac}}{\lambda_i} = \frac{c_{vac}}{c_i} \quad . \tag{4.17}$$

Generally speaking, the refractive index depends on the material and the frequency of the radiation.

The *refractivity* is defined as the difference of the refractive index and unity: $n_i - 1$. Like the refractive index, it obviously is a dimensionless quantity: [-].

4.6.1 Snell's Law

At the interface of two materials with different refractive indices n_1 and n_2 light rays are refracted. The direction of propagation changes obeying *Snell's law*:

$$n_1 \sin(\psi_1) = n_2 \sin(\psi_2) \quad , \tag{4.18}$$

where ψ_1 and ψ_2 denote the ray's angle to the interface's normal in the two materials. Snell's law can readily be derived from (4.17) using Huygens' elementary waves.

A special form of Snell's law can be derived for a system with a spherically symmetric refractive index $n(r)$, cf. Balluch and Lary [1997, eq. 17] or Kertz [1969, p. 46]. *Snell's law for spherical symmetry* is valid for Earth's atmosphere:

$$r_1\, n(r_1) \sin(\psi(r_1)) = r_2\, n(r_2) \sin(\psi(r_2)) = \text{const.} \quad , \tag{4.19}$$

where r is the radius coordinate of the system. Due to the geometry of the system, $\psi(r_1)$ and $\psi(r_2)$ are identical with the zenith angles of the light ray at the two radii.

The constant in (4.19) has different values for light rays with different geometries. Thus it is characteristic for each light ray. Snell's law for spherical symmetry is used in appendix A to derive refractive ray tracing formulae for the terrestrial atmosphere.

4.6.2 Parametrisations

Edlén

Edlén [1966] has determined a parametrisation of the refractive index of **dry air** using measured data. His *dispersion formula* yields the wavelength dependence of the refractive index depending on wavenumber, pressure, and temperature[5]:

$$(n[\text{-}] - 1) \cdot 10^8 = \left(8\,342.13 + \frac{2\,406\,030}{130 - \sigma^2[\mu\text{m}^{-2}]} + \frac{15\,997}{38.9 - \sigma^2[\mu\text{m}^{-2}]}\right) \cdot \frac{0.00138823\; p[\text{torr}]}{1 + 0.003671\; T[^\circ\text{C}]} \quad , \tag{4.20}$$

where σ, p, and T are the vacuum wavenumber, pressure, and temperature.

The first factor in (4.20) is called *dispersion factor*. It describes the wavenumber-dependent refractive index of dry air at standard conditions. The second factor is a *density correction factor*, which calculates the density using the equation of state

$$pV/(RT) = 1 - \epsilon_T p \quad . \tag{4.21}$$

[5]The units of the original literature are used in this section as the conversion to other units introduces errors, see below.

The experimental data, from which (4.20) was derived, lie in the ranges 200–2000 nm, 100–800 torr and 5–30 °C. The uncertainty of (4.20) is estimated to be $\pm 5 \cdot 10^{-8}$. For further details consult Edlén [1966].

The dispersion formula is of the so-called *Sellmeier form* $\sum_i A_i(\sigma_i^2 - \sigma^2)^{-1}$ with three terms. The first is reduced to a constant. The interpretation of the other two terms is to assume absorption at discrete wavenumbers with $\sigma^2 = 38.9\,\mu\mathrm{m}^{-2}$ and $\sigma^2 = 130\,\mu\mathrm{m}^{-2}$, corresponding to the wavelengths $\lambda = 160.3\,\mathrm{nm}$ and $\lambda = 87.7\,\mathrm{nm}$. Nevertheless, the modelled physical properties are absorption continua, namely the dissociation continuum of the oxygen molecule with a maximum around $\lambda = 145\,\mathrm{nm}$ and the absorption continua of the nitrogen and oxygen molecules with $\lambda \lesssim 100\,\mathrm{nm}$.

The refractive index of **carbon dioxide** is about 50 % larger than that of air. However, the influence of the atmospheric abundance with a partial pressure of 0.23 torr at standard conditions is smaller than the uncertainty of the dispersion formula (4.20). Therefore it can safely be neglected in model calculations.

Water vapour has a refractive index which is about 15 % smaller than that of dry air. Edlén [1966] derives an additive correction term Δn for the modelling of **moist air**. It may be applied to the refractive index from (4.20) in the visible wavelength region near $T = 20\,^\circ\mathrm{C}$, $p = 760\,\mathrm{torr}$, and $p_{\mathsf{H_2O}} = 10\,\mathrm{torr}$ partial pressure of water vapour:

$$\Delta n[\text{-}] \cdot 10^8 = -p_{\mathsf{H_2O}}[\mathrm{torr}](5.722 - 0.0457\,\sigma^2[\mu\mathrm{m}^{-2}]) \quad . \tag{4.22}$$

Peck and Reeder

Updates of the dispersion factor for air at standard conditions (with 0.033% carbon dioxide) can be found in Peck and Reeder [1972]. They account for additional measurements and are more accurate, mainly for $\lambda > 1000$ nm. Their wider-range formula is valid for 185 nm $< \lambda <$ 2000 nm and standard conditions with an uncertainty of $3 \cdot 10^{-8}$:

$$(n[\text{-}] - 1) \cdot 10^8 = 8\,060.51 + \frac{2\,480\,990}{132.274 - \sigma^2[\mu\mathrm{m}^{-2}]} + \frac{17\,455.7}{39.32957 - \sigma^2[\mu\mathrm{m}^{-2}]} \quad . \tag{4.23}$$

Since only the gradient of the refractive index affects the refractive bending of light rays, this improvement over (4.20) is widely considered to be minor. Thus (4.20) is still commonly used.

Bates

Tabulated values of the refractive index of air for $200\,\mathrm{nm} < \lambda < 1\,000\,\mathrm{nm}$ are derived from further measurements by Bates [1984]. However, the differences to (4.23) are small, i.e., below 0.1 %.

GOMETRAN and *SCIARAYS*

Transforming (4.23) to the units[6] common in the radiative transfer models GOMETRAN (see Section 5.3) and in *SCIARAYS*, yields the dispersion formula

$$(n[\text{-}]-1)\cdot 10^8 = \left(8342.13 + \frac{24.06030}{1.3\cdot 10^{-4} - \lambda^{-2}[\text{nm}^{-2}]} + \frac{1.5997\cdot 10^{-2}}{3.89\cdot 10^{-5} - \lambda^{-2}[\text{nm}^{-2}]}\right)\cdot \frac{0.283644\, p[\text{hPa}]}{T[\text{K}] - 0.745} \quad . \tag{4.24}$$

MODTRAN

Kneizys et al. [1996, p. 20] claim to use the dispersion formula (4.20) for dry air in the radiative transfer model MODTRAN (see Section 5.3). They obtain the following parametrisation upon unit conversion:

$$(n[\text{-}]-1)\cdot 10^8 = \left(8\,343 + \frac{18\,508}{1-(\sigma[\text{cm}^-1]/114\,000)^2} + \frac{411}{1-(\sigma[\text{cm}^-1]/62\,400)^2}\right)\cdot \frac{0.292277\, p[\text{hPa}]}{T[\text{K}]} \quad . \tag{4.25}$$

For standard conditions and $\lambda = 500\,\text{nm}$ the parametrisations (4.24) and (4.25) yield refractivities differing by $\approx 2\,\%$. This difference can be attributed to rounding errors during the conversion of units, the use of the ideal gas law instead of the equation of state (4.21), and the use of the updated dispersion formula (4.23).

[6] $\lambda[\text{nm}] = 10^3/\sigma[\mu\text{m}^{-1}]$, $p[\text{hPa}] = 1.333224\, p[\text{torr}]$, $T[\text{K}] = T[^\circ\text{C}] + 273.15$

Chapter 5

Radiative Transfer

5.1 Definitions of Radiative Quantities

5.1.1 Characteristics of the Atmosphere

The *absorption coefficient* $\alpha(\vec{r})$ and the *scattering coefficient* $\sigma(\vec{r})$ describe the attenuation of a radiation beam due to absorption and scattering in a medium. They have the unit $[\mathrm{m}^{-1}]$ and generally depend on the *location* $\vec{r}$, but not on the direction $\vec{\Omega}$ of the propagation of the radiation. They also depend on the wavelength λ of the radiation, but the wavelength index is skipped for better readability. The formulae remain unambiguous since this thesis treats *monochromatic radiative transfer modelling* where the calculations for different wavelengths are decoupled, see Section 5.2.2.

The absorption coefficient $\alpha(\vec{r})$ is also called *true absorption coefficient*. It is the sum of the individual absorption coefficients $\alpha_i(\vec{r})$ of all absorbing species and aerosol types i:

$$\alpha(\vec{r}) = \left(\sum_i \alpha_{ai}(\vec{r})\right) + \left(\sum_i \chi_i(p(\vec{r}), T(\vec{r}))\; n_i(\vec{r})\right) \;, \tag{5.1}$$

where α_{ai} denotes an aerosol absorption coefficient and χ_i and n_i are the absorption cross section and the number density of a molecule. The cross sections may depend on the location via the pressure and temperature.

Likewise, the scattering coefficient $\sigma(\vec{r})$ is the sum of the scattering coefficients of all scattering processes i:

$$\sigma(\vec{r}) = \sum_i \sigma_i(\vec{r}) \;. \tag{5.2}$$

In Earth's atmosphere, Rayleigh scattering and scattering can be distinguished. The latter is generally caused by a mixture of several different aerosol types.

The scattering processes redistribute the light in all directions. The *phase functions* $\phi_i(\vec{r}, \vec{\Omega}, \vec{\Omega}')$[-] characterise the scattering in the direction $\vec{\Omega}'$ of light arriving from direction $\vec{\Omega}$ at the location $\vec{r}$ due to the scattering processes i. The phase functions are often

normalised to 4π. In this work, they will be normalised to unity to enable a more comprehensive notation of some formulae, which are frequently:

$$\oint \phi_i(\vec{r}, \vec{\Omega}, \vec{\Omega}') \, \mathrm{d}\vec{\Omega}' = 1 \tag{5.3}$$

The phase functions cannot be summed directly, instead the *effective phase function* $\phi_i(\vec{r}, \vec{\Omega}, \vec{\Omega}')$ is defined by:

$$\sigma(\vec{r}) \, \phi(\vec{r}, \vec{\Omega}, \vec{\Omega}') \equiv \sum_i \sigma_i(\vec{r}) \, \phi_i(\vec{r}, \vec{\Omega}, \vec{\Omega}') \; , \tag{5.4}$$

where the summation usually covers all scattering processes. When it only covers the aerosols, the *effective aerosol phase function* is obtained. The effective phase function is convenient for writing the equations of the radiative transfer theory, but the program package *SCIARAYS* uses the right hand side of (5.4) in order to minimise the administrative and computational overhead.

The *extinction coefficient*[1] $\kappa(\vec{r})[\mathrm{m}^{-1}]$ is the sum of scattering and absorption coefficients and the *single scattering albedo* $\bar{\omega}_\circ(\vec{r})$[-] is the ratio of scattering and extinction coefficients:

$$\kappa(\vec{r}) \equiv \sigma(\vec{r}) + \alpha(\vec{r}) \tag{5.5}$$

$$\bar{\omega}_\circ(\vec{r}) \equiv \frac{\sigma(\vec{r})}{\kappa(\vec{r})} \tag{5.6}$$

Thus the extinction coefficient for each wavelength depends on the trace gas concentrations, the aerosol extinction, temperature and pressure.

5.1.2 Path Coordinates

Geometrical Path Coordinate

Let s denote the *geometrical path coordinate* of a light ray: It is zero at a freely chosen reference point on the ray, e.g., the observer's position, and decreases toward the light source, see Figure 5.1. Its absolute value is the geometrical distance to the reference point.

Optical Depth Coordinate

The *optical depth*[2] $\tau(s)$ of each point may be measured backwards on the path[3], see Figure 5.1. The optical depth is defined to be zero at the reference point and to vary according to the differential equation

$$\mathrm{d}\tau(s) = -\kappa(s) \, \mathrm{d}s \; . \tag{5.7}$$

[1] German: *Extinktionskoeffizient* or *optische Dichte* [Kurosu, 1997]

[2] German: *optische Tiefe*

[3] Sometimes it is also defined forwards on the path, in that case the minus sign in (5.7) disappears [e.g., Rybicki and Lightman, 1979, p. 12].

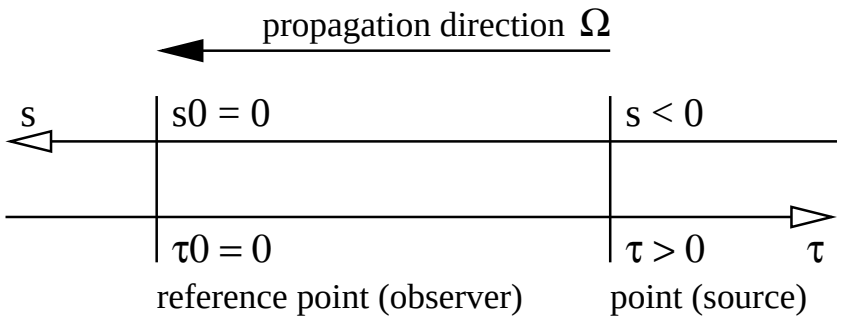

Figure 5.1: Path coordinate s and optical depth τ.

Thus the optical depth τ of a source with path coordinate s w.r.t. a reference point at location $\vec{r}_0$ can be expressed as

$$\tau(s) \equiv \tau(\vec{r}_0, \vec{\Omega}, s) \equiv \int_s^0 \kappa(\vec{\mathbf{r}}_s(s'))\, \mathrm{d}s' \ , \tag{5.8}$$

where $\vec{\mathbf{r}}_s(.)$ denotes a parametrisation of the path of the radiation travelling in the direction $\vec{\Omega}$ and ending at the reference point $\vec{r}_0$:

$$\vec{\mathbf{r}}_s(s) \equiv \vec{\mathbf{r}}_s(\vec{r}_0, \vec{\Omega}, s) \equiv \vec{r}_0 + s \cdot \vec{\Omega} \ . \tag{5.9}$$

The parameters $\vec{r}_0$ and $\vec{\Omega}$ are omitted from the argument lists of the optical depth τ (5.8) and of the path parametrisation (5.9) for clarity.

Since the extinction coefficient κ is always positive[4] in the atmosphere, $\vec{\mathbf{r}}(s)$ can be inverted unambiguously to obtain the path parametrised by the optical depth:

$$\vec{\mathbf{r}}_\tau(\tau) \equiv \vec{\mathbf{r}}_s(\vec{r}_0, \vec{\Omega}, s(\tau)) \ . \tag{5.10}$$

For the sake of better readability of the argument lists of all quantities, the path coordinate s and the optical depth τ will be written instead of the corresponding path parametrisations (5.9) and (5.10), e.g.,

$$I(s, \vec{\Omega}) \equiv I(\vec{\mathbf{r}}_s(s), \vec{\Omega}) \tag{5.11}$$

$$I(\tau, \vec{\Omega}) \equiv I(\vec{\mathbf{r}}_\tau(\tau), \vec{\Omega}) \ . \tag{5.12}$$

In many formulations of the theory of radiative transfer, the optical depth τ is a coordinate which is superior to the geometrical path coordinate s in two respects:

- The radiative transfer equation becomes simpler.
- Regions with strong absorption and scattering are enlarged, while those with weak absorption and scattering are minified in the coordinate system given by the optical depth.

The optical depth of a point w.r.t. a reference point is also called the *optical length*

[4]The physical interpretation of $\kappa > 0$ is: The induced emission is weaker than the sum of true absorption and scattering. $\kappa < 0$ describes the optically active media in lasers for instance.

between these two points [Lenoble, 1985].

Optical Thickness

In contrast to the optical depth, the *optical thickness*[5] τ is not a coordinate, but a property of a particular object and a particular viewing geometry: It is defined as the optical depth of a light source situated at the opposite side of the object. An object is called *optically thin*, if its optical thickness is smaller than unity. Otherwise it is *optically thick*.

In the treatment of plane-parallel atmospheres, the *optical depth* of a height is frequently defined as the optical thickness of the atmospheric layers above the height [e.g., Lenoble, 1985].

5.1.3 Characteristics of the Radiation Field

Several conventions are in use for defining the quantities of the radiation field. Here, the formalism of Rybicki and Lightman [1979] and Sedlmayr [1994] is extended and modified to achieve a comprehensible formulation of the equations implemented in *SCIARAYS*. The approach is consistent with the standard textbooks on atmospheric radiation by Lenoble [1985, 1993].

Specific Radiance

The *specific radiance*[6] $R_{*\lambda}(\vec{r},\vec{\Omega})$ is the basic quantity characterising the unpolarised radiation field. It is defined as the energy flux per unit area, unit solid angle and unit wavelength interval through an area located at $\vec{r}$ and oriented perpendicularly to $\vec{\Omega}$. Its unit is $[\mathrm{W\,m^{-2}\,sr^{-1}\,nm^{-1}}]$ and it depends on location $\vec{r}$ (3 dimensions), direction $\vec{\Omega}$ (2 dimensions) and wavelength λ. Thus the specific radiance generally is a 6-dimensional quantity[7].

Spectrally Integrated

The *radiance* $R_*(\vec{r},\vec{\Omega})$ $[\mathrm{W\,m^{-2}\,sr^{-1}}]$ is obtained for a spectral interval $(\lambda, \lambda+\Delta\lambda)$, e.g., representing a spectrometer pixel, by integration of the specific radiance (optionally convolving it with a slit function):

$$R_*(\vec{r},\vec{\Omega}) \equiv \int_{\lambda}^{\lambda+\Delta\lambda} R_{*\lambda'}(\vec{r},\vec{\Omega})\,\mathrm{d}\lambda' \tag{5.13}$$

[5] German: *optische Dicke* [Richter, 1997, p. 45] or *optische Dichte* [Bogumil, 2001]

[6] The indices λ and $*$ are used to mark "specific" quantities and quantities in "physical units" as opposed to spectrally integrated and sun-normalised quantities, see below.

[7] The "specific" counterparts of the following quantities are skipped as the radiative transfer models introduced later are formulated with the "integrated" quantities.

The *flux* $F_{\vec{\Omega}}(\vec{r})$ is the radiant power flux per unit area $[\mathrm{W\,m^{-2}}]$ across a plane located at $\vec{r}$ and oriented perpendicular to the direction $\vec{\Omega}$:

$$F_{\vec{\Omega}}(\vec{r}) \equiv \oint R_*(\vec{r},\vec{\Omega}')\,\cos(\angle[\vec{\Omega},\vec{\Omega}'])\,\mathrm{d}\vec{\Omega}' \quad , \tag{5.14}$$

where $\angle[\vec{\Omega},\vec{\Omega}']$ denotes the angle between the two directions $\vec{\Omega}$ and $\vec{\Omega}'$.

The *emission coefficient* $\varepsilon_*(\vec{r},\vec{\Omega})$ describes the gain of intensity at the location $\vec{r}$ in the direction $\vec{\Omega}$ due to internal and external sources $\varepsilon_{*s}(\vec{r},\vec{\Omega})$ and due to scattering:

$$\varepsilon_*(\vec{r},\vec{\Omega}) = \sigma(\vec{r}) \oint \phi(\vec{r},\vec{\Omega},\vec{\Omega}')\,R_*(\vec{r},\vec{\Omega}')\,\mathrm{d}\vec{\Omega}' + \varepsilon_{*s}(\vec{r},\vec{\Omega}) \tag{5.15}$$

Its unit is $[\mathrm{W\,m^{-3}\,sr^{-1}}]$. The ubiquitous thermal emission is modelled by using the Planck function as internal source (after spectral integration).

The *source function* $J_*(\vec{r},\vec{\Omega})$ $[\mathrm{W\,m^{-2}\,sr^{-1}}]$ is defined as the ratio of emission and extinction coefficient:

$$\begin{aligned} J_*(\vec{r},\vec{\Omega}) &\equiv \frac{\varepsilon_*(\vec{r},\vec{\Omega})}{\kappa(\vec{r})} && (5.16)\\ &= \bar{\omega}_\circ(\vec{r}) \oint \phi(\vec{r},\vec{\Omega},\vec{\Omega}')\,R_*(\vec{r},\vec{\Omega}')\,\mathrm{d}\vec{\Omega}' + \frac{\varepsilon_{*s}(\vec{r},\vec{\Omega})}{\kappa(\vec{r})} && (5.17)\\ &\approx \bar{\omega}_\circ(\vec{r}) \oint \phi(\vec{r},\vec{\Omega},\vec{\Omega}')\,R_*(\vec{r},\vec{\Omega}')\,\mathrm{d}\vec{\Omega}' \quad . && (5.18) \end{aligned}$$

Sun-Normalised

The *irradiance* F_* is the power flux per unit area $[\mathrm{W\,m^{-2}}]$ of the direct solar radiation just outside the Earth's atmosphere through a plane perpendicular to the direction of its propagation.

Normalising the radiance, emission coefficient and source function with the irradiance yields the *sun-normalised radiance* $I(\vec{r},\vec{\Omega})$ $[\mathrm{sr^{-1}}]$, the *sun-normalised emission coefficient* $\varepsilon(\vec{r},\vec{\Omega})$ $[\mathrm{m^{-1}\,sr^{-1}}]$ and the *sun-normalised source function* $J(\vec{r},\vec{\Omega})$ $[\mathrm{sr^{-1}}]$:

$$\begin{aligned} I(\vec{r},\vec{\Omega}) &\equiv \frac{R_*(\vec{r},\vec{\Omega})}{F_*} && (5.19)\\ J(\vec{r},\vec{\Omega}) &\equiv \frac{J_*(\vec{r},\vec{\Omega})}{F_*} && (5.20)\\ &\approx \bar{\omega}_\circ(\vec{r}) \oint \phi(\vec{r},\vec{\Omega},\vec{\Omega}')\,I(\vec{r},\vec{\Omega}')\,\mathrm{d}\vec{\Omega}' && (5.21)\\ \varepsilon(\vec{r},\vec{\Omega}) &\equiv \frac{\varepsilon_*(\vec{r},\vec{\Omega})}{F_*} && (5.22)\\ &= \kappa(\vec{r},\vec{\Omega})\,J(\vec{r},\vec{\Omega}) && (5.23)\\ &\approx \sigma(\vec{r}) \oint \phi(\vec{r},\vec{\Omega},\vec{\Omega}')\,I(\vec{r},\vec{\Omega}')\,\mathrm{d}\vec{\Omega}' && (5.24) \end{aligned}$$

where the approximative terms hold for an absorbing and scattering atmosphere with negligible thermal emission. On the day-side of the Earth's atmosphere, this approximation is almost exact for the UV-vis wavelength range and also good for the NIR spectral range.

5.2 Two Forms of the Radiative Transfer Equation

5.2.1 General Formulation

The *integro-differential form of the radiative transfer equation* (*RTE*) for each wavelength can be written for an arbitrary geometry [e.g., Sedlmayr, 1994]:

$$\vec{\Omega} \cdot \nabla_{\vec{r}} R_{*\lambda}(\vec{r}, \vec{\Omega}) = \kappa(\vec{r}) \left(J_{*\lambda}(\vec{r}, \vec{\Omega}) - R_{*\lambda}(\vec{r}, \vec{\Omega}) \right) \tag{5.25}$$

$$J_{*\lambda}(\vec{r}, \vec{\Omega}) = \bar{\omega}_\circ(\vec{r}) \oint \phi(\vec{r}, \vec{\Omega}, \vec{\Omega}') \, R_{*\lambda}(\vec{r}, \vec{\Omega}') \, \mathrm{d}\vec{\Omega}' + J_{*S\lambda}(\vec{r}, \vec{\Omega}) \, . \tag{5.26}$$

The second summand in (5.25) models the attenuation of the radiation, while the first describes additional sources of radiation: The first term in (5.26) models elastic scattering in the direction $\vec{\Omega}$ and the second term represents internal and external sources.

An equivalent formulation employs the geometrical path coordinate s in the direction $\vec{\Omega}$:

$$\frac{\mathrm{d}R_{*\lambda}(s, \vec{\Omega})}{\mathrm{d}s} = \kappa(s) \left(J_{*\lambda}(s, \vec{\Omega}) - R_{*\lambda}(s, \vec{\Omega}) \right) \, . \tag{5.27}$$

Substituting the differential optical depth $\mathrm{d}\tau$ from (5.7) for the differential path coordinate $\mathrm{d}s$ leads to the most compact form of the RTE:

$$\frac{\mathrm{d}R_{*\lambda}(\tau, \vec{\Omega})}{\mathrm{d}\tau} = R_{*\lambda}(\tau, \vec{\Omega}) - J_{*\lambda}(\tau, \vec{\Omega}) \, . \tag{5.28}$$

The RTE can be integrated formally by considering the quantity $R_{*\lambda} \, e^{-\tau}$. Using (5.28), its derivative w.r.t. τ can be expressed as

$$\frac{\mathrm{d}R_{*\lambda}(\tau, \vec{\Omega}) \, e^{-\tau}}{\mathrm{d}\tau} = \left(\frac{\mathrm{d}R_{*\lambda}(\tau, \vec{\Omega})}{\mathrm{d}\tau} - R_{*\lambda}(\tau, \vec{\Omega}) \right) e^{-\tau} \tag{5.29}$$

$$= -J_{*\lambda}(\tau, \vec{\Omega}) \, e^{-\tau} \, . \tag{5.30}$$

Thus by formal integration of (5.28) the radiance at the reference point $\tau_0 = 0$ (therefore $e^{-\tau_0} = 1$) is:

$$R_{*\lambda}(\tau_0,\vec{\Omega}) = R_{*\lambda}(\tau_0,\vec{\Omega})\,e^{-\tau_0} \tag{5.31}$$

$$= R_{*\lambda}(\tau_1,\vec{\Omega})\,e^{-\tau_1} + \int_{\tau_1}^{\tau_0} \frac{\mathrm{d}R_{*\lambda}(\tau,\vec{\Omega})\,e^{-\tau}}{\mathrm{d}\tau}\,\mathrm{d}\tau \tag{5.32}$$

$$= R_{*\lambda}(\tau_1,\vec{\Omega})\,e^{-\tau_1} + \int_{\tau_0}^{\tau_1} J_{*\lambda}(\tau,\vec{\Omega})\,e^{-\tau}\mathrm{d}\tau \ , \tag{5.33}$$

where τ_1 is the optical depth of an arbitrary point. It obviously is useful to choose a point at which the radiance is known.

A common *integral form of the radiative transfer equation* is obtained by substituting the path coordinate s for the optical depth τ and using (5.23) and $s_0 = 0$:

$$R_{*\lambda}(s_0,\vec{\Omega}) = R_{*\lambda}(s_1,\vec{\Omega})\;e^{-\tau(s_1)} + \int_{s_0}^{s_1} \varepsilon_{*\lambda}(s,\vec{\Omega})\;e^{-\tau(s)}\,\mathrm{d}s \tag{5.34}$$

$$\varepsilon_{*\lambda}(\vec{r},\vec{\Omega}) = \sigma(\vec{r}) \oint R_{*\lambda}(\vec{r},\vec{\Omega}')\,\phi(\vec{r},\vec{\Omega},\vec{\Omega}')\,\mathrm{d}\vec{\Omega}' \; + \varepsilon_{*s\lambda}(\vec{r},\vec{\Omega}) \ , \tag{5.35}$$

where s_1 is the path coordinate of a point with known radiance. The first summand in (5.34) represents the radiance which has been transmitted from s_1 to s_0 and attenuated on the way. The second summand models the transmission and attenuation of the radiation which is emitted at all points between s_1 and s_0.

5.2.2 UV-vis Measurements of the Terrestrial Atmosphere

In the UV-vis radiance field on the dayside of Earth's atmosphere, the thermal emission is negligible[8]. Furthermore, the contribution of inelastic scattering only has such a small influence that it can be corrected for by fitting a so-called Ring-spectrum instead of treating it as an additional source in the RTE [Vountas et al., 1998, Vountas, 1999b]. Therefore, the source function and the emission coefficient can be well approximated by the terms due to elastic scattering only:

$$J_{*\lambda}(\vec{r},\vec{\Omega}) = \bar{\omega}_\circ(\vec{r}) \oint \phi(\vec{r},\vec{\Omega},\vec{\Omega}')\,R_*(\vec{r},\vec{\Omega}')\,\mathrm{d}\vec{\Omega}' \tag{5.36}$$

$$\varepsilon_{*\lambda}(\vec{r},\vec{\Omega}) = \sigma(\vec{r}) \oint \phi(\vec{r},\vec{\Omega},\vec{\Omega}')\,R_*(\vec{r},\vec{\Omega}')\,\mathrm{d}\vec{\Omega}' \ . \tag{5.37}$$

The approximation describes an absorbing and scattering atmosphere. In this case the radiance field is proportional to the illumination, i.e., the irradiance F_*. Therefore, it is useful to divide the RTE by the irradiance to obtain the

[8] In the NIR wavelength range, the influence of thermal emission is not completely negligible, but it is a minor effect.

integro-differential form of the RTE for UV-vis scattering measurements

$$\vec{\Omega} \cdot \nabla_{\vec{r}} I(\vec{r}, \vec{\Omega}) = \kappa(\vec{r}) \left(J(\vec{r}, \vec{\Omega}) - I(\vec{r}, \vec{\Omega}) \right) \tag{5.38}$$

$$\text{with} \quad J(\vec{r}, \vec{\Omega}) = \bar{\omega}_\circ(\vec{r}) \oint \phi(\vec{r}, \vec{\Omega}, \vec{\Omega}')\, I(\vec{r}, \vec{\Omega}')\, \mathrm{d}\vec{\Omega}' \tag{5.39}$$

and the

integral form of the RTE for UV-vis scattering measurements

$$I(s_0, \vec{\Omega}) = \underbrace{I(s_1, \vec{\Omega})\, e^{-\tau(s_1)}}_{I_{\text{direct}}} + \underbrace{\int_{s_1}^{s_0} \varepsilon(s, \vec{\Omega})\, e^{-\tau(s)} \mathrm{d}s}_{I_{\text{diffuse}}} \tag{5.40}$$

$$\text{with} \quad \varepsilon(s, \vec{\Omega}) = \sigma(s) \oint \phi(s, \vec{\Omega}, \vec{\Omega}')\, I(s, \vec{\Omega}')\, \mathrm{d}\vec{\Omega}' \tag{5.41}$$

$$\tau(s) = \int_s^0 \kappa(s')\, \mathrm{d}s' \ , \tag{5.42}$$

where s_1 is the coordinate of the boundary of the atmosphere.

In (5.40), the radiance is split into the *direct radiance* I_{direct} and the *diffuse radiance* I_{diffuse}. The former is the solar radiation which is transmitted to each point of the atmosphere without being absorbed or scattered, while the latter is radiation which has undergone at least one scattering event.

Since the diffuse radiance at each point $\vec{r}$ depends on the radiance at all other points, the RTE is *non-local* and cannot be integrated readily, but has to be evaluated for the whole atmosphere simultaneously. Several approaches to solve this problem are discussed in the next section.

The equations (5.38) and (5.40) hold for the sun-normalised radiance $[\mathrm{sr}^{-1}]$, source function$[\mathrm{sr}^{-1}]$ and emission coefficient$[\mathrm{sr}^{-1}]$. They are "specific" quantities, which describe a single wavelength, but generally not a wavelength interval. However, for a small spectral interval with constant[9] optical properties, they can be identified with the spectrally integrated quantities for this interval. Therefore, these formulations of the RTE are suitable for the description of measurements in the UV-vis spectral range by instruments of SCIAMACHY's type.

[9] In reality, there exists no spectral interval with constant optical properties in Earth's atmosphere. However, the discrete nature of computer calculations implies the assumption of constant optical properties in both, the wavelength and the spacial dimensions. Precautions have to be taken to justify this assumption. SCIAMACHY's UV and vis measurements have a sufficient spectral resolution to assert this assumption for the spectral dimension.

5.3 Model Types

Due to the inherent non-locality, the radiative transfer equations (5.38) or (5.40) for UV-vis scattering measurements cannot be solved directly. All current radiative transfer models employ some approximation or an iterative algorithm. This section introduces four principally different approaches for solving the RTE and four radiative transfer models (RTMs) implementing them.

The widely used RTM *MODTRAN* [Kneizys et al., 1996] is not covered in this section. It employs the *stream approximation* to compute the diffuse radiance, compare Isaacs et al. [1986] for more details on this method. MODTRAN is not applicable for the simulation of limb scattering measurements as the sphericity of the atmosphere is not properly accounted for. (Still other approaches of radiative transfer modelling are described in Caudill et al. [1997], Dahlback and Stamnes [1991], Herman et al. [1994, 1995b,a], Stamnes et al. [1988], Kylling et al. [1995].)

5.3.1 Integro-Differential Equation

The integro-differential form (5.38) of the RTE can be solved for the radiance field $I(\vec{r}, \vec{\Omega})$ with the method of finite differences by approximating the geometry [Rozanov et al., 1997a]: The atmosphere is assumed to be horizontally stratified and even plane-parallel.

In the RTM *GOMETRAN* [Rozanov et al., 1997a,b, Rozanov and Eichmann, 1997], the direct radiance is calculated in a spherical atmospheric model [Rozanov and Eichmann, 1997]. Then it is used to compute the external source function for the diffuse radiance field. In a second step, the diffuse radiance field is obtained by solving the integro-differential form of the RTE using the approximation of a plane-parallel geometry. The two steps are visualised in Figure 5.2. They constitute the so-called *pseudo-spherical* approximation to the geometry.

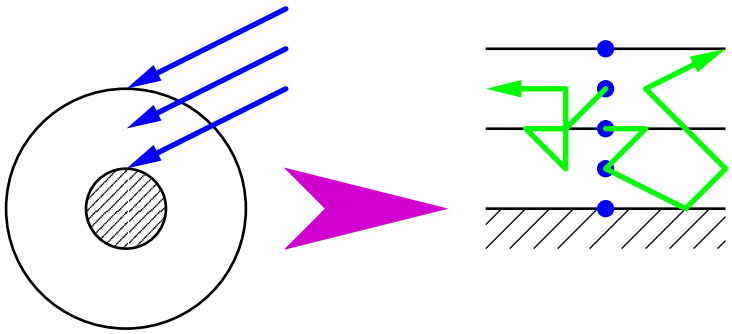

Figure 5.2: Pseudo-spherical solution of the integro-differential RTE.

This method allows to derive analytical formulae for the *weighting functions*, i.e., the derivatives of the radiance w.r.t. the atmospheric model parameters [Rozanov et al.,

1997b]. Such weighting functions are needed in the retrieval process. The computation of the weighting functions is accelerated by calculating them from analytical formulae.

The RTM GOMETRAN is successfully used for retrievals from the nadir viewing spectrometer GOME aboard the satellite ERS-2 [Burrows et al., 1999]. For the retrievals the measurements are simulated by selecting the appropriate components of the diffuse radiance field. For the simulation of limb measurements, however, the plane-parallel approximation of the diffuse radiance field is not valid since the great profiling capabilities of the limb measurements exploit the sphericity of Earth's atmosphere.

Thus the approach of solving the integro-differential RTM for a plane-parallel atmosphere cannot be used for modelling limb measurements.

5.3.2 Integral Equation

The r.h.s. of the integral form (5.40) of the RTE can be evaluated if the emission coefficient ε is available. By approximating ε, an approximative solution of (5.40) can be found in fully spherical geometry. The most obvious approximation is to compute ε from (5.41) with the radiance approximated by the direct radiance. This approximation is called *single-scattering approximation*. It is depicted in Figure 5.3. The emission coefficient is integrated over the so-called *line of sight*.

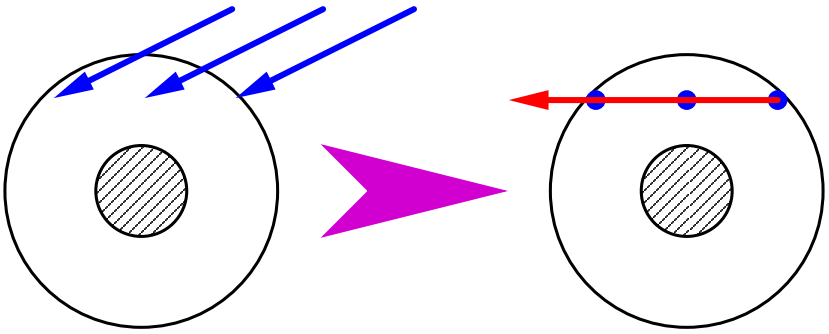

Figure 5.3: Single-scattering solution of the integral form of the RTE with integration over the line of sight (red).

Obviously, the single-scattering approximation can be used in (5.41) to obtain a better approximation of the emission coefficient ε, with which the second order of scattering can also be modelled. The surface reflection can be treated similarly. This approach is implemented in *SCIARAYS*, see Chapter 6. The sphericity of the atmosphere is completely accounted for.

The analytical formulae for the weighting functions are easily derived and implemented for a solution of the integral form of the RTE. Additionally, the first two orders of scattering can be computed relatively fast. Therefore, this type of radiative transfer model is well suited for theoretical studies of limb scattering measurements. For the re-

trieval from real measurements, the influence of higher orders of scattering would have to be compensated.

5.3.3 Orders of Scattering

The integral form (5.40–5.42) of the RTE can be used to calculate the full radiance field iteratively. The method of an *orders of scattering model* is illustrated in Figure 5.4.

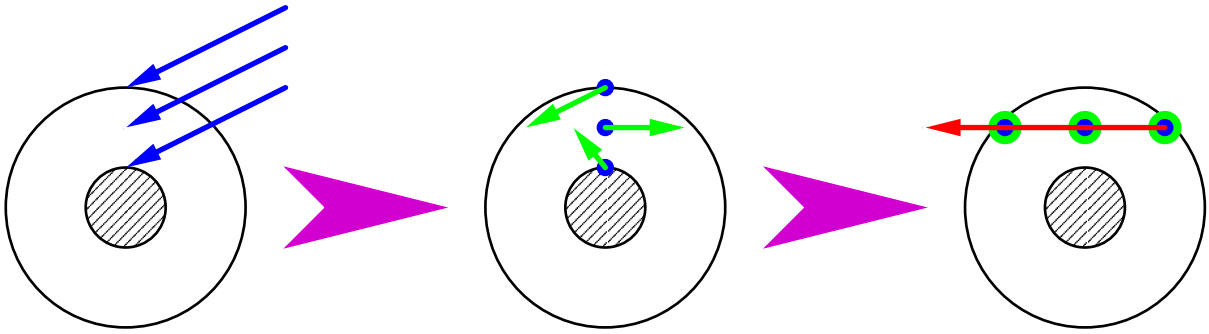

Figure 5.4: Orders of Scattering: the first two orders.

In the first iteration step, the single-scattered radiances in all directions at all points in the atmosphere are calculated like in an integral model (Section 5.3.2). This single-scattered radiance field is used in the second iteration step to obtain the emission coefficient from (5.41), which is then used to solve the integral equation (5.40) for the radiances due to the second order of scattering.

Each iteration step employs the radiance field from the last step to obtain the emission coefficient and radiance field corresponding to the next order of scattering. The iterative process is continued until some convergence criterion is met.

Finally, the radiances of all iteration steps are added to obtain the modelled radiance, possibly solving the RTE once more.

5.3.4 Combination

The advantages of the integro-differential and integral solution methods for the RTE can be combined by using the diffuse radiance field computed with the pseudo-spherical approximation along with the direct radiance for the computation of the emission coefficient in (5.41).

The three steps of this approach are visualised in Figure 5.5: First the direct radiance field is calculated in spherical geometry, from this the diffuse radiance field is calculated in plane-parallel geometry with the integro-differential form (5.38) of the RTE, finally the direct and the diffuse radiances are used to calculate the emission coefficient in the integral formulation (5.40) of the RTE.

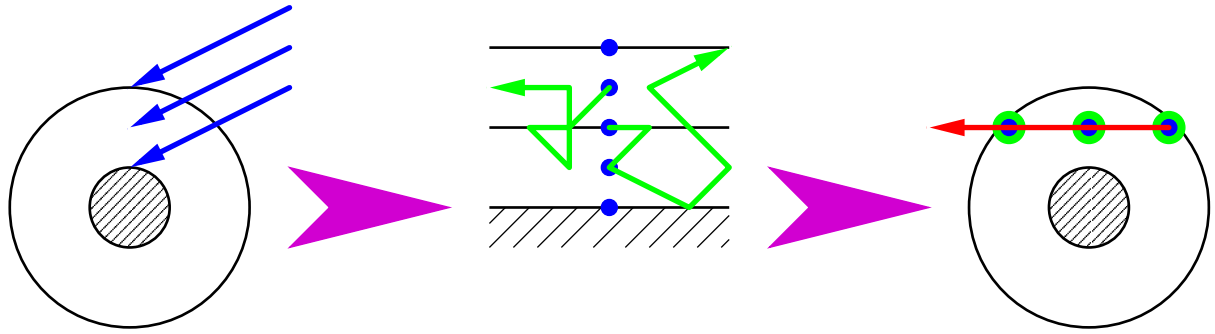

Figure 5.5: Combination of integral and integro-differential equations.

Analogously to the way, the next order of scattering can be obtained in the orders-of-scattering approach, the solution obtained with the combined approach can be improved iteratively. This was implemented in the RTM *CDIPI* by Rozanov et al. [2000], see also Evans [1998].

5.3.5 Monte Carlo

The *Monte Carlo* (MC) method is conceptually different from all other methods mentioned in this chapter: Instead of solving equations for the continuous radiance, the interactions of a large ensemble of photons with the atmosphere is simulated, see Figure 5.6. Then the radiance is calculated from the properties of this ensemble.

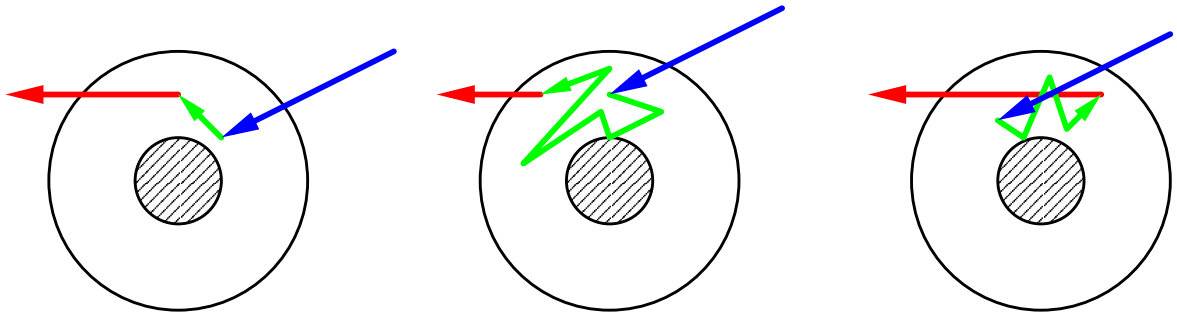

Figure 5.6: Simulation of photon paths for Monte Carlo modelling.

Monte Carlo models are ideal reference models as they can simulate the radiance in an arbitrary geometry with every desired precision, including all orders of scattering. Their disadvantage is that they require large ensembles to achieve good accuracy, say, of 0.1 %. Thus they are slow. Additionally, no weighting functions are computed along with the radiance. For both reasons, Monte Carlo models are not suitable for retrievals.

The fully spherical Monte Carlo model *SIRO* has been developed by Oikarinen et al. [1999] for the simulation of UV-vis limb scattering measurements. It has been used for the validation of the RTM in *SCIARAYS*, see Section 6.4.

Chapter 6

The Radiative Transfer Model in *SCIARAYS*

6.1 Overview

The radiative transfer model (RTM) in *SCIARAYS* evaluates the integral form (5.40) of the radiative transfer equation (RTE). According to Section 5.3.2 it is therefore an integral model. It is, however, more sophisticated than a single-scattering model as four additional ray paths are modelled. The ray paths are described individually in the Section 6.2.2 and depicted in Figure 6.1 on page 61.

The observational geometry may be chosen arbitrarily. Section 6.2.3 discusses the applicability of the ray paths for the different types of observational geometry.

The model is optimised for application in limb retrievals in three respects:

- The atmosphere's sphericity can be fully accounted for.
- Weighting functions for all atmospheric model parameters are computed along with the radiances from analytical formulae[1].
- Repeated calls to the RTM during an iterative retrieval process are fast since the path lengths are calculated only once, during the initialisation. Subsequent[2] calls have access to the stored (accumulated) path lengths from the initialisation.

The parametrisations (5.9) of all light rays are determined according to the ray tracing formulae derived in appendix A. Therefore, the atmosphere can be assumed to be either spherical or plane-parallel and refractive bending of the rays may be modelled or not.

[1] See Section 6.5 and Chapter 8 for more information on weighting functions and their significance.

[2] "Subsequent" refers to different atmospheric trial profiles and to other wavelengths, when the wavelength dependence of the refraction can be neglected.

The following physical effects are currently modelled by *SCIARAYS*:

- Rayleigh scattering
- aerosol scattering
- trace gas absorption with tabulated temperature-dependent cross sections
- Lambertian surface reflection,

while the model is approximative by neglecting

- multiple scattering, i.e., third and higher orders of scattering
- clouds
- horizontal inhomogeneities
- thermal emissions
- wavelength dependence of the albedo
- aerosol absorption.

Furthermore, the radiative transfer equation is solved once for each measurement pixel. In the NIR spectral region, line-by-line or correlated-k calculations will be needed to model the radiance with sufficient accuracy for retrievals from SCIAMACHY's measurements [Buchwitz et al., 2000].

See Chapter 11.5 for discussions of the influences of these limitations on the calculated precisions.

The input and output parameters of the RTM in *SCIARAYS* and their units are summarised in Table 6.1.

Table 6.1: Units of the Atmospheric Input and Output of *SCIARAYS*

	input	output
solar zenith angle	$[^\circ]$	
solar azimuth angle	$[^\circ]$	
tangent altitudes	$[\mathrm{km}]$	
trace gas number density profiles	$[10^5\,\mathrm{cm}^{-3}]$	
temperature profile	$[\mathrm{K}]$	
pressure profile	$[\mathrm{hPa}]$	
aerosol scattering coefficient profile	$[\mathrm{km}^{-1}]$	
albedo	$[-]$	
radiances/irradiance		$[\mathrm{sr}^{-1}]$
trace gas weights		$[\mathrm{sr}^{-1}/10^5\,\mathrm{cm}^{-3}]$
temperature weights		$[\mathrm{sr}^{-1}/\mathrm{K}]$
pressure weights		$[\mathrm{sr}^{-1}/\mathrm{hPa}]$
aerosol scattering coefficient weights		$[sr^{-1}/\mathrm{km}^{-1}]$
albedo weights		$[\mathrm{sr}^{-1}]$

6.2 The Rays in *SCIARAYS*

All ray paths described in this subsection are depicted in Figure 6.1.

6.2.1 Naming Conventions

Each of *SCIARAYS*' six ray paths from the sun through the atmosphere to the observer is composed of up to three individual rays, see Figure 6.1. The three rays will be identified by the following names and symbols:

LOS The *line-of-sight* is the (red) ray which ends in the observers eye. Quantities of this ray shall be marked by a bullet: "•", e.g., $\overset{\bullet}{x}$.

LFS The *line-from-sun* is the (blue) ray which originates at the sun. Quantities of this ray shall be marked by a star: "$*$", e.g., $\overset{*}{x}$.

LFA The *line-from-atmosphere* is the (green) ray which (possibly) connects the LOS and the LFS. Quantities of this ray shall be marked by a circle: "$\circ$", e.g., $\overset{\circ}{x}$.

For instance, $\overset{\bullet}{\tau}\,(\overset{\bullet}{s})$ denotes the optical depth (as seen by the observer) of the point on the LOS with LOS-path coordinate s (cf. Figure 5.1). On the other hand, $\overset{*}{\tau}\,(\overset{\bullet}{s})$ denotes the optical depth of the sun as seen from the point on the LOS with LOS-path coordinate s.

6.2.2 Ray Paths in *SCIARAYS*

Direct Radiation: D

The first summand I_{direct} of (5.40) describes the directly transmitted solar radiance. It will also be denoted I_{D}. Since the sun is approximated by a point source, its angular dependence is of the type of a delta function $\delta(\vec{\Omega})$. Therefore, the *direct transmittance* $\overset{*}{T}$ of the atmosphere from the sun to the point under consideration will be useful:

$$\overset{*}{T} \equiv e^{-\overset{*}{\tau}} \tag{6.1}$$

$$= \oint I_{\text{D}}(\vec{\Omega})\,\frac{\mathrm{d}\vec{\Omega}}{4\pi}\,, \tag{6.2}$$

where $\overset{*}{\tau}$ is the optical depth of the sun. With this, the direct radiance obviously is:

$$I_{\text{D}}(\overset{\bullet}{s}_b, \vec{\Omega}) = \overset{*}{T}\,(\overset{\bullet}{s}_b)\,\delta(\vec{\Omega}) \tag{6.3}$$

$$= e^{-\overset{*}{\tau}(\overset{\bullet}{s}_b)}\,\delta(\vec{\Omega}) \tag{6.4}$$

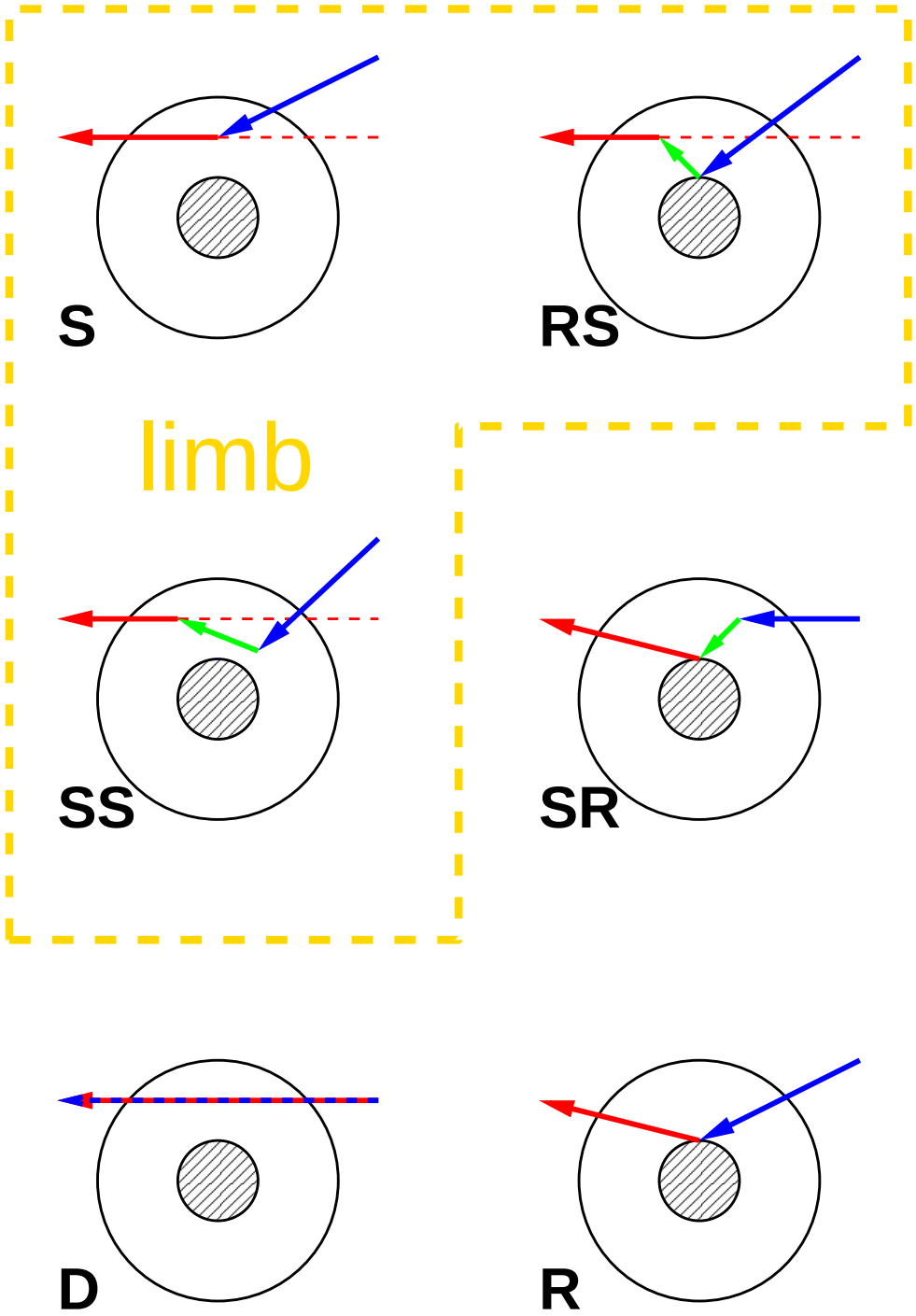

Figure 6.1: Ray paths modelled by *SCIARAYS*. The modelled paths from the sun through the atmosphere to an observing satellite are shown. The paths which are applicable in limb geometry are marked yellow. The LOS is red, the LFS is blue and the LFA is green.

Reflected Radiance: R

When the observer's line of sight hits the ground, the solar radiation I_{R} which is transmitted to the ground of the atmosphere and then reflected directly to the observer is modelled with the following approximation of the first term, I_{direct}, of (5.40). The incoming radiation is the direct radiance I_{D}. It is reflected with the albedo A and reflection phase function ρ (see Section 4.4) and attenuated on its path to the observer:

$$I_{\mathrm{R}}(\overset{\bullet}{s_b}, \vec{\Omega}) = \int_{\mathrm{sky}} I_{\mathrm{D}}(\overset{\bullet}{s_a}, \vec{\Omega}')\, A\, \rho(\vec{\Omega}')\, \mathrm{d}\vec{\Omega}'\ e^{-\overset{\bullet}{\tau}(\overset{\bullet}{s_a})} \tag{6.5}$$

$$= A\, \rho(\vec{\Omega}_*)\, e^{-\overset{\bullet}{\tau}(\overset{\bullet}{s_a}) - \overset{*}{\tau}(\overset{\bullet}{s_a})}\ . \tag{6.6}$$

Single-Scattered Radiance: S

Just approximating the emission coefficient ε in (5.41) with the directly transmitted radiance I_{D} yields the *single-scattered radiance* I_{S}:

$$I_{\mathrm{S}}(\overset{\bullet}{s_b}, \vec{\Omega}) = \int_{\overset{\bullet}{s_a}}^{\overset{\bullet}{s_b}} \sigma(s) \oint \phi(s, \vec{\Omega}, \vec{\Omega}')\, I_{\mathrm{D}}(s, \vec{\Omega}')\, \mathrm{d}\vec{\Omega}'\ e^{-\overset{\bullet}{\tau}(s)} \mathrm{d}s \tag{6.7}$$

$$= \int_{\overset{\bullet}{s_a}}^{\overset{\bullet}{s_b}} \sigma(s) \phi(s, \vec{\Omega}, \vec{\Omega}_*)\, e^{-\overset{\bullet}{\tau}(s) - \overset{*}{\tau}(s)} \mathrm{d}s\ , \tag{6.8}$$

where $\vec{\Omega}_*$ denotes the direction of the direct solar radiation. The first summand in (5.40) is neglected here, and so will it be in the forthcoming ray paths.

Second Order of Scattered Radiance: SS

Using the single-scattered radiance I_{S} for the calculation of the emission coefficient ε in (5.41) yields the radiance I_{SS} of the *second order of scattering*:

$$I_{\mathrm{SS}}(\overset{\bullet}{s_b}, \vec{\Omega}) = \int_{\overset{\bullet}{s_a}}^{\overset{\bullet}{s_b}} \sigma(s) \oint \phi(s, \vec{\Omega}, \vec{\Omega}')\, I_{\mathrm{S}}(s, \vec{\Omega}')\, \mathrm{d}\vec{\Omega}'\ e^{-\overset{\bullet}{\tau}(s)} \mathrm{d}s \tag{6.9}$$

$$= \int_{\overset{\bullet}{s_b}}^{\overset{\bullet}{s_a}} \sigma(s) \oint \phi(s, \vec{\Omega}, \vec{\Omega}') \int_{\overset{\circ}{s_b}}^{\overset{\circ}{s_a}} \sigma(s') \phi(s', \vec{\Omega}', \vec{\Omega}_*)\, e^{-\overset{\circ}{\tau}(s') - \overset{*}{\tau}(s')} \mathrm{d}s'\ \mathrm{d}\vec{\Omega}'\ e^{-\overset{\bullet}{\tau}(s)}\, \mathrm{d}s \tag{6.10}$$

Reflected-then-Scattered Radiance: RS

The radiance due to radiation which has been first reflected on the ground and then scattered in the atmosphere shall be called *reflected-then-scattered radiance* I_{RS}. It is modelled analogously to I_{SS} with the second summand in (5.40). The emission coefficient (5.41) is approximated by the reflected radiance I_{R}:

$$I_{\mathrm{RS}}(\overset{\bullet}{s}_b, \vec{\Omega}) = \int_{\overset{\bullet}{s}_a}^{\overset{\bullet}{s}_a} \sigma(s) \int_{\text{ground}} \phi(s, \vec{\Omega}, \vec{\Omega}')\, I_{\mathrm{R}}(s, \vec{\Omega}')\, \mathrm{d}\vec{\Omega}'\ \ e^{-\overset{\bullet}{\tau}(s)} \mathrm{d}s \tag{6.11}$$

$$= \int_{\overset{\bullet}{s}_a}^{\overset{\bullet}{s}_a} \sigma(s) \int_{\text{ground}} \phi(s, \vec{\Omega}, \vec{\Omega}')\, A\, \rho(\vec{\Omega}_*)\, e^{-\overset{\circ}{\tau}(\overset{\circ}{s}_a) - \overset{*}{\tau}(\overset{\circ}{s}_a)}\, \mathrm{d}\vec{\Omega}'\ \ e^{-\overset{\bullet}{\tau}(s)} \mathrm{d}s \tag{6.12}$$

Scattered-then-Reflected Radiance: SR

The radiance I_{SR} due to radiation which has been first scattered in the atmosphere and then reflected on the ground shall be called *scattered-then-reflected radiance*. In analogy to the reflected radiance I_{R}, it is modelled with the first summand in (5.40) by approximating the incoming radiation with the single-scattered radiance I_{S}:

$$I_{\mathrm{SR}}(\overset{\bullet}{s}_b, \vec{\Omega}) = \int_{\text{sky}} I_{\mathrm{S}}(\overset{\bullet}{s}_a, \vec{\Omega}')\, A\, \rho(\vec{\Omega}')\, \mathrm{d}\vec{\Omega}'\ \ e^{-\overset{\bullet}{\tau}(\overset{\bullet}{s}_a)} \tag{6.13}$$

$$= \int_{\text{sky}} \int_{\overset{\circ}{s}_a}^{\overset{\circ}{s}_b} \sigma(s) \phi(s, \vec{\Omega}', \vec{\Omega}_*)\, e^{-\overset{\circ}{\tau}(s) - \overset{*}{\tau}(s)}\, \mathrm{d}s\ \ A\, \rho(\vec{\Omega}')\, \mathrm{d}\vec{\Omega}'\ \ e^{-\overset{\bullet}{\tau}(\overset{\bullet}{s}_a)} \tag{6.14}$$

6.2.3 Observational Geometries in *SCIARAYS*

The RTM in *SCIARAYS* can be used to model an arbitrary observational geometry: The observer's altitude level and viewing direction can be chosen freely. Depending on this selection, only some of the ray paths described above are applicable.

The contribution of the direct radiance I_{D} must be switched on or off manually by the user. All other contributions are evaluated or set to zero automatically. Additionally, the user may neglect any particular subset of ray paths.

Space-Borne Limb

In limb geometry only radiation which is scattered in the direction of the satellite is observed, see Figure 6.1:

$$I(\vec{r}, \vec{\Omega}) \approx I_{\mathrm{S}}(\vec{r}, \vec{\Omega}) + I_{\mathrm{SS}}(\vec{r}, \vec{\Omega}) + I_{\mathrm{RS}}(\vec{r}, \vec{\Omega}) \tag{6.15}$$

Space-borne Nadir

In nadir geometry the observed radiation contains additional contributions from reflection to the satellite:

$$I(\vec{r}, \vec{\Omega}) \approx I_{\mathrm{S}}(\vec{r}, \vec{\Omega}) + I_{\mathrm{SS}}(\vec{r}, \vec{\Omega}) + I_{\mathrm{RS}}(\vec{r}, \vec{\Omega}) + I_{\mathrm{R}}(\vec{r}, \vec{\Omega}) + I_{\mathrm{SR}}(\vec{r}, \vec{\Omega}) \tag{6.16}$$

Space-borne Occultation

The directly transmitted radiation dominates occultation measurements. Scattered radiances contribute additionally:

$$I(\vec{r},\vec{\Omega}) \approx I_{\mathrm{D}}(\vec{r},\vec{\Omega}) + I_{\mathrm{S}}(\vec{r},\vec{\Omega}) + I_{\mathrm{SS}}(\vec{r},\vec{\Omega}) + I_{\mathrm{RS}}(\vec{r},\vec{\Omega}) \tag{6.17}$$

Ground-based

Ground-based scattering (zenith or off-axis) and occultation measurements are modelled with the same ray path types as space-borne limb and occultation measurements, respectively:

$$I(\vec{r},\vec{\Omega}) \approx \overbrace{I_{\mathrm{D}}(\vec{r},\vec{\Omega}) + \underbrace{I_{\mathrm{S}}(\vec{r},\vec{\Omega}) + I_{\mathrm{SS}}(\vec{r},\vec{\Omega}) + I_{\mathrm{RS}}(\vec{r},\vec{\Omega})}_{\text{scattering}}}^{\text{occultation}} \tag{6.18}$$

Airborne

For airborne scattering (limb, off-axis, zenith) and occultation measurements, exactly the same considerations and formulae as for their space-borne or ground-based counterparts apply.

6.3 Discretisation

The formulation of the radiative transfer equation described in Section 6.2 contains integrals but not derivatives. In *SCIARAYS*, these integrals are solved by *quadrature*, i.e., numerical integration [Press et al., 1992, section 4.0].

Two types of integrals occur: integrals over solid angles and integrals over rays. The underlying discretisation formulae are introduced in Section 6.3.1 and their application to the radiative transfer equation is given in the subsequent Section 6.3.2.

Spherical coordinates are used throughout all routines. The direction $\vec{\Omega}$ of a light ray is given in terms of zenith and azimuth angles. A horizontally stratified atmosphere is assumed. In a spherical or plane-parallel refractive atmosphere the direction $\vec{\Omega}$ is not constant along a ray. Therefore it is substituted by a modified parametrisation $\Omega(s)$ in the integrations over s in all formulae.

6.3.1 General Approach

Integration over Solid Angles

All integrations over solid angles $\vec{\Omega}$ are performed using the azimuth angle ϕ and the cosine $\mu = \cos(\psi)$ of the local zenith angle ψ[3]:

$$\int x(\vec{\Omega})\,\mathrm{d}\vec{\Omega} = \int_0^{2\pi}\int_a^b x(\mu,\phi)\,\mathrm{d}\mu\,\mathrm{d}\phi \tag{6.19}$$

with:
$$a=-1,\quad b=1 \quad \text{for integration over the whole sphere} \tag{6.20}$$
$$a=-1,\quad b=\mu_{\text{horizon}} \quad \text{for integration over the ground} \tag{6.21}$$
$$a=0,\quad b=1 \quad \text{for integration over the sky,} \tag{6.22}$$

where the altitude-dependent μ_{horizon} characterises the apparent zenith angle of the horizon. Since integration just over the sky is always performed at ground level (see Section 6.2.2), $a = 0$ can be used as lower limit of the μ-integration in (6.22).

Using $m_{\max}$ (and $p_{\max}$) equidistant points μ_m (and ϕ_p), the *extended midpoint rule* [Press et al., 1992, (4.1.19)] yields the quadrature of (6.19):

$$\int_0^{2\pi}\int_a^b x(\mu,\phi)\,\mathrm{d}\mu\,\mathrm{d}\phi = \frac{2\pi}{m_{\max}}\frac{b-a}{p_{\max}}\sum_{m=1}^{m_{\max}}\sum_{p=1}^{p_{\max}} x_{m,p} \tag{6.23}$$

$$= \frac{2\pi(b-a)}{k_{\max}}\sum_{k=1}^{k_{\max}} x_k \tag{6.24}$$

with:
$$x_{(p-1)*m_{\max}+m} \equiv x_{m,p} \equiv x(\mu_m,\phi_p) \tag{6.25}$$
$$k_{\max} \equiv m_{\max}\times p_{\max}\ . \tag{6.26}$$

This is an open formula, i.e., the boundaries of the integration intervals are not evaluated.

Integration along Rays

The evaluation of the line-integral of any function $x(s)$ along a ray uses the discrete ray points introduced in appendix A. Thus the ray path lengths Δs_j (see appendix A) are the appropriate quadrature weights:

$$\int_{s_a}^{0} x(s)\,\mathrm{d}s = \sum_{j=1}^{npts} x_j\,\Delta s_j, \tag{6.27}$$

with:
$$x_j \equiv x(s_j)\ , \tag{6.28}$$

where s_a is the path coordinate of the most distant point on the ray and $npts$ is the number of discrete points, which represent the whole ray.

[3]The transformation to μ is equivalent to *Gaussian quadrature* [Press et al., 1992, Section 4.5].

When the line-integral covers only a part of the ray, the quadrature weight of the last point has to be reduced by half of its ray path length:

$$\int_{s<s_a}^{0} x(s)\,\mathrm{d}s \;=\; \left(\sum_{j=1}^{n<npts} x_j\,\Delta s_j\right) - \frac{1}{2}x_n\,\Delta s_n\;. \tag{6.29}$$

The assumption of a horizontally homogeneous atmosphere implies that all functions depend on the altitude solely, i.e., $x(s) = x(z(s))$, $X_i \equiv x(z(s_j))$. In this case, the summations in (6.28) and (6.29) can be transformed to iterate over all altitude levels instead of all ray points. Thereby the number of summations is reduced:

$$\int_{s}^{0} x(s)\,\mathrm{d}s \quad = \quad \sum_{j=1}^{npts} x_j\,\Delta s_j = \sum_{i=1}^{nlays} X_i\,\Delta l_i \tag{6.30}$$

$$\text{with:} \qquad \Delta l_i \equiv \sum_{j=1}^{npts} \delta_{i,level_j}\,\Delta s_j \tag{6.31}$$

$$\text{or:} \qquad \Delta l_i \equiv \left(\sum_{j=1}^{n<npts} \delta_{i,level_j}\,\Delta s_j\right) - \frac{1}{2}\,\Delta s_n\;. \tag{6.32}$$

The *accumulated ray path lengths* Δl_i sum up all ray path lengths Δs_j which correspond to the same altitude level j.

Applying (6.32) to (5.8), a discrete formula for the optical depth at each point of a ray in a horizontally homogeneous atmosphere is obtained:

$$\tau(s) = \int 0_s\kappa(s')\,\mathrm{d}s' \;=\; \sum_{i=1}^{nlays} \kappa_i \Delta l_i \tag{6.33}$$

For the optical thickness of each individual ray the same formula is obtained from (6.31):

$$\tau = \int_{s_{\max}}^{0} \kappa(s')\,\mathrm{d}s' \;=\; \sum_{i=1}^{nlays} \kappa_i \Delta l_i \tag{6.34}$$

The optical thickness of a whole ray path, which consists of several — say: three — rays, is the sum the the rays individual optical thicknesses. Since all contributions are sums over the altitude levels, the accumulated ray path lengths Δl of the individual rays can be collected in the *collected ray path lengths* ΔL:

$$\tau \;=\; \overset{\bullet}{\tau} + \overset{\circ}{\tau} + \overset{*}{\tau} \tag{6.35}$$

$$\;=\; \sum_{i=1}^{nlays} \kappa_i\,\Delta L_i \tag{6.36}$$

$$\text{with:}\quad \Delta L_i \;\equiv\; \overset{\bullet}{\Delta l}_i + \overset{\circ}{\Delta l}_i + \overset{*}{\Delta l}_i\;. \tag{6.37}$$

The advantage of this formulation is that the optical thickness can be calculated with few arithmetic operations, while the geometrical properties scenario and the optical properties of the atmosphere are separated: The accumulated ray path lengths remain the same for the calculations of all wavelengths and all atmospheric profiles. Thus they can be pre-computed and stored once. Afterwards, they are available for all steps in a (non-linear) retrieval process.

6.3.2 Application to the Ray Paths

Discretising the integral expressions for the ray path radiances given in Section 6.2.2, the following summation formulae are obtain:

Direct Radiation: D

From (6.1):

$$\overset{*}{T} = \exp\left(-\sum_{i=1}^{nlays} \kappa_i \, \Delta L_i^D\right) \tag{6.38}$$

$$\text{with:} \quad \Delta L_i^D \equiv \overset{*}{\Delta} l_i \tag{6.39}$$

Reflected Radiance: R

From (6.6):

$$I_{\mathrm{R}}(\overset{\bullet}{s}_b, \vec{\Omega}) = v^R \, A \, \exp\left(-\sum_{i=1}^{nlays} \kappa_i \, \Delta L_i^R\right) \tag{6.40}$$

$$\text{with:} \quad \Delta L_i^R \equiv \overset{\bullet}{\Delta} l_i + \overset{*}{\Delta} l_i \tag{6.41}$$

$$v^R = \rho(\vec{\Omega}') \tag{6.42}$$

Single Scattering: S

From (6.8):

$$I_{\mathrm{S}}(\overset{\bullet}{s}_b, \vec{\Omega}) = \sum_{j=1}^{\overset{\bullet}{npts}} v_j^S \, \sigma_j \, \exp\left(-\sum_{i=1}^{nlays} \kappa_i \, \Delta L_{i,j}^S\right) \tag{6.43}$$

$$\text{with:} \quad \Delta L_{i,j}^S \equiv \overset{\bullet}{\Delta} l_i \, (\overset{\bullet}{s}_j) + \overset{*}{\Delta} l_i \, (\overset{\bullet}{s}_j) \tag{6.44}$$

$$v_j^S \equiv \phi(s_j, \vec{\Omega}, \vec{\Omega}_*) \tag{6.45}$$

$$\sigma_j \equiv \sigma(z(s_j)) \tag{6.46}$$

Second Order of Scattered Radiance: SS

From (6.10):

$$I_{\mathrm{S}}(\overset{\bullet}{s}_b,\vec{\Omega}) = \sum_{\overset{\bullet}{j}=1}^{\overset{\bullet}{npts}} \overset{\bullet}{\sigma}_{\overset{\bullet}{j}} \frac{4\pi}{k_{\max}} \sum_{k=1}^{k_{\max}} \overset{\bullet}{\phi}_{k,\overset{\bullet}{j}} \sum_{\overset{\circ}{j}=1}^{\overset{\circ}{npts}} \overset{\circ}{\sigma}_{\overset{\circ}{j},k,\overset{\bullet}{j}} \overset{\circ}{\phi}_{\overset{\circ}{j},k,\overset{\bullet}{j}} \exp\left(-\sum_{i=1}^{nlays} \kappa_i \, \Delta L^{SS}_{i,\overset{\circ}{j},k,\overset{\bullet}{j}}\right)$$

$$= \sum_{j=1}^{\overset{\bullet}{npts}\cdot k_{\max}\cdot\overset{\circ}{npts}} v_j^{SS} \, \overset{\bullet}{\sigma}_j \overset{\circ}{\sigma}_j \exp\left(-\sum_{i=1}^{nlays} \kappa_i \, \Delta L^{SS}_{i,j}\right) \tag{6.47}$$

$$\text{with:} \quad \Delta L^{SS}_{i,j} = \overset{\bullet}{\Delta} l_i \, (\overset{\bullet}{s}_j) + \overset{\circ}{\Delta} l_i \, (\overset{\circ}{s}_j) + \overset{*}{\Delta} l_i \, (\overset{\circ}{s}_j) \tag{6.48}$$

$$v_j^{SS} \equiv \frac{4\pi}{k_{\max}} \, \overset{\bullet}{\sigma}_{\overset{\bullet}{j}} \overset{\circ}{\sigma}_{\overset{\circ}{j},k,\overset{\bullet}{j}} \tag{6.49}$$

Reflected-then-Scattered Radiance: RS

From (6.12)[4]:

$$I_{\mathrm{RS}}(\overset{\bullet}{s}_b,\vec{\Omega}) = \sum_{\overset{\bullet}{j}=1}^{\overset{\bullet}{npts}} \sigma_{\overset{\bullet}{j}} \frac{2\pi(\mu_{\mathrm{horizon},j}+1)}{k_{\max}} \sum_{k=1}^{k_{\max}} \phi_{\overset{\bullet}{j},k} \, A \, \rho_{\overset{\bullet}{j},k} \exp\left(-\sum_{i=1}^{nlays} \kappa_i \, \Delta L^{RS}_{i,\overset{\bullet}{j},k}\right) \tag{6.50}$$

$$= \sum_{j=1}^{\overset{\bullet}{npts}\cdot k_{\max}} v_j^{RS} \, A \, \sigma_j \exp\left(-\sum_{i=1}^{nlays} \kappa_i \, \Delta L^{RS}_{i,\overset{\bullet}{j},k}\right) \tag{6.51}$$

$$\text{with:} \quad \Delta L^{RS}_{i,\overset{\bullet}{j},k} = \overset{\bullet}{\Delta} l_i \, (\overset{\bullet}{s}_{\overset{\bullet}{j}}) + \overset{\circ}{\Delta} l_i \, (\overset{\circ}{s}_{\overset{\bullet}{j},k}) + \overset{*}{\Delta} l_i \, (\overset{\circ}{s}_{a\overset{\bullet}{j},k}) \tag{6.52}$$

$$v_j^{RS} \equiv \frac{2\pi(\mu_{\mathrm{horizon},j}+1)}{k_{\max}} \phi_{\overset{\bullet}{j},k} \, \rho_{\overset{\bullet}{j},k} \tag{6.53}$$

Scattered-then-Reflected Radiance: SR

From (6.14):

$$I_{\mathrm{SR}}(\overset{\bullet}{s}_b,\vec{\Omega}) = \frac{2\pi}{k_{\max}} \sum_{k=1}^{k_{\max}} A \, \rho_k \sum_{\overset{\circ}{j}=1}^{\overset{\circ}{npts}} \sigma_{\overset{\circ}{j}} \phi_{\overset{\circ}{j}} \exp\left(-\sum_{i=1}^{nlays} \kappa_i \, \Delta L^{SR}_{i,k,\overset{\circ}{j}}\right) \tag{6.54}$$

$$= \sum_{j=1}^{k_{\max}\cdot\overset{\circ}{npts}} v_j^{SR} \, A \, \sigma_j \exp\left(-\sum_{i=1}^{nlays} \kappa_i \, \Delta L^{SR}_{i,k,\overset{\circ}{j}}\right) \tag{6.55}$$

[4]The actual implementation uses one more approximation for RS: The scattering phase function $\phi_{\overset{\bullet}{j},k}$ is always determined for $90\,^\circ$ scattering angle.

$$\text{with:} \quad \Delta L^{SR}_{\overset{\circ}{i,k,j}} = \overset{\bullet}{\Delta} l_i \, (\overset{\bullet}{s}_a) + \overset{\circ}{\Delta} l_i \, (\overset{\circ}{s}_{\overset{\circ}{k,j}}) + \overset{*}{\Delta} l_i \, (\overset{\circ}{s}_{\overset{\circ}{k,j}}) \tag{6.56}$$

$$v^{SR}_j = \frac{2\pi}{k_{\max}} \rho_k \, \phi_{\overset{\circ}{j}} \tag{6.57}$$

General Formulation: R+S+SS+RS+SR

The quadrature terms of all ray paths except direct transmission can be represented by a common formula:

$$I(\overset{\bullet}{s}_b, \vec{\Omega}) = \sum_j \underbrace{v_j \, [\sigma_{i1_j}]^{\delta^{S1}_j} \, [\sigma_{i2_j}]^{\delta^{S2}_j} \, [A]^{\delta^R_j} \exp\left(- \sum_{i=1}^{nlays} \kappa_i \, \Delta L_{i,j} \right)}_{\equiv I_j} \tag{6.58}$$

where δ^{S1}_j, δ^{S2}_j and δ^R_j are set to unity for rays which involve scattering, also second scattering and surface reflection, respectively. Otherwise, they are set to zero. Thereby factors marked with square brackets $[.]$ are set to unity for some indices j. I_j is the radiance due to the j-th ray path.

Only the albedo A, the scattering coefficients σ and the extinction coefficient κ depend on the modelled wavelength or atmospheric model[5]. All other parameters remain the same throughout all forward model evaluations of one retrieval process. Therefore, they are calculated only once and stored for subsequent use.

6.4 Validation

To validate the atmospheric radiative transfer model in *SCIARAYS*, comparisons with other radiative transfer models are performed.

6.4.1 Comparison to MODTRAN

The refractive ray tracing routines of *SCIARAYS* are validated by comparison with calculations of MODTRAN [Kneizys et al., 1996] in single scattering mode. This mode of MODTRAN does not include albedo, and the refractive bending cannot be switched off, so

- spherical, refractive ray tracing and
- Rayleigh scattering

are assumed. The relative deviation of *SCIARAYS* from MODTRAN is shown in Figure 6.2. These calculations were performed for a tangent height of $1\,\mathrm{km}$, a solar zenith

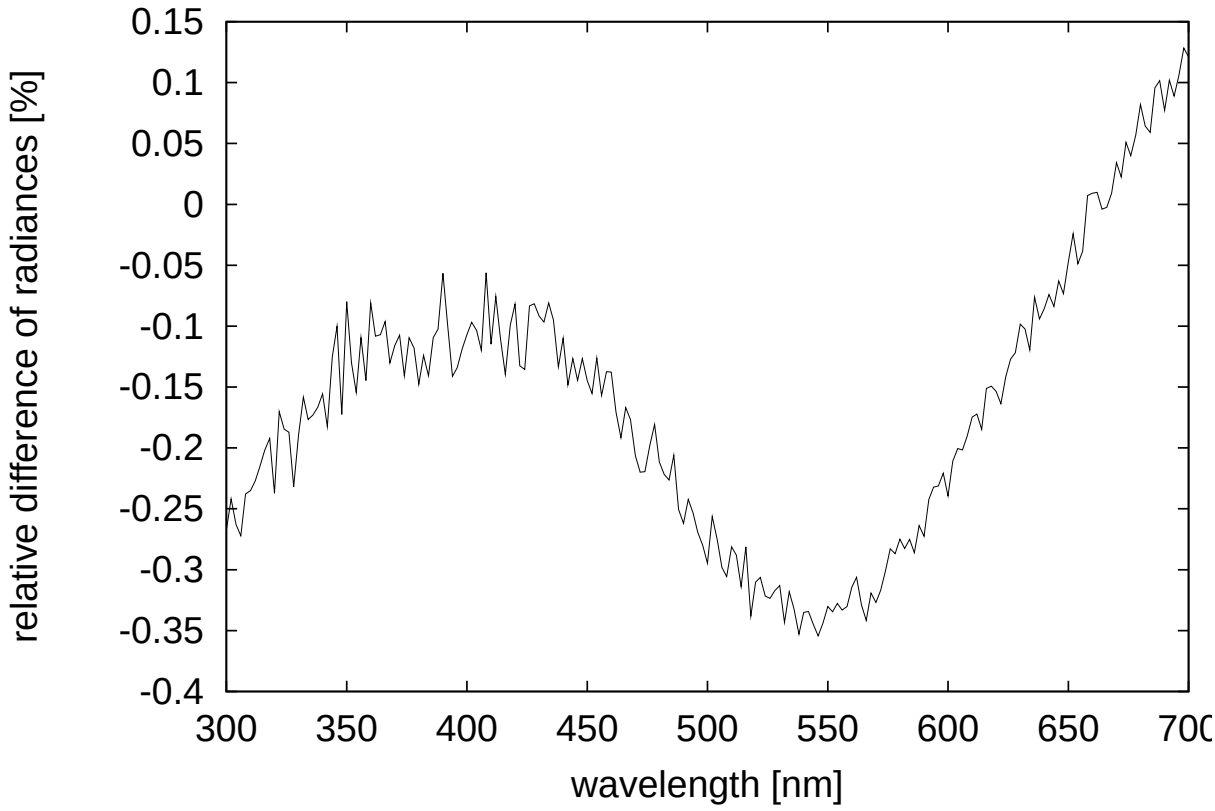

Figure 6.2: Relative difference of the radiance computed by *SCIARAYS* as compared to output from MODTRAN.

angle of $89\,^\circ$ and a relative azimuth of $60\,^\circ$. The scenario is chosen to maximise the effect of refraction.

The high frequency signal in Figure 6.2 can be interpreted as numerical noise of either *SCIARAYS* or MODTRAN. It is estimated to be of about $0.1\,\%$. Since the two codes exhibit a wavelength-dependent, systematic deviation of less than $0.35\,\%$, the spherical, refractive ray tracing and first order of Rayleigh scattering appear to be accurate to $0.35\,\%$ or less.

6.4.2 Comparison to SIRO

The limb radiances at five wavelengths in the spectral range 300–$700\,\mathrm{nm}$ are computed with *SCIARAYS* and compared to calculations with the Monte Carlo (MC) model SIRO [Oikarinen, 1999]. In order to achieve consistency between the two models, *SCIARAYS* is used with the ray paths S and RS only (see Figure 6.1), and SIRO has been modified by

[5]Strictly spoken, the aerosol scattering phase function can vary, too, but this effect is currently neglected as no retrieval of this parameter is anticipated.

Liisa Oikarinen of the Finnish Meteorological Institute (*FMI*) to simulate one scattering event and possibly one surface reflection only. The comparison is performed for the three scenarios defined in Table 6.2 in a model atmosphere comprising

- spherical, geometric ray tracing
- Rayleigh scattering
- ozone absorption
- Lambertian surface reflection.

Figure 6.3 shows the comparison for scenario A. The calculated radiances are given in the top plot, while the relative difference to SIRO along with SIRO's statistical standard deviation is depicted in the bottom plot. The standard deviation can be interpreted as the precision of a Monte Carlo calculation.

In the spectral range 350–$700\,\mathrm{nm}$, the two models agree within $0.5\,\%$. This conforms well with the precision of the Monte Carlo calculations. Due to the large solar zenith angle the scenario A cannot be used for the validation of surface reflection. However, it can be concluded that the spherical, geometric ray tracing, the Rayleigh scattering and the trace gas absorption modules perform together with an accuracy of below $1\,\%$ for the singly scattered radiance.

At $300\,\mathrm{nm}$, the models differ by $3\,\%$ whereas the precision of the MC model is estimated to be below $1\,\%$. Since the radiance at $300\,\mathrm{nm}$ is very small due to ozone absorption, the relative difference between the models corresponds to a rather small absolute difference, see Figure 6.3, bottom plot. The difference between the two models is probably caused by numerical limitations in either of them.

The results for the scenarios B and C are shown in Figure 6.4. Again the radiances are plotted on the top and the relative differences along with SIRO's standard deviation on the bottom.

The values for scenario C with vanishing albedo support the findings from scenario A: *SCIARAYS* is validated within the limits of the MC calculations, i.e., $1\,\%$. But

Table 6.2: Scenarios for Comparison to SIRO

	A	B	C
solar zenith angle [deg]	88	30	
azimuth angle [deg]	90	90	
albedo	1		0
tangent height [km]	10		
profiles (p, T, O_3)	US std. atm. 76		

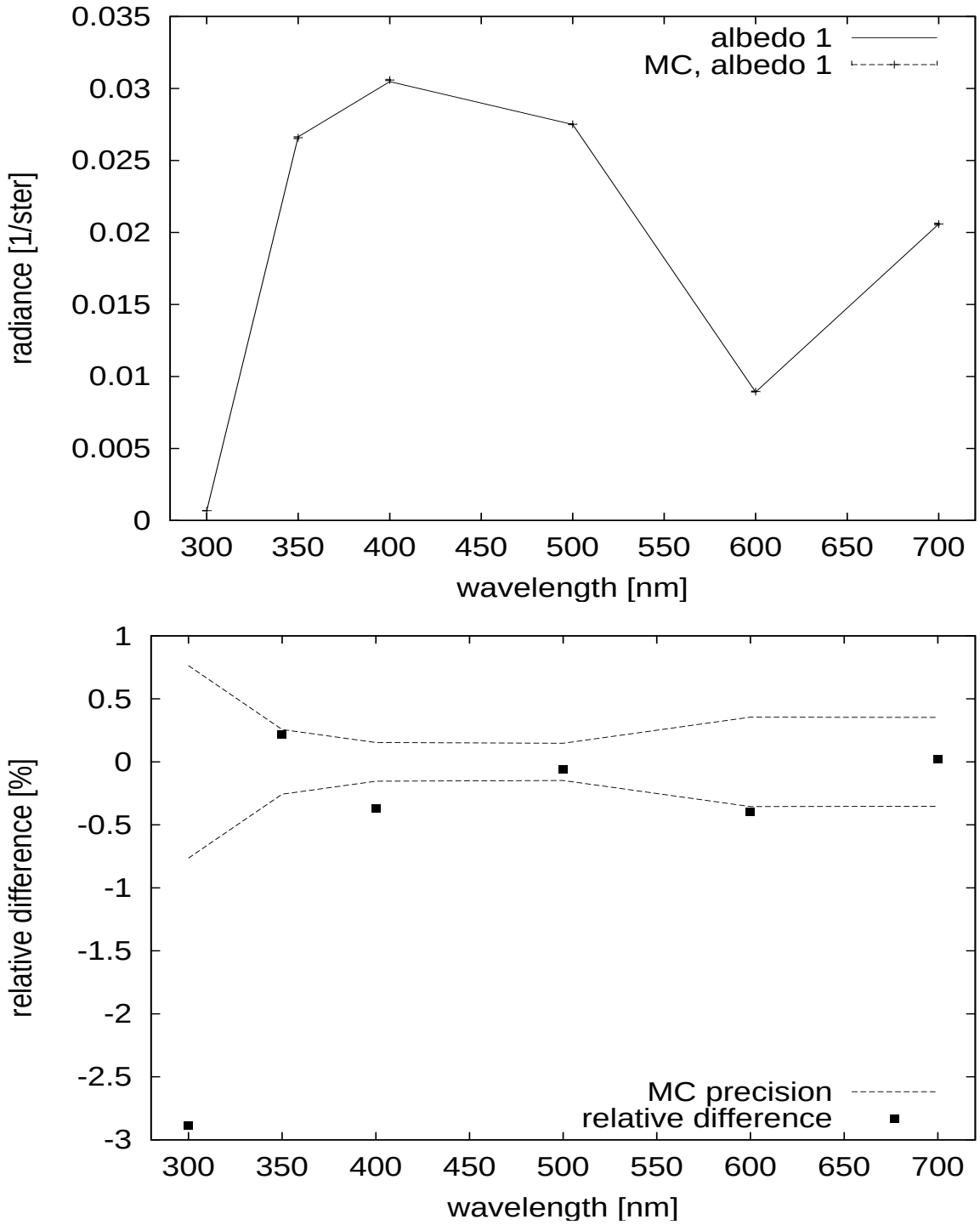

Figure 6.3: Comparison between *SCIARAYS* and the Monte Carlo (MC) model SIRO for scenario A. TOP: sun-normalised radiances (The MC results are given with error bars according its statistical standard deviation.) BOTTOM: relative differences.

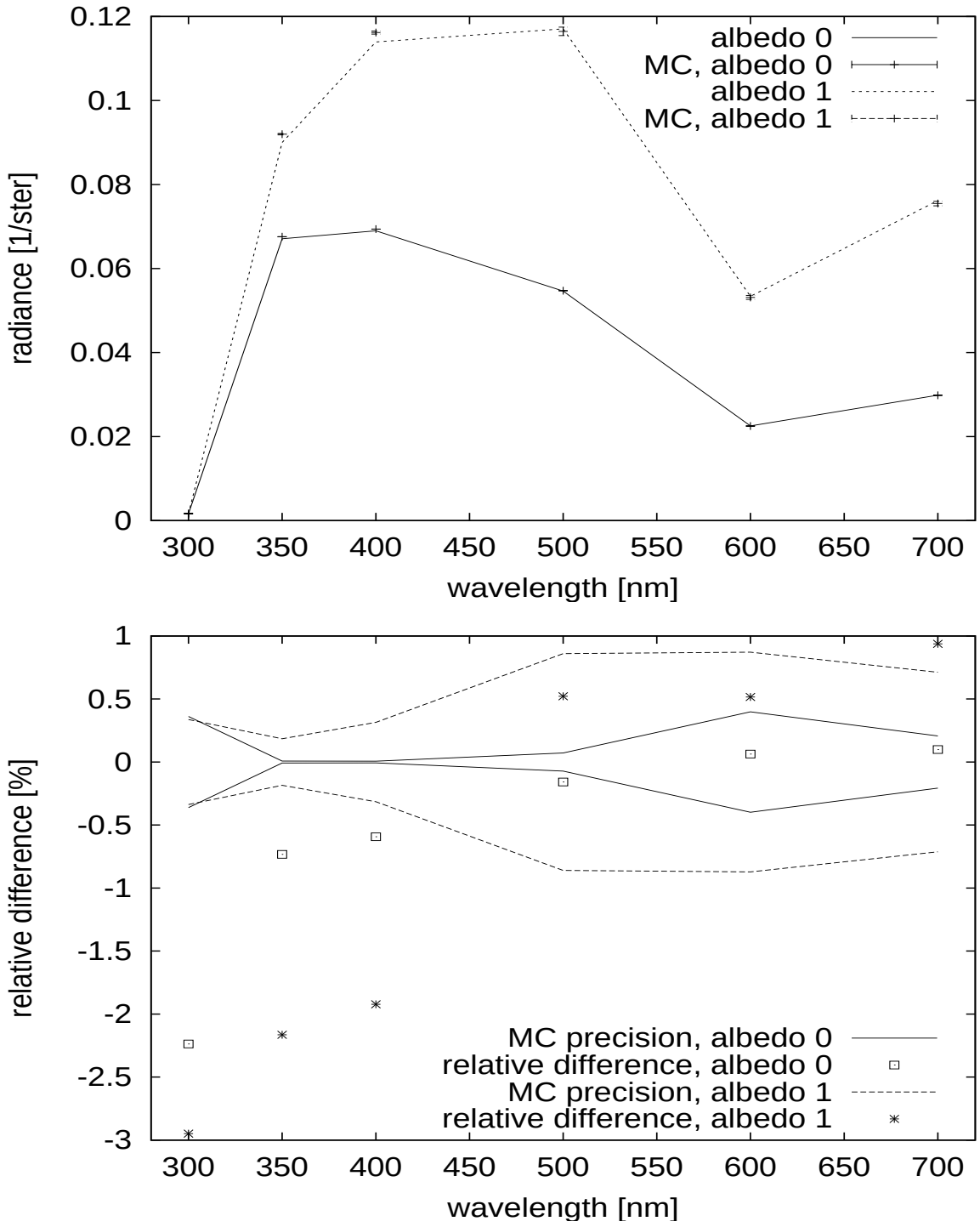

Figure 6.4: Comparison between *SCIARAYS* and the Monte Carlo (MC) model SIRO for scenarios B (albedo 0) and C (albedo 1). TOP: sun-normalised radiances (The MC results are given with error bars according its statistical standard deviation.): BOTTOM: relative differences.

there might be inaccuracies of several percent for very small radiance values[6].

The results for scenario B exhibit an additional difference of 1–2 %, which must be attributed to the simulation of surface reflection. Since surface reflection can be seen as a part of multiple scattering, which is not completely modelled by *SCIARAYS*, the accuracy of 1–2 % for this ray path is sufficient for all applications of *SCIARAYS*.

6.4.3 Comparison to GOMETRAN

The aerosol initialisation routines of GOMETRAN [Rozanov et al., 1997a] are well established. The aerosol treatment in *SCIARAYS* is tested by comparison to GOMETRAN calculations. Since GOMETRAN does not operate in limb viewing geometry, a

- nadir measurement with
- refractive bending,
- O_3 and NO_2 absorption,
- Rayleigh scattering, and
- aerosol scattering (stratospheric background, 23 km tropospheric visibility)

is simulated using a solar zenith angle of 89 °. In order to avoid GOMETRAN's pseudo-spherical approximation, only single scattering is modelled.

The relative difference between the two models is plotted in Figure 6.5. The models agree within 0.5 % in the UV spectral region and within 2 % in the visible range. A systematic increase of the difference with increasing wavelength is apparent. It can be traced back to the fact that *SCIARAYS* uses less terms than GOMETRAN in the Legendre series for expanding the aerosol scattering phase function. The underlying reason for the wavelength dependence of the difference is therefore the fact that aerosol scattering as compared to Rayleigh scattering is the more dominant the longer the wavelength is.

Unlike molecules, individual aerosol particles differ from each other and the radiative transfer has to model the continuously varying properties of the aerosol ensemble. Therefore, the aerosol properties, especially their wavelength dependence, can never be modelled with the same accuracy as the properties of, say, molecular absorption. From this point of view, the achieved accuracy of the aerosol treatment of 2 % appears to be sufficient for all applications in the near future. If better accuracy were required, it could easily be achieved be taking into account more terms in the mentioned Legendre series.

[6] However, the fact that the Monte Carlo model's standard deviations virtually vanish at 350 and 400 nm raises doubts concerning their applicability as measure of the Monte Carlo model's precision, thereby weakening any conclusions on accuracy.

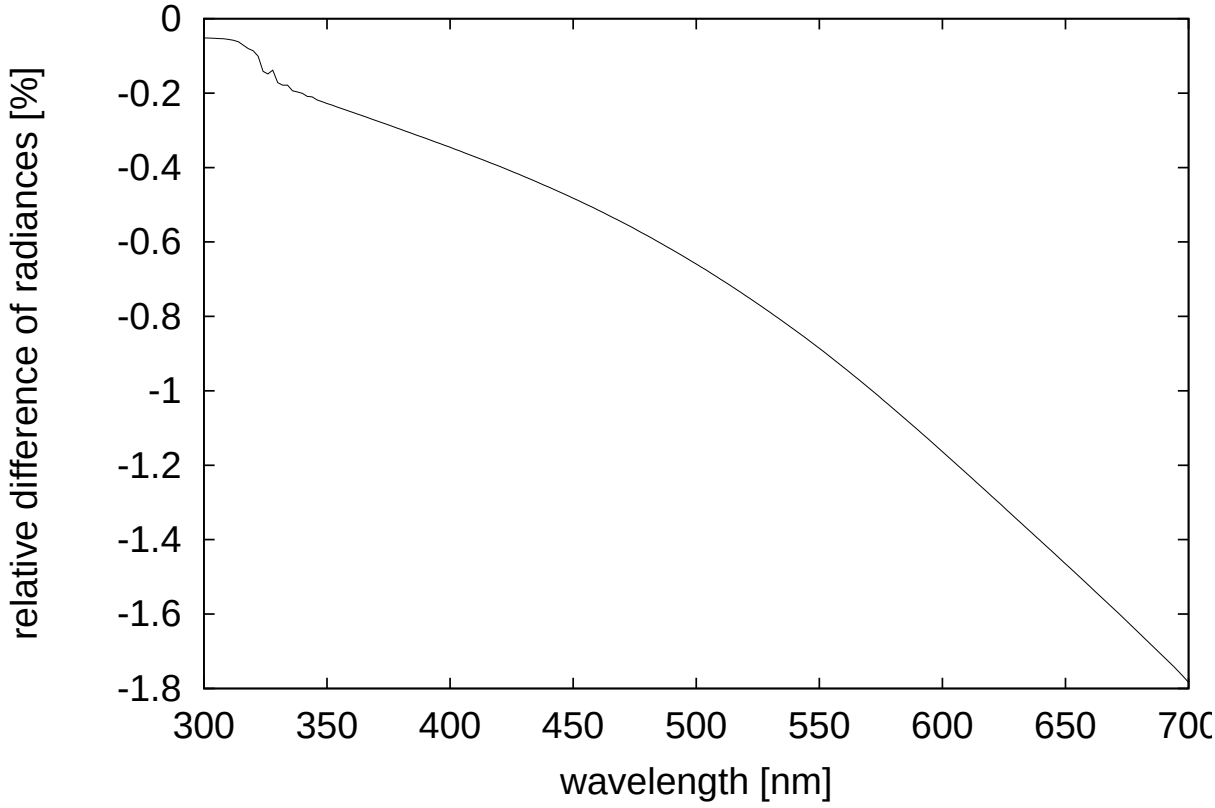

Figure 6.5: Relative difference of the radiance computed by *SCIARAYS* as compared to output from GOMETRAN including O_3, NO_2, refraction and aerosols for solar zenith angle $89\,^\circ$ and single scattering.

6.5 Weighting Functions

6.5.1 Introduction

The derivatives of the modelled radiance w.r.t. the model parameters are called *weighting functions*[7]. They are required more or less explicitly by all retrieval algorithms. The optimal estimation method used in this thesis requires an explicit calculation of the weighting functions, see Chapter 8.

Since atmospheric RTMs depend non-linearly on the model parameters, their weighting functions depend on the model parameters. The weighting functions are also

[7] In the "real" world, the radiance $I(x)$ measured by one pixel is a functional of, say, one continuous function x, the atmospheric profile. Therefore, a weighting function of the measurement is the ratio of the variation δI of the radiance due to the variation δx of the profile: $\delta I/\delta x$. Nevertheless, the simpler concept of derivatives is sufficient in the context of numerical retrieval since it describes any **discrete** model and retrieval completely.

called *linearisation* of the model as they specify the linear tangent model of a non-linear model.

Normalisations

Three different representations of the weighting functions are commonly used depending on the focus of the discussion. In order to prevent misunderstandings, the following naming convention is introduced for this thesis:

Absolute-absolute weighting functions W^{aa} are the plain, non-normalised derivatives. For instance,

$$W_T^{\mathrm{aa}} \equiv \frac{\mathrm{d}I}{\mathrm{d}T} \quad \left[\frac{\mathrm{sr}^{-1}}{\mathrm{K}}\right] \tag{6.59}$$

is the absolute change $[\mathrm{sr}^{-1}]$ of (sun-normalised) radiance at one wavelength due to a change of $1\,\mathrm{K}$ in the temperature at one altitude level.

Relative-absolute weighting functions W^{ra} are the derivatives w.r.t. the normalisation of a model parameter. For instance,

$$W_T^{\mathrm{ra}} \equiv T\frac{\mathrm{d}I}{\mathrm{d}T} \quad \left[\mathrm{sr}^{-1}\right] \tag{6.60}$$

specifies the absolute change $[\mathrm{sr}^{-1}]$ of (sun-normalised) radiance at one wavelength due to a change of $100\,\%$ in the temperature at one altitude level.

Relative-relative weighting functions W^{rr} are derivatives, which are normalised w.r.t. the radiance and the model parameter. For instance,

$$W_T^{\mathrm{aa}} \equiv \frac{T}{I}\frac{\mathrm{d}I}{\mathrm{d}T} \quad [\text{-}] \tag{6.61}$$

is the the dimensionless quantity which describes the relative change of the radiance at one wavelength due to a relative change of $100\,\%$ in the temperature at one altitude level.

Computational Methods

There are two conceptually different methods of calculating weighting functions:

***numerical perturbation*:** After the calculation of the radiances, the RTM may be evaluated a second time with one parameter perturbed. The fraction of differences can then be used as approximation for the derivative. The magnitude of the perturbation must be chosen small enough to avoid interference by the non-linearity of the RTM, but large enough to avoid numerical precision problems[8].

[8] An algorithm with adaptive magnitude selection can be found in Press et al. [1992, Section 5.7]. It involves, however, several calls to the RTM.

Since each altitude level of a profile is described by its own parameter, the RTM typically has to be evaluated several hundred times to obtain a full set of weighting functions. In an iterative fitting process, the weighting functions must be recalculated in every iteration. Evaluating the RTM so many times would require a prohibitively large amount of computational resources. Therefore, numerical perturbation cannot be used for weighting function calculation in an operational or near-real-time limb measurement processor.

***quasi-analytical computation*:** If the type of the RTM allows to derive analytical expressions for the weighting functions, these can be evaluated numerically along with the radiances.

Since the same quantities, e.g., path lengths, are required for both the radiances and the weighting functions, the additional computational burden for all parameter's weighting functions is typically similar to the one for the radiance computations alone. Therefore, quasi-analytical computation is the only feasible method for models used in profile retrievals.

This method is also called *analytical computation* in the literature.

It is performed by *SCIARAYS* for all model parameters.

6.5.2 Implemented Analytical Expressions

In this subsection, analytical expressions for the absolute-absolute weighting functions are derived from *SCIARAYS'* general RT formula (6.58).

The partial derivatives of the radiance w.r.t. the scattering and extinction coefficient at altitude level i will be used:

$$\frac{\partial I}{\partial \kappa_i} = \sum_j v_j \left[\sigma_{i1_j}\right]^{\delta_j^{S1}} \left[\sigma_{i2_j}\right]^{\delta_j^{S2}} [A]^{\delta_j^R} \left(-\Delta L_{i,j}\right) \exp\left(-\sum_{i'=1}^{nlays} \kappa_{i'} \Delta L_{i',j}\right) \tag{6.62}$$

$$= -\sum_j \Delta L_{i,j} I_j \tag{6.63}$$

$$\frac{\partial I}{\partial \sigma_i} = \sum_j v_j \left(\frac{\partial [\sigma_{i1_j}]^{\delta_j^{S1}}}{\partial \sigma_i} \left[\sigma_{i2_j}\right]^{\delta_j^{S2}} + \left[\sigma_{i1_j}\right]^{\delta_j^{S1}} \frac{\partial [\sigma_{i2_j}]^{\delta_j^{S2}}}{\partial \sigma_i}\right) [A]^{\delta_j^R} \exp\left(-\sum_{i'=1}^{nlays} \kappa_{i'} \Delta L_{i',j}\right)$$

$$= \sum_j v_j \left(\delta_j^{S1} \left[\sigma_{i2_j}\right]^{\delta_j^{S2}} + \left[\sigma_{i1_j}\right]^{\delta_j^{S1}} \delta_j^{S2}\right) [A]^{\delta_j^R} \exp\left(-\sum_{i'=1}^{nlays} \kappa_{i'} \Delta L_{i',j}\right) \tag{6.64}$$

$$= \sum_j \frac{\delta_j^{S1} \left[\sigma_{i2_j}\right]^{\delta_j^{S2}} + \left[\sigma_{i1_j}\right]^{\delta_j^{S1}} \delta_j^{S2}}{\left[\sigma_{i1_j}\right]^{\delta_j^{S1}} \left[\sigma_{i2_j}\right]^{\delta_j^{S2}}} I_j \tag{6.65}$$

Albedo

The weighting function for the albedo is:

$$W_A^{\mathrm{aa}} = \frac{\mathrm{d}I}{\mathrm{d}A} \tag{6.66}$$

$$= \sum_j \delta_j^R \, v_j \, [\sigma_{i1_j}]^{\delta_j^{S1}} \, [\sigma_{i2_j}]^{\delta_j^{S2}} \, \exp\left(- \sum_{i=1}^{nlays} \kappa_i \, \Delta L_{i,j} \right) \tag{6.67}$$

$$= \frac{1}{A} \sum_j \delta_j^R \, I_j \tag{6.68}$$

Trace Gas Concentrations

The weighting functions for the trace gas concentration $n_{m,i}$ of a species m at the altitude level i is:

$$W_{n_{m,i}}^{\mathrm{aa}} = \frac{\mathrm{d}I}{\mathrm{d}n_{m,i}} \tag{6.69}$$

$$= \frac{\partial I}{\partial \kappa_i} \frac{\mathrm{d}\kappa_i}{\mathrm{d}n_{m,i}} \tag{6.70}$$

$$\text{with:} \quad \frac{\mathrm{d}\kappa_i}{\mathrm{d}n_{m,i}} = \chi_m \, , \tag{6.71}$$

where the cross section has to be chosen at the appropriate temperature and pressure of the altitude level i, see (5.1).

Temperature

The weighting functions for the temperature T_i at the altitude level i depends on the temperature dependence of the scattering and the extinction coefficients:

$$W_{T_i}^{\mathrm{aa}} = \frac{\partial I}{\partial \sigma_i} \frac{\mathrm{d}\sigma_i}{\mathrm{d}T_i} + \frac{\partial I}{\partial \kappa_i} \frac{\mathrm{d}\kappa_i}{\mathrm{d}T_i} \tag{6.72}$$

$$\text{with:} \quad \frac{\mathrm{d}\sigma_i}{\mathrm{d}T_i} = -\frac{\sigma_i}{T_i} \tag{6.73}$$

$$\frac{\mathrm{d}\kappa_i}{\mathrm{d}T_i} = \frac{\partial \kappa_i}{\partial \sigma_i} \frac{\mathrm{d}\sigma_i}{\mathrm{d}T_i} + \sum_{m=1}^{nmols} \left. \frac{\mathrm{d}\chi_m}{\mathrm{d}T} \right|_{T_i} n_{m,i} \tag{6.74}$$

$$= \sum_m \left. \frac{\mathrm{d}\chi_m}{\mathrm{d}T} \right|_{T_i} n_{m,i} - \frac{\sigma_i}{T_i} \, . \tag{6.75}$$

The weighting functions for temperature include contributions of the temperature dependence of the absorption cross sections as well contributions from the Rayleigh scattering coefficients which is proportional to the neutral density, see (4.6). The latter depends on temperature by means of the ideal gas law (4.7).

The strongest temperature dependence of absorption cross sections in the UV-vis spectra region occurs in the Huggins bands of ozone. This is one of the reasons why ozone profile retrieval from the nadir-looking GOME instrument is possible [de Beek, 1998].

Pressure

The weighting functions for the pressure p_i at the altitude level i looks analogous to the one for temperature:

$$W_{p_i}^{\mathrm{aa}} = \frac{\partial I}{\partial \sigma_i}\frac{\mathrm{d}\sigma_i}{\mathrm{d}p_i} + \frac{\partial I}{\partial \kappa_i}\frac{\mathrm{d}\kappa_i}{\mathrm{d}p_i} \tag{6.76}$$

$$\text{with:} \quad \frac{\mathrm{d}\sigma_i}{\mathrm{d}p_i} = \frac{\sigma_i}{p_i} \tag{6.77}$$

$$\frac{\mathrm{d}\kappa_i}{\mathrm{d}T_i} = \frac{\partial \kappa_i}{\partial \sigma_i}\frac{\mathrm{d}\sigma_i}{\mathrm{d}p_i} + \sum_{m=1}^{nmols}\left.\frac{\mathrm{d}\chi_m}{\mathrm{d}p}\right|_{p_i} n_{m,i} \tag{6.78}$$

$$= \sum_{m}\left.\frac{\mathrm{d}\chi_m}{\mathrm{d}p}\right|_{p_i} n_{m,i} + \frac{\sigma_i}{p_i}\,. \tag{6.79}$$

Owing to the ideal gas law (4.7) the derivative of the scattering coefficient w.r.t. pressure is positive.

The pressure dependence of all trace gas absorption cross sections vanishes in the UV-vis spectral region. On the other hand, it must and can be accounted for in the NIR spectral region[9].

Aerosol Scattering Coefficient

The weighting functions for the aerosol scattering coefficient $\sigma_{a,i}$ at the altitude level i have a concise form as the aerosol scattering coefficient is an additive component of the scattering and extinction coefficients:

$$W_{\sigma_{a,i}}^{\mathrm{aa}} = \frac{\partial I}{\partial \sigma_i}\frac{\mathrm{d}\sigma_i}{\mathrm{d}\sigma_{a,i}} + \frac{\partial I}{\partial \kappa_i}\frac{\mathrm{d}\kappa_i}{\mathrm{d}\sigma_{a,o}} \tag{6.80}$$

$$= \frac{\partial I}{\partial \sigma_i} + \frac{\partial I}{\partial \kappa_i} \tag{6.81}$$

6.5.3 Consistency Checks

SCIARAYS' quasi-analytically computed weighting functions are verified by checking their consistency with the radiance calculations: They are required to reproduce weight-

[9] The temperature dependence of absorption in the NIR makes accurate tangent height retrievals from SCIAMACHY feasible.

ing functions computed by numerical perturbation within the accuracy limits of the latter method. Here, a perturbation of $1\,\%$ is employed.

The relative-absolute weighting functions for a test scenario with a tangent height of $10\,\mathrm{km}$, solar zenith angle of $30\,^\circ$, relative azimuth between line of sight and solar position of $20\,^\circ$ and an albedo of 0.3 are presented in Figures 6.6 and 6.7. The US standard atmosphere 1976[10] with O_3 and NO_2 is used. Aerosols conforming to a standard GOMETRAN scenario[11] are also included. The atmosphere is discretised in steps of $1\,\mathrm{km}$ from 0 to $60\,\mathrm{km}$. The computation is performed for a wavelength of $350\,\mathrm{nm}$ with geometric ray tracing accounting for one order of scattering plus surface reflection.

For the albedo, the quasi-analytical value is $6.068 \cdot 10^{-3}$ while the numerical value is $6.008 \cdot 10^{-3}$. These values differ by $1\,\%$, the magnitude of the parturbation. The difference is expected since the non-linearity of radiative transfer affects the computation of the numerical weighting functions.

The top plot of Figure 6.6 shows the weighting functions for O_3 and NO_2. The ratios of the quasi-analytical weighting functions and the numerically generated ones displayed in the bottom plot of Figure 6.6 lie almost exactly at 1.01, again displaying the non-linearity of radiative transfer.

The weighting functions for pressure and temperature are shown in the top plot of Figure 6.7. From the fact that they are roughly of the same magnitude, but of opposite direction, it can be concluded that the main effect is due to density changes, i.e., Rayleigh scattering. The slight difference in magnitude arises from the temperature dependence of the ozone absorption.

The ratio of the quasi-analytical pressure weighting function with the numerical one is shown in the bottom plot of Figure 6.6. Apart from the non-linearity effect, the weighting functions differ by up to $10\,\%$ between $10\,\mathrm{km}$ and $15\,\mathrm{km}$. The weighting functions themselves becomes very small in this altitude regime as they change theirs signs. Therefore, the absolute difference between the two weighting functions is so small that the quasi-analytical weighting function can be considered very accurate.

It can be concluded that all[12] quasi-analytically computed weighting functions are highly consistent with the radiance calculation. Since the latter is validated in Section 6.4, the weighting functions are considered validated, too.

[10] The values are extracted from MODTRAN.

[11] stratospheric background, $23\,\mathrm{km}$ tropospheric visibility

[12] The consistency of the weighting functions for the aerosol scattering coefficients has been checked successfully, too.

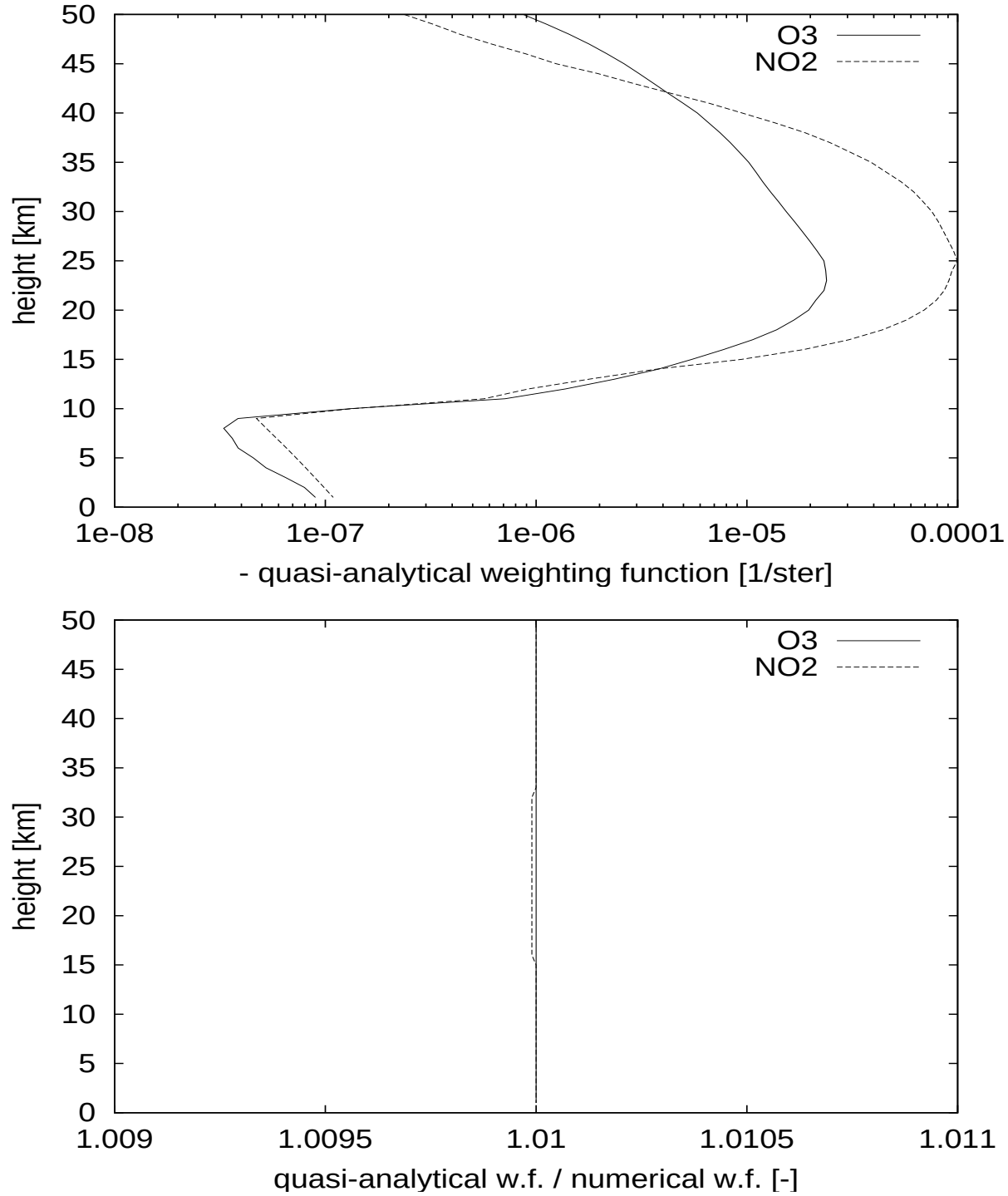

Figure 6.6: TOP: Absolute values of relative-absolute weighting functions for O_3 and NO_2 computed with *SCIARAYS*. All original values are negative. BOTTOM: Ratio of quasi-analytical and numerically generated weighting functions. $\lambda = 350\,\mathrm{nm}$.

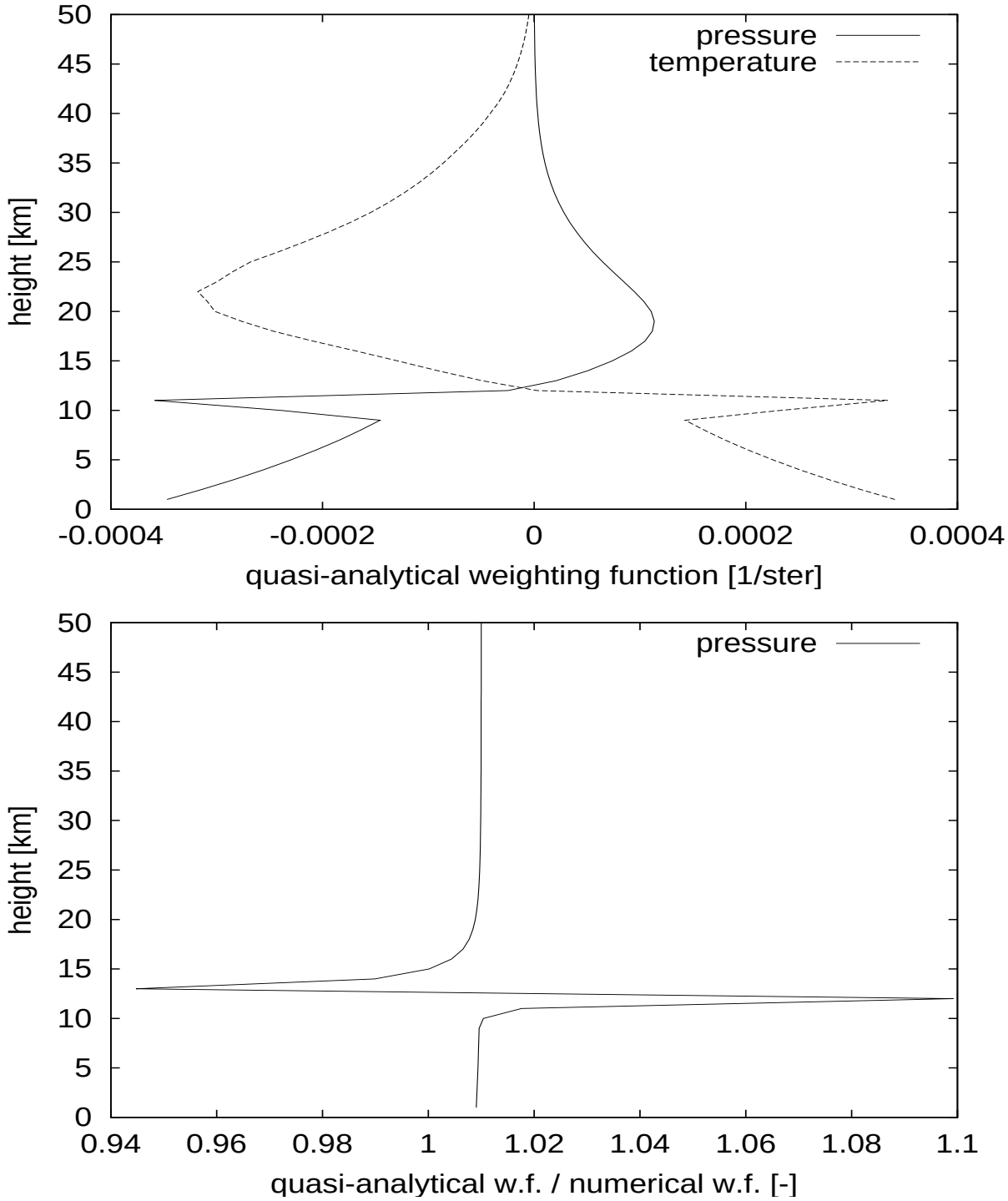

Figure 6.7: TOP: Relative-absolute weighting functions for pressure and temperature computed with *SCIARAYS*. BOTTOM: Ratio of quasi-analytical and numerically generated weighting functions for pressure. $\lambda = 350\,\mathrm{nm}$.

Chapter 7

The Instrument Simulator in *SCIARAYS*

7.1 Introduction

For the simulation of a measurement, the instrumental response to the simulated atmospheric radiation has to be modelled. Additionally, the magnitude of each pixel's noise must be calculated for the inversion algorithm (see Chapter 8). These two tasks are performed by an instrument model.

It is the nature of any measurement that a representation of the measured quantity is produced. For instance, SCIAMACHY — being a diode array spectrometer — records the counts [binary units] of the pixels after a predefined integration time as a representation[1] of the charges of the diodes, which, in turn, represent the radiance. The counts are stored in the so-called *level 0* data product. The *level-0-to-1 data processor* transforms the counts back to radiance units and stores them in the *level 1* data product.

Thus the level 1 radiances always reflect the following properties of the instrument (and the level-0-to-1 data processor) besides the atmospheric specific radiances:

spectral integration: The atmospheric specific radiance is convolved with the instrument's spectral slit function, i.e., the "specific radiance" (per unit wavelength) is converted to the (spectrally integrated) "radiance". For SCIAMACHY, this is particularly important in the NIR spectral range, where the spectral variability of the optical properties of the atmosphere is not resolved [Buchwitz, 2000].

spacial integration: SCIAMACHY is producing a 2-dimensional image of Earth's radiance field by scanning the atmosphere, see Section 3. During the process of measuring one spacial pixel, the spacial radiance field is convolved with the *instantaneous field of view* (*FOV*). In Section 7.3, the influence of the vertical extend of a limb measurement's FOV is modelled.

noise: The precision of any detector is limited by some form of noise in the radiant energy to which the detector responds; in the detector itself, or in the electronic system following the detector.

[1] more technical: analog to digital conversion (*ADC*)

- The *photon noise* and the *shot noise* arise owing to the quantified nature of the radiation field (photons) and of the charge read from the detector (electrons). They are statistical quantities which vary with the detected radiance.
- The combined noise from all signal-independent noise terms in the detector, e.g., due to dark current uncertainty, and the electronics is termed *readout noise*, here.

Section 7.2 describes the noise parametrisation in *SCIARAYS*, which models the actual performance of SCIAMACHY.

calibration: Errors of the radiometric and wavelength calibration of the instrument are systematic. They are not considered in the instrument model of *SCIARAYS* since all systematic errors are modelled and corrected as well as possible by the level-0-to-1 data processor. During the retrieval, i.e., the level-1-to-2 processing, radiometric and wavelength calibration errors can partially be compensated by using a differential fitting approach and the so-called *shift and squeeze* algorithm [Hoogen, 1998, p. 82], respectively.

7.2 Measurement Noise

The instrument model in *SCIARAYS* calculates the measurement noise from the simulated limb measurement sequence and an irradiance spectrum extracted from MODTRAN [Kneizys et al., 1996]. The noise parametrisation is based on the readout noise and the throughput of SCIAMACHY as measured in the laboratory by Hoogeveen and de Vries [2000]. It is described below. For a detailed description of noise in a photon-detecting device refer to Kruse [1980], Wolfe and Zissis [1989].

In this section, the variables are defined following de Vries and Hoogeveen [1999] in order to maintain consistency with the SCIAMACHY-related literature. The definitions are summarised in Table 7.1.

de Vries and Hoogeveen [1999, (1)] state an expression for the noise of the signal:

$$\sigma_S = \frac{1}{t_{exp}} \sqrt{\frac{\sqrt{(S + S_{dark}) t_{exp}}^2 + \sigma_{readout}^2}{n_{coadd}}} \,, \tag{7.1}$$

where the term $\sqrt{(S + S_{dark}) t_{exp}}$ expresses the shot noise $[\mathrm{el}]$ which arises from the discrete nature of the electrons read from the detector. The underlying connection between specific radiance R and measured signal S $[\mathrm{el}/\mathrm{sec}]$ is given by the instrument *throughput* $[\mathrm{el}/(\mathrm{phot}/\mathrm{cm}^2/\mathrm{nm}/\mathrm{sr})]$:

$$S = T \cdot R \,. \tag{7.2}$$

It can be used to derive an expression for the sun-normalised radiance R/I and its noise, both in $[1/\mathrm{sr}]$, from (7.1):

$$\frac{R}{I} \;=\; \frac{S}{TI} \tag{7.3}$$

Table 7.1: Variable Definitions of this Chapter

symbol	name	units
R	(specific) radiance	$[\mathrm{phot/\,sec\,/cm^2/nm/sr}]$
I	irradiance	$[\mathrm{phot/\,sec\,/cm^2/nm}]$
S	signal (corrected for electronic offset)	$[\mathrm{el/\,sec}]$
T	throughput	$[\mathrm{el/(phot/cm^2/nm/sr)}]$
t_{exp}	exposure time	$[\mathrm{sec}]$
S_{dark}	sum of detector dark current ...	
	... and thermal background signal	$[\mathrm{el/\,sec}]$
n_{coadd}	number of digital coadditions	[-]
$\sigma_{readout}$	readout noise	$[\mathrm{el}]$
σ_S	noise of signal	$[\mathrm{el/\,sec}]$
$\sigma_{R/I}$	noise of sun-normalised radiance	$[1/\mathrm{sr}]$

$$\sigma_{R/I} = \frac{\sigma_S}{TI} \tag{7.4}$$

$$= \frac{1}{TIt_{exp}}\sqrt{\frac{\sqrt{(S+S_{dark})t_{exp}}^2+\sigma^2_{readout}}{n_{coadd}}} \tag{7.5}$$

$$= \frac{1}{TIt_{exp}}\sqrt{\frac{\sqrt{(T\cdot I\cdot (R/I)+S_{dark})t_{exp}}^2+\sigma^2_{readout}}{n_{coadd}}}\quad . \tag{7.6}$$

Typical limb measurements of SCIAMACHY will have the following properties:

$$t_{exp} = 0.375\ \mathrm{sec} \qquad (0.3\ \mathrm{sec}\ \text{for ACE, see section 11}) \tag{7.7}$$

$$n_{coadd} = 1 \tag{7.8}$$

$$S_{dark} = 0 \qquad (\text{valid in the UV-vis [Noël, 2000, 1998]}) \tag{7.9}$$

The wavelength-dependent throughput of the flight model of SCIAMACHY has been measured in the laboratory during the *OPTEC 5* campaign [Hoogeveen and de Vries, 2000]. The results are depicted in Figure 7.1. In *SCIARAYS*, the throughput of SCIAMACHY is parametrised by the stepwise linear function shown in Figure 7.2. For the ACE study (Chapter 11), a parametrisation with constant values in each channel has been chosen, see Figure 7.3. In order to model the potential performance of a newly built spectrometer of SCIAMACHY type, the values correspond to the best measured performance of each channel.

The readout noise reported by Hoogeveen and de Vries [2000] is shown in Figure 7.4. The higher and more widely scattered values in the channels 7 and 8 reflect the different detector materials necessary for the detection of NIR photons (as opposed to UV-vis photons) and its higher sensitivity to thermal noise. The readout noise is parametrised by a stepwise linear function in *SCIARAYS*, too. The function is depicted in Figure 7.5.

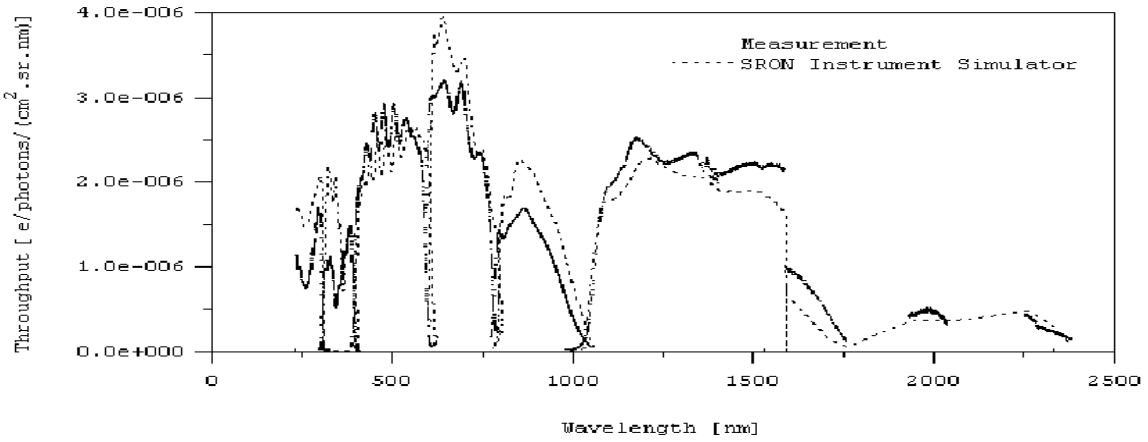

Figure 7.1: Throughput of SCIAMACHY measured during OPTEC 5. (graphics by J. de Vries [Hoogeveen and de Vries, 2000, figure 3.3.2-1])

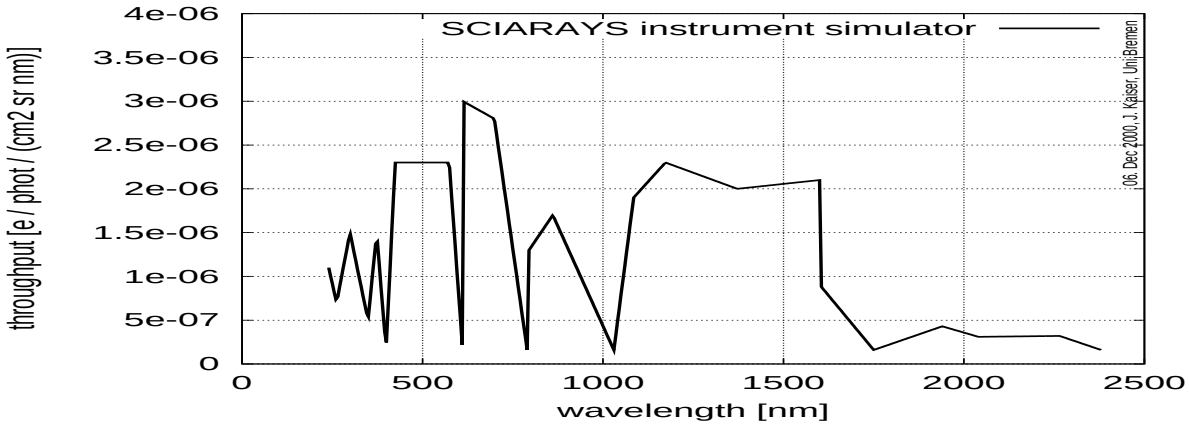

Figure 7.2: *SCIARAYS'* throughput parametrisation of SCIAMACHY.

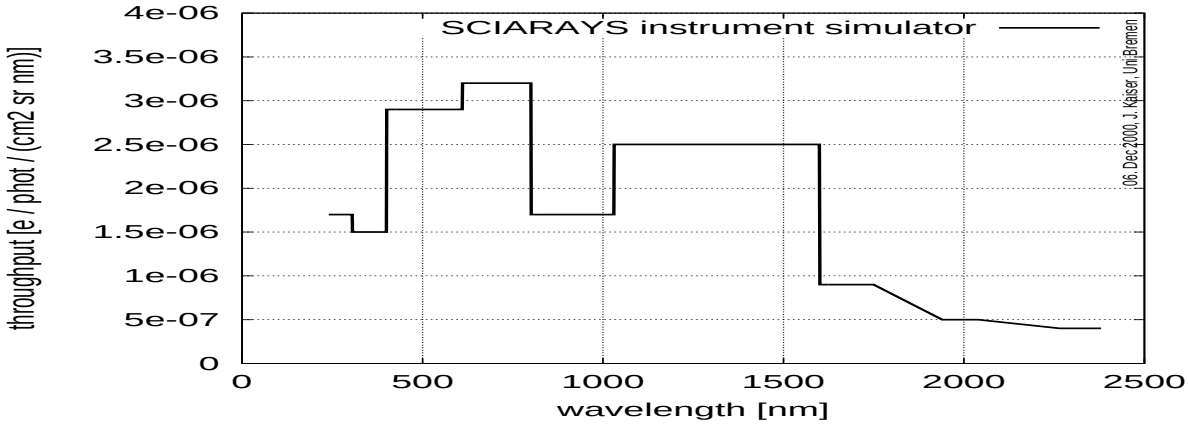

Figure 7.3: *SCIARAYS'* throughput parametrisation for ACE.

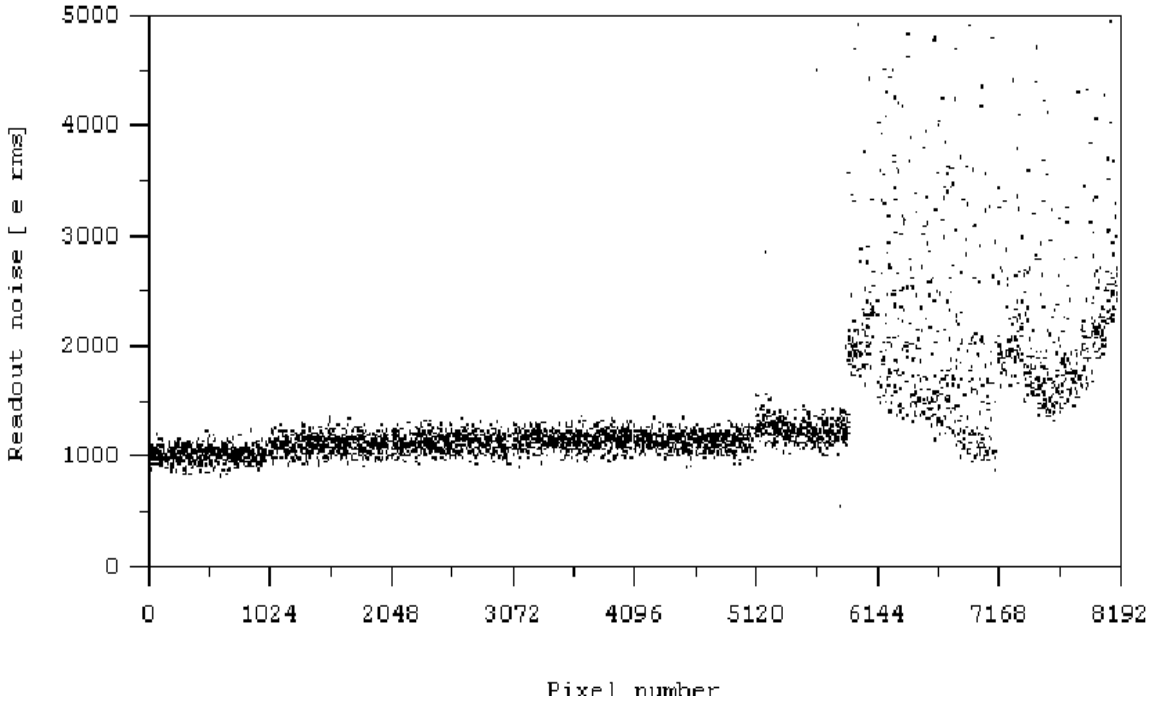

Figure 7.4: Readout noise of SCIAMACHY measured during OPTEC 5. (graphics by J. de Vries [Hoogeveen and de Vries, 2000, figure 3.3.2-2])

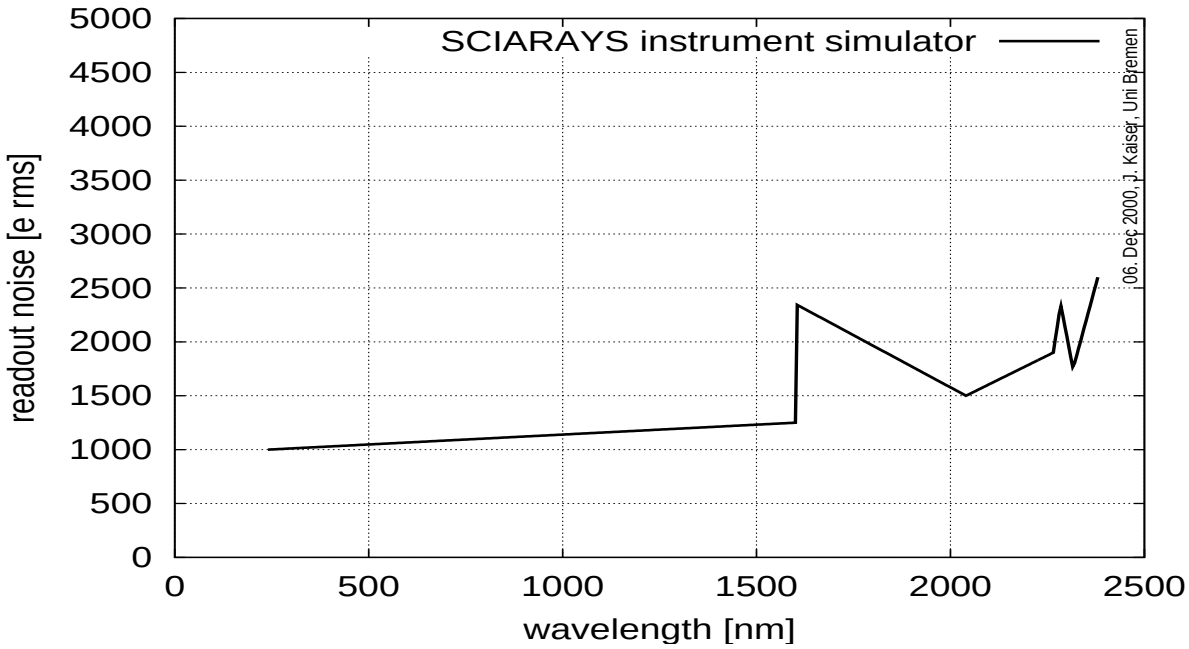

Figure 7.5: *SCIARAYS*' readout noise parametrisation of SCIAMACHY. Beware, the x-axis is different from the one of Figure 7.4!

The implementation in *SCIARAYS* uses the values (7.7–7.9) and the parametrisations of the throughput and the readout noise (Figures 7.2, 7.5) to compute the noise of the sun-normalised radiance from (7.6). Using this, the user can readily obtain the *signal to noise ratio*:

$$\frac{S}{\sigma_S} \equiv \frac{R/I}{\sigma_{R/I}} . \tag{7.10}$$

7.3 Field of View

Recall from Section 3.3 that SCIAMACHY performs limb scans with $3\,\mathrm{km}$ tangent height step size and a $2.6\,\mathrm{km}$ height of the instantaneous FOV at the tangent point. The instrumental response is approximately constant in the FOV and vanishes outside [Hoogeveen, 1999]. Thus the instrument convolves the atmospheric radiance with a vertical slit function which closely resembles a boxcar function with $2.6\,\mathrm{km}$ full width at the tangent point.

The instrument model in *SCIARAYS* pre-computes the atmospheric radiance and weighting functions on a fine tangent height grid. Then the values inside the instantaneous FOV of each nominal measurement tangent height are averaged.

The default setting for SCIAMACHY ($1\,\mathrm{km}$ fine tangent height step, $2.6\,\mathrm{km}$ FOV) averages the radiances and weighting functions at the nominal tangent height and tangent heights $1\,\mathrm{km}$ below and above.

For the ACE study (Chapter 11), the predefined fine tangent heights are $0.333333\,\mathrm{km}$ apart. Since SCIAMACHY's FOV geometry of $2.6\,\mathrm{km}$ vertical extend is assumed, this results in averaging seven values for each nominal tangent height. However, due to overlap of the FOVs of adjacent nominal tangent heights, for each additional nominal tangent height only three forward model calculations have to be performed.

7.4 Implementation

The instrument model in *SCIARAYS* is implemented in the module `instrument`. It incorporates the calls to the radiative transfer model. It has to be initialised and ended explicitly. In between, it can be called with the input and output arguments summarised in Table 7.2.

The noise calculation and the FOV integration can be switched on and off individually. Optionally, Gaussian random noise is applied to the radiance output.

Table 7.2: Input and Output of the Instrument Simulator

	initialisation input	input	output
irradiance	$[\mathrm{W/nm/m^2}]$		
wavelength grid	$[\mathrm{nm}]$		
nominal tangent heights	$[\mathrm{km}]$		
FOV width	$[\mathrm{km}]$		
fine tangent height distance	$[\mathrm{km}]$		
atmospheric state		see Tab. 6.1	
radiances			$[1/\mathrm{sr}]$
1σ-noise			$[1/\mathrm{sr}]$
weighting functions			see Tab. 6.1

Chapter 8

Inversion with Optimal Estimation

Humans were naked worms; yet they had an internal model *of the world. In the course of time up to present, this model has been updated many times (...) Inverse problem theory tries to describe the rules human beings should use for quantitative updating.*

Albert Tarantola [Tarantola, 1987]

(An) Inverse problem is when we want to infer the state from measurements which are not related to the state in a simple, obvious form.

Olivier Talagrand (CNRS, Paris) at the RAL/Oxford Spring School 2001

8.1 Formulating the Inverse Problem

The statements by Albert Tarantola and Olivier Talagrand show that the notion *inverse problem* is ill-defined. To a certain extent, it remains vague and a matter of the personal point of view. Nevertheless, everybody agrees that the retrievals of atmospheric state parameters from satellite measurements belong to this category.

During all satellite measurements of Earth's atmosphere, the radiation which emerges from the atmosphere is observed instead of the desired atmospheric parameters. For given parameters the radiance can be modelled with a radiative transfer model (RTM), but not vice versa. The inverse problem is to estimate the atmospheric parameters from the measurements without explicitly inverting the RTM. (Which is not possible.)

The *optimal estimation* formalism introduced by Rodgers [1976a] uses additional information on the atmospheric state, the so-called *a priori*. It is widely accepted as a standard technique in atmospheric remote sensing and employed exclusively for the studies in this thesis.

8.1.1 A Linear, Discrete World

Measurement and State (-Vectors)

Due to the ubiquitous use of computers, most measurements nowadays yield a set of discrete values instead of a continuous function. Any such measurement can be represented by a *measurement vector* $\mathbf{y}$ of dimension m:

$$\mathbf{y} = [y_1, y_2, \dots y_m]^T \tag{8.1}$$

In the case of SCIAMACHY, one spectrum in the wavelength range 240–2380 nm is represented by roughly 8000 spectral points. One limb scan typically consists of 20 spectra at various tangent heights. Thus $m \approx 160,000$. Presently, it is necessary to use only a subset of these points in order to make large numbers of retrievals feasible on the available computer resources. The best choice of such a subset is a wide area of research itself.

The parameters which shall be determined with the measurement may include scalar values, e.g., surface albedo, and continuous functions, e.g., the ozone concentration profile. The continuous functions may even be multi-dimensional like aerosol extinction, which depends on height and wavelength. In principle, no continuous function can be derived from a discrete set of measured values as such a problem is intrinsically under-determined. Thus the continuous parameters have to be discretised: They can be represented by values at discrete height levels or by a limited number of coefficients of some expansion into continuous functions. Assembling all parameters yields the *state vector* $\mathbf{x}$ of dimension n:

$$\mathbf{x} = [x_1, x_2, \dots x_n]^T \tag{8.2}$$

Beside the atmospheric parameters, the state vector can include other parameters describing, e.g., the instrumental drifts or molecular properties.

Since the measurement and the state parameters are represented by discrete values, the algebra of finite-dimensional vector spaces can be employed to describe and solve the inverse problem instead of the Hilbert space algebra, see also Wunsch [1996].

Forward Model (-Matrix)

In a mathematical sense, the radiance is the response of the atmosphere to a prescribed state. It is described by the *forward function* $\mathbf{f}(.)$. Real measurements are contaminated with an unknown measurement error ϵ:

$$\mathbf{y} = \mathbf{f}(\mathbf{x}) + \epsilon \quad . \tag{8.3}$$

It is characteristic for inverse problems that the forward function exists, i.e., is unambiguous, and can be approximated with an explicit *forward model* $\mathbf{F}(.)$:

$$\mathbf{y} = \mathbf{F}(\mathbf{x}) + \epsilon \quad , \tag{8.4}$$

where the error ϵ incorporates contributions from the measurement error and the shortcomings of the forward model.

If the forward model is linear, it can be specified completely with the *forward model matrix* $\mathbf{K}$:

$$\mathbf{y} = \mathbf{K}\,\mathbf{x} + \epsilon \quad . \tag{8.5}$$

In this thesis, $\mathbf{K}$ is generally referred to as *weighting function matrix* since the term *forward model matrix* would be misleading in the context of nonlinear forward models.

The forthcoming formalism has been developed for linear problems. It can also be applied to moderately nonlinear problems, see Section 8.4. So, let the weighting function matrix $\mathbf{K}$ be a valid representation of the forward model $\mathbf{F}(.)$.

8.1.2 Statistical Properties

Measurements with associated uncertainties as well as knowledge of a state are most generally described by *probability density function*s (pdf). Since specifying a complete *pdf* involves too much data for virtually any case, commonly only the first two moments, i.e., the *expectation value* $\widehat{.}$ and the *variance* σ^2, are specified. For a continuous scalar random variable x with the *pdf* $\rho(x)$, they are given by:

$$\widehat{x} = \int x\,\rho(x)\,\mathrm{d}x \tag{8.6}$$

$$\sigma_x^2 = \widehat{(x-\widehat{x})^2} \tag{8.7}$$

$$= \int (x-\widehat{x})^2\,\rho(x)\,\mathrm{d}x \quad . \tag{8.8}$$

Giving these two values but nothing else is equivalent to stating that the probability distribution is *Gaussian* (or *Normal*) with *standard deviation* σ:

$$\rho(x) = \frac{1}{\sqrt{2\pi}\,\sigma}\exp\left[-\frac{1}{2}\left(\frac{x-\widehat{x}}{\sigma}\right)^2\right] \tag{8.9}$$

If the random variable is a vector $\mathbf{x}$, the expected value is computed element by element. In analogy to (8.6), this shall be denoted by:

$$\widehat{\mathbf{x}} = \int \mathbf{x}\,\rho(\mathbf{x})\,\mathrm{d}\mathbf{x} \quad , \tag{8.10}$$

where $\rho(\mathbf{x})$ is the *pdf* of the vector.

A *covariance matrix* $\mathbf{S}$ is the multi-dimensional generalisation of the variance. Its elements S_{ij} are defined by:

$$S_{ij} = \widehat{(x_i-\widehat{x_i})(x_j-\widehat{x_j})} \tag{8.11}$$

$$= c_{ij}\,\sigma_i\,\sigma_j \quad . \tag{8.12}$$

The diagonal elements are the variances σ^2 of the elements and the off-diagonal elements describe the *linear correlation coefficients* $c_{ij} \in [-1, 1]$ between the elements.

Using the covariance matrix, the Gaussian distribution for an n-dimensional vector is:

$$\rho(\mathbf{x}) = \sqrt{\frac{|\mathbf{S}^{-1}|}{(2\pi)^n}} \exp\left[-\frac{1}{2}(x - \widehat{x})^T \mathbf{S}^{-1}(x - \widehat{x})\right] \quad , \tag{8.13}$$

where $|.|$ denotes the determinant of a matrix and $\mathbf{S}$ is required to be non-singular. The latter implies that no element of $\mathbf{x}$ is known exactly. This is the exact reason for describing the knowledge of a state in terms of a *pdf* instead of simply providing the value of a vector.

8.1.3 The Inverse Problem

Using the notation and interpretation introduced above, the particular inverse problem investigated in this thesis is:

Given a measurement $\mathbf{y}$ with associated covariance[1] $\mathbf{S}_\mathbf{y}$ and *a priori* knowledge $\mathbf{x}_a$ with covariance $\mathbf{S}_a$, what are the expected value $\widehat{\mathbf{x}}$ and the covariance $\widehat{\mathbf{S}}$ of the resulting *pdf* of the state? The weighting function matrix $\mathbf{K}$, which is relating a state and its measurement by (8.5), is assumed to be known.

8.2 The Optimal Retrieval

The solution to this particular inverse problem has been derived by Rodgers [1976b]. The *retrieved state* $\widehat{\mathbf{x}}$ is the mean of the resulting *pdf*. It is a weighted mean [Rodgers, 2000, (2.30)]:

$$\widehat{\mathbf{x}} = \left(\mathbf{K}^T \mathbf{S}_\mathbf{y}^{-1} \mathbf{K} + \mathbf{S}_a^{-1}\right)^{-1} \left(\mathbf{K}^T \mathbf{S}_\mathbf{y}^{-1} \mathbf{y} + \mathbf{S}_a^{-1} \mathbf{x}_a\right) \quad . \tag{8.14}$$

The contributions of the measurement $\mathbf{y}$ and of the *a priori* state $\mathbf{x}_a$ are weighted relative to each other with the inverses $\mathbf{S}_\mathbf{y}^{-1}$ and $\mathbf{S}_a^{-1}$ of their covariance matrices[2].

The covariance matrix $\widehat{\mathbf{S}}$ of the resulting *pdf* is obtained by "inverse" summation of the covariance matrices of the measurement and the *a priori*:

$$\widehat{\mathbf{S}} = \left(\mathbf{K}^T \mathbf{S}_\mathbf{y}^{-1} \mathbf{K} + \mathbf{S}_a^{-1}\right)^{-1} \quad , \tag{8.15}$$

where $\mathbf{S}_\mathbf{y}$ is projected into the vector space of states by the weighting functions $\mathbf{K}$.

[1] Strictly speaking, it is the covariance of the measurement's error.

[2] The so-called *contribution function* matrix $\mathbf{D}$ (of the measurement) is the Jacobean of the retrieved state w.r.t. the measurement vector: $\mathbf{D} = \frac{\partial \widehat{\mathbf{x}}}{\partial \mathbf{y}} = \left(\mathbf{K}^T \mathbf{S}_\mathbf{y}^{-1} \mathbf{K} + \mathbf{S}_a^{-1}\right)^{-1} \mathbf{K}^T \mathbf{S}_\mathbf{y}^{-1}$

8.3 Characterisation

The diagonal elements of the covariance matrix $\widehat{\mathbf{S}}$ specify the variances σ_i^2 of the retrieved parameters x_1 and the off-diagonal elements yield the *linear correlation coefficients* $c_{i,j}$ between the i-th and j-th parameter:

$$\sigma_i^2 = \widehat{S}_{i,i} \tag{8.16}$$

$$c_{i,j} = \frac{\widehat{S}_{i,j}}{\sigma_i \, \sigma_j} \quad . \tag{8.17}$$

Theoretically, the retrieved state $\widehat{\mathbf{x}}$ can be expressed as a function of the *true state* $\mathbf{x}$ [Rodgers, 2000, (2.45, 2.58)]:

$$\widehat{\mathbf{x}} = \mathbf{A}\,(\mathbf{x} - \mathbf{x}_a) + \mathbf{x}_a + \widehat{\mathbf{S}}\,\mathbf{K}^T\mathbf{S}_\mathbf{y}^{-1}\,\epsilon \tag{8.18}$$

$$\text{with} \quad \mathbf{A} = \left(\mathbf{K}^T\,\mathbf{S}_\mathbf{y}^{-1}\,\mathbf{K} + \mathbf{S}_a^{-1}\right)^{-1}\,\mathbf{K}^T\mathbf{S}_\mathbf{y}^{-1}\,\mathbf{K} \tag{8.19}$$

$$= \widehat{\mathbf{S}}\,\mathbf{K}^T\mathbf{S}_\mathbf{y}^{-1}\,\mathbf{K} \tag{8.20}$$

$$= \mathbf{D}\,\mathbf{K} \quad , \tag{8.21}$$

where the *averaging kernel matrix* $\mathbf{A}$ is the Jacobean of the retrieved state w.r.t. the true state:

$$\mathbf{A} = \frac{\partial\widehat{\mathbf{x}}}{\partial\mathbf{x}} \quad . \tag{8.22}$$

It can be evaluated for an actual retrieval and carries useful information[3] on the *smoothing error* (see below) and the origin of the information contained in the retrieved *pdf*. The elements of the i-th row of $\mathbf{A}$ express the relative contributions of the elements of the true state on the i-th retrieved parameter.

The diagonal elements of $\mathbf{A}$ show the influence of the corresponding true values on their retrieved counterparts: A value of one implies complete domination (the ideal case), while a vanishing element indicates that there is no relation at all between the true and the retrieved value (no information on this parameter in the measurement).

Likewise, the remaining, off-diagonal elements of the i-th row of $\mathbf{A}$ show the relative influence of the other parameter's true values on the i-th retrieved parameter. These influences cause the *smoothing error* of retrieved profiles. Therefore, the *vertical resolution* at a particular altitude can be obtained as the width, e.g., full width at half maximum (*FWHM*), of the averaging kernel for this altitude.

In the case of a perfect measurement and retrieval, the averaging kernels would equal the unity matrix and the true state would be retrieved: In this case only the true

[3]The averaging kernel matrix depends on the chosen retrieval units, e.g., number density, VMR, or relative deviation from an *a priori*. The interpretation which is presented here is valid, if all retrieval parameters have a similar magnitude, i.e., for the latter two units. For any given state $\mathbf{x}$, the averaging kernel matrix $\mathbf{A}$ may be transformed into a form suitable for the presented interpretation by scaling its i,j-th element A_{ij} with x_j/x_i.

value of each parameter influences its retrieved value and the vertical resolution equals the retrieval grid spacing. For every real retrieval all elements of $\mathbf{A}$ should satisfy $0 \lesssim A_{i,j} \lesssim 1$.

The sum of all elements of a row of $\mathbf{A}$ is sometimes called the *measurement response* [Eriksson, 1999]. When it is close to unity, the retrieved value is completely determined by the measurement, i.e., the true value. Otherwise, the remaining difference to unity quantifies the relative influence of the *a priori* estimate on the retrieved value.

8.4 Nonlinear Problems

Up to this point, the optimal estimation formalism for linear forward models (8.5) has been presented. It can be extended to yield valid solutions for nonlinear forward models which behave approximately linearly within the error bounds of the measurement. These forward models are said to be *moderately nonlinear* [Rodgers, 2000, p. 81]. The solution can be characterised with the formalism developed for linear problems, but finding it requires an iterative process.

Linearising the model about an appropriately chosen *linearisation state* $\mathbf{x}_i$ yields:

$$\mathbf{y} - \mathbf{y}_i = \mathbf{K}_i \, (\mathbf{x} - \mathbf{x}_i) + \epsilon \tag{8.23}$$

$$\text{with:} \quad \mathbf{y}_i = \mathbf{F}(\mathbf{x}_i) \tag{8.24}$$

$$\mathbf{K}_i = \left. \frac{\partial \mathbf{F}(\mathbf{x})}{\partial \mathbf{x}} \right|_{\mathbf{x}_i} \quad , \tag{8.25}$$

where the $(m \times n)$-dimensional *weighting function matrix* $\mathbf{K}_i$ is the Jacobean of the nonlinear forward model $\mathbf{F}(.)$. It is also called the *tangent linear model* at the reference point $\mathbf{x}_i$.

The formalism for the inversion of linear forward models is applied by substituting (8.23) for the forward model (8.4). Thereby, the retrieved state covariance matrix becomes dependent on the linearisation point $\mathbf{x}_i$, cf. (8.15):

$$\widehat{\mathbf{S}}_{i+1} = \left(\mathbf{K}_i^T \, \mathbf{S}_\mathbf{y}^{-1} \, \mathbf{K}_i + \mathbf{S}_a^{-1} \right)^{-1} \quad . \tag{8.26}$$

The calculation of the retrieved value also needs to take into account the values $\mathbf{x}_i$ and $\mathbf{y}_i$ at the linearisation point, cf. (8.14), Rodgers [2000, (5.8)]:

$$\widehat{\mathbf{x}}_{i+1} = \mathbf{x}_i + \widehat{\mathbf{S}}_{i+1} \, \left(\mathbf{K}_i^T \, \mathbf{S}_\mathbf{y}^{-1} \, (\mathbf{y} - \mathbf{y}_i) + \mathbf{S}_a^{-1} \, (\mathbf{x}_a - \mathbf{x}_i) \right) \quad . \tag{8.27}$$

Since the retrieved state $\widehat{\mathbf{x}}_{i+1}$ generally is closer to the true state than $\mathbf{x}_i$, it is a better linearisation point than $\mathbf{x}_i$. The calculations (8.24–8.27) should therefore be repeated with the new linearisation point $\mathbf{x}_{i+1} \equiv \widehat{\mathbf{x}}_{i+1}$. This repetitive process is a Gauss-Newton iteration, which will lead to a consistent solution state $\widehat{\mathbf{x}}$ with covariance $\widehat{\mathbf{S}}$, if the forward model is moderately nonlinear, as mentioned above.

The *a priori* state $\mathbf{x}_a$ is the best estimate of the state before the evaluation of the measurement $\mathbf{y}$. Thus it is the obvious choice for the initial linearisation point.

A convergence criterion has to be chosen to stop the iteration. Several sensible choices are listed below. They can also be used simultaneously. The iteration may be stopped, when ...

... the improvements $|\widehat{\mathbf{x}}_{i+1} - \widehat{\mathbf{x}}_i|$ of all state elements are smaller than a predefined precision requirement.

... the improvements $|\widehat{\mathbf{x}}_{i+1} - \widehat{\mathbf{x}}_i|$ of the state elements are smaller than their corresponding standard deviations from $\widehat{\mathbf{S}}_{i+1}$, or a fraction thereof.

... the residual measurement $\mathbf{y}_i - \mathbf{y}$ becomes smaller in absolute value than the measurement noise given by $\mathbf{S}_\mathbf{y}$.

Part III

APPLICATIONS

Outline of the Applications

The program package *SCIARAYS* has been designed for retrievals from UV-vis-NIR limb measurements. Therefore, it computes weighting functions for all atmospheric model parameters efficiently. Using these weighting functions, averaging kernels and theoretical retrieval precisions can be calculated.

Chapter 9 illustrates the general form of the weighting functions and averaging kernels for UV-vis-NIR limb measurements.

The vertical resolution of ozone retrievals and its relationship to the retrieval precision is investigated in Chapter 10.

Chapter 11 presents a study of the theoretical precisions of a future UV-vis-NIR limb sensor envisaged in the Atmospheric Chemistry Explorer study for the European Space Agency.

In Chapter 12, radiances and weighting functions computed with *SCIARAYS* are compared to those computed with a model comprising full multiple scattering (CDIPI). Test retrievals prove that a more simple model is appropriate for calculating the weighting functions than for calculating the radiances.

The RTM in *SCIARAYS* has been combined with the photo-chemical model *BRAPHO*. The resulting program, *SLACO*, has been used successfully for inverse modelling of tropospheric BrO from ground-based zenith sky observations [Müller et al., 1999] and of stratospheric NO_3 from ground-based lunar transmission measurements [Schlieter, 2001]. SLACO is described *en detail* in Müller [2001].

Chapter 9

Properties of Limb Scattering Measurements

9.1 Radiance and Noise

Radiance

Since SCIAMACHY measures atmospheric spectra at all tangent heights of a limb scan, the measured quantity is a 2-dimensional radiance field with one wavelength dimension and one tangent height dimension. The upper plot of Figure 9.1 shows a simulation of the radiance field performed with *SCIARAYS* for a typical SCIAMACHY measurement. Each pair of wavelength and tangent height values is assigned a colour-coded radiance value. The colour-coding is done on a logarithmic scale to account for the measurement's wide dynamic range.

The terrestrial atmosphere and its constituents cause typical features of limb scattering measurements:

- The radiance increases roughly exponentially with decreasing tangent height since the air density and thus the Rayleigh scattering near the tangent point increase exponentially.

- The radiance decreases for increasing wavelengths as Rayleigh and (most) aerosol scattering are weaker at longer wavelengths.

- Below about $340\,\mathrm{nm}$ wavelength and $30\,\mathrm{km}$ tangent height, the radiance has only a small tangent height dependence. This is explained by the strong absorption in the Hartley-Huggins bands of ozone, which, besides protecting life on Earth's surface, is also blocking the UV radiation from tangent heights in or below the stratospheric ozone layer.

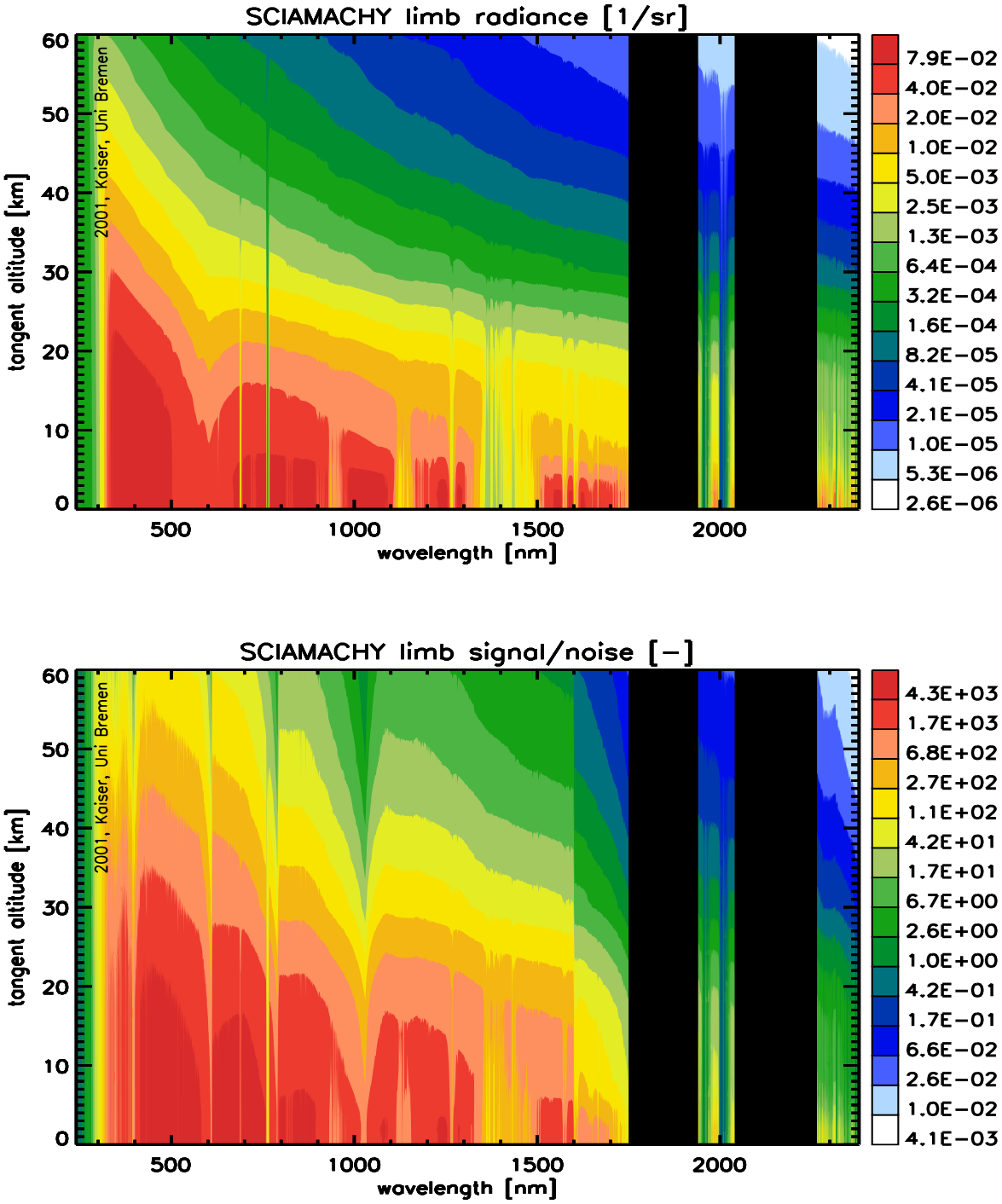

Figure 9.1: Radiance values (upper plot) and signal/noise values (lower plot) for a limb scan and SCIAMACHY's whole spectral range.

- Clear absorption signatures are visible from the
  - Chappuis bands of ozone around $600\,\mathrm{nm}$, the
  - oxygen-A band near $760\,\mathrm{nm}$, and
  - various water vapour bands throughout the NIR spectral region.

  The water vapour bands are particularly strong for tropospheric tangent heights and relatively weak for stratospheric ones, reflecting the water vapour profile.

Signal-to-Noise

The precision with which each radiance value is measured by an instrument is described by the signal-to-noise ratio. The signal-to-noise ratio field for the typical SCIAMACHY measurement is depicted in the lower plot of Figure 9.1. The same axes as in the upper plot are used and the signal-to-noise ratio is colour-coded logarithmically.

The wavelength dependence of SCIAMACHY's throughput manifests itself in steps and dips (compare to Figure 7.2). Beside this effect, the wavelength and tangent height dependence of the signal-to-noise ratio qualitatively resembles that of the radiance as the dominating term, i.e., shot noise, is given by the square root of the signal.

In signal-to-noise plots of smaller spectral regions, the Fraunhofer lines of the solar spectrum are also manifest, see, e.g., the fine structure in the bottom plots of the Figures 9.5–9.7. The influence of the Fraunhofer lines is also strong for the radiance, but it is divided out by sun-normalisation.

9.2 Weighting Functions

The limb measurement weighting function of an atmospheric parameter is generally a 3-dimensional quantity since a different value exists for each wavelength, for each tangent height and for each level of the parameter profile. Since 3-dimensional quantities are hard to visualise, the values of the weighting function are presented in several 1- and 2-dimensional sub-spaces in this section.

In order to illustrate some general properties of the weighting functions of limb measurements, the weighting functions of a selected subset of atmospheric parameters are present here. Visualisations of the weighting functions of the other trace gas parameters can be found in appendix B.

Profile Level and Tangent Altitude

The weighting functions of O_3 in two different sub-spaces are depicted in Figures 9.2 and 9.3. For each case, the three normalisations introduced in Section 6.5 are given in

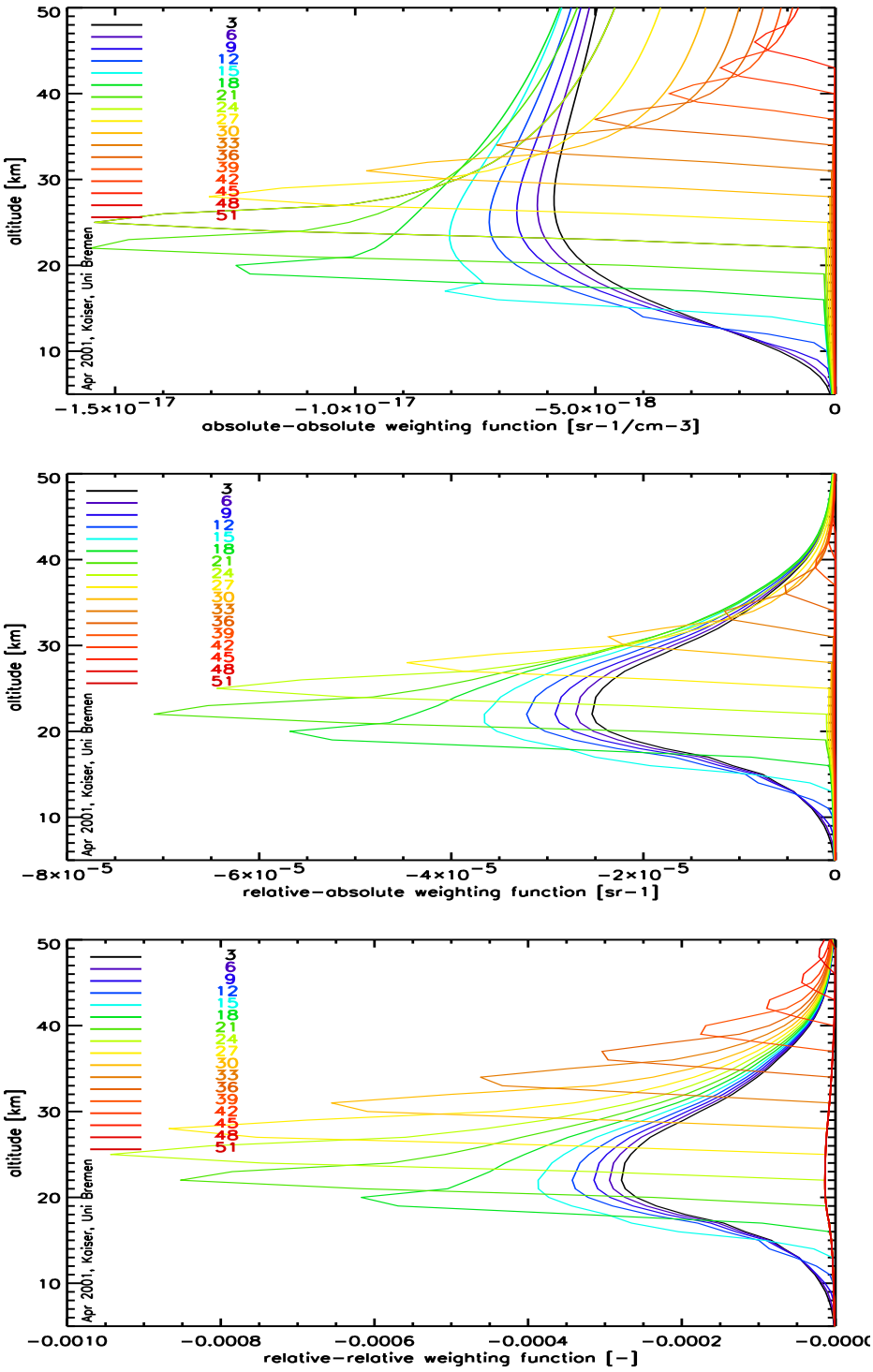

Figure 9.2: Ozone profile weighting functions at $360\,\mathrm{nm}$ wavelength for several tangent altitudes (given in km) as functions of the profile altitude level: three different normalisation methods. The vertical resolution is $1\,\mathrm{km}$.

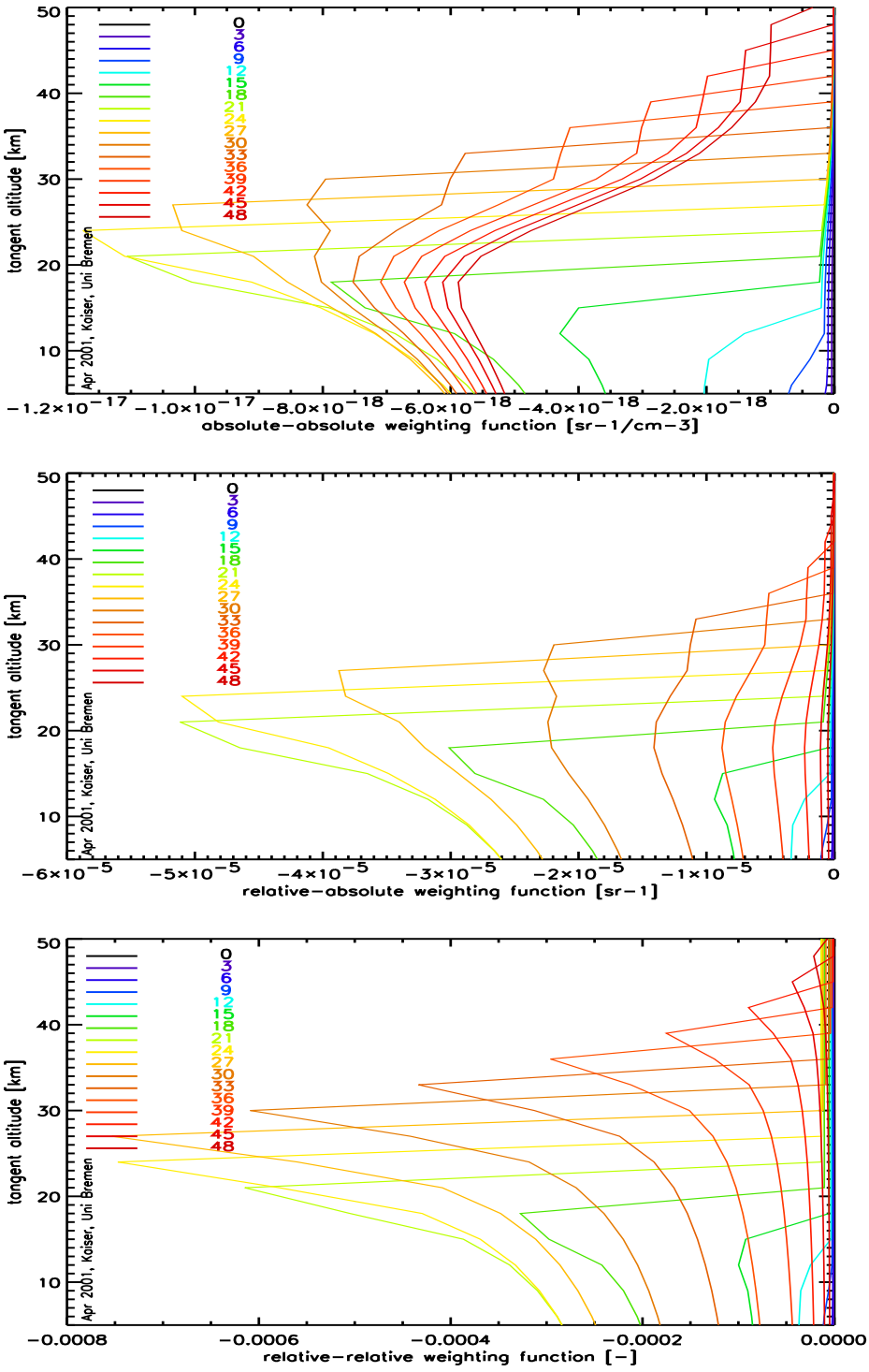

Figure 9.3: Ozone weighting functions of several profile altitudes levels (given in km) at 360 nm wavelength as functions of tangent altitude: three different normalisation methods. The tangent altitude resolution is 3 km.

separate plots[1]:

The profiles of the top plot of Figure 9.2 show the absolute-absolute O_3 weighting function in the **subspace of parameter profile levels**. Each plotted profile exhibits how much (in radiance units $[\mathrm{sr}^{-1}]$) the sun-normalised radiance at $360\,\mathrm{nm}$ and for the tangent altitude $[\mathrm{km}]$ given in the legend would change if the number densities $[\mathrm{cm}^{-3}]$ at the various profile levels were changed. For instance, if there were $1\,\mathrm{cm}^{-3}$ more O_3 molecules at $31\,\mathrm{km}$ height, the sun-normalised radiance at $360\,\mathrm{nm}$ for $30\,\mathrm{km}$ tangent height would be weaker by $1 \cdot 10^{-17}\,\mathrm{sr}^{-1}$.

The radiance for stratospheric tangent heights is mostly influenced by the O_3 concentration near and slightly above the tangent height. The part of the profile above the tangent height has a significant influence, while the layers below contribute only little. Thus a pronounced step directly below the tangent height occurs in the weighting function. The step is expected since the line of sight traverses all atmospheric levels above the tangent point, but not those below. This feature is also typical for occultation measurement geometry. It is the key to the good vertical resolution of retrievals from limb and occultation measurements.

The sharp steps of the weighting functions reflect a difference to retrievals from nadir measurements, in which the profile information is drawn from broad peaks at different altitudes instead of steps [Hoogen et al., 1999].

The middle plot of Figure 9.2 features the relative-absolute O_3 weighting function in the same subspace as above. Each plotted profile exhibits how much (in radiance units $[\mathrm{sr}^{-1}]$) the sun-normalised radiance at $360\,\mathrm{nm}$ and for the tangent altitude $[\mathrm{km}]$ given in the legend would change if the number densities at the various profile levels were changed by a certain fraction. For instance, if there were $100\,\%$[2] more O_3 molecules at $22\,\mathrm{km}$ height, the sun-normalised radiance at $360\,\mathrm{nm}$ for $21\,\mathrm{km}$ tangent height would be weaker by $1 \cdot 10^{-5}\,\mathrm{sr}^{-1}$.

Since these weighting functions are well suited to describe the effect of relative deviations of the parameter, they reflect the properties of the original parameter profile. When compared to the top plot, the influence of the O_3 number density profile with its maximum in the lower stratosphere appears in all profiles: They are more pronounced in the lower stratosphere and damped above and below, while the relative magnitudes at each individual profile level (height) are preserved. The steps at the tangent heights are also eminent.

The bottom plot of Figure 9.2 displays the relative-relative O_3 weighting function in the same subspace as above. Each plotted profile exhibits how much (in relative units) the sun-normalised radiance at $360\,\mathrm{nm}$ and for the tangent altitude $[\mathrm{km}]$ given

[1] A solar zenith angle of $65\ \mathrm{deg}$ is assumed. All ray paths of *SCIARAYS* and the field of view of SCIAMACHY are accounted for.

[2] Since the weighting functions are linearisations of a non-linear problem, an additional effect must be expected for such a large fraction. This caution applies to the whole discussion in this section.

in the legend would change if the number densities at the various profile levels were changed by a certain fraction. For instance, if there were $100\,\%$ more O_3 molecules at $36\,\mathrm{km}$ height, the sun-normalised radiance at $360\,\mathrm{nm}$ for $36\,\mathrm{km}$ tangent height would be weaker by $0.03\,\%$.

Since these weighting functions describe the relative effect on the radiances, the profiles for higher tangent heights (with smaller radiances) become more pronounced, while the shape of each function is the same as the corresponding relative-absolute weighting function. Thus the step at the tangent height is still preserved.

The profiles of the top plot of Figure 9.3 show the absolute-absolute O_3 weighting function in the **subspace of tangent heights**. Each plotted profile exhibits how much (in radiance units $[\mathrm{sr}^{-1}]$) the number density $[\mathrm{cm}^{-3}]$ at the profile level, given in the legend, influences the sun-normalised radiance at $360\,\mathrm{nm}$ for all tangent altitudes $[\mathrm{km}]$. For instance, if there were $1\,\mathrm{cm}^{-3}$ more O_3 molecules at $15\,\mathrm{km}$ height, the sun-normalised radiance at $360\,\mathrm{nm}$ for $15\,\mathrm{km}$ tangent height would be weaker by $4 \cdot 10^{-18}\,\mathrm{sr}^{-1}$. Thus each weighting function profiles shows which measurement points (tangent altitudes) are influenced by an individual retrieval parameter.

The O_3 concentration at a particular profile level mostly influences the radiances for tangent altitudes which are below or equal to the profile level as the line of sights for these tangent altitudes pass through the profile level. Therefore, the weighting functions are large for the tangent altitudes below or equal to each profile level and slightly above. Thus the characteristic step at the point where tangent altitude and profile level are equal reappears.

Additionally, the weighting function profiles decrease with larger tangent heights in the stratosphere since the radiance signal itself decreases. Below about $20\,\mathrm{km}$, the weighting functions decrease with smaller tangent altitudes. A possible explanation is the fact that the line of sight has the longest path through the atmospheric layers just above the tangent altitude.

The profiles of the middle plot of Figure 9.3 show the relative-absolute O_3 weighting function in the subspace of tangent heights. Each plotted profile exhibits how much (in radiance units $[\mathrm{sr}^{-1}]$) a relative change [-] of the density at the profile level, given in the legend, influences the sun-normalised radiance at $360\,\mathrm{nm}$ for all tangent altitudes $[\mathrm{km}]$. For instance, if there were 100% more O_3 at $18\,\mathrm{km}$ height, the sun-normalised radiance at $360\,\mathrm{nm}$ for $18\,\mathrm{km}$ tangent height would be weaker by $3 \cdot 10^{-5}\,\mathrm{sr}^{-1}$.

Each of the weighting functions has the same shape as in the top plot, but the functions corresponding to levels with high O_3 number densities are emphasised as a relative change in O_3 density implies a larger absolute change than at the other levels.

The profiles of the bottom plot of Figure 9.3 show the relative-relative O_3 weighting function in the subspace of tangent heights. Each plotted profile exhibits how much (in relative units) a relative change [-] of the density at the profile level, given in the legend, influences the sun-normalised radiance at $360\,\mathrm{nm}$ for all tangent altitudes $[\mathrm{km}]$.

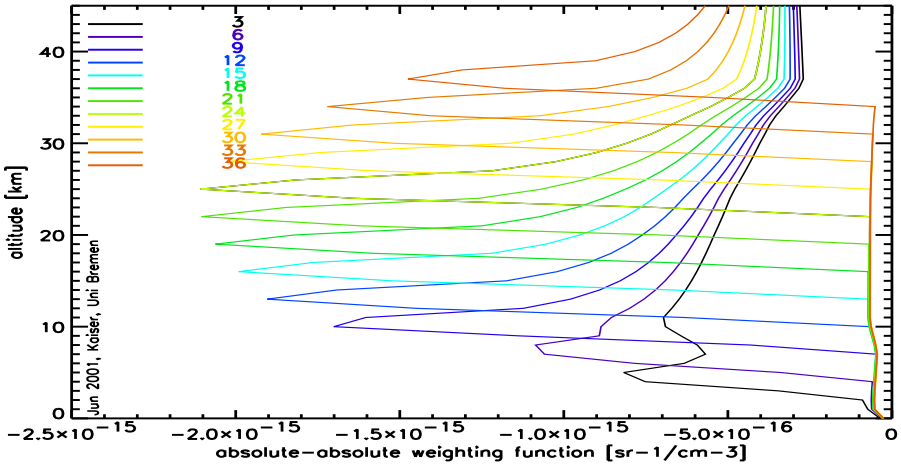

Figure 9.4: Ozone profile weighting functions at $790\,\mathrm{nm}$ wavelength for several tangent altitudes (given in km) as functions of the profile altitude level. Only single scattering and surface reflection are modelled. Compare to top plot of Figure 9.2

For instance, if there were $100\,\%$ more O_3 molecules at $36\,\mathrm{km}$ height, the sun-normalised radiance at $360\,\mathrm{nm}$ for $36\,\mathrm{km}$ tangent height would be weaker by $0.03\,\%$.

The lower parts of the functions are damped as compared to the middle plot since an absolute change in radiance of given magnitude $[\mathrm{sr}^{-1}]$ corresponds to a smaller fraction of the radiance, which is larger for lower tangent heights.

The advantage of displaying the relative-relative weighting functions is that the effect of a relative change of a parameter can be compared directly to the signal/noise of the measurement. This is done in Figures 9.5–9.7 below.

Spectral Dependence

The weighting functions of Figure 9.2 all vanish below about $15\,\mathrm{km}$ profile level. This effect occurs as the line of sight is optically thick for tangent heights below about $15\,\mathrm{km}$ due to the strong Rayleigh scattering at $360\,\mathrm{nm}$ wavelength. Weighting functions for $790\,\mathrm{nm}$, where Rayleigh scattering is much weaker, are shown in Figure 9.4 for several tangent altitudes. A comparison with the top plot of Figure 9.2 reveals that measurement at shorter wavelengths contain more influence (and thus information) from the upper parts of the atmosphere, while measurements at longer wavelengths are more sensitive to the lower parts of the atmosphere.

The question, which parts of a limb measurements are most sensitive to one individual parameter, say the O_3 concentration at the $15\,\mathrm{km}$ height level, is answered by the weighting function of this parameter in the 2-dimensional tangent altitude and wavelength subspace. Such a weighting function is displayed as colour-coded contour plot in the top of Figure 9.5. This plot has the same axis the ones in Figure 9.1. The weighting function is normalised to be relative w.r.t. the parameter and the radiance. Thus the

$15\,\mathrm{km}$-line of the bottom plot of Figure 9.3 is a vertical cut with a constant wavelength value of $360\,\mathrm{nm}$ through the colour-coded contour.

From the top plot of Figure 9.5 it is evident that the features of the weighting function at $360\,\mathrm{nm}$ qualitatively appear at all other wavelengths as well. The weighting function is the largest for a tangent height just below the profile level under consideration. It is large for tangent heights below and small for those above the level.

The Huggins and Chappuis bands obviously dominate the weighting function for O_3 at $15\,\mathrm{km}$. The Hartley band at smaller wavelengths does not appear since the absorption is so strong that this profile level is not reached by solar radiation[3]. The influence of the Huggins bands is damped by strong Rayleigh scattering, so that measurements in the Chappuis bands appear to be most sensitive[4] to O_3 at this profile level.

The bottom plot of Figure 9.5 shows the relative noise, i.e., noise/signal, of SCIAMACHY for the same tangent altitude and wavelength range. The colour-coding is also identical. Thus every measurement point which has a larger weighting function than relative noise could, in principle, be used to retrieve the parameter. The relative precision of a retrieval would be given by the ratio of the relative noise and the weighting function. For O_3 at the $15\,\mathrm{km}$ level this would be possible with measurement points in the Huggins as well as in the Chappuis bands.

Of course, for SCIAMACHY's hyperspectral measurements, the precisions are improved by retrieving from several, say m, measurement points. The improvement is by a factor of $\sqrt{m}$. For species with less prominent absorption features or less abundant species than O_3 this statistical approach is necessary.

BrO is an example for a trace gas whose retrieval requires the statistical approach. Its weighting function at the $15\,\mathrm{km}$ level of the profile is depicted in Figure 9.6 along with SCIAMACHY's relative noise.

The weighting function is smaller than the relative noise by a factor of 10 or more everywhere. Thus only by retrieving from more than 100 measurement points, information on this BrO profile level can in principle be obtained from the measurement.

Figure 9.7 shows the weighting function for CH_4 at $15\,\mathrm{km}$ profile height as an example for a trace gas absorbing in the NIR spectral region. The features and retrieval considerations pointed out for O_3 and BrO apply to this case as well. The weighting functions for other trace gases at $15\,\mathrm{km}$ profile height can be found in appendix B.

[3]Nor could radiation from $15\,\mathrm{km}$ penetrate the stratospheric ozone layer outwards reach a satellite.

[4]It shall be noted that a particular retrieval algorithm might still extract most information from the Huggins bands owing to their strong differential structure.

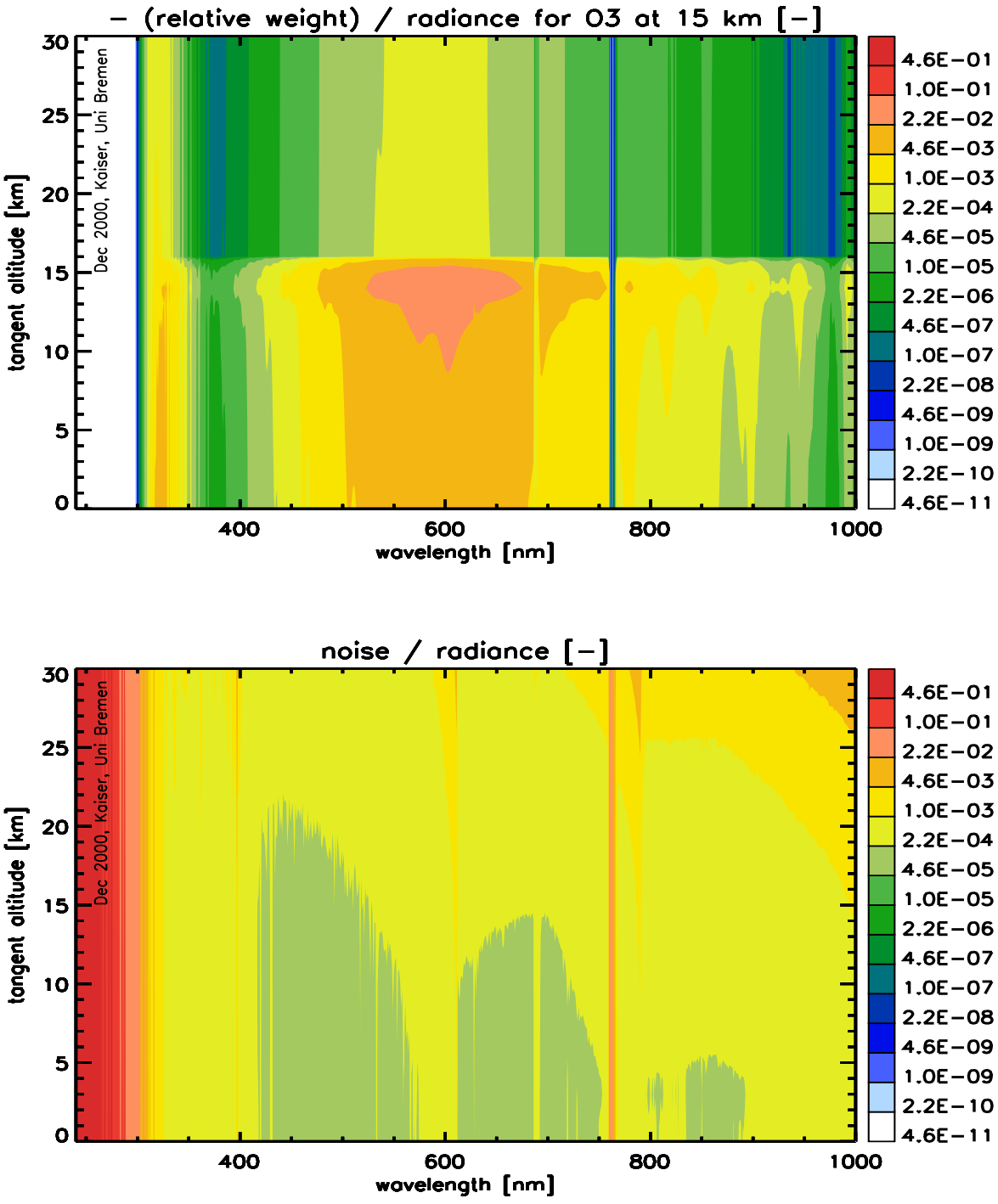

Figure 9.5: Relative-relative weighting function of the 15 km-level of the O_3 profile (top) and SCIAMACHY's relative noise (bottom).

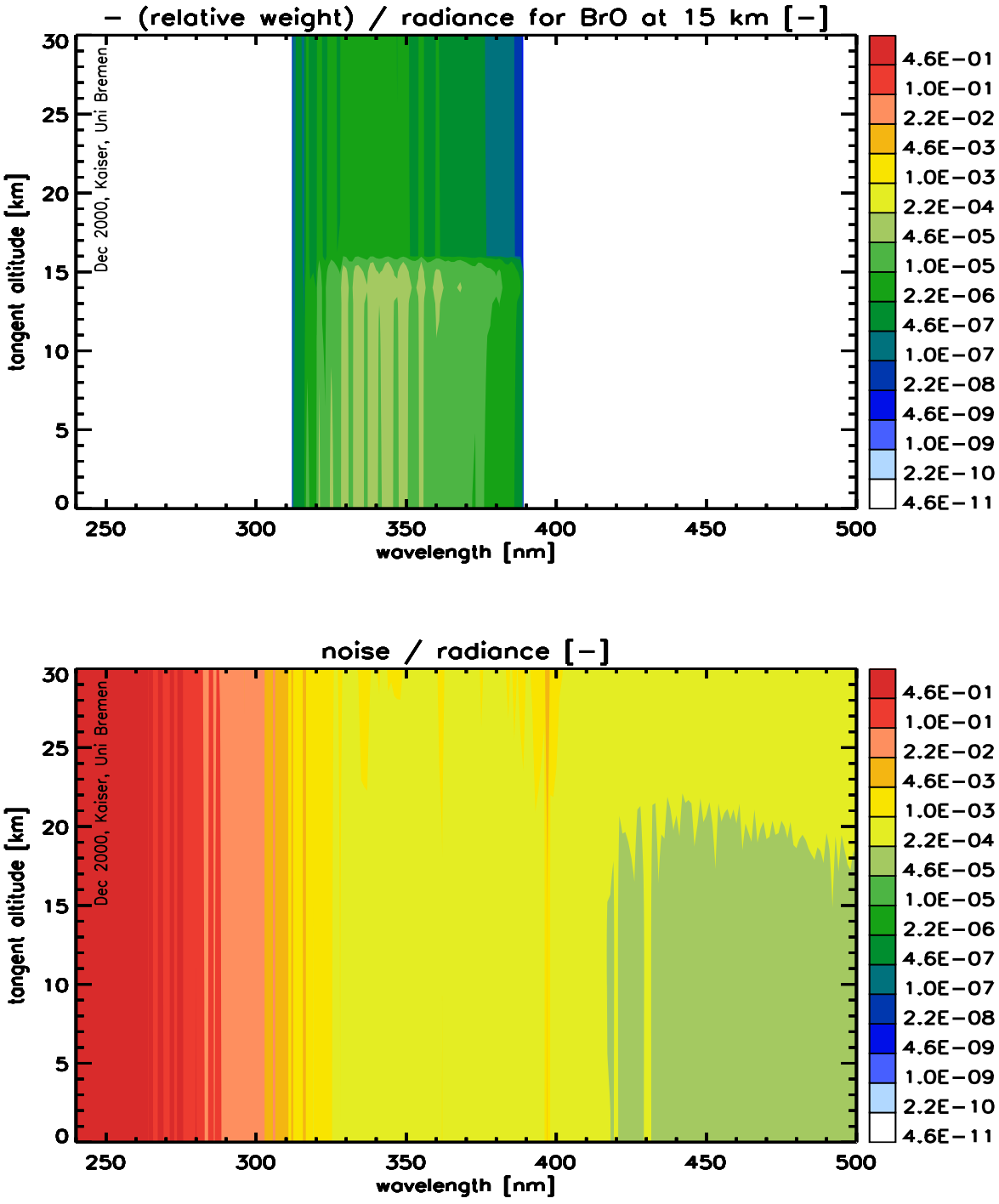

Figure 9.6: Relative-relative weighting function of the 15 km-level of the BrO profile (top) and SCIAMACHY's relative noise (bottom).

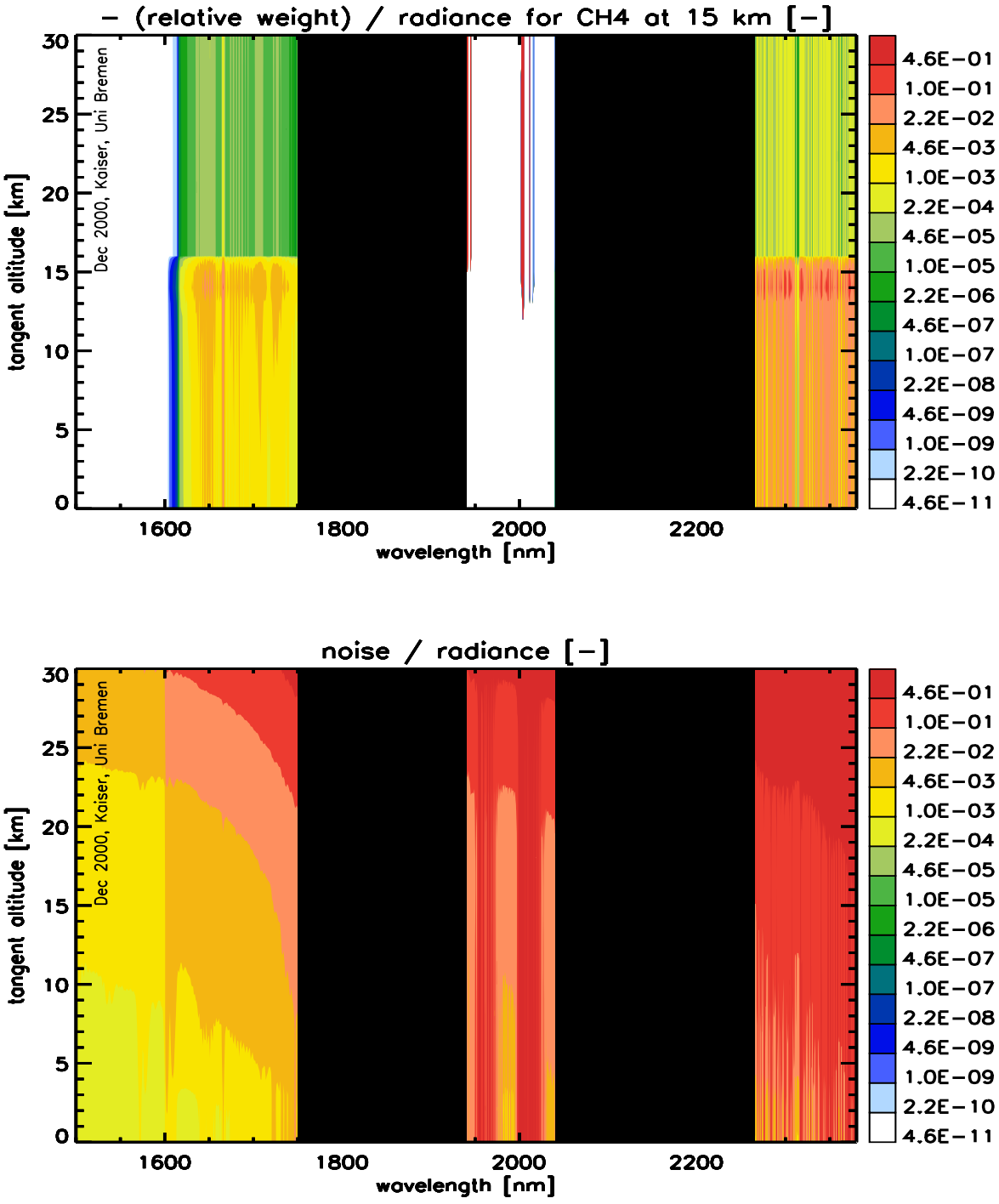

Figure 9.7: Relative-relative weighting function of the 15 km-level of the CH_4 profile (top) and SCIAMACHY's relative noise (bottom).

9.3 Averaging Kernels

Since the weighting functions of O_3 and BrO in Figures 9.5 and 9.6 are relatively strong and with differential structure in the wavelength range 300–$370\,\mathrm{nm}$, it would be reasonable to retrieve O_3 and BrO from this wavelength range. The averaging kernels which would characterise such a retrieval with 467 spectral points are shown in Figure 9.8. They include the influence of all correlations between O_3, NO_2, BrO, pressure, and temperature profile retrieval parameters. All parameters are retrieved as relative deviations from the *a priori* values. An *a priori* uncertainty of $100\,\%$ is assumed.

The top plot of Figure 9.8 depicts the rows of the averaging kernel matrix[5] for O_3. Above $10\,\mathrm{km}$ altitude, the averaging kernels perfectly peak at their corresponding altitudes and vanish everywhere else. Accordingly, the measurement responses, i.e., the sums over the corresponding matrix rows, equal one. Here, a retrieval without smoothing error and without *a priori* contamination can be expected. Thus the vertical resolution is $3\,\mathrm{km}$.

Comparing to the O_3 weighting function and SCIAMACHY's noise in Figure 9.5, it becomes clear that "near-perfect" retrievals are possible since the O_3 absorption signal is much larger than the measurement noise. By suppressing the *a priori* influence for stratospheric O_3, the optimal estimation algorithm purposely "collapses" to a straightforward least-squares algorithm.

The O_3 averaging kernel for the $6\,\mathrm{km}$ level has a peak at the correct altitude, but it is weaker than 0.7. Since the kernel has contributions from the neighbouring levels, i.e., 3 and $9\,\mathrm{km}$, a smoothing error occurs. However, the measurement response is close to one, indicating that the influence of the *a priori* is minor. The averaging kernel for the $3\,\mathrm{km}$ level peaks at the wrong altitude, i.e., $9\,\mathrm{km}$. Therefore, little useful information on this level is contained in the measurement[6]. This is reflected in a very small value of the measurement response. However, it should be kept in mind that these error discussions for the troposphere are of a somewhat theoretical nature as other errors due to interfering clouds and horizontal inhomogeneities are dominant there.

Further properties of the averaging kernels of O_3 are discussed in chapter 10.

The bottom plot of Figure 9.8 depicts the rows of the averaging kernel matrix[7] and the measurement response for BrO. Since the latter is close to unity (> 0.8) for 12–$36\,\mathrm{km}$, it can be concluded that the BrO profile in this altitude range is retrieved with only little *a priori* interference. It is clear from the FWHMs as well as from the peak values that a smoothing error occurs. It is the smallest (10–$20\,\%$) for between $18\,\mathrm{km}$ and $24\,\mathrm{km}$.

Comparing to the BrO weighting function and SCIAMACHY's noise in Figure 9.6, it becomes clear that good retrievals are possible even though the signal is smaller than the

[5] Strictly speaking, it is the O_3 sub-block of the averaging kernel matrix for all retrieval parameters.

[6] Improved tropospheric averaging kernels are obtained for measurements in the visible spectral region.

[7] Strictly speaking, it is the BrO sub-block of the averaging kernel matrix for all retrieval parameters.

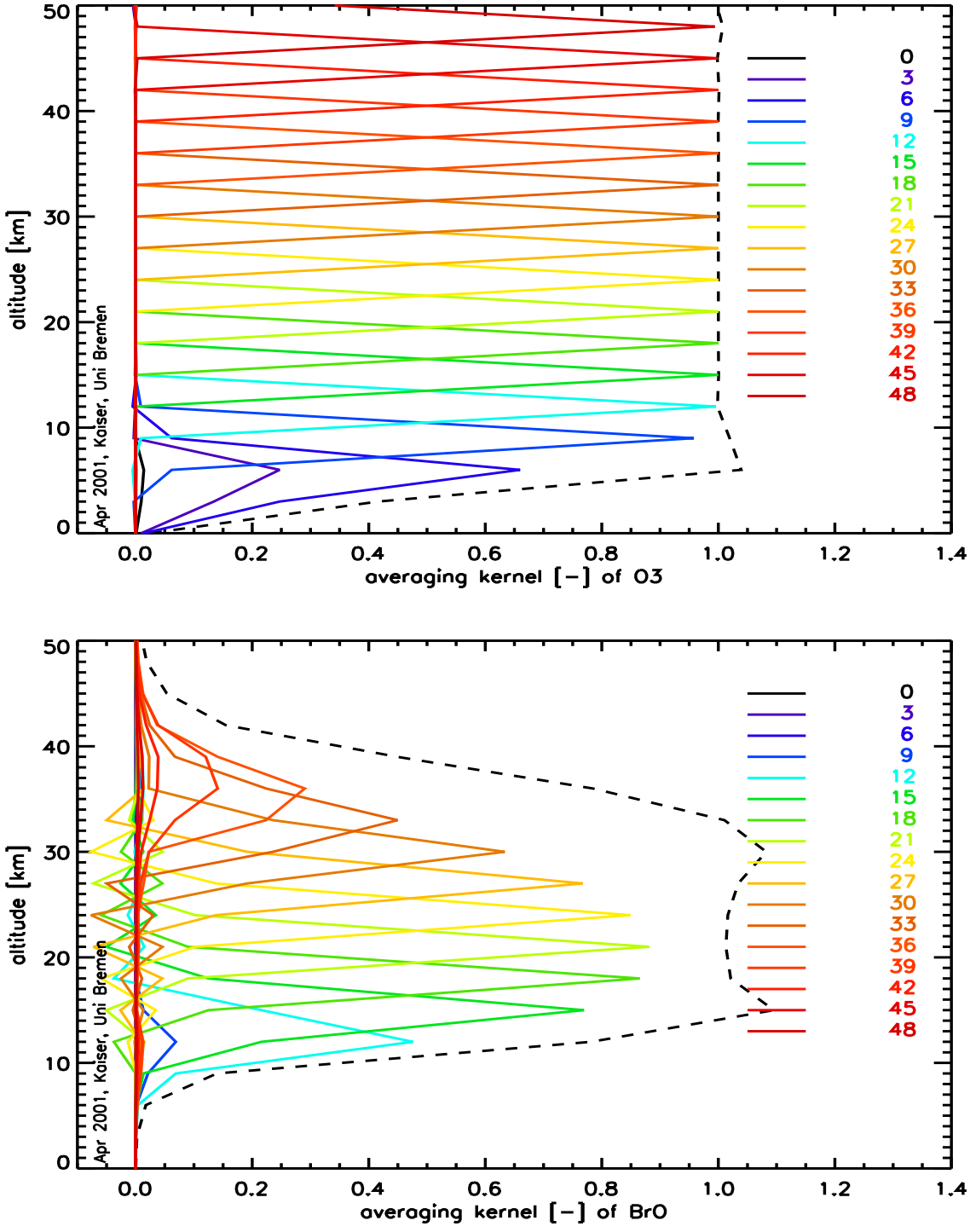

Figure 9.8: Averaging kernels of O_3 (top) and BrO (bottom) for a retrieval from the 300–370 nm spectral range. The rows of the matrix are plotted in different colours. The corresponding altitudes are given in [km]. The dashed line shows the measurement response. The vertical resolution is 3 km.

noise. This is achieved with the statistical interpretation of a large number of spectral points.

Below $12\,\mathrm{km}$ and above $36\,\mathrm{km}$, the measurement response for BrO is small (< 0.2). Therefore, the retrieved profile mostly reflects the *a priori* one. This is consistent with the fact that the individual kernel functions have low, broad peaks at the wrong altitudes or vanish completely.

Chapter 10

Vertical Resolution vs. Retrieval Error

10.1 Introduction

For the interpretation of UV-vis-NIR limb measurements, retrieval height levels equal to the measurements' tangent heights are commonly used. For instance, Bovensmann et al. [1999] assume a retrieval grid with $3\,\mathrm{km}$ vertical spacing according to SCIAMACHY's tangent height step size of $3\,\mathrm{km}$. The reason for this choice is the fact that the tangent step size is thought to limit the vertical resolution.

The actually achievable resolution of a retrieval with the optimal estimation method can be estimated from the averaging kernels width. Thus the *vertical resolution* is measured as the full width at half maximum (*FWHM*) of the averaging kernels. (This approach is adopted in the ACE study, see Chapter 11.) For limb measurements in general, the FWHM can be different, i.e., larger or smaller, than the tangent height step size.

In this chapter, the *vertical resolution* shall be the smallest vertical extend of a detectable profile feature. A close relationship to the magnitude of the feature will emerge. This relationship has already been discussed by Backus and Gilbert [1968, 1970] and used in their inversion method.

The vertical resolution of O_3 retrievals as estimated from the averaging kernel widths is verified here with test retrievals and compared to the geometric constraints of the measurement, i.e., tangent height step size and field-of-view (FOV) height.

10.2 Averaging Kernels

Figure 10.1 shows averaging kernels for selected heights of the O_3 profile. The resolution of the plot is $1\,\mathrm{km}$. The averaging kernels are calculated with the radiative transfer and instrument models in *SCIARAYS* assuming ray paths for single scattering and surface reflection followed by one scattering event ("S" and "RS" in Figure 6.1). The tangent step size of $3\,\mathrm{km}$ and the sequence ranges from $1\,\mathrm{km}$ to $55\,\mathrm{km}$. The noise and the FOV-integration with $2.6\,\mathrm{km}$ vertical extent at the tangent height correspond to the real values of SCIAMACHY (Chapter 7).

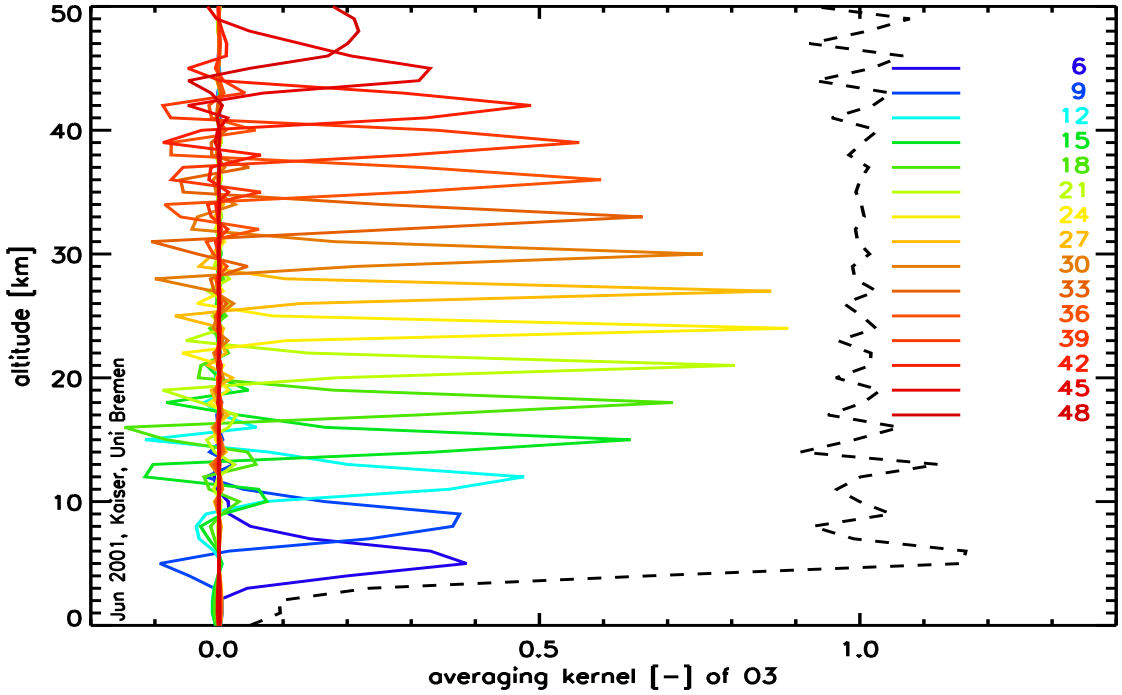

Figure 10.1: O_3 averaging kernels of selected altitudes for a retrieval from the 315–325 nm and 740–790 nm spectral ranges. The dashed line shows the measurement response. This figure is analogous to Figure 9.8, but the vertical resolution is 1 km.

The atmospheric model takes Rayleigh scattering, O_3 and NO_2 absorption, aerosol scattering and absorption, and surface reflection with an albedo of 0.5 into account. The aerosols correspond to stratospheric background conditions and all other profiles conform to the US standard atmosphere 1976.

For the measurement scenario solar zenith and azimuth angles of 30° and 40°, respectively, were assumed. The retrieval simultaneously uses two fit windows at 315–325 nm and 740–790 nm with spectral step sizes of 0.2 nm and 1.0 nm, respectively. The *a priori* standard deviation is assumed to be 100 %. O_3 and NO_2 are retrieved simultaneously.

The FWHMs of the averaging kernels suggest the following vertical resolution: Between 5 km and 10 km and above 45 km, it is about 3 km, reflecting the extent of the field of view and the tangent altitude step size. In between, the averaging kernels are evidently more narrow, indicating a vertical resolution of even better than 2 km. This effect results from the simultaneous use of many spectral points with different mean photon paths in the retrieval. It is due to the *hyperspectral advantages* of SCIAMACHY. The same principle allows profile retrievals from the nadir UV-measurements of GOME [Hoogen et al., 1999].

Since the response function in Figure 10.1 is close to unity for all altitudes above

$5\,\mathrm{km}$, the *a priori* influence is small throughout the whole stratosphere and in the upper troposphere.

The averaging kernels in Figure 10.1 are theoretical values. They become worse when other parameters are retrieved simultaneously. On the other hand, they improve when more spectral points are used.

The dependence of the averaging kernels on the selected spectral windows is demonstrated in Figure 10.2, in which the averaging kernels for retrievals from the two spectral windows are plotted individually.

The response functions show that the two spectral ranges facilitate retrievals from different height regions: Retrievals from the short-wavelength window are limited to the O_3 profile above $12\,\mathrm{km}$, while those from the long-wavelength window are limited to profile levels between $5\,\mathrm{km}$ and $40\,\mathrm{km}$. The retrieval region of the combined spectral windows is the superset of the individual retrieval regions: 5–$50\,\mathrm{km}$, see Figure 10.1.

In the height region 12–$30\,\mathrm{km}$, for which both windows contain information, the averaging kernels of a combined retrieval (Figure 10.1) are more narrow than those of a retrievals from the individual windows (Figure 10.2). Thus the combination of retrieval windows improves the vertical resolution of the retrieval.

The averaging kernels of retrievals from the long-wavelength window (Figure 10.2, bottom) have a width of $3\,\mathrm{km}$ or more, reflecting SCIAMACHY's tangent height step size. Those of retrievals from the short-wavelength window (Figure 10.2, top) are clearly more narrow. The O_3 absorption cross section has stronger differential structures in the short-wavelength region. Thus the improvement of the vertical resolution beyond SCIAMACHY's geometrical limits must also be attributed to variations of the atmospheric light paths due to the differential structure of the absorption.

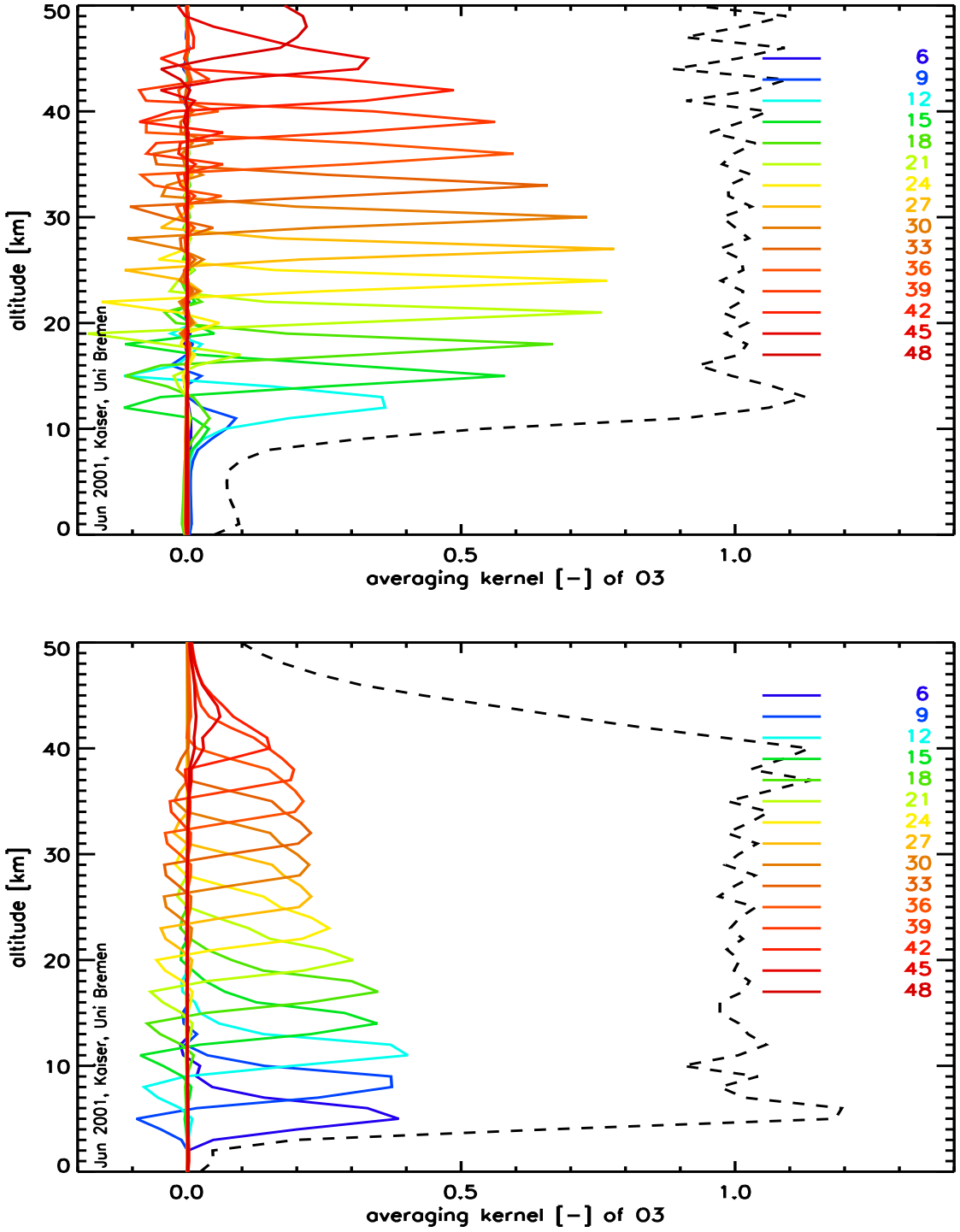

Figure 10.2: O_3 averaging kernels of selected altitudes for retrievals from the 315–325 nm spectral range (top) and from the 740–790 nm spectral range (bottom). The dashed lines show the measurement responses. The vertical resolution is 1 km. Compare to Figure 10.1.

10.3 Retrieval Tests

In order to verify the vertical resolution derived from the averaging kernels of the theoretical analysis, twenty synthetic limb measurements have been created. From these, twenty profiles have been retrieved. The statistical properties of the ensemble of the retrieved profiles are depicted in Figures 10.3–10.6 and discussed in this section.

The following procedure has been performed for two perturbed O_3 profiles with $3\,\mathrm{km}$ and $1\,\mathrm{km}$ vertical resolution:

1. Simulate a limb measurement sequence for the scenario specified in the last section with the RTM (both spectral ranges combined).
2. Apply the field of view integration of SCIAMACHY with the instrument model.
3. Add twenty different random noise vectors a with Gaussian characteristic according to SCIAMACHY's performance to obtain twenty synthetic measurements.
4. Perform twenty retrievals using a non-linear optimal estimation algorithm and non-perturbed *a priori* information.
5. Calculate the mean retrieved, the mean retrieval error and the retrieval standard deviation (1σ) from the ensemble of the twenty retrieved profiles.

In both cases the standard profile has been severely ($-70\,\%$) "perturbed" at the $15\,\mathrm{km}$ altitude level.

For the retrievals with $3\,\mathrm{km}$ vertical resolution, i.e., the scale of the FOV and the tangent altitude step size, an *a priori* with half the concentration of the standard profile and $100\,\%$ standard deviation was used, so that the true profile is at the 1σ distance of the *a priori*. The mean retrieved profile and the retrieval standard deviation are shown in Figure 10.3 along with the true, perturbed profile and the *a priori* profile and its standard deviation. Except for the lowermost level, the retrieval obviously converges well to the true profile.

In Figure 10.5 the mean retrieval error and the mean retrieval standard deviation are plotted. The retrieval converges correctly as the mean retrieval error is clearly smaller than its standard deviation. Therefore, the standard deviation gives the 1-σ precision of the retrieval. Above the perturbation, the retrieval precision is so good that other influences than the measurement noise appear to be the limiting factor. From the perturbation level down to the upper troposphere, the retrievals have a precision of $\approx 2\%$.

For the retrievals with $1\,\mathrm{km}$ vertical resolution the standard profile was used as *a priori* with $50\,\%$ standard deviation. The true profile, the *a priori* profile and the mean retrieved profile with standard deviations are plotted in Figure 10.4. The mean retrieval error and the retrieval standard deviations are shown in Figure 10.6.

It can be seen that retrievals actually converge to the true profile with $1\,\mathrm{km}$ vertical resolution. However, the error at each of the retrieval levels may become as large as 20–$30\,\%$. This means that the geometric limitations of the tangent height step size and

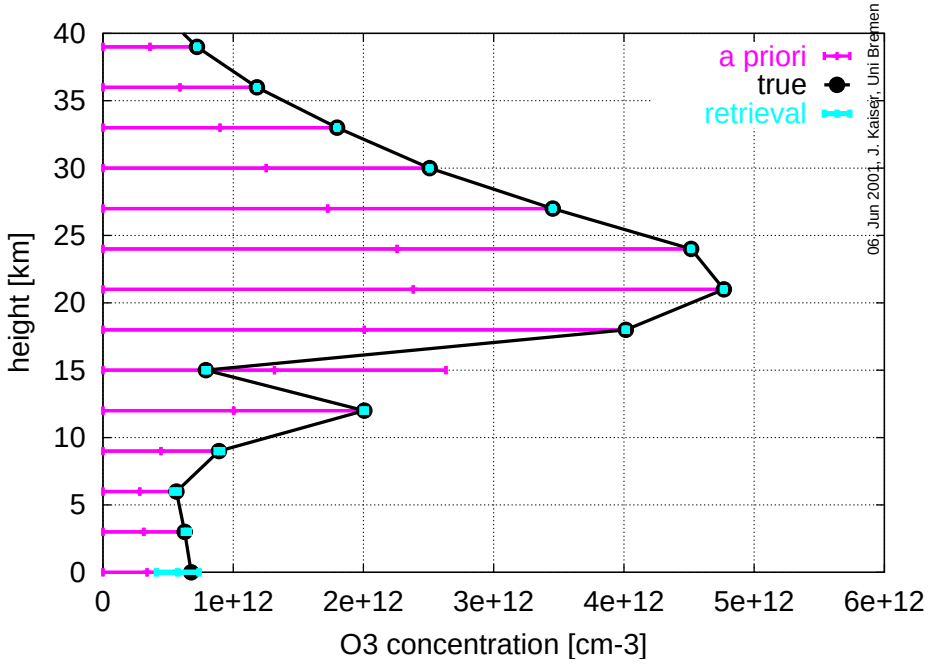

Figure 10.3: Ensemble statistics of O_3 retrieval with $3\,\mathrm{km}$ vertical resolution.

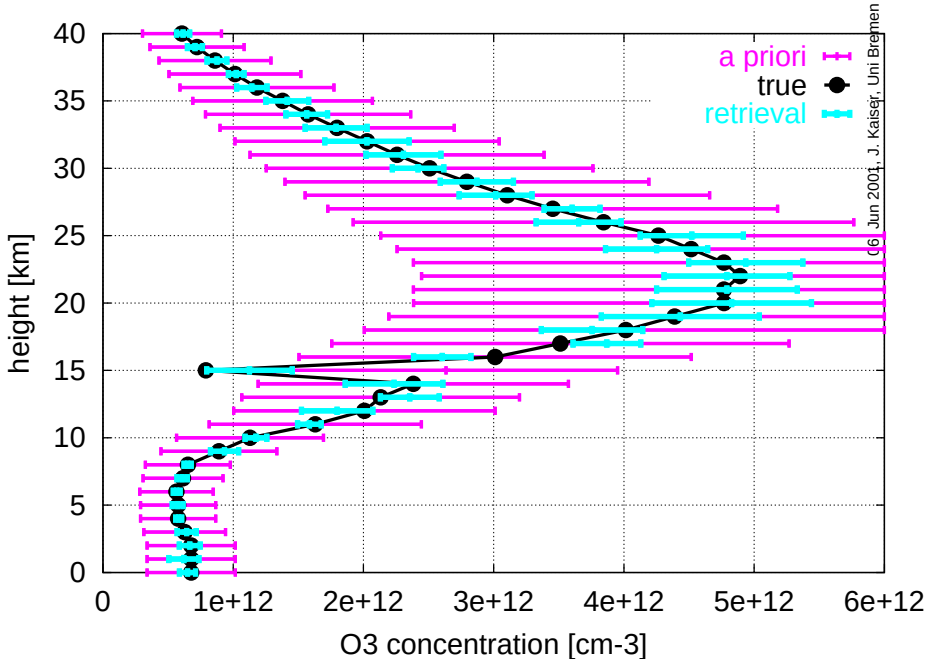

Figure 10.4: Ensemble statistics of O_3 retrieval with $1\,\mathrm{km}$ vertical resolution.

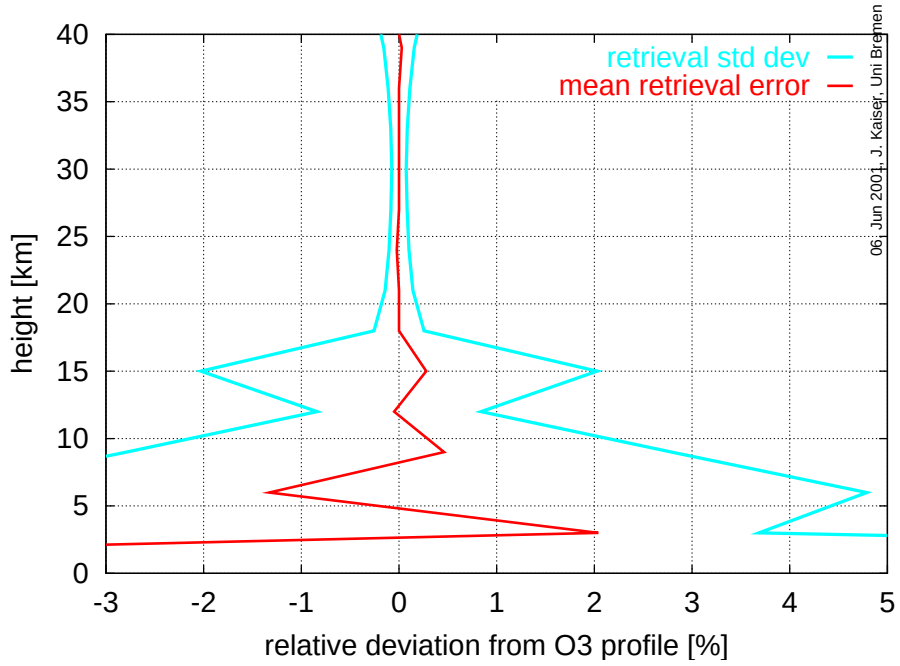

Figure 10.5: Ensemble statistics of O_3 retrieval with $3\,\mathrm{km}$ vertical resolution.

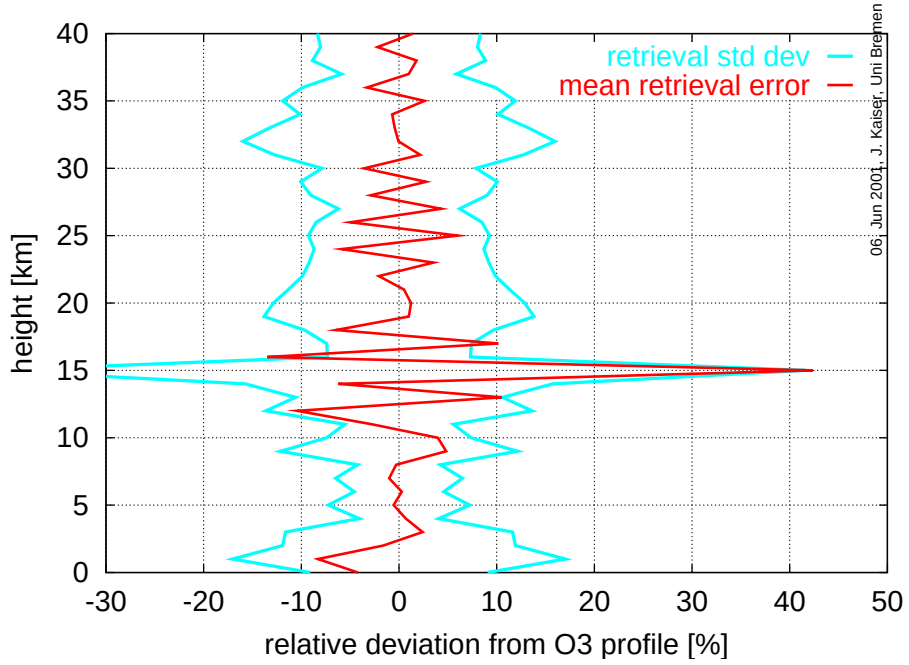

Figure 10.6: Ensemble statistics of O_3 retrieval with $1\,\mathrm{km}$ vertical resolution.

the instrument FOV can be overcome to yield profile information on a finer vertical scale.

The retrieval error at $15\,\mathrm{km}$ is strongly propagated upwards to the $16\,\mathrm{km}$ and $17\,\mathrm{km}$ profile levels, but only weakly downwards. The area of relatively strong correlation reflects the assumed tangent height sequence and FOV integration: The FOV of the measurement with $16\,\mathrm{km}$ tangent height extends from $14.7\,\mathrm{km}$ to $17.3\,\mathrm{km}$.

When using the precision and vertical resolutions of this chapter for further studies, it should be kept in mind that they are theoretical quantities which neglect correlations with other retrieval parameters and forward model approximations, the most serious of which is the absence of cloud. They can be expected to limit the retrieval range to the stratosphere and the uppermost troposphere.

On the other hand, the exact values change when different fit windows are used. Thus further spectral points of SCIAMACHY yield additional information.

10.4 Conclusions

The trade-off between vertical resolution and retrieval precision becomes obvious in the test retrievals from an ensemble of noisy measurements: The vertical resolution can be improved at the cost of degrading precision.

Therefore, the vertical resolution of a sensor can only be specified for a desired precision or vice versa. For instance, SCIAMACHY can be expected to have a precision of 1–$2\,\%$ for the O_3 profile at $3\,\mathrm{km}$ vertical resolution and a precision of 20–$30\,\%$ at $1\,\mathrm{km}$ vertical resolution.

The vertical resolution found in test retrievals is consistent with the FWHM of the averaging kernels.

The improvement of the vertical resolution beyond the geometric limitations of the instrument can be achieved owing to the hyperspectral capabilities of SCIAMACHY. It implies that the investigations of different atmospheric topics will require different retrieval schemes for identical measurements.

The assessment of the vertical resolution and retrieval precision of SCIAMACHY has been presented at the Fifth European Symposium on Stratospheric Ozone in 1999 in St. Jean de Luz, France, and is published in Kaiser et al. [2000].

Chapter 11

Sensitivities of a Limb Sensor

11.1 Introduction

The European Space Agency (ESA) has commissioned the so-called *ACE study* firstly to define mission objectives and observational requirements for an Atmospheric Chemistry Explorer (ACE) mission commencing in 2008 and, secondly, to assess systematically the observational capabilities with which to address these requirements [ESA, 2000]. To accomplish the latter task, the full range of passive remote-sensing techniques is analysed on a common basis through retrieval simulations.

This chapter analyses the information content of a limb-viewing UV-vis-NIR measurement. In general, the common basis of input parameters and analysis methods of ACE is obeyed. Instrument-specific parameters, which are not prescribed by the common ACE basis, are chosen according to the performance of ESA's SCIAMACHY instrument, see chapters 3 and 7.

The analysis method is described in Section 11.2 and the measurement scenario and retrieval setup are detailed in Section 11.3. The results of the calculations are shown in Section 11.4 and further sources of errors, which could not be assessed quantitatively in the framework of this study, are discussed in Section 11.5. Finally, the findings are summarised in Section 11.6.

11.2 Method

Theoretical precisions and other retrieval diagnostics are determined in a five step process:

1. An atmospheric state (profiles, albedo...) and a measurement geometry (solar coordinates) are assumed. For these, sun-normalised radiances (radiance over irradiance) at many tangent heights and their weighting functions (derivatives) w.r.t. all retrieval parameters are calculated with the radiative transfer model (RTM) in *SCIARAYS*, see Chapter 6.

2. The instrument model in *SCIARAYS* convolves the radiances and weighting functions to simulate a limb measurement sequence with a realistic field of view at predefined tangent altitudes, see Chapter 7.

3. The measurement covariance matrix for this simulated limb measurement sequence is computed by the instrument model.

4. Using the weighting function matrix and the measurement error covariance matrix along with the covariance matrix of the *a priori* state, the *a posteriori* covariance matrix, the averaging kernel matrix and the *a posteriori* correlation matrix are computed according to Rodgers' optimal estimation formalism, see Chapter 8.

5. The retrieval diagnostics are computed from the *a posteriori* covariance matrix, the averaging kernel matrix and the *a posteriori* correlation matrix and written to files.

The individual steps are described in more detail in the following sections.

11.2.1 Radiative Transfer Model *SCIARAYS*

The RTM in *SCIARAYS* computes sun-normalised radiances for a given atmospheric state and measurement geometry. Besides the radiances, weighting functions for all atmospheric state parameters are computed quasi-analytically.

The model solves the integral form of the radiative transfer equation in spherical coordinates. Thereby the radiance is approximated by the first two orders of scattering and one term for surface reflection. The ray paths which are modelled by *SCIARAYS* for limb measurements are depicted in Figure 6.1, along with other ray paths which may be modelled with *SCIARAYS* for other observational geometries.

A detailed description can be found in Chapter 6. The validation of an early version of *SCIARAYS* is published by Kaiser et al. [1999].

11.2.2 Inversion Formalism

The weighting function matrix $\mathbf{K}$ for all retrieval parameters and all measurement points and the measurement error covariance matrix $\mathbf{S}_\mathrm{y}$ for all measurement points are used for calculating the inversion diagnostics following the optimal estimation formalism by Rodgers [1976b]. Additionally, a diagonal *a priori* covariance matrix $\mathbf{S}_a$ is used, see Section 11.3.5 for detailed values.

The optimal estimation method is derived in Chapter 8. Here, the relevant formulae for the present context are recaptured: The *a posteriori* covariance matrix $\widehat{\mathbf{S}}$, the *contribution function* matrix $\mathbf{D}$, the averaging kernel matrix $\mathbf{A}$ and the *a posteriori correlation matrix* $\mathbf{C}$ are calculated as

$$\widehat{\mathbf{S}} = (\mathbf{K}^T \mathbf{S}_\mathrm{y}^{-1} \mathbf{K} + \mathbf{S}_a^{-1})^{-1} \tag{11.1}$$

$$\mathbf{D} = \widehat{\mathbf{S}}\, \mathbf{K}^T \mathbf{S}_\mathrm{y}^{-1} \tag{11.2}$$

$$\mathbf{A} = \mathbf{D}\,\mathbf{K} \tag{11.3}$$

$$\mathbf{C}(i,j) = \frac{\widehat{\mathbf{S}}(i,j)}{\sqrt{\widehat{\mathbf{S}}(i,i)\;\widehat{\mathbf{S}}(j,j)}}\,. \tag{11.4}$$

11.2.3 Diagnostics Output (number density — VMR)

The theoretical precisions $\widehat{\sigma}(i)$ are obtained from the diagonal elements of the *a posteriori* covariance matrix:

$$\widehat{\sigma}(i) = \sqrt{\widehat{\mathbf{S}}(i,i)}\,. \tag{11.5}$$

For trace gases, theoretical precisions $\widehat{\sigma}(i)$ are computed as number densities. They are converted to volume mixing ratios (VMRs) by division by the neutral density, which in turn is computed with the ideal gas law from pressure and temperature.

Thus an error in temperature would introduce an error in neutral density which would then imply an additional error in VMRs due to the conversion from number densities. However, this additional error is misleading and should be neglected: It would impose a lower limit of about 3.5 % on all VMR precisions of all investigated instruments. This would make the task of comparing the capabilities of different instruments impossible by raising all precisions to the same level of ≈3.5 %. Therefore, this error is not accounted for. Nevertheless, the correlations to the temperature uncertainties are included in the theoretical precisions in that temperature is retrieved simultaneously.

The averaging kernel matrix $\mathbf{A}$ and the *a posteriori* correlation matrix $\mathbf{C}$ are used directly, i.e., without further transformation, to determine the other retrieval diagnostics.

The vertical resolution is computed from a linear interpolation of the each parameter's averaging kernel column[1]. Thus its value cannot become smaller than the retrieval grid spacing, i.e., $2\,\mathrm{km}$ in this study[2]. An investigation of the behaviour in the limit of an infinitely fine retrieval grid is desirable but beyond the scope of the current investigation.

11.3 Measurement Scenarios

11.3.1 Measurement Geometry

The solar coordinates at the tangent points are chosen to be $65\,^\circ$ zenith angle and $40\,^\circ$ azimuth angle w.r.t. line of sight. These values are typical for SCIAMACHY measurements at $45\,^\circ$ North in March (see Chapter 3).

[1] Since the averaging kernel matrix is not normalised, it should not strictly be interpreted in the standard fashion presented in Section 8.3. However, the vertical resolution can be determined from these averaging kernels' FWHMs as the concentrations of neighbouring layers have similar orders of magnitude.

[2] In regions without information from the measurement, the averaging kernel has no maximum and the algorithm for automatic FWHM computation may produce smaller values.

Since no requirements regarding the field of view (FOV) are prescribed by ACE, a height of the FOV of $2.6\,\mathrm{km}$ at the tangent point is assumed. This value corresponds to SCIAMACHY's field of view as build. The tangent height scan sequence is chosen consistently with the main study: 50 tangent heights from 3 to $52\,\mathrm{km}$ are evaluated. This corresponds to a step size of $1\,\mathrm{km}$. The range was chosen to investigate the performance in the target retrieval region of 5–$50\,\mathrm{km}$.

11.3.2 Atmospheric Profiles and Albedo

The atmospheric profiles of trace gases, pressure and temperature are taken from the ACE data base. All values represent profiles for mid latitudes, i.e., $45\,^\circ$ North.

The aerosol scattering profile is taken from the GOMETRAN data base. It corresponds to stratospheric background conditions. The tropospheric visibility is $23\,\mathrm{km}$ with a marine type boundary layer.

A value of 0.3 is assumed for the albedo.

11.3.3 Retrieval Parameter Grouping and Spectral Points

The retrieval parameters are treated in two groups with absorption features in separate spectral regions. Thus the correlations between the two groups can be neglected. The parameter groups are listed in Table 11.1. The spectral ranges are those of SCIAMACHY measurements and the step sizes roughly equal SCIAMACHY's spectral resolution. Due to oversampling, SCIAMACHY will record about twice as many spectral points. All parameters except the albedo are profiles with a vertical step size of $2\,\mathrm{km}$.

11.3.4 Cross Sections

The absorption cross sections of all referenced trace gases are plotted in Figures 4.1–4.3.

The cross sections of O_3 and NO_2 have been measured for several temperatures in the laboratory with the SCIAMACHY and GOME spectrometers by Bogumil et al. [1999] and Burrows et al. [1998]. Thus the cross sections themselves have the spectral resolution of SCIAMACHY. They are used with proper temperature interpolation. For BrO, OClO, ClO, HCHO, and SO_2 only cross section at one temperature are used for this study.

The absorption cross sections of H_2O, CH_4, CO_2, CO, N_2O and O_2 are extracted from the HITRAN data base and convolved with SCIAMACHY's slit function before use in the radiative transfer. They are generated temperature dependently. The pressures are chosen in a way to ensure correct results for the stratosphere, where pressure is a function of temperature. Thus the cross sections in troposphere are computed with correct temperatures but wrong pressures. This implies an approximation to the radiative transfer, the effect of which has to be discussed.

Table 11.1: Retrieval parameter grouping: The set of retrieval parameters is divided into two groups and retrieved from separate spectral regions.

group	UV-vis	NIR
retrieval parameters (results shown)	O_3 NO_2 BrO OClO ClO T p albedo	H_2O CH_4 CO_2 CO N_2O
retrieval parameters (for error correlation)	H_2O	O_3 T p albedo
fixed parameter	O_2	O_2
spectral region step size	240 – 400 nm 0.25 nm	800 – 1030 0.5 nm
spectral region step size	401 – 800 nm 0.5 nm	1031 – 1750 nm 1.5 nm
spectral region step size		1940 – 2040 nm 0.22 nm
spectral region step size		2265 – 2380 nm 0.26 nm

11.3.5 *A Priori*

The *a priori* standard deviation values are chosen conforming to the ACE requirements:

- 1000 % for BrO
- 300 % for all other trace gases
- 10 K for temperature.

Albedo and pressure are retrieval parameters not anticipated by ACE. They are assigned the following *a priori* uncertainties:

- 200 % for albedo
- 10 % for pressure.

11.4 Results

The computed theoretical precisions and retrieval diagnostics of parameter group "UV-vis" are plotted in the Figures 11.1–11.8, those of parameter group "NIR" in Figures 11.9–11.13.

The top plots of the figures show the assumed true values (blue "state"), the *a priori* standard deviations (green "a priori precision"), and the calculated theoretical retrieval precisions (red "a posteriori precision") in absolute units. The latter is calculated according to (11.5) from the *a posteriori* covariance matrix. The offsets between the states and the *a priori* standard deviations reflect the fact that the latter are defined relative to the states, i.e., in percent.

The middle plots exhibit the calculated theoretical retrieval precisions in relative units (red "a posteriori precision [%]"). They are just the ratios of the red and the blue curves from the top plots.

The vertical resolution computed as FWHM of the averaging kernels is also shown in the middle plot (green "vertical resolution [km]"). It is computed as FWHM of the averaging kernel columns[3]. In regions with noticeable[4] retrieval precision, it is technically limited to values above (or equal to) the retrieval profile gridding of $2\,\mathrm{km}$.

The bottom plots show further retrieval diagnostics which are computed from the averaging kernel matrices:

The red "product AK peak" is the largest value of the averaging kernel column[5]. A value near unity signals that the parameter is actually retrieved from the measurement, while values below unity indicate that additional *a priori* information is used.

[3]Only the square block of the averaging kernel matrix, which corresponds to the appropriate profile, is used.

[4]*a posteriori* $<$ *a priori*

[5]Again, only the square block of the averaging kernel matrix, which corresponds to the appropriate profile, is used.

The pink "max|x_CM|" gives the largest absolute values of the linear correlation coefficients with other retrieval parameters. Thus smoothing of the profile is not represented in it. (Look for the vertical resolution in the middle plots.)

The green "full AK sum" and the blue "product AK sum" are the sums over the full averaging kernel columns and the parts of the column, which correspond to the parameter profile. These values cannot be interpreted easily since the averaging kernel matrix is not normalised.

The relative retrieval precisions depicted in the figures are summarised in Table 11.2 on page 152.

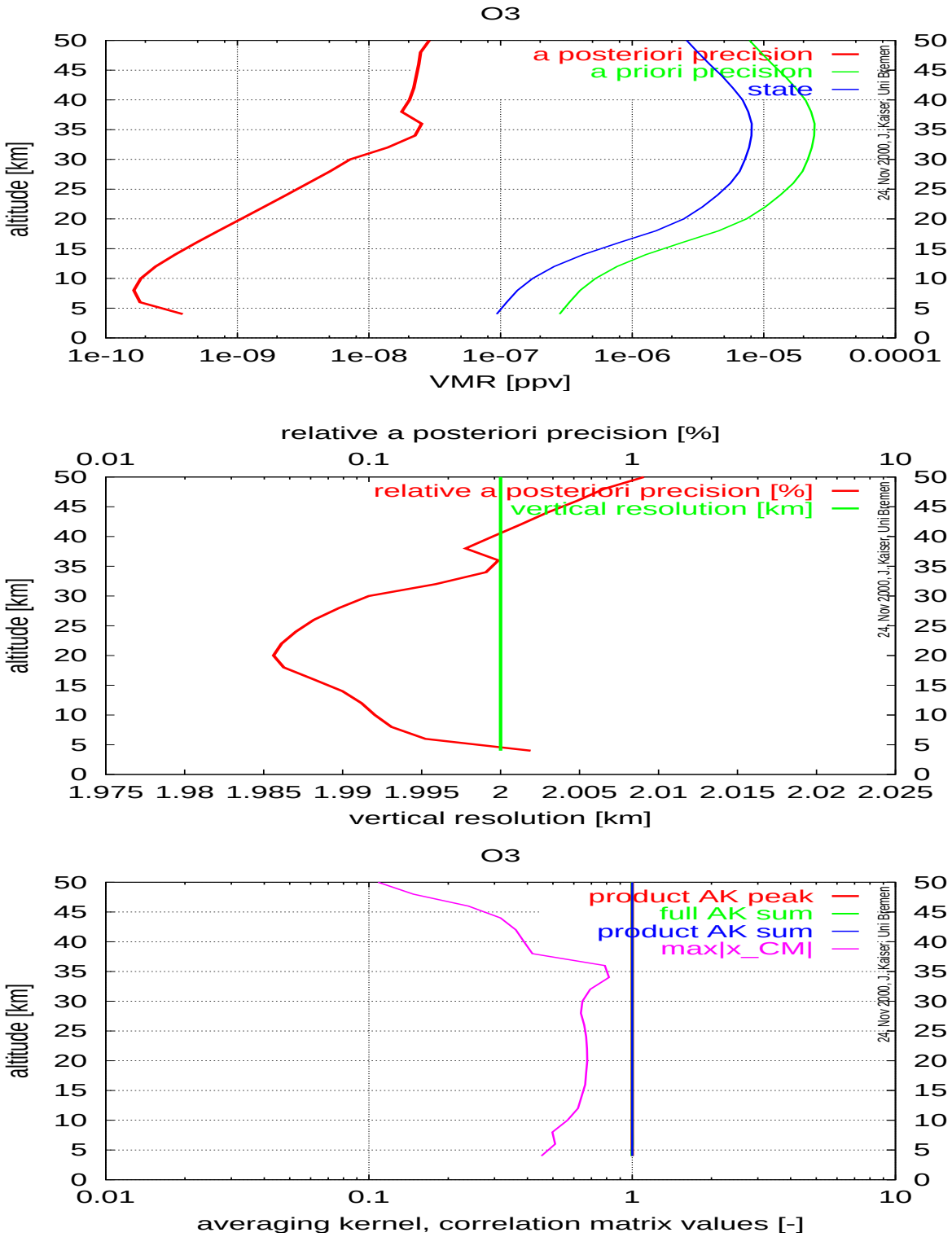

Figure 11.1: Theoretical precision results for O_3.

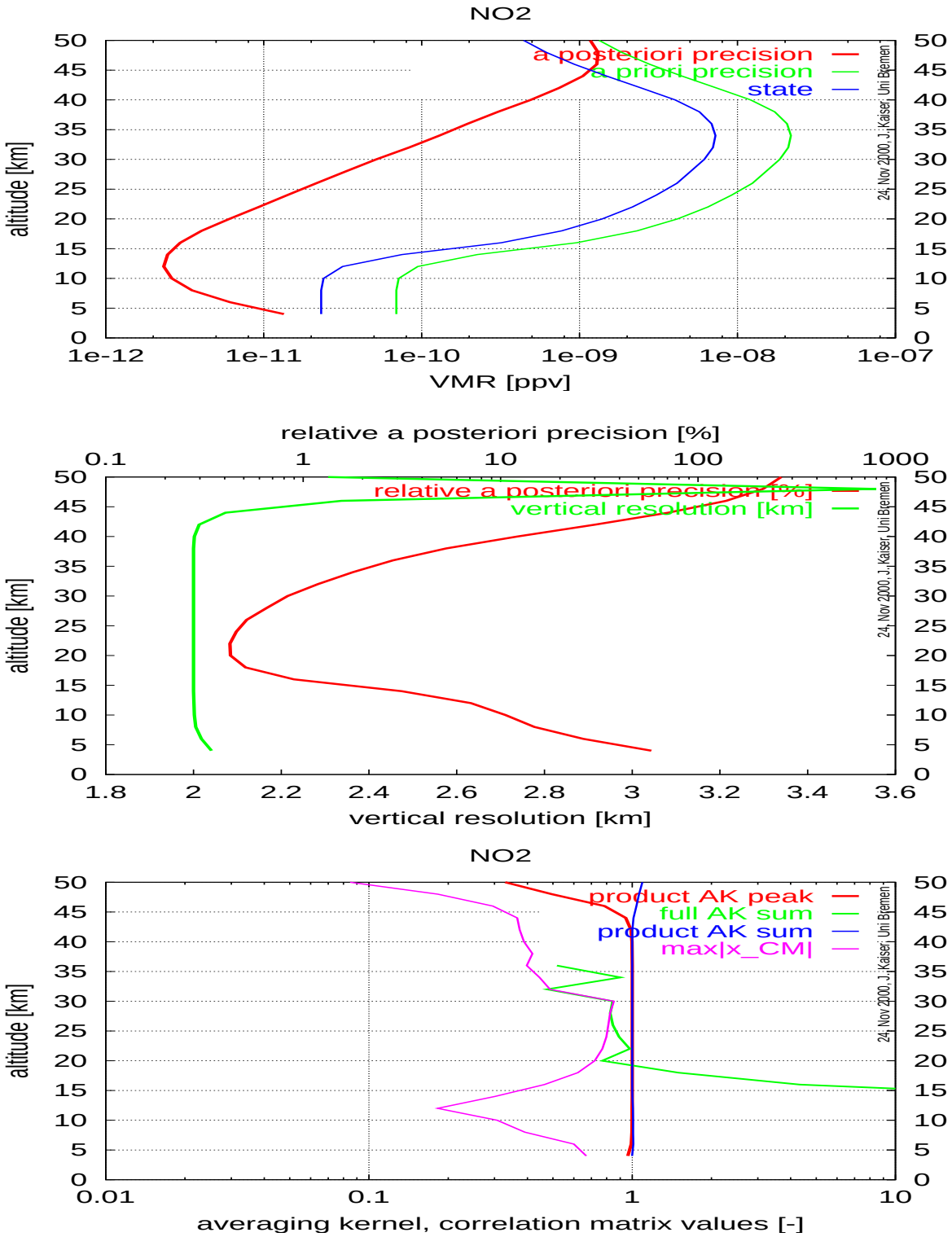

Figure 11.2: Theoretical precision results for NO_2.

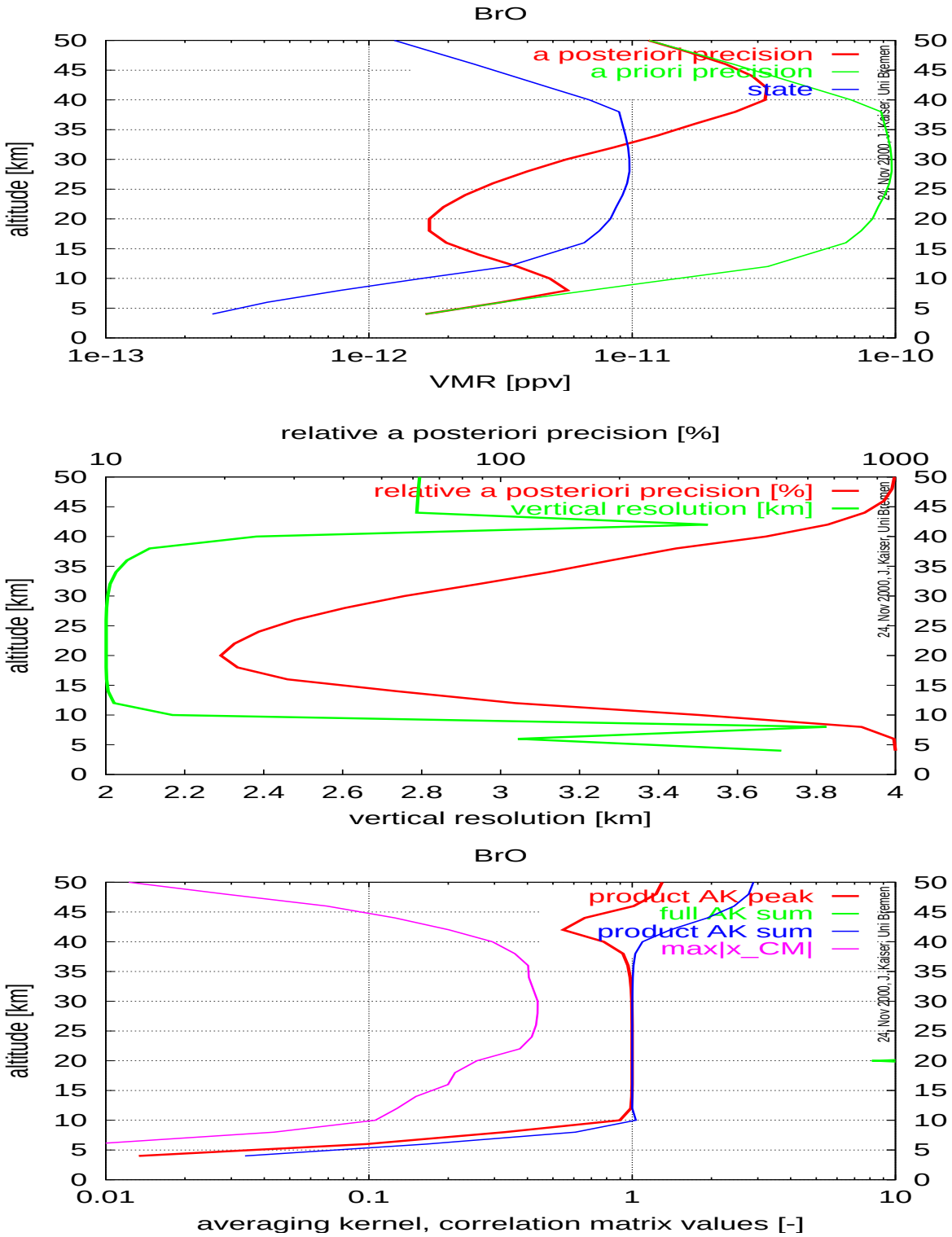

Figure 11.3: Theoretical precision results for BrO.

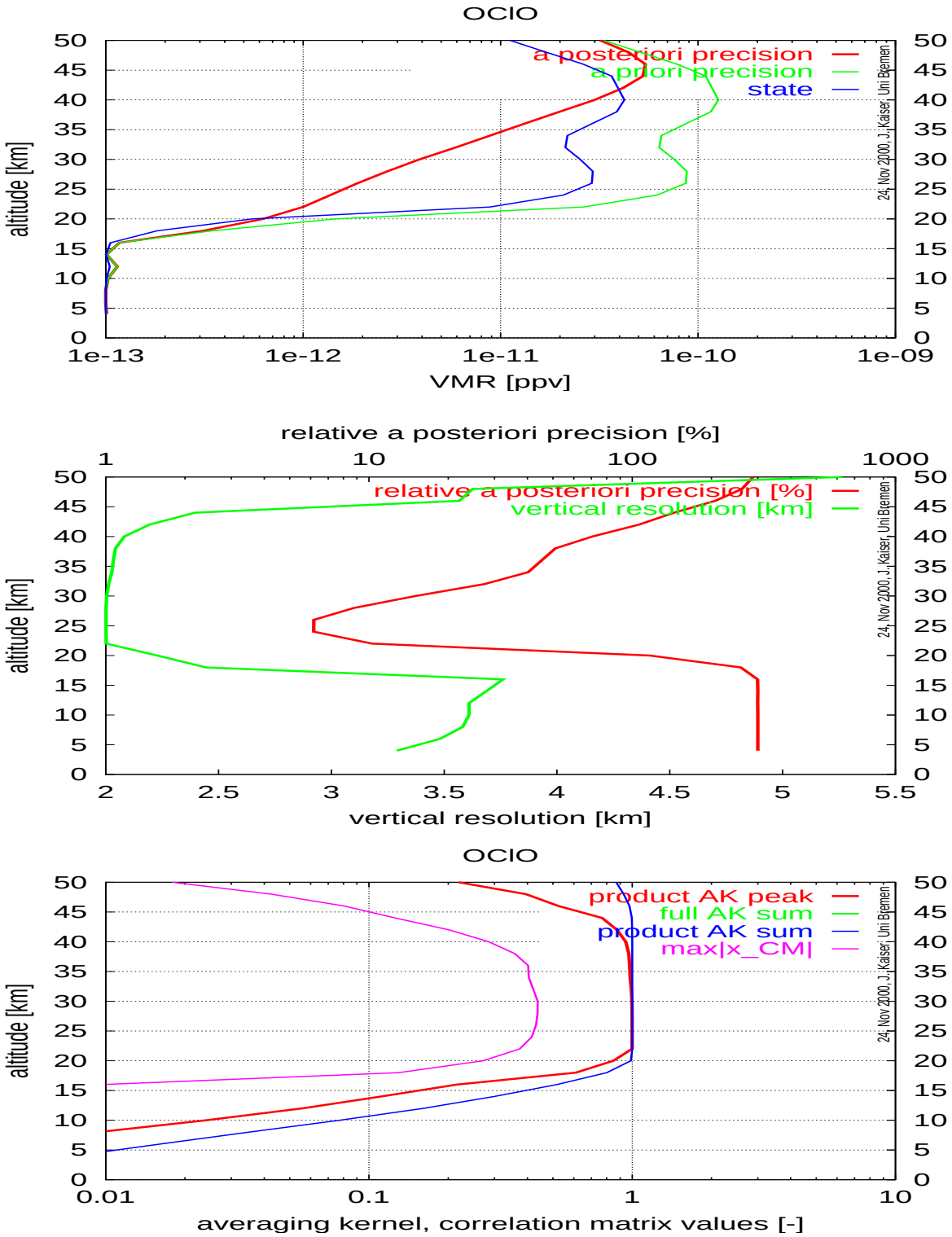

Figure 11.4: Theoretical precision results for OClO.

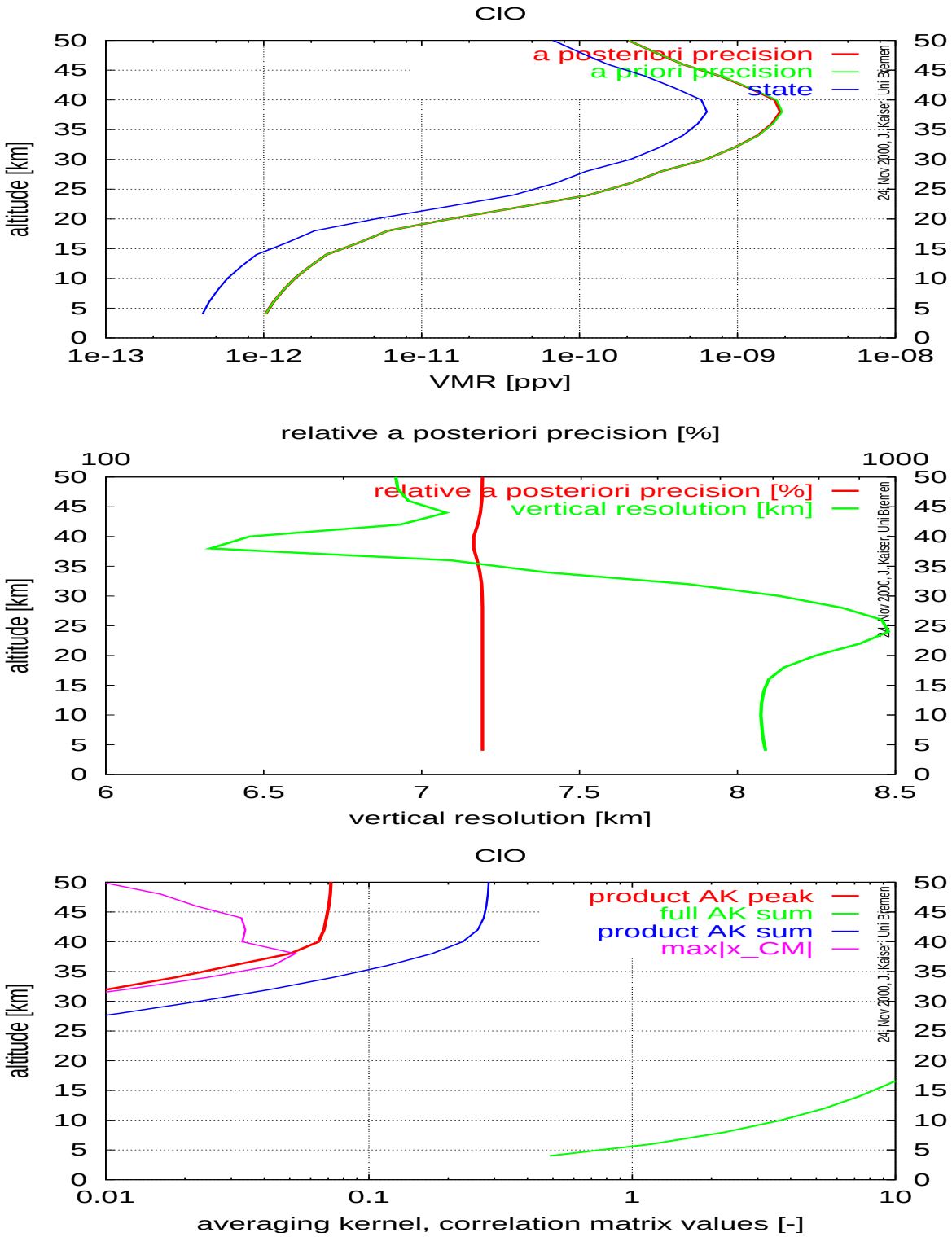

Figure 11.5: Theoretical precision results for ClO.

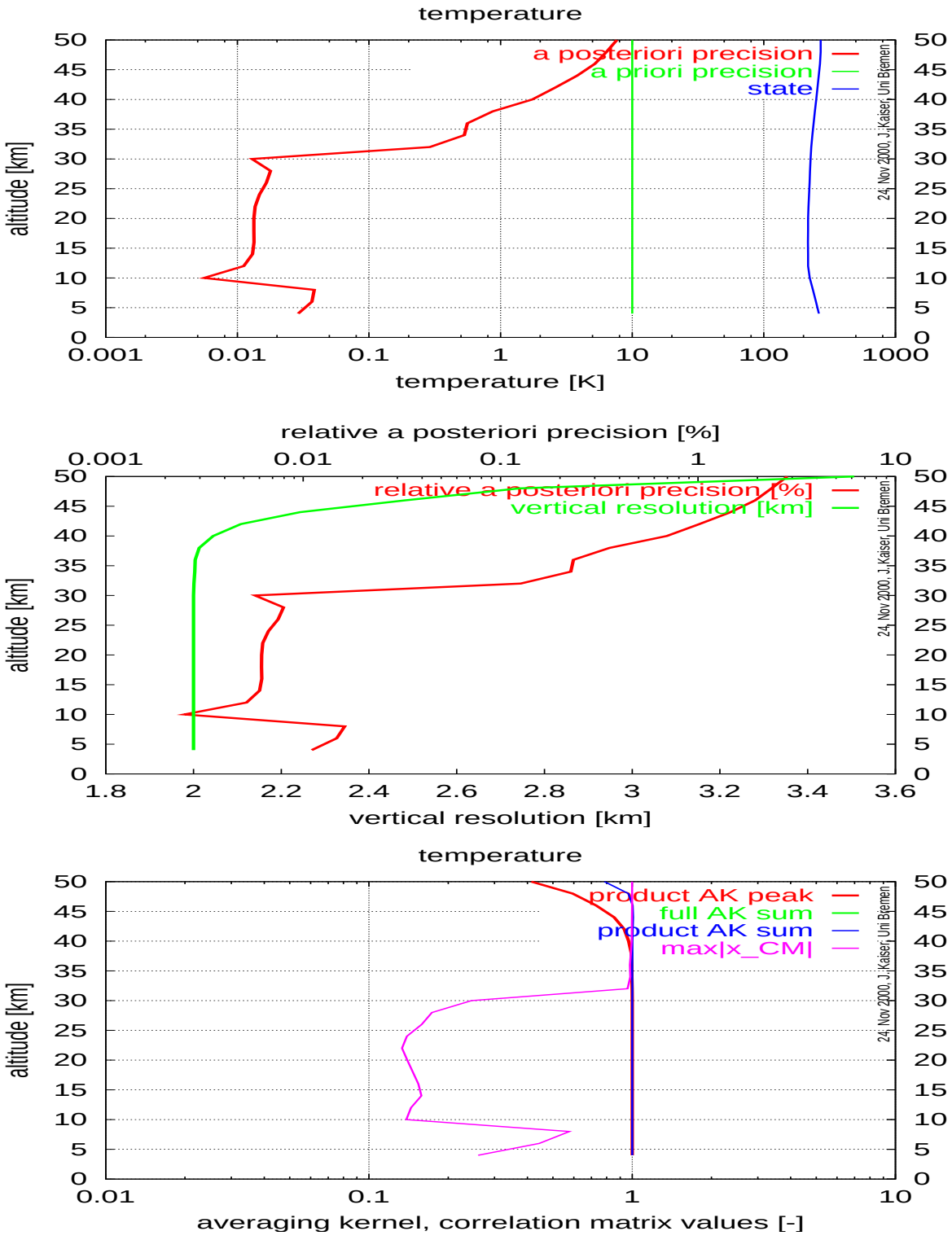

Figure 11.6: Theoretical precision results for temperature. Beware: These results are derived from UV-vis only, while SCIAMACHY's measurements will contain significantly more information in the NIR.

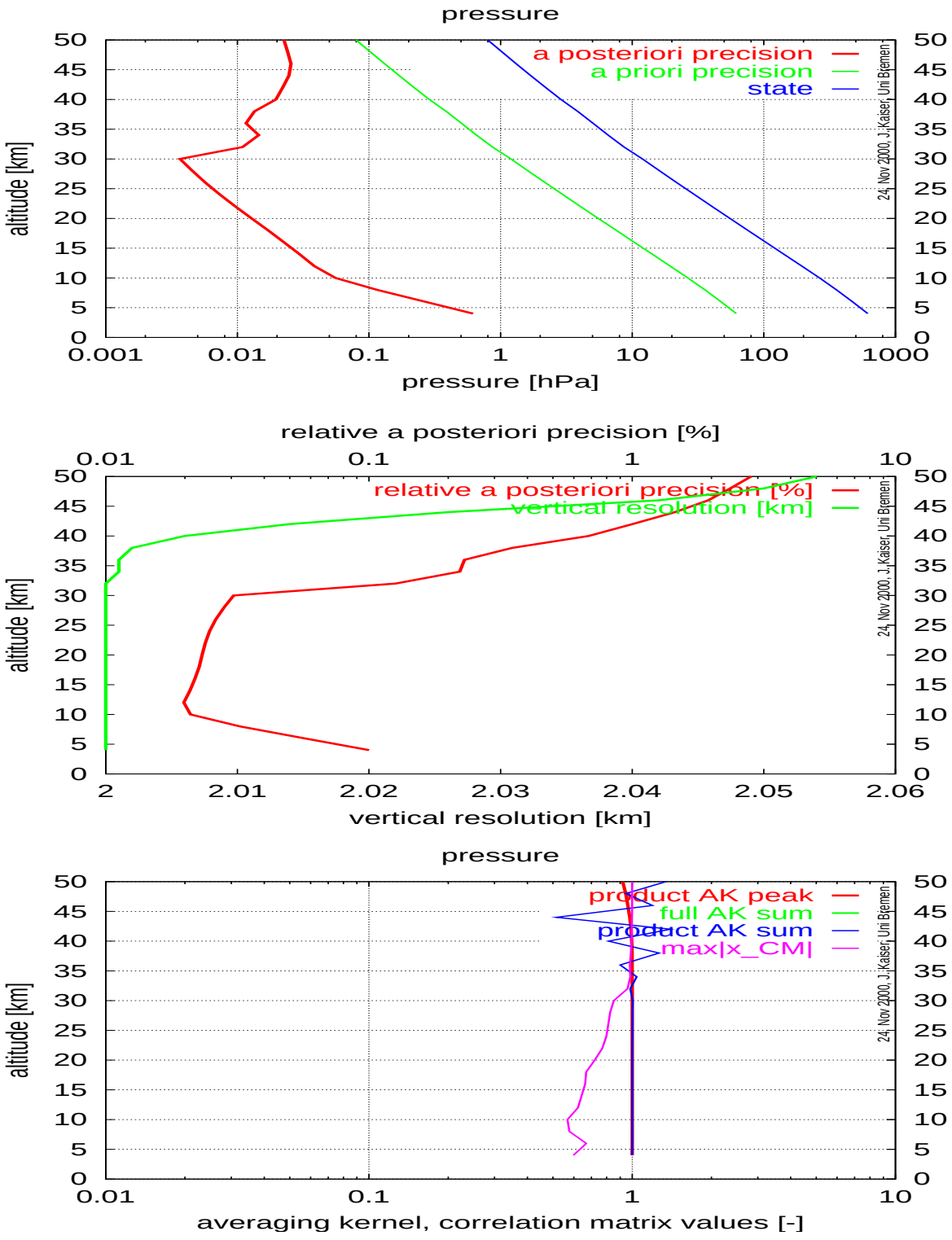

Figure 11.7: Theoretical precision results for pressure. Beware: These results are derived from UV-vis only, while SCIAMACHY's measurements will contain significantly more information in the NIR.

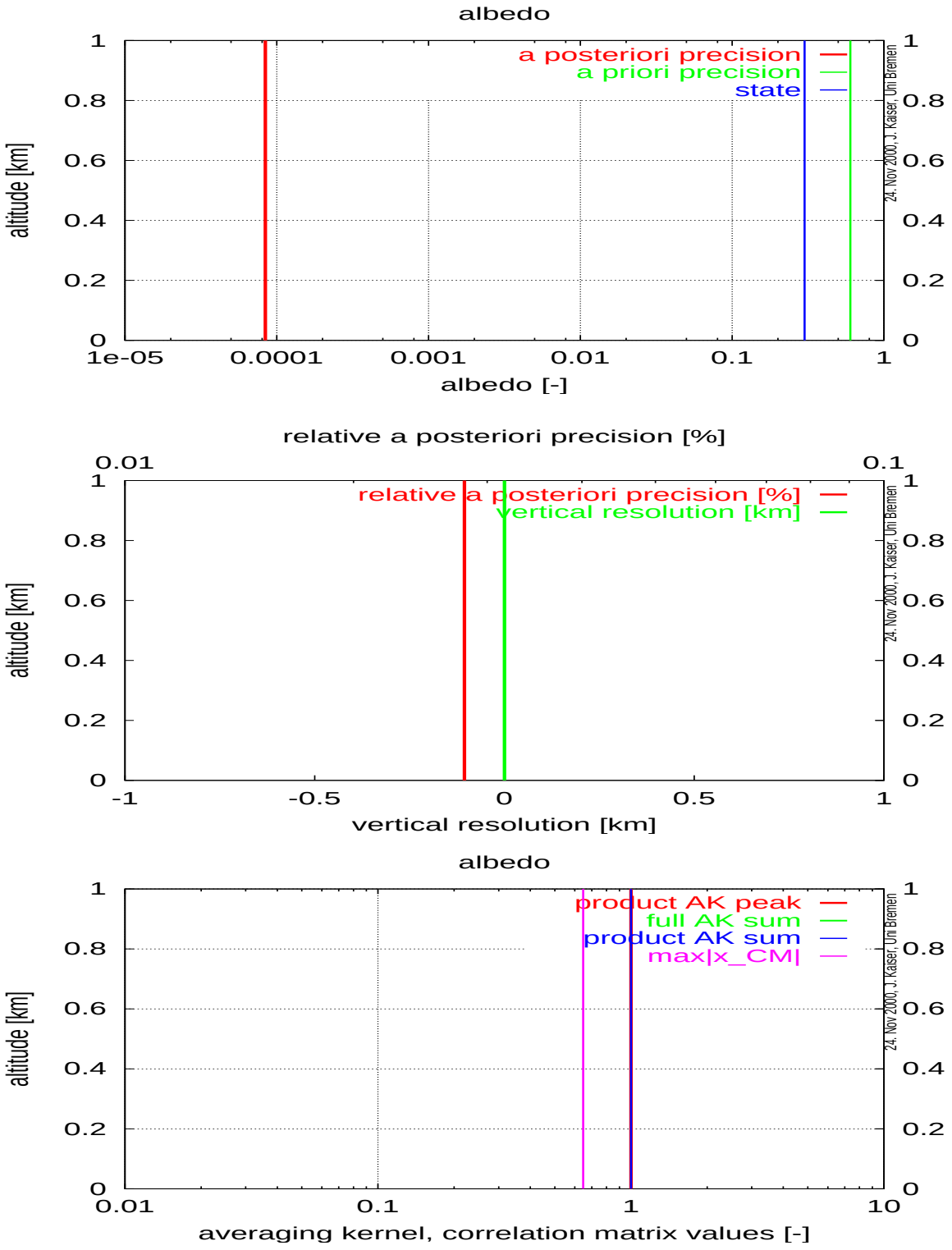

Figure 11.8: Theoretical precision results for albedo. This is a scalar parameter, which has been spread over the altitude only for plotting.

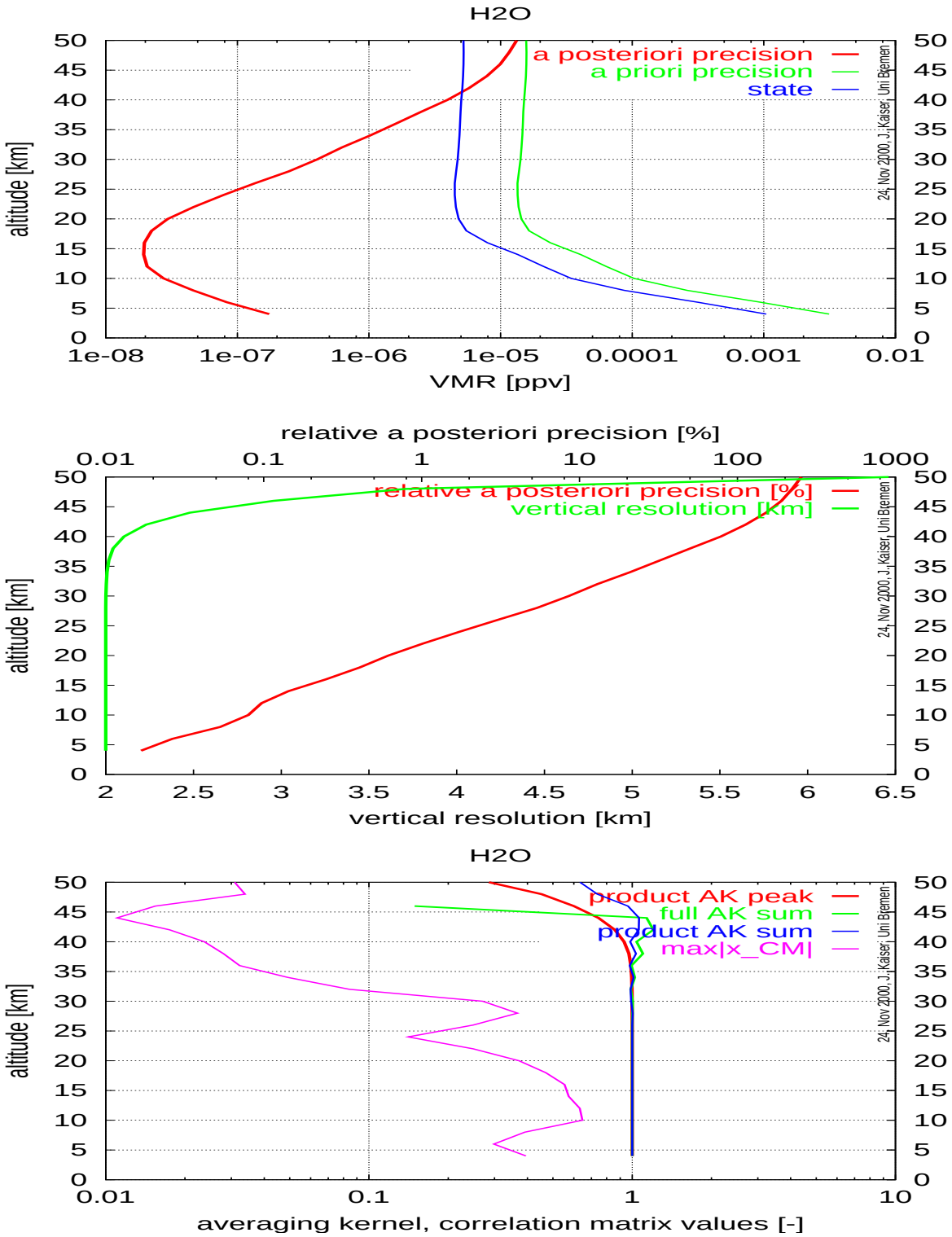

Figure 11.9: Theoretical precision results for H_2O.

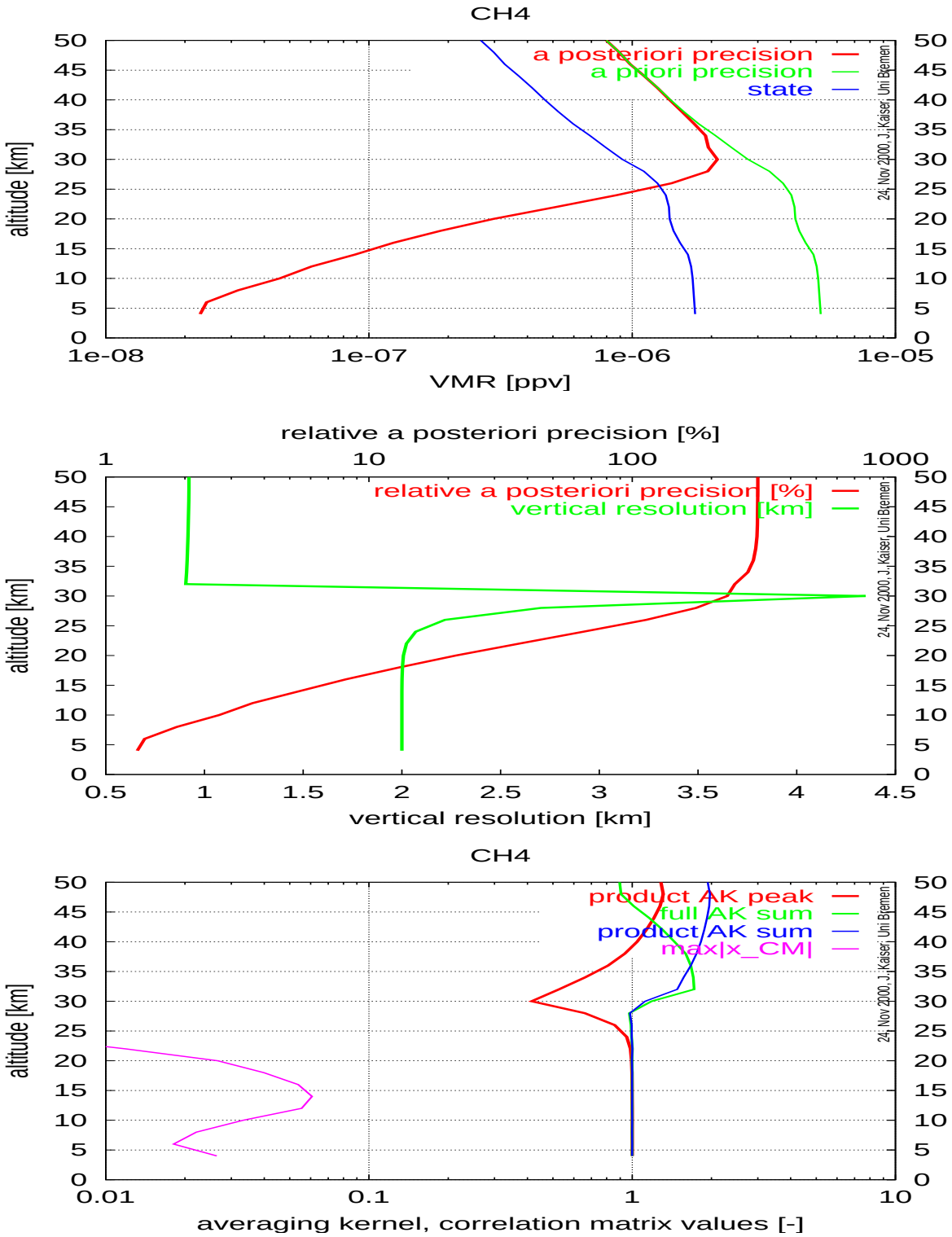

Figure 11.10: Theoretical precision results for CH_4.

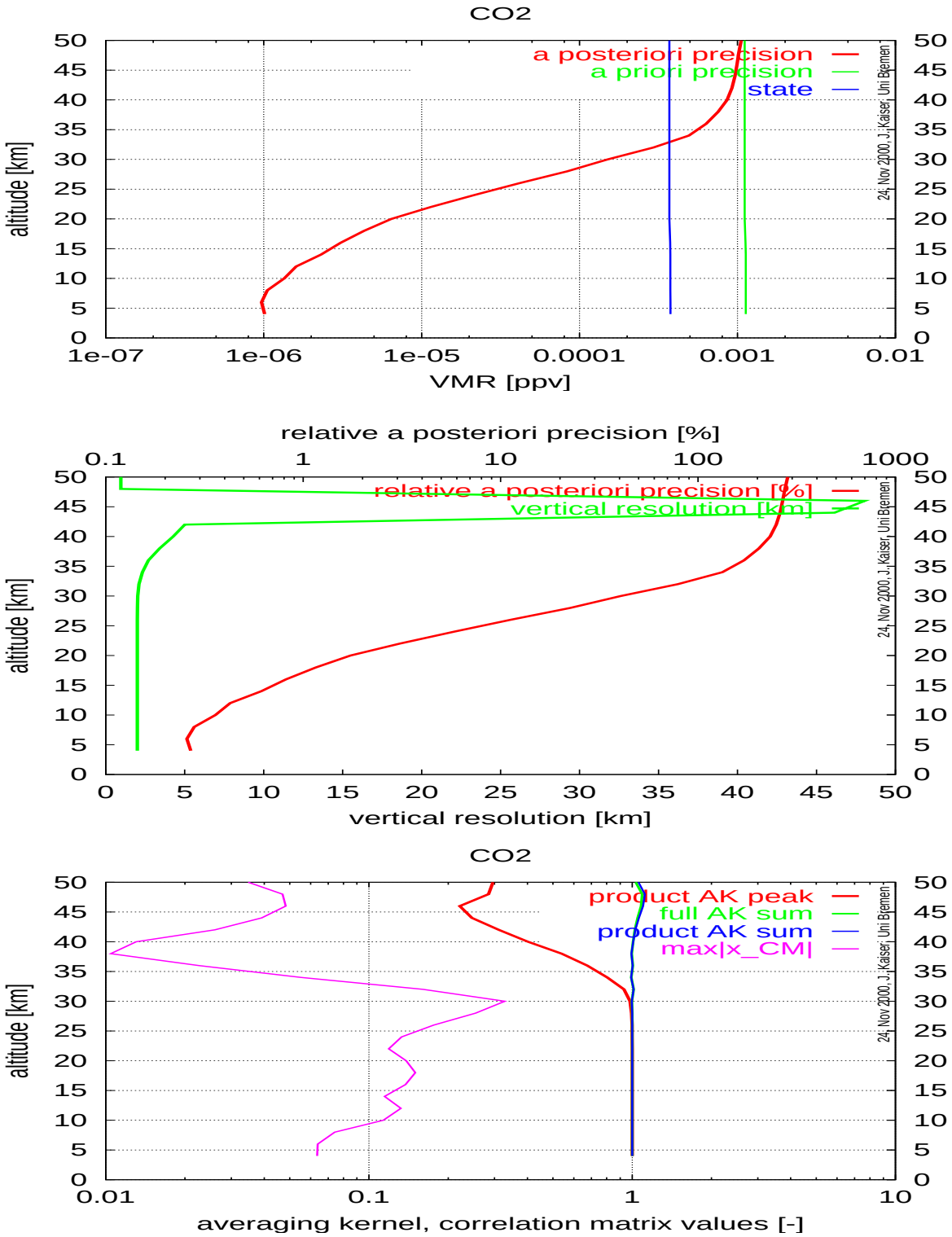

Figure 11.11: Theoretical precision results for CO_2.

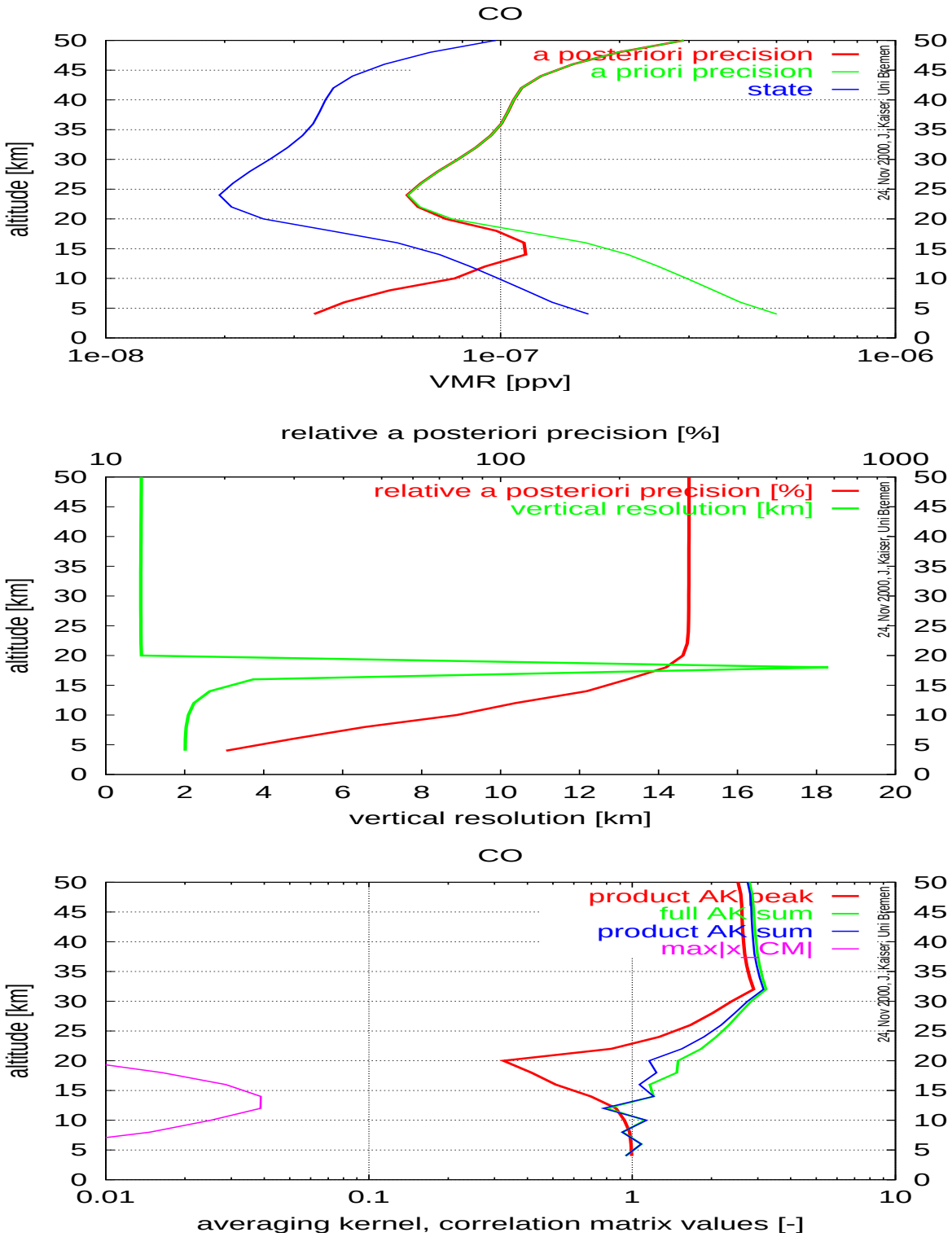

Figure 11.12: Theoretical precision results for CO.

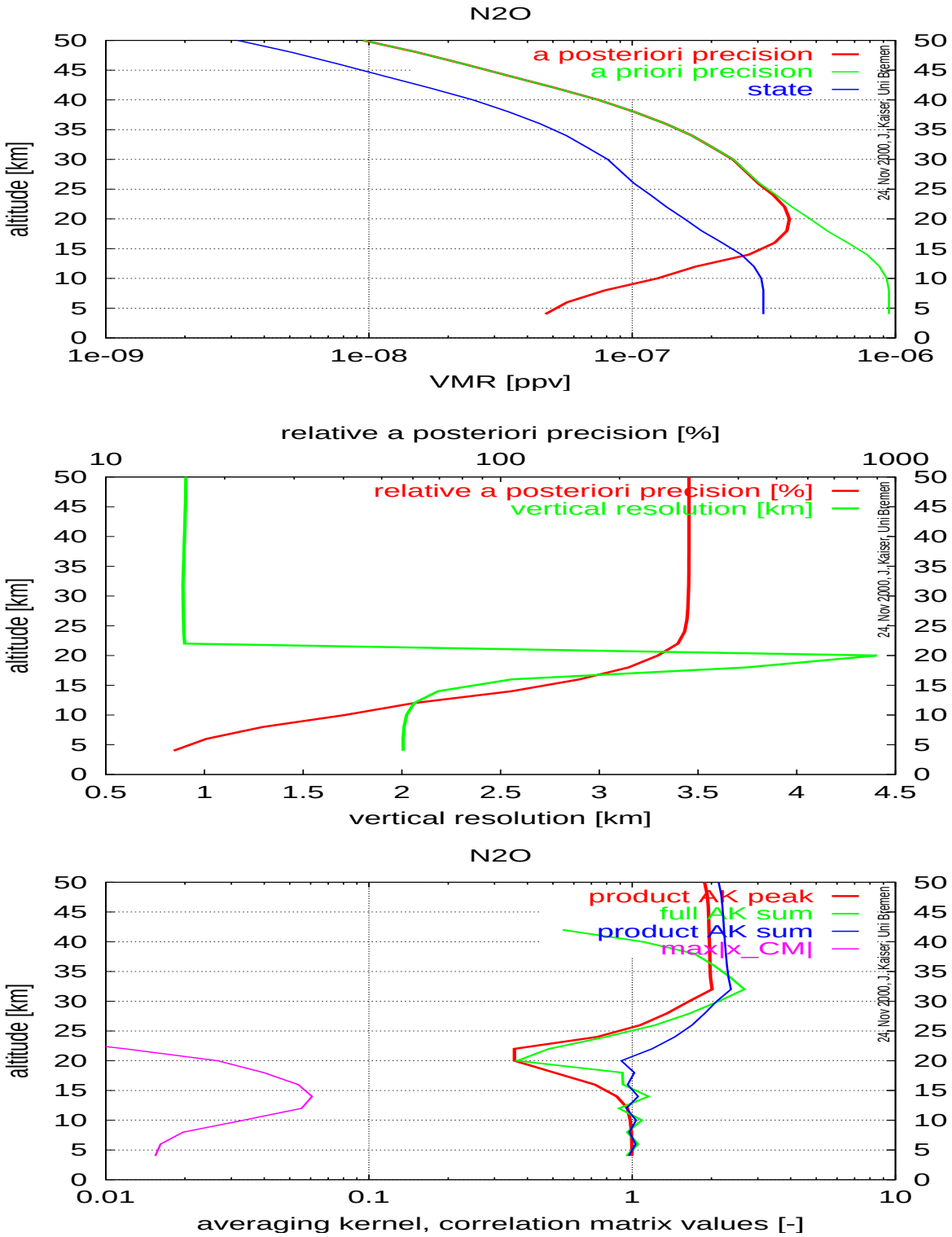

Figure 11.13: Theoretical precision results for N_2O.

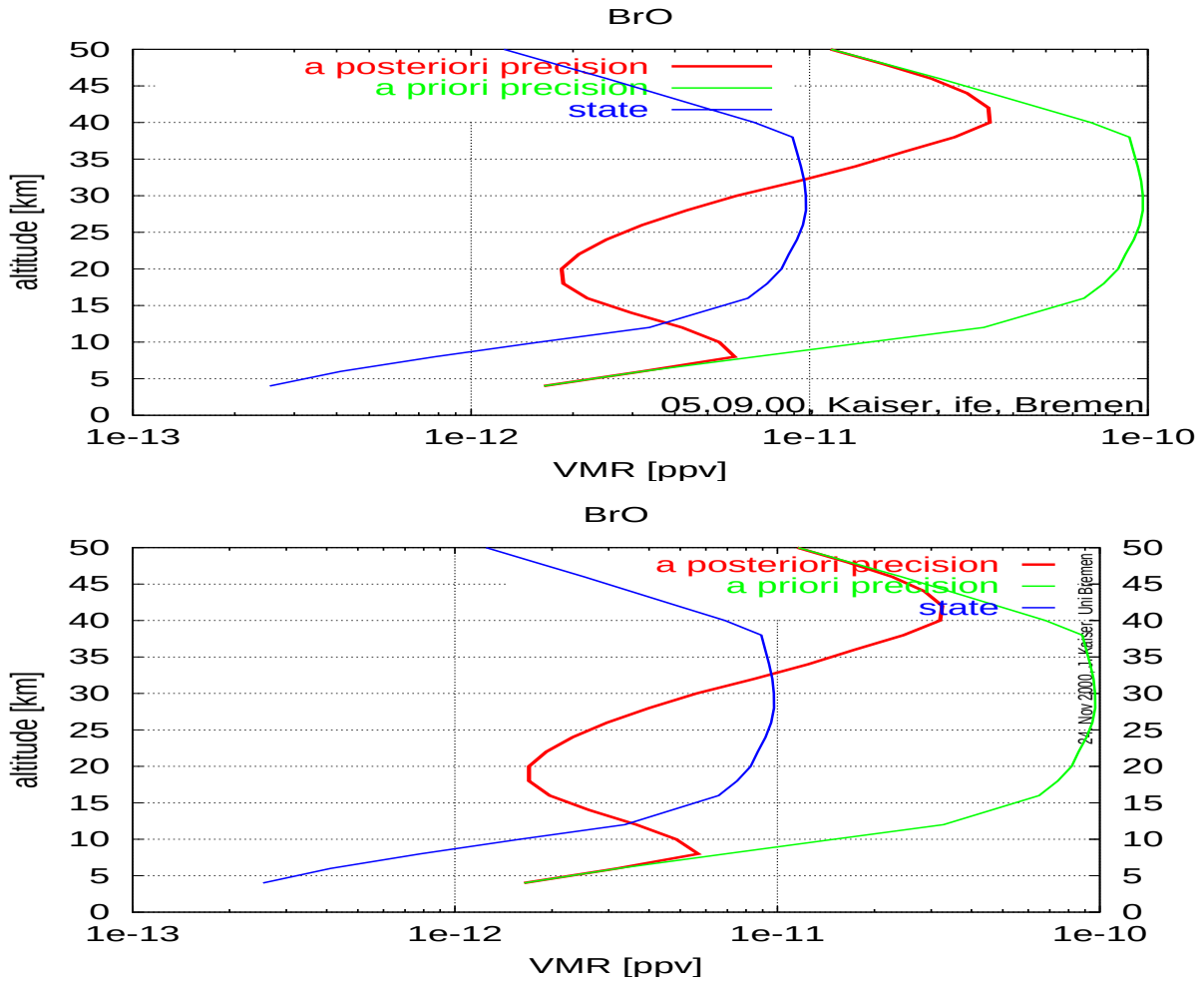

Figure 11.14: Theoretical precision results for BrO calculated with only one order of scattering and reflection (top) and with two orders of scattering and reflection (bottom).

11.5 Further Error Sources

11.5.1 Multiple Scattering

The results shown in Section 11.4 have been computed with *SCIARAYS* including two orders of scattering and one ray path modelling the reflection of the direct light on the ground followed by one scattering event. To assess the influence of full multiple scattering on the precisions, the calculations for parameter group "UV-vis" (see Table 11.1) are repeated without the second order of scattering. As an example, the resultant precision for BrO is plotted in Figure 11.14 along with the precision of Figure 11.3, which has been derived using two orders of scattering.

It becomes evident that higher orders of scattering have only a minor, i.e., hardly visible, influence on the theoretical retrieval precision. This effect can be explained by

the fact that the weighting functions from multiple scattering and single scattering calculations exhibit the same sharp step at the tangent altitude, see Figure 12.6 and Kaiser et al. [2001a]. The presented precisions can be regarded as conservative estimates as the weighting functions from multiple scattering calculations are about $20\,\%$ larger than the used ones.

This holds for the other retrieval parameters as well as for BrO.

For the sake of computational efficiency the second order of scattering will be neglected in the forthcoming discussions of the refraction and the retrieval algorithm (sections 11.5.2 and 11.5.3).

11.5.2 Refraction

The influence of refraction on the retrieval precisions is demonstrated for NO_2 retrieval from the wavelength range 300–$700\,\mathrm{nm}$ with a step size of $2\,\mathrm{nm}$. A scan sequence of 25 tangent altitudes from 2 to $50\,\mathrm{km}$ is used and the field of view integration is switched off.

The resultant precisions are plotted in Figure 11.15. They prove that the influence of refraction is limited to the lower stratosphere and the troposphere as expected from the density gradient in the atmosphere. Since the influence of refraction is in the range of (only) 10–20 % in the lower stratosphere and since it actually improves the calculated precisions, neglecting refraction in the main part of this study appears to be a safe, conservative approximation.

11.5.3 Retrieval Algorithm

The group of Jacek Stegman at the University of Stockholm (*MISU*) has also been calculating theoretical precisions for a UV-vis limb sensor within the framework of the ACE study. They assume a retrieval algorithm with two separate steps for the spectral and the spatial inversions. In the spectral inversion an additional polynom is fitted to the spectra. From theoretical considerations, this *differential approach* can be expected to yield larger precision values than the *absolute method* employed throughout this chapter.

In order to give an idea of the influence of the retrieval algorithm, precisions for NO_2 retrieval from the wavelength range 703–$742\,\mathrm{nm}$ ($0.2\,\mathrm{nm}$ steps) were calculated according to the *absolute method* described in Section 11.2. They are plotted as solid line in Figure 11.16. With the same weighting functions, the theoretical precisions of a retrieval algorithm which incorporates a *differential fit* to each tangent altitude's spectrum are calculated. The obtained precision profile is shown as dashed line in Figure 11.16.

The "differential" precisions are systematically and significantly worse than the "absolute" ones. This was to be expected from theoretical considerations. It shows that "differential" precisions characterise an instrument along with a "differential" retrieval algorithm. On the contrary, the "absolute" precisions, which are shown everywhere else in this chapter, characterise **only the instrument**: The better any particular retrieval

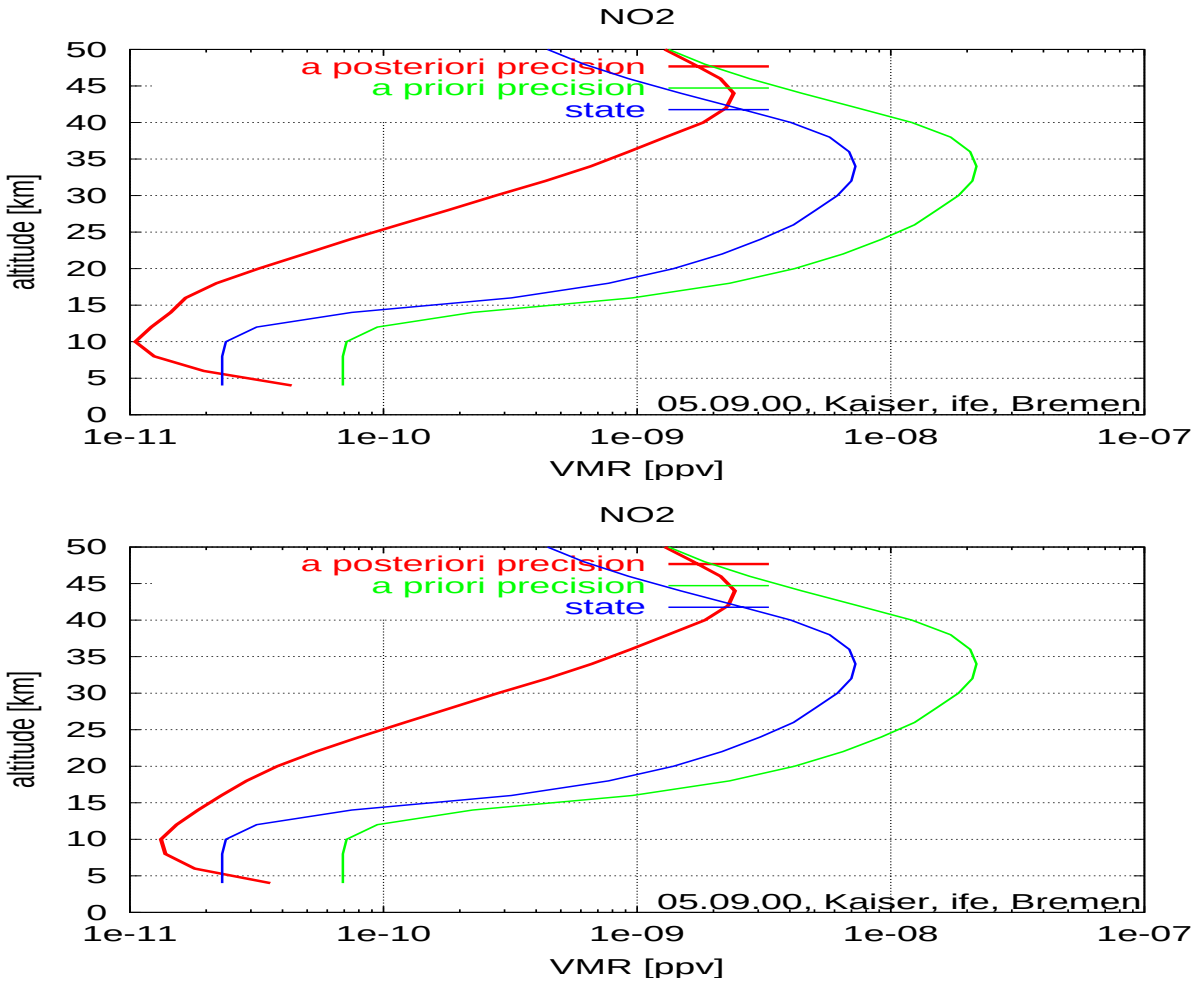

Figure 11.15: Theoretical precision results for NO_2 calculated for a simplified scenario with refractive (top) and with geometrical (bottom) ray tracing.

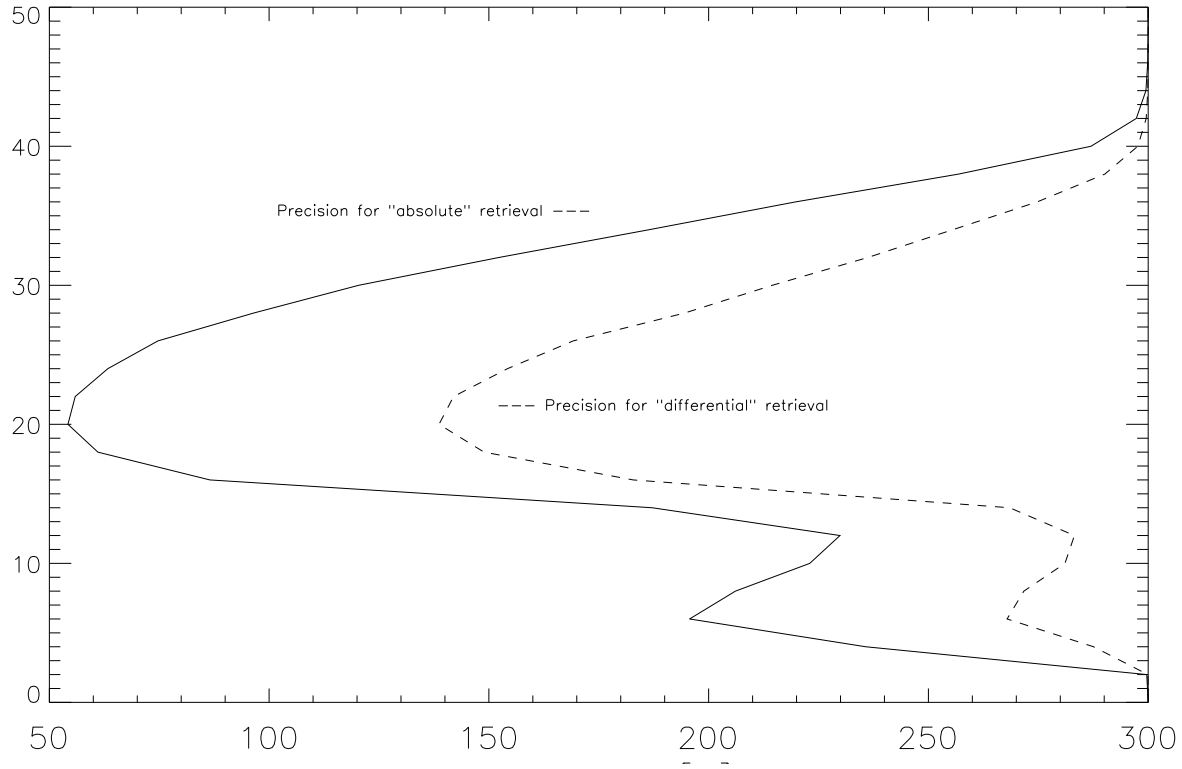

Figure 11.16: Theoretical precision results for NO_2 retrieved from 702–743 nm using a differential retrieval approach compared to the absolute approach used throughout this study. (graphics by V. Rozanov)

algorithm is the closer it will approach this limit, but no particular algorithm can be expected to fully reach it.

The magnitude of the improvement of an "absolute" method over a "differential" one is noteworthy. It stresses how much information can be gained by very carefully calibrating the instrument to make an "absolute" retrieval method applicable. In principle, SCIAMACHY is self-calibrating in that it regularly records solar irradiance spectra. However, this approch requires an extremely well characterised sun diffusor and a correct polarisation correction.

Stegman et al. have calculated NO_2 precisions for retrieval from the same wavelength range. A comparison of the "differential" precision of Figure 11.16 with their results reveals an excellent agreement: Their precision profile has its minimum of 150 % at 22 km. This consistency strongly supports the correctness of the results of both calculations.

11.5.4 Temperature–Pressure–Aerosols–Albedo–Pointing

Air density, aerosol and pointing profiles, and albedo all have a broadband influence on the measured UV-vis-NIR spectra. Thus they can be expected to exhibit relatively strong correlations in the retrieval. This holds even more for "differential" retrieval strategies.

Albedo

The albedo is assumed to be wavelength independent in this study. This is obviously unrealistic.

In view of the very good theoretical precision obtained from the UV-vis wavelength range (Figure 11.8) it can be expected that, say, six parameters for the wavelength dependence will be distinguishable with satisfactory precision of no more than one order of magnitude larger.

The correlations of the retrieved albedo with other retrieval parameters have proven to be negligibly small.

Temperature–Pressure–Density

Air density, pressure and temperature are linked by the ideal gas law. Thus, only two of these parameters are independent and once any two of them can be retrieved, the third one can determined, too.

The physical processes, which enable a retrieval of these parameters, are the following: Rayleigh scattering is proportional to the air density. Absorption cross sections are (relatively weakly) temperature dependent in the UV-vis region and (relatively strongly) temperature and pressure dependent in the NIR region. Since *SCIARAYS* currently does not model the pressure dependence of absorption cross sections, the temperature profile is essentially retrieved from the temperature dependence of the cross

sections; the pressure from Rayleigh scattering[6].

The temperature and pressure precisions presented in Section 11.4 (Figures 11.6, 11.7) are derived only from the wavelength region 240–$800\,\mathrm{nm}$ in order to minimise the influence of the approximation in the radiative transfer in the NIR region.

To demonstrate the temperature retrieval capabilities from O_3 and NO_2 cross sections alone, the precision calculations for parameter group "UV-vis" (see Table 11.1) were repeated for the wavelength range 240–$550\,\mathrm{nm}$ without the regions of O_2 and H_2O absorption. The resultant theoretical precisions are shown in Figure 11.17. Temperature and pressure are now harder to distinguish than with H_2O included (compare to Figures 11.6, 11.7). The O_3 precision is also affected (compare to Figure 11.1). Thus the results of Section 11.4 have to be interpreted as a rather qualitative demonstration of the temperature retrieval potential of the NIR region. However, Figure 11.17 exhibits a substantial potential for stratospheric temperature retrieval from the UV-vis region, too.

Aerosols

Aerosol parameter profiles would be retrieved mainly from aerosol scattering. The task would be to separate the wavelength dependence of aerosol scattering ($\propto \lambda^{\alpha}$, $\alpha \approx -1$) from the one of Rayleigh scattering ($\propto \lambda^{-4}$). Therefore, correlations with aerosol retrieval will mostly affect the pressure precisions, but not so much the temperature precisions. This is caused by the fact that the latter can be derived to a larger extent from the cross section's temperature dependences (see above).

Aerosol scattering coefficient profile theoretical precision estimations from single wavelengths of SCIAMACHY limb measurements lead to very satisfactory values of about 1 %. Even though correlations have not been included in these estimates, it is anticipated that aerosol and Rayleigh scattering are easily distinguished in a retrieval from a large wavelength range within the UV-vis-NIR.

The precisions of the trace gas retrievals will not be affected by simultaneous aerosol retrieval for two reasons:

- The correlations with broadband structures is already included by the simultaneous pressure retrieval. Thus the uncertainty of the broadband scattering coefficient profile is accounted for. This uncertainty is not affected by the question of whether it arises from Rayleigh scattering, described by pressure, or from aerosol scattering.

- The weighting functions of trace gases absorption are always negative, while those connected to scattering processes, i.e., pressure, temperature and aerosols, change their sign depending on the tangent height, see Figure 6.7. Since the problem

[6] A diffential retrieval algorithm would rely on the temperature and pressure dependence of the O_2 A-band and CO_2 lines while the VMRs of O_2 and CO_2 would be assumed to be known, i.e., constant. In the lower atmosphere, additional information is contained in the O_4 bands.

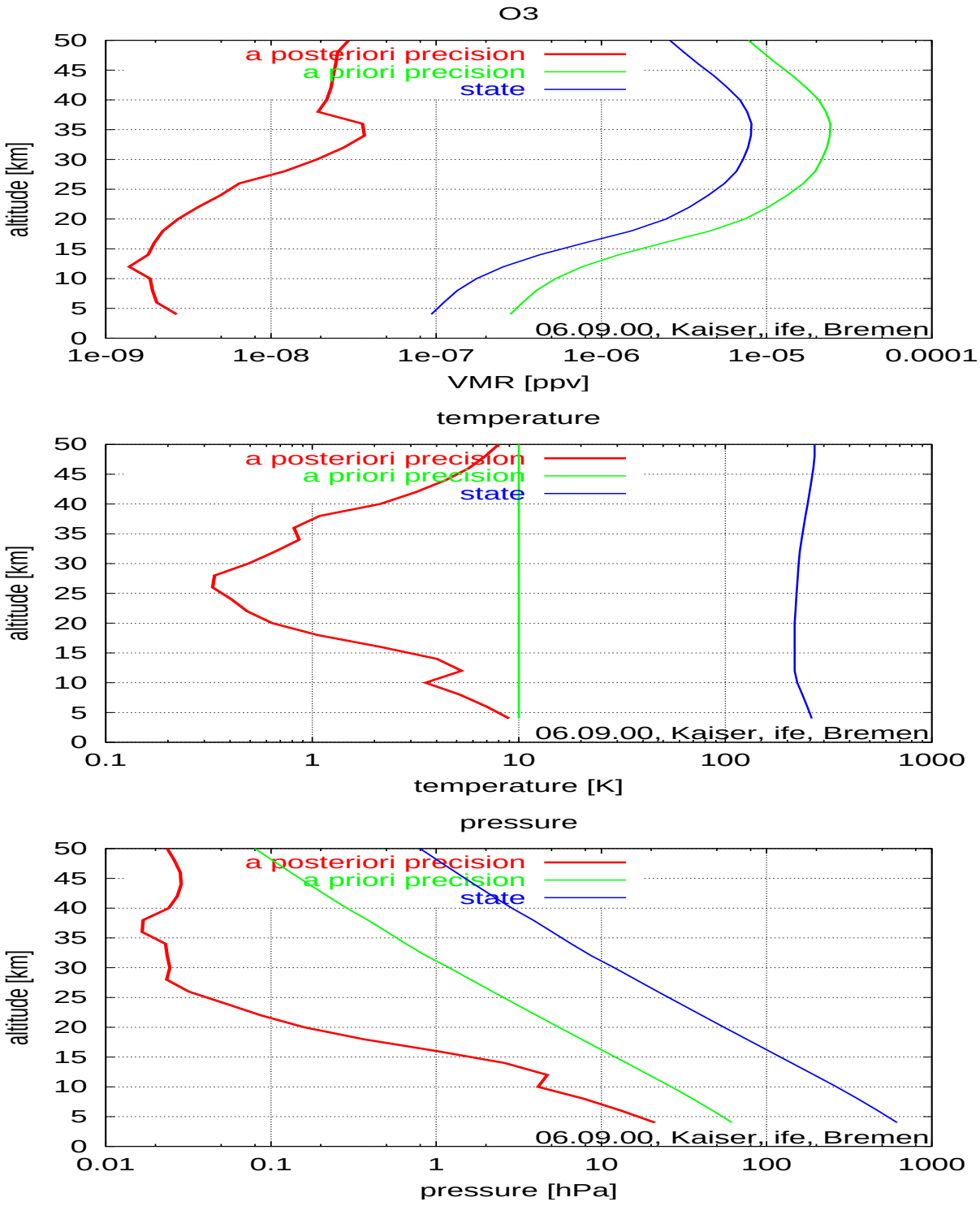

Figure 11.17: O_3, temperature and pressure profile precisions derived in the 240–550 nm range neglecting H_2O absorption.

of distinguishing these two types of weighting functions is well-posed, retrieval parameters describing absorption generally have only minor correlations to parameters describing scattering processes.

Pointing

Once two out of the three parameters temperature, pressure and density can be retrieved independently, information on the pointing of the instrument will also be available via the hydrostatic equilibrium a priori assumption and one *a priori* value of pressure at ground level.

Such a pointing retrieval will be performed with SCIAMACHY's measurements. An assessment of the process is ongoing work.

11.5.5 Horizontal Inhomogeneities

The influence of horizontal gradients in the atmosphere on the precisions of a profile retrieval is not investigated. It is not anticipated to retrieve them from a single limb measurement sequence and the retrieved profiles must be interpreted as average or effective values.

In the future, additional observations like SCIAMACHY's matching nadir measurements will be used along with limb measurements for simultaneous retrievals of vertically and horizontally resolved parameter fields.

11.5.6 Spectral Uncertainties

The UV-vis absorption cross sections have been measured with a typical accuracy of several percent. Since the differential structure of the cross sections is more accurately known, a lower limit of $1\,\%$ for all retrieval parameters is assumed. This may turn out to be the limiting factor in some cases.

11.5.7 Clouds

Statistics from SAGE II measurements show that about 50 % of the scans reach down to $5\,\mathrm{km}$ altitude without cloud interference. Since SCIAMACHY has a horizontally wider field of view ($240\,\mathrm{km}$ compared to $5\,\mathrm{km}$ at the tangent point of SAGE II), a significantly smaller fraction of the scans will be cloud-free. Therefore, most of the retrieval height ranges will be limited by the cloud top height[7] of optically thick clouds.

The vertical structure of optically thin clouds may be retrieved as an aerosols profile. Such clouds do not limit the retrieval height range.

[7] Future advanced algorithms may overcome this limitation by modelling the radiative transfer in the clouds. Owing to the long paths inside the clouds, this may even enhance the retrieval precisions in the troposphere.

A strong influence on the retrieval precisions above the cloud top is not anticipated in analogy to the easily distinguished albedo effect (see above). Also, Oikarinen et al. [1999] have shown that the horizontal inhomogeneities of the albedo of $100\,\mathrm{km}$ extent can safely be neglected in the radiance calculations. Similarly, clouds below the tangent points should not affect the retrieval precisions severely.

11.5.8 Forward Model IR Approximation

SCIARAYS currently solves the radiative transfer equation exactly once for each measured spectral point, i.e., it does not perform any line-by-line or correlated-k calculation. To compensate for this, the absorption cross sections in the NIR are convolved with a slit function of SCIAMACHY's spectral resolution. Because of the non-linearity of the radiative transfer and because the cross sections in the NIR vary on a finer scale than the spectral resolution, this is a severe approximation. Therefore, radiance calculations need to employ the line-by-line or the correlated-k method.

This topic arises in SCIAMACHY's channels 4–6, i.e., below $1750\,\mathrm{nm}$ wavelength, where ro-vibrational structures of H_2O, CH_4 and O_2 are not resolved. However, as H_2O absorption lines are very abundant in SCIAMACHY's spectral range, large numbers of sensitive pixels for every measurement scenario and tangent altitude exist. Therefore, the theoretical precisions of H_2O are considered trustworthy.

In the channels 7 and 8, i.e., above 1940 nm wavelength, SCIAMACHY has a spectral resolution which resolves the tropospheric[8] absorption lines of CH_4, CO_2, CO and N_2O with typically 2–4 spectral points. Therefore, the problem of the IR approximation does not arise in a theoretical study and the presented precision results for these gases can be trusted in the UT/LS region, too.

If, for any trace gas, there is only a small number of absorption lines in one measurement pixel, the convolved cross section is much smaller than the cross section in any of the individual lines. If the radiative transfer is in saturation for these lines, then the pixel is insensitive to the concentration of this trace gas. Nevertheless, the radiative transfer using the convolved cross section may calculate significant weighting functions, thereby deriving good retrieval precisions. This way, the retrieval precisions may theoretically be underestimated due to the approximation. However, test calculations for small optical windows have shown that the effect is small and that the precisions are in good agreement with those obtained by line-by-line calculations.

11.6 Conclusions

Theoretical precisions have been calculated for profile retrievals on a $2\,\mathrm{km}$ grid from a limb UV-vis-NIR sensor of SCIAMACHY type which is measuring according to the common ACE scenario. The calculations include error contributions from signal/noise,

[8] Absorption lines in the stratosphere more narrow due to less pressure broadening.

spatial and spectral resolution of the instrument and all correlations between retrieval parameters. A good (as compared to the signal/noise values) calibration of the instrument is assumed.

Even though many of the calculated precision values lie below 1 %, the influence of further sources of errors, e.g., spectroscopic uncertainties, will prevent real retrievals to become more precise than 1 %. Therefore, the theoretical precisions summarised in Table 11.2 can be anticipated.

Table 11.2: Anticipated Theoretical Precisions. (Pressure is used as dummy for all broadband effects.)

	UT (5–12 km)	LS (12–24 km)	MS (24–36 km)	US (36–45 km)
O_3	1 %	1 %	1 %	1 %
NO_2	40–10 %	10–1 %	1–10 %	10–100 %
BrO	—	100–25 %	$\leq$30 %	—
OClO	—	—	10–50 %	—
ClO	—	—	—	—
H_2O	1 %	1–2 %	2–20 %	20–200 %
CH_4	5 %	5–100 %	—	—
CO_2	1 %	1–10 %	10–100 %	—
CO	30–100 %	—	—	—
N_2O	25–100 %	—	—	—
temperature	1 K	1 K	1 K	—
pressure/density	1 %	1 %	1–10 %	10–40 %

It should be kept in mind that relative trace gas precisions, i.e., [%], strongly depend on the parameter profiles. On the other hand, precisions given in units of trace gas density or volume mixing ratio, e.g., [ppv], are less dependent on the profiles. Therefore, ClO may well be identified during episodes of strong chlorine activation [Kaiser et al., 2001b].

A comparison of the presented results with those of Jacek Stegman and Philippe Baron of the University of Stockholm shows excellent agreement. This suggests that grave approximations and errors have been avoided in both calculations.

Thus it can be concluded that a UV-vis-NIR limb sensor like SCIAMACHY will provide detailed, vertically resolved information for studies of the stratosphere as well as the region of the upper troposphere and lower stratosphere.

The theoretical precisions presented in this chapter are published in Kaiser et al. [2001c], additional precisions for a high latitude scenario can be found in Kaiser et al. [2001b].

Chapter 12

Comparison to Multiple Scattering

For the retrieval of stratospheric and upper tropospheric parameter profiles from limb measurements a radiative transfer model (RTM) is needed which fully takes into account the atmosphere's sphericity and also computes weighting functions analytically, i.e., accurately and with relatively little additional computational effort (see Section 3.5).

Two fully spherical radiative models were developed at the University of Bremen as extensions to the radiative RTM GOMETRAN: *SCIARAYS* and CDIPI. The former is fast and approximative, while the latter is relatively slow and accurate.

In this chapter, calculations of the two RTMs are compared and the possibility of approximating the weighting functions is tested.

12.1 Model Assumptions

The fundamental differences of the two RTMs are summarised in Table 12.1.

SCIARAYS is the model which has been developed for this thesis. It is an approximative RTM in that it models only the three most important ray paths through the atmosphere: the first and second order of scattering (*single* and *double scattering*) and reflection of the direct solar light at the ground followed by direct scattering into the line of sight (*reflection-then-scattering*). Thereby the radiance is systematically underestimated. Its main advantage is that it computes the weighting functions for all atmospheric model parameters analytically along with the atmospheric radiances. Since it is fast, it is a candidate for use in a non-linear retrieval procedure with many calls to the forward model.

CDIPI is a fully spherical RTM which computes the multiply scattered radiance field iteratively. Weighting functions are calculated by numerical perturbation of 0.1 %. The model is used as reference in the comparison of this chapter. For a description of the general approaches of CDIPI refer to Section 5.3.

To prevent distraction by features of solar irradiance sun-normalised radiances are shown.

Table 12.1: Radiative Transfer Models for Approximation Comparisons

CDIPI	
geometry	fully spherical
ray paths	full multiple scattering (*MS*)
weighting fcts.	numerical perturbation

SCIARAYS	
geometry	fully spherical
ray paths	single scattering (*S*) double scattering (*SS*) reflection-then-scattering (*RS*)
weighting fcts.	analytically

Table 12.2: Atmospheric Model for Approximation Comparisons

absorption	O_3, NO_2
scattering	Rayleigh, aerosols
stratospheric aerosols	background
tropospheric aerosols	23 km visibility
other profiles	US std. atm. 1976
albedo	0.3, Lambertian refl.

Throughout this study, a horizontally homogeneous, cloud free, spherical atmosphere is assumed. Its physical properties are listed in Table 12.2.

12.2 Model Comparisons

12.2.1 Dependence on Wavelength

Synthetic limb spectra have been calculated with both radiative transfer models: Figure 12.1 shows examples of sun-normalised radiance computed with CDIPI (multiple scattering: MS) and *SCIARAYS* (*S+RS+SS*) for 18 km tangent altitude. The individual contributions of ray paths are also given: single scattering (S), double scattering (SS) and reflection-then-scattering (RS).

The absorption of the Hartley-Huggins and Chappuis bands can be seen clearly. Between these bands, the wavelength dependence of Rayleigh scattering leads to larger values for smaller wavelengths.

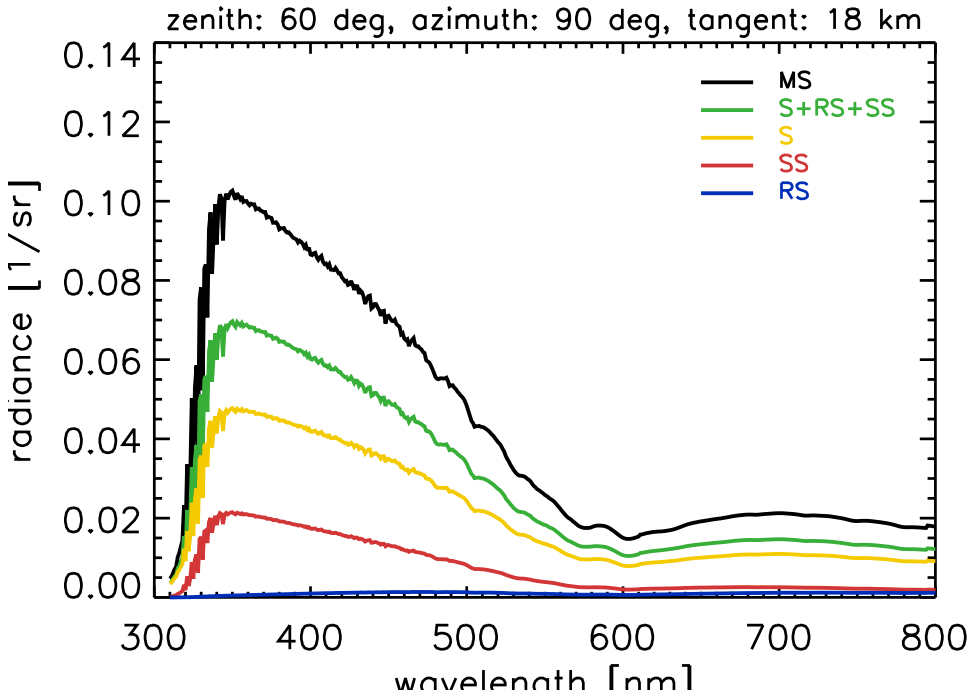

Figure 12.1: Sun-normalised limb radiance spectra computed with several ray paths.

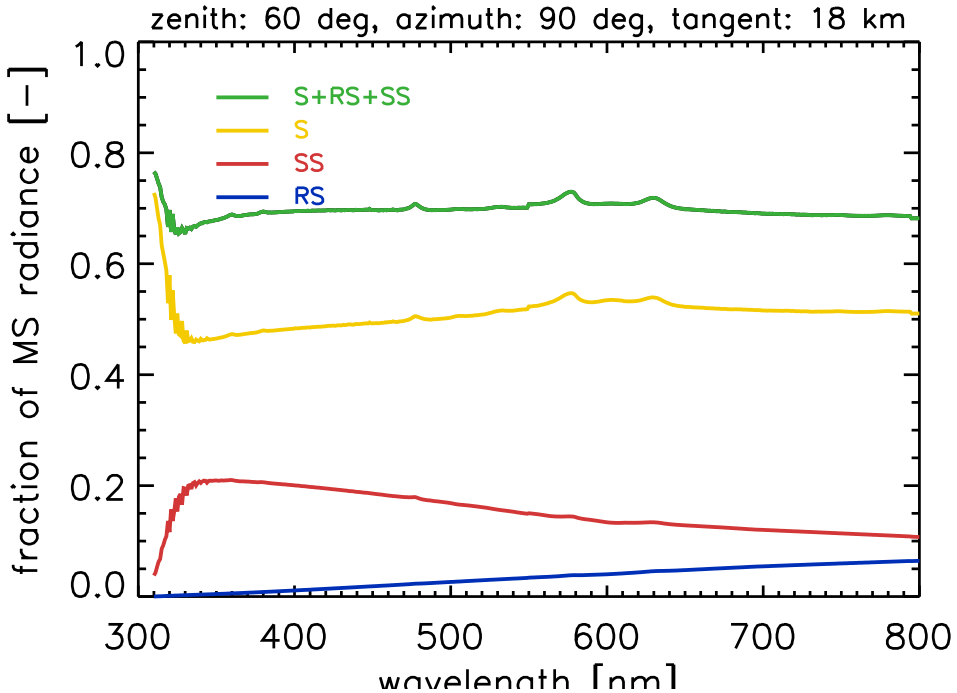

Figure 12.2: Fractions of the reference spectrum covered by several ray paths.

Figure 12.2 illustrates the ratios of the results with *SCIARAYS*'s ray path approximations to the multiply scattered radiance. It becomes evident that single scattering becomes the dominant ray path for limb measurements around 300 nm wavelength and below, where the radiation can not penetrate the stratospheric ozone layer.

Above 300 nm wavelength, single scattering accounts for about 50 % of the total radiance. The influence of the second order of scattering drops off with increasing wavelength. The influence of reflection-then-scattering, on the contrary, increases for longer wavelengths. This can be attributed to the smaller optical depth of the atmosphere at these wavelengths.

The inclusion of all ray paths of *SCIARAYS* yields a description of about 70 % of the total radiance. Even though the ratio to the total radiance remains generally flat throughout the visible wavelength range, some ozone absorption features still appear.

12.2.2 Dependence on Solar Coordinates

The ratios of the approximated radiances by *SCIARAYS* to the total radiances by CDIPI at 500 nm are plotted for 18 km tangent altitude and various solar coordinates in Figures 12.3–12.5.

Single scattering (*S*) accounts for about 45 % (high sun) to 90 % (low sun) of the total radiance. The approximations of *SCIARAYS* cover about 60 % (high sun) to 95 % (low sun) of the total radiance.

Comparing different azimuth angles, the single-scattering approximation is best for $0\,^\circ$. This is attributed to forward scattering by aerosols. The single-scattering approximation is worst for $90\,^\circ$ owing to the minimum in the phase function of Rayleigh scattering.

The contribution of reflection-then-scattering (*RS*) is of the same magnitude as that of double scattering (*SS*) for scenarios with high sun. Considering that much higher albedos occur in reality and in view of Figure 12.2. One can conclude that this ray path can become as important as single scattering (*S*) for longer wavelengths. This is consistent with the idea that, in an optically thin atmosphere with perfectly reflecting surface, the line of sight is illuminated by the reflected light as strongly as by the direct light[1].

12.2.3 Ozone Weighting Functions

SCIARAYS computes weighting functions along with the radiance analytically, i.e., with little additional computational effort. In Figure 12.6 such weighting functions (*S*+*RS*+*SS*) at 330 nm wavelength and 18 km tangent height are compared (for the whole ozone profile) to those computed by numerical perturbation with CDIPI (*MS*). The individual contributions (*S*, *RS*, *SS*) of the ray path approximations are also shown. The solar zenith angle is set to $80\,^\circ$ and the azimuth angle is $30\,^\circ$.

[1] More precisely, the up-welling and down-welling fluxes approach equality.

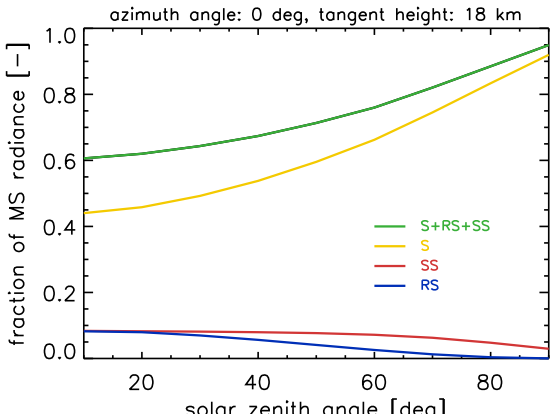

Figure 12.3: Solar zenith dependence of modelled fraction of radiance for $0\,^\circ$ azimuth angle.

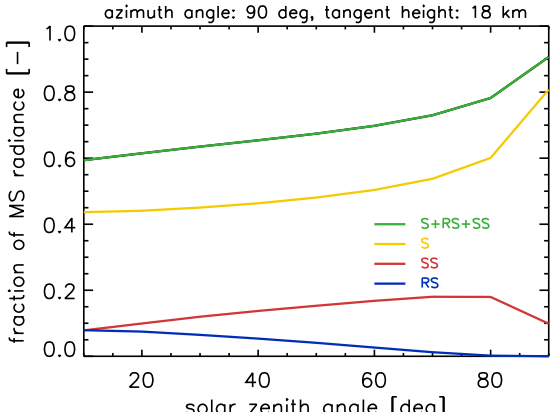

Figure 12.4: Solar zenith dependence of modelled fraction of radiance for $90\,^\circ$ azimuth angle.

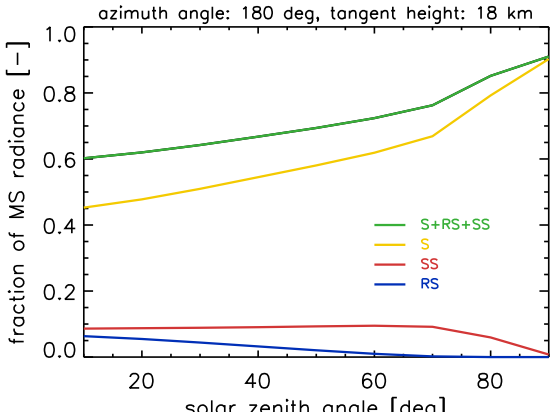

Figure 12.5: Solar zenith dependence of modelled fraction of radiance for $180\,^\circ$ azimuth angle.

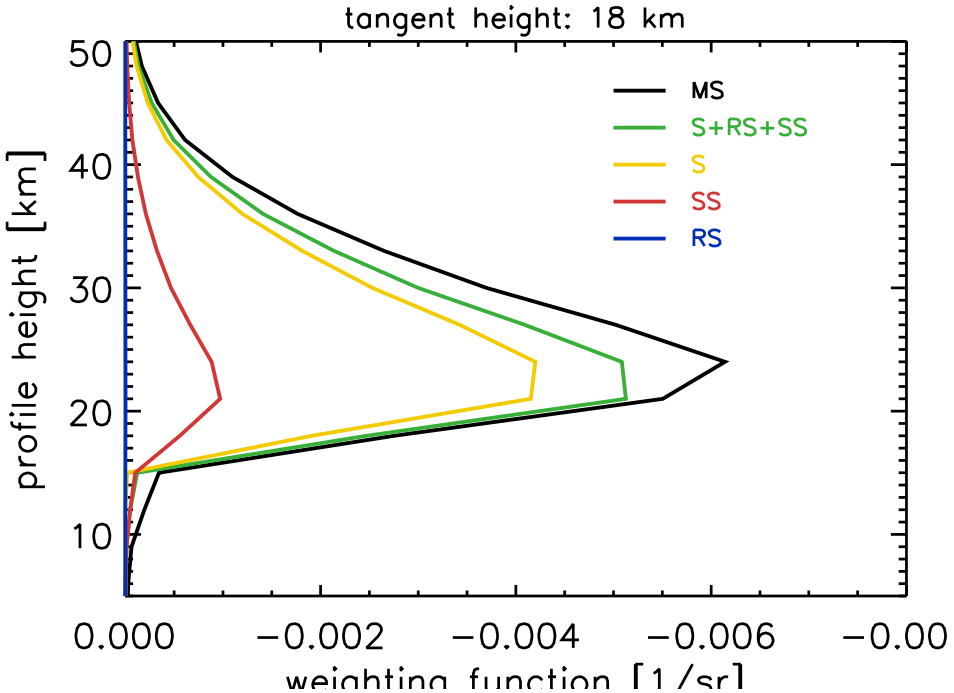

Figure 12.6: Weighting functions of the O_3 profile for 330 nm wavelength and 18 km tangent height

The weighting functions of *SCIARAYS* (*S+RS+SS*) and CDIPI (*MS*) agree to within about 10 %.

The sharp step below the tangent height is the crucial feature for the profiling qualities of limb sensors. It is hardly smeared by multiple scattering. Therefore, a good vertical resolution of the retrieved profiles can be expected.

The step is well approximated by *SCIARAYS*. This suggests the use of an approximative RTM for computation of the weighting functions in a retrieval algorithm.

12.3 Test Retrievals

In the previous section, the use of approximated weighting functions has been suggested. The current section presents the results of test retrievals with approximated weighting functions supporting this suggestion.

An ensemble of twenty synthetic limb measurement sequences has been computed with *SCIARAYS* using two orders of scattering and surface reflection (*S+RS+SS*) and also considering a realistic random noise contribution.

From each synthetic measurement sequence, three spectral windows were used to retrieve O_3 and NO_2, employing the differential optimal estimation algorithm of *SCIARAYS*. During the retrievals, the full (*S+RS+SS*) radiances have been computed, but the weighting functions have been approximated by considering single scattering (*S*) only.

Table 12.3: Measurement Scenario and Retrieval Setup

	NO_2	O_3 (UV)	O_3 (NIR)
trace gases	NO_2, O_3		NO_2, O_3, H_2O, O_2
true profiles	45 ° N, see Section 11.3		
aerosol model	stratospheric background		
albedo	0.3		
refraction	no		
field of view integration	no		
solar zenith angle	30 °		
solar azimuth angle	60 °		
tangent height step size	3 km		
fit window	420–460 nm	320–340 nm	740–780 nm
number of spectral points	81		
a priori profile	80 % of true profile		
a priori standard deviation	30 %		
profile spacing	3 km		
order of wavelength polynomial	2		
order of tangent height polynomial	2		

Thus three ensembles of retrieved profiles (once NO_2 and twice O_3) have been created. The measurement scenario and the retrieval setup are detailed in Table 12.3. The properties of these three ensembles of retrieved profiles will be presented in the remaining part of this section.

The Figures 12.7–12.9 illustrate individual members of the three retrieval profile ensembles. The retrieved profiles with their precisions calculated from the *a posteriori* covariance matrices, plotted as error-bars, are shown along with the true profiles and the used *a priori* profiles with their standard deviations.

Figure 12.7 exhibits the good NO_2 profile retrieval capabilities of SCIAMACHY in the stratosphere: Between 9 and 42 km height the retrieved profile matches the true profile within the calculated precision bounds, while the *a priori* values lie well outside the precision bounds. Below 9 km, on the contrary, both the retrieved values and their precisions approach the *a priori* values and precisions. Thus in this height region no information is gained from the measurement. It will become evident in Figure 12.10 that the same holds above 42 km.

The two retrieved O_3 profiles shown in Figures 12.8 and 12.9 demonstrate the *hyperspectral advantage* of SCIAMACHY: Profile information at different atmospheric heights can be obtained from measurements in different spectral regions. Since the UV radiation can hardly penetrate the atmosphere due to the absorption in the stratospheric ozone layer and the strong Rayleigh scattering, no profile information can be gained from the UV window. That is the reason why the retrieval approaches the *a priori* in the lower

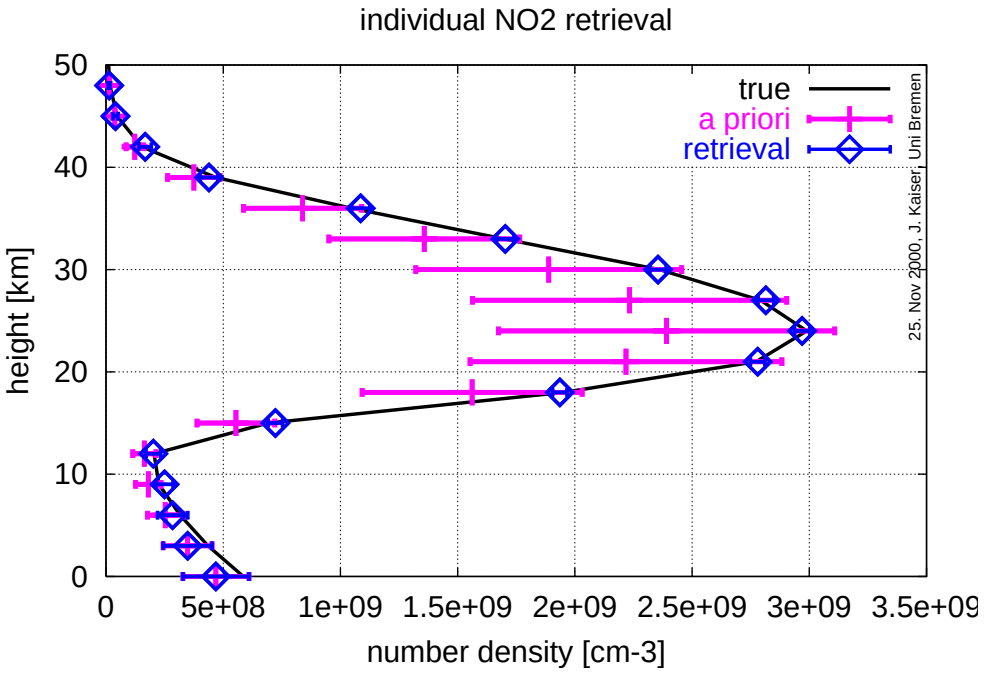

Figure 12.7: Individual test retrieval of NO_2 with approximated weighting functions.

part of Figure 12.8. On the other hand, the weak Rayleigh scattering of radiation with longer wavelengths weakens the signal from the upper stratosphere. Therefore the upper part of the retrieval in Figure 12.9 has relatively large errors and oscillates around the true profile. However, the NIR measurements are superior to the UV measurements for profiling of the lowermost stratosphere and even the troposphere, as can be seen in Figure 12.9.

An ensemble of retrieved profiles is characterised by its mean value and its standard deviation. Likewise, an ensemble of calculated retrieval precisions will be characterised be its mean value. The following properties are depicted in Figures 12.10–12.12:

mean retrieval error is the difference of the mean retrieved profile and the true profile. Plotting the difference instead of the mean profile itself facilitates comparisons to the precisions and the standard deviation.

retrieval std dev is the standard deviation of the retrieved profiles. It is identical to the standard deviation of their differences to the true profile, i.e., the retrieval error.

mean retrieval precision is the mean value of the calculated *a posteriori* precisions.

a priori precision is the assumed standard deviation of the *a priori* profile. It is plotted for orientation.

Figure 12.10 depicts the properties of the NO_2 retrieval ensemble. The height range on which no information is contained in the measurement can be identified by com-

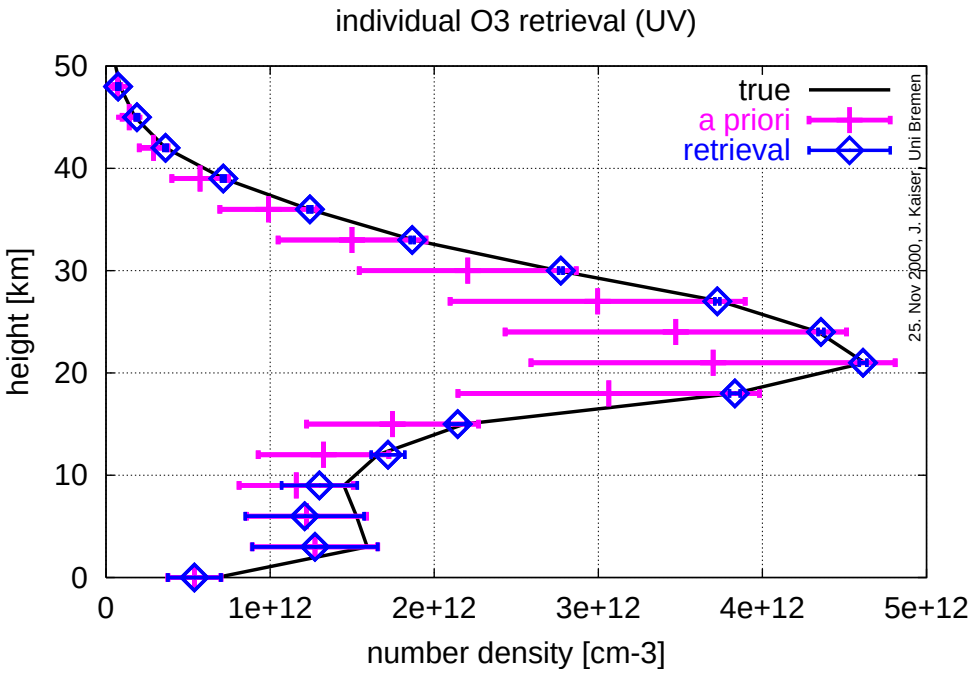

Figure 12.8: Individual test retrieval of O_3 from the UV spectral region with approximated weighting functions.

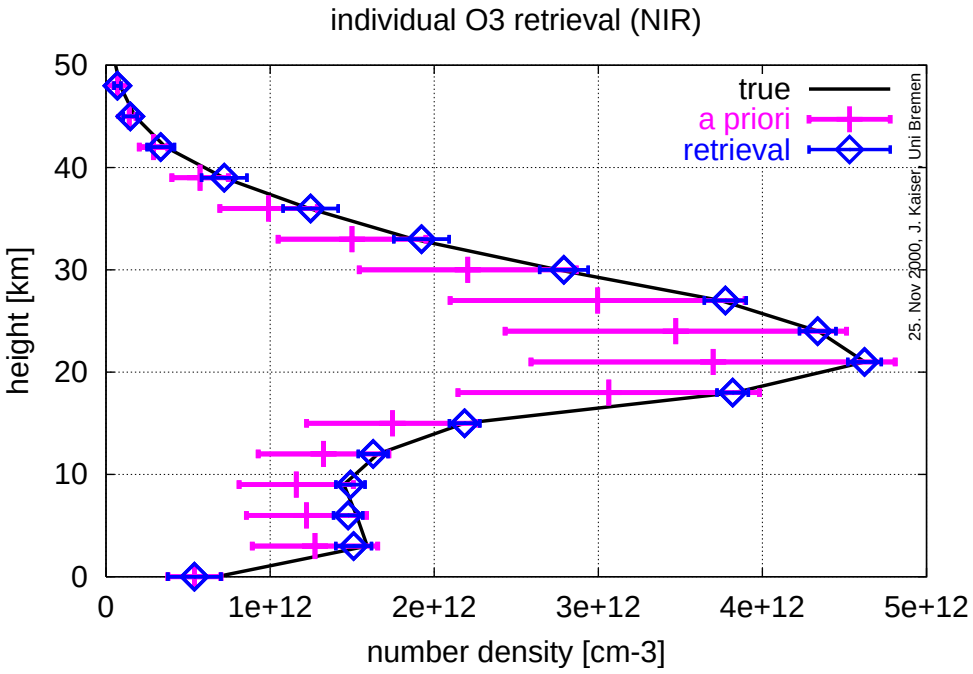

Figure 12.9: Individual test retrieval of O_3 from the NIR spectral region with approximated weighting functions.

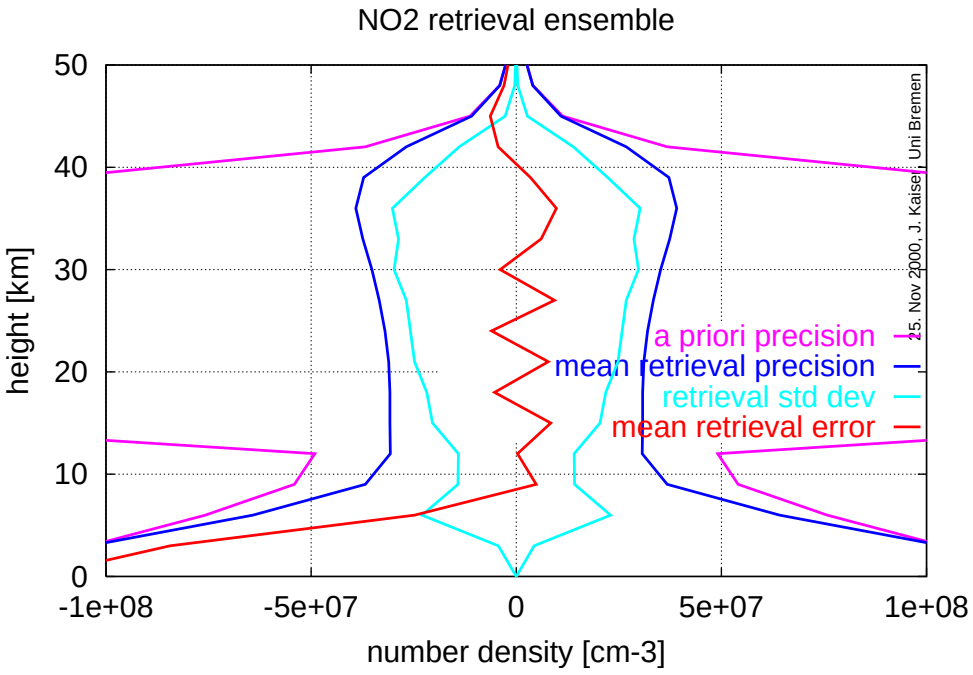

Figure 12.10: Ensemble of test retrievals of NO_2 with approximated weighting functions.

paring the *a priori* and the mean retrieval precisions: Only between approximately 10 and 40 km the mean retrieval precision is significantly smaller than the *a priori* precision, indicating information gain from the measurement. Below and above this region, the retrieved profiles are dominated by the *a priori*, not by the measurement. This is consistent with the fact that the mean retrieval error is systematically negative outside 10–40 km[2], while it oscillates around zero inside this height region.

In the height region 10–40 km, the retrieved profiles are dominated by the measurement. The fact that the mean retrieval error lies well within the bounds given by $\pm$ its standard deviation proves that the retrievals converge to the correct result even though the used weighting functions are "only" approximative.

Furthermore, the mean calculated retrieval precision is systematically larger than the standard deviation of the retrieval error. This means that the algorithm actually *overestimates* the error of the retrieval. The calculated precisions are therefore *conservative* estimates. This feature reflects the fact that weighting functions calculated with the single scattering approximation are generally smaller in magnitude than those calculated with additional ray paths, see Figure 12.6. Since the precisions are calculated from the weighting functions, the feature can be expected from theoretical considerations.

The properties of the two ensembles of O_3 profile retrievals from an UV and a NIR spectra window are shown in Figures 12.11 and 12.12. The height regions with profile information from the measurements exhibit the same features as in Figure 12.10: The

[2]Recall from Table 12.3 that the *a priori* profile is systematically smaller than the true.

mean retrieval precision is much smaller than the *a priori* precision and the retrieval standard deviation is non-vanishing[3].

The retrievals from the UV clearly yield more precise profile information throughout the stratosphere than the retrievals from the NIR, but the latter make retrievals from the upper troposphere feasible.

In both cases, the retrievals converge correctly since the mean retrieval errors are bounded by the retrieval standard deviations in the regions with little *a priori* influence.

The mean calculated retrieval precision above ≈ 25 km approximately equals the retrieval standard deviation in the UV retrieval. This supports the consistency of the retrieval algorithm as the single-scattering approximation is generally considered to be valid in the UV for tangent heights above the ozone layer.

Everywhere else, the calculated retrieval precision is a *conservative* estimate like in the case of the NO_2 retrievals as the retrieval standard deviation is actually is smaller.

[3]When there is no information in the measurement, the retrieval always converges to the *a priori* profile. Therefore, the standard deviation approaches zero. On the other hand, where the measurement contains information, the measurement noise affects the retrieval with a magnitude of the order of the computed retrieval precision.

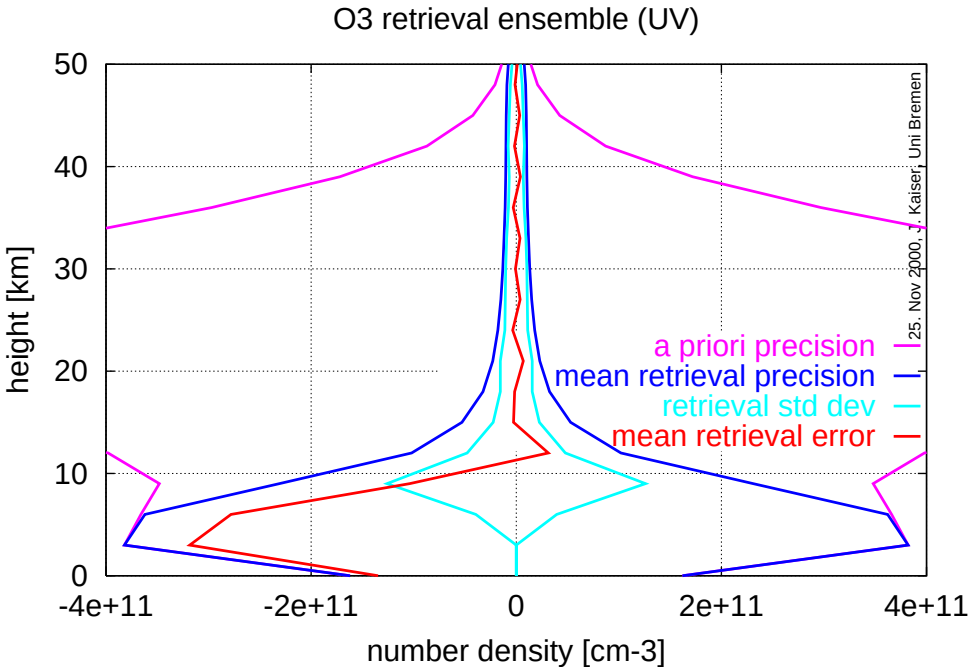

Figure 12.11: Ensemble of test retrievals of O_3 from the UV spectral region with approximated weighting functions.

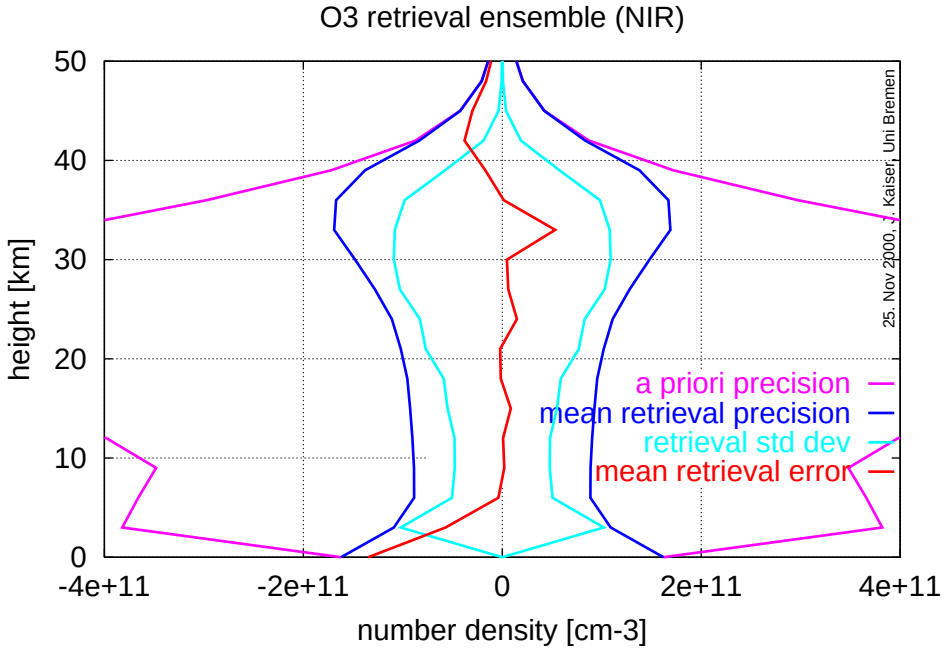

Figure 12.12: Ensemble of test retrievals of O_3 from the NIR spectral region with approximated weighting functions.

12.4 Summary

In this chapter, the influence of several approximations on limb radiances and their weighting functions has been compared and the suitability of approximative weighting functions for the retrieval has been tested.

The comparisons of simulated limb radiances with 18 km tangent altitude show that the single scattering approximation yields between 45 % and 95 % of Earth's radiance, depending on wavelength and solar coordinates. The remaining discrepancy to the multiply scattered radiance can be further reduced (by about 40 %) in *SCIARAYS* by accounting for additional ray paths.

Strong spectral absorption features are under-represented in the approximative model.

The analytical, approximated weighting functions for the ozone profile agree relatively well with the reference weighting function. This holds particularly for the important feature at the tangent height. It suggests their usability in a retrieval algorithm for future real limb measurements.

The O_3 and NO_2 profile retrieval tests prove that the single-scattering approximation actually can be used for the calculation of weighting functions in a retrieval process: The retrievals converge to the true profile.

Calculating the retrieval precision with approximative weighting functions slightly overestimates the retrieval error. Such precisions can therefore be regarded as conservative estimates.

The comparison of radiances and weighting functions has been presented at the International Radiation Symposium 2000 in St. Petersburg, Russia, and is being published in [Kaiser et al., 2001a]. There, we have already suggested to use approximated weighting functions in retrievals.

Part IV

EPITOME

Chapter 13

Summary, Conclusions, and Outlook

13.1 Summary and Conclusions

Human activity is altering Earth's atmosphere on a global scale. The most striking examples are the stratospheric ozone depletion and the global warming. Appropriate political reaction requires constant monitoring of the atmosphere and forecasting of the anthropogenic influences. Satellite-based observations of the atmosphere are more or less directly required for both tasks. (Chapter 2)

The spectrometer SCIAMACHY will be launched aboard the European satellite Envisat in October 2001. It will measure atmospheric radiance spectra extending from the UV to the NIR spectral region, i.e., 240–$2380\,\mathrm{nm}$, with a moderate resolution of 0.24–$1.5\,\mathrm{nm}$. Since Envisat will be in a sun-synchronous polar orbit, global coverage of the measurements is achieved.

Owing to SCIAMACHY's hyperspectral capabilities, a large set of atmospheric parameters will be retrieved simultaneously from each individual measurement. Among the retrieval targets are the trace gases O_3, NO_2, OClO, BrO, SO_2, HCHO, H_2O, CH_4, CO_2, CO, and N_2O. Additionally, temperature, aerosol and cloud parameters will be determined.

SCIAMACHY will operate in three measurement geometries: nadir, limb and occultation. Limb measurements contain well-resolved profile information on the atmospheric constituents. Since they are conceptually new, advanced retrieval algorithms and radiative transfer models (*RTM*s) need to be developed for the retrieval. (Chapter 3)

In this thesis, such a program package has been developed: *SCIARAYS*. It consists of a new RTM, an instrument model and retrieval algorithms for retrievals from ultraviolet-visible-near-infrared (*UV-vis-NIR*) limb measurements.

The new RTM in *SCIARAYS* fulfills the following requirements of retrievals from UV-vis-NIR limb scattering measurement:

- fully spherical atmospheric model geometry,
- several orders of scattering and reflection in the atmosphere,
- computational efficiency for radiance calculations,
- computational efficiency for weighting function calculations for all atmospheric model parameters.

The efficiency of radiance calculations is achieved by approximating the multiple scattering of the radiation with two orders of scattering or surface reflection. The weighting function calculations are accelerated further by evaluating analytical formulae for the weighting functions (*quasi-analytical* calculations).

The RTM has been validated by comparisons to other RTMs (SIRO, MODTRAN, and GOMETRAN). The agreement for single scattering, possibly preceded by surface reflection, is generally better than $1\,\%$. The second order of scattering is intrinsically less accurate: Its contribution is accurate to 5–$25\,\%$ depending on used computer resources. This is significantly smaller than the additional effect of higher orders of scattering in the UV-vis spectral range (5–$40\,\%$ of the radiance).

The weighting function calculations have been validated by the numerical perturbation technique. They are as accurate as the radiances. However, the effect of additional orders of scattering is smaller than for the radiances, i.e., $10\,\%$. (Chapter 6)

The new RTM is unique in that no other published RTM complies to all four requirements. (Chapter 5)

The new instrument model in *SCIARAYS* yields signal-to-noise values for SCIAMACHY and performs the vertical convolution with SCIAMACHY's field-of-view[1]. It models SCIAMACHY's real characteristics as measured in the laboratory. The signal-to-noise values are vital for all retrieval algorithms, while the field-of-view integration is necessary for estimates of the vertical resolutions. (Chapter 7)

Retrieval algorithms based on the optimal estimation formalism have also been implemented in *SCIARAYS*. (Chapter 8)

The the whole package *SCIARAYS* has been used to characterise limb retrievals from a UV-vis-NIR spectrometer like SCIAMACHY.

Radiances, signal-to-noise values, and weighting functions for the trace gas retrieval targets have been calculated for the whole spectral range of SCIAMACHY. (Chapter 9,

[1]The field-of-view is equivalent to the antenna function for longer wavelengths.

Appendix B)

Averaging kernels have been calculated for several measurement scenarios. (Chapters 9, 10, and 11)

The averaging kernels and test retrievals show that the vertical resolution of retrievals from SCIAMACHY's limb measurements can be improved beyond the geometrical limits of the instrument. Even though SCIAMACHY operates with a tangent step size of $3\,\mathrm{km}$ and a field-of-view with $2.6\,\mathrm{km}$ vertical extent at the tangent height, retrievals with a finer vertical profile resolution can be performed. This effect is caused by the hyperspectral capabilities of SCIAMACHY: The light ray paths through the atmosphere are different for different wavelengths and many spectral points reduce the statistical uncertainty.

As a trade-off for better vertical resolution, the retrieval precision gets worse. Thus O_3 profile features with $1\,\mathrm{km}$ vertical extent can be identified with a precision of 20–$30\,\%$, while retrievals on a $3\,\mathrm{km}$ profile grid achieve a precision of $1\,\%$.

The trade-off between vertical resolution and retrieval precision implies that the choice of retrieval parameters needs to be adapted to the investigated atmospheric phenomenon. For instance, studying tropopause folds requires a good vertical resolution, while excellent retrieval precision might be more important for studying the stratospheric chemistry. (Chapter 10)

Detailed theoretical retrieval precisions for a UV-vis-NIR limb sensor of SCIAMACHY type have been calculated depending on profile altitude. The results are summarised in Table 11.2. The precision of O_3 and H_2O profile retrievals will be limited by uncertainties in the spectroscopic data base rather than by the signal-to-noise of the detector.

Generally, the measurements of trace gases with absorption signatures in the UV-vis spectral region exhibit the best precision in the lower and middle stratosphere, while those of trace gases with absorption signatures in the NIR have better precision for lower profile heights. The conclusion is that a UV-vis-NIR limb sensor like SCIAMACHY is well suited for studying the vertical structure of the stratosphere, especially the lower stratosphere, and also of the upper troposphere above cloud top.

For instance, O_3 profiles with the nominal vertical resolution ($3\,\mathrm{km}$ for SCIAMACHY) can be measured with $1\,\%$ theoretical precision. Retrieved H_2O profiles have a theoretical precision of 1–$2\,\%$ in the upper troposphere and lower stratosphere. The dynamical behaviour in the tropopause region can be studied using these tracers for stratospheric and tropospheric air.

NO_2 profiles can be measured with 1–$10\,\%$ theoretical precison in the lower and middle stratosphere. These measurements will provide further insight into the stratospheric chemistry, especially the denoxification and ozone depletion. (Chapter 11)

The radiances and weighting functions calculated with *SCIARAYS* have been com-

pared to those calculated with the radiative transfer model CDIPI, which accounts for full multiple scattering, but is much much slower. The second order of scattering and reflection modelled by *SCIARAYS* yields 60–95 % of the full multiply scattered radiance, depending on wavelength and solar coordinates.

Due to the approximation of the multiple scattering, *SCIARAYS*' radiances should be used with caution for retrievals from real limb measurements. Since the contribution of multiple scattering is weaker in spectral regions with longer wavelengths, it is thought to be applicable for retrievals from the NIR and even the visible region.

The simulated weighting functions agree within 10 %. Their feature at the tangent height is particularly well reproduced. Therefore, *SCIARAYS*' weighting functions can be used to calculate theoretical precision estimates and averaging kernels. In conformance with this, test retrievals with approximate weighting functions converge correctly. Thus the approximate weighting functions of *SCIARAYS* are well suited for retrievals from SCIAMACHY's limb measurements. (Chapter 12)

Furthermore, the RTM in *SCIARAYS* and the photo-chemical box model BRAPHO have been combined to the program SLACO. This program has been used successfully for advanced retrievals from ground-based DOAS [Müller, 2001] and lunar transmission [Schlieter, 2001] measurements in Ny Ålesund and Bremen.

13.2 Outlook

Future work will be clearly directed toward the completion of a fast processor for limb retrievals from SCIAMACHY's measurements. Due to the numerical efficiency of *SCIARAYS*, this processor should be able to deliver *near-real-time* service with limited computer resources.

The following steps appear to be necessary for the completion of such a processor:

1. In order to perform retrievals from the NIR spectral region, a more sophisticated treatment, i.e., correlated-k, of the line absorption needs to be implemented.

2. The pressure and temperature dependencies of carbon dioxide, oxygen, and possibly the oxygen dimer O_4 will then be used for independent retrievals of pressure and temperature profiles and the tangent heights. Accurate tangent height retrieval is crucial as its quality may be the precision limiting factor for some trace gas retrievals.

3. A suitable parametrisation of aerosol scattering can be used to retrieve aerosol parameter profiles.

4. The optimal, smallest spectral windows for the retrieval need to be identified. For this, the actual performance of SCIAMACHY's individual pixels should be accounted for.

5. Interfaces for the access to real measurements and for the archiving and visual presentation of retrieval results need to be implemented.

The accuracy of the processor needs to be assessed carefully. Owing to the approximation in *SCIARAYS*, its applicability may be restricted to the vis-NIR spectral range. The improvement in accuracy and applicability due to the following two methods should be investigated further:

- modifications of the measurement vector, e.g., normalisation of all radiances by division with those at a reference tangent height

- acceleration of the numerical calculations by approximating the weighting functions, while calculating more accurate radiances (see Section 12.3).

Following this outlook, a functional, fast limb processor for many atmospheric parameter profiles can be anticipated.

Part V

APPENDICES

Appendix A

Ray Tracing

This appendix gives derivations of the ray tracing formulae, which are a central part of the radiative transfer model in *SCIARAYS*.

A.1 Representing a Ray

The radiative transfer model *SCIARAYS* traces light rays in the opposite direction of their physical propagation, i.e., as if they were travelling from the sensor through the atmosphere to the sun. This *backward ray tracing* is common in single-scattering models and also known from Monte-Carlo models [e.g., Oikarinen, 1999].

Figures A.1 and A.2 depict two types of light rays in a spherical atmosphere. In both figures the atmosphere is marked by its lower and upper bounds, the *bottom of atmosphere* (*BOA*) and the *top of atmosphere* (*TOA*). The centre of Earth is the point of symmetry. It is chosen as origin O of the coordinate system. The starting point of each ray is called S and its direction is marked with an arrow.

All rays are of one of the following types:

- A *sky-bound* ray starts by travelling upwards , i.e., the zenith angle $\psi_S \leq \pi/2$. All its points are on the same side of the tangent point T as the starting point S. This situation is depicted in Figure A.1, where P_1 is an arbitrary example point of the ray.

- A *ground-bound* ray starts by travelling downwards, i.e., the zenith angle $\psi_S > \pi/2$. Points P_1 and P_3 on both sides of the tangent point T are part of the ray. This situation is depicted in Figure A.2.

Analogously, individual points with $\psi \leq \pi/2$ will be called *sky-bound* and points with $\psi_S > \pi/2$ will be called *ground-bound*.

For each ray the *ray coordinate system* can be chosen in such a way that the starting point lies on the positive part of the z-axis and that the ray is contained in the part of the x-y-plane with positive x-values. Thus all azimuth coordinates ϕ of ray points vanish.

Conventionally, the polar coordinate is non-negative. Requiring this, the azimuth coordinate of the tangent point would equal π for a sky-bound ray. However, in the present context, the formulae are simplified by requiring a vanishing azimuth coordinate in the ray coordinate system. Thus the polar coordinate may become negative.

In view of Figure A.2 it is evident that — unlike in a plane-parallel atmospheric model — the ray cannot be parametrised by the height or radius of its points. Instead, the polar coordinate θ is an non-ambiguous parameter. The distance to a reference point on the ray or the zenith angle can also be used as parameters.

In the discrete world of computer simulations each ray is represented by a set of ray points. Points which are equidistant in one of the non-ambiguous parameters mentioned above would be an obvious choice for such a set. However, the intersections of the ray with predefined height levels are often a more convenient choice since the optical properties at the points are readily accessible in a discrete model. Another common choice is a set of equidistant points along the ray [e.g., Kneizys et al., 1983].

A ray can be identified by stating the radius, polar and azimuth coordinates of its starting point and its viewing direction. Using these values, formulae for the computations of the following properties at all ray points are derived in this chapter:

$level$	index of the height level.
θ	polar coordinate in the ray coordinate system
ψ	zenith angle of the ray
Δs	path length in a shell corresponding to the height level
$\theta_\star$	astronomical solar zenith angle at the point
$\phi_\star$	astronomical solar azimuth angle at the point.

Knowing $level$ is equivalent to knowing the radius coordinate. For the interpretation and computation of the solar coordinates refer to Section A.4. Another important property of a ray representation is the number $npts$ of its points.

If the ray leaves the atmosphere immediately into space or Earth's surface, it can be represented by one point with vanishing path length.

A.2 Geometric Ray Tracing

A.2.1 Plane-Parallel Atmosphere

Any Ray

The polar coordinate θ is not meaningful in plane-parallel geometry: It can be set to zero for all points.

The number $npts$ of points of a ray and their height levels (given by the height level

index $level$) can be determined depending on the ray type:

- Sky-bound rays have points at the starting level and all higher levels.
- Ground-bound rays have points at the starting level and all lower levels.
- Horizontal rays are a special case in a plane-parallel atmosphere, see below.

The path length Δs_i of the i-th point is given by the difference of the heights (more general: radii) r_{i+1} and r_{i-1} of the neighbouring points and the zenith angle ψ:

$$\Delta s_i = \left| \frac{r_{i+1} - r_{i-1}}{2 \cos(\psi)} \right| = \frac{r_{i+1} - r_{i-1}}{2 \cos(\psi)} \ . \tag{A.1}$$

For the first and last point of the ray, an analogous formula with the point itself and the adjacent point can be used.

Horizontal Ray

If the cosine of the zenith angle equals zero, the ray is horizontal. This case can be approximated with two points and very large path lengths. The actual value of "very large" depends on the computer hardware in use.

Solar Ray

If the cosine of the astronomical solar polar coordinate is positive, there exist solar rays which reach all atmospheric height levels: It is simply the ray with a zenith angle equal to the astronomical solar polar coordinate and azimuth angle equal to minus the astronomical solar azimuth coordinate.

A.2.2 Spherical Atmosphere

Tangent Point Coordinates

First of all, the coordinates of the tangent point T are calculated from the radius coordinate r_S and the zenith angle ψ_S of the starting point S by considering the right triangle OST in Figures A.1 and A.2:

$$r_T = r_S \sin(\psi_S) \ , \tag{A.2}$$

where the identity $\sin(\alpha) \equiv \sin(\pi - \alpha)$ (α arbitrary) is used in the case of a ground-bound ray.

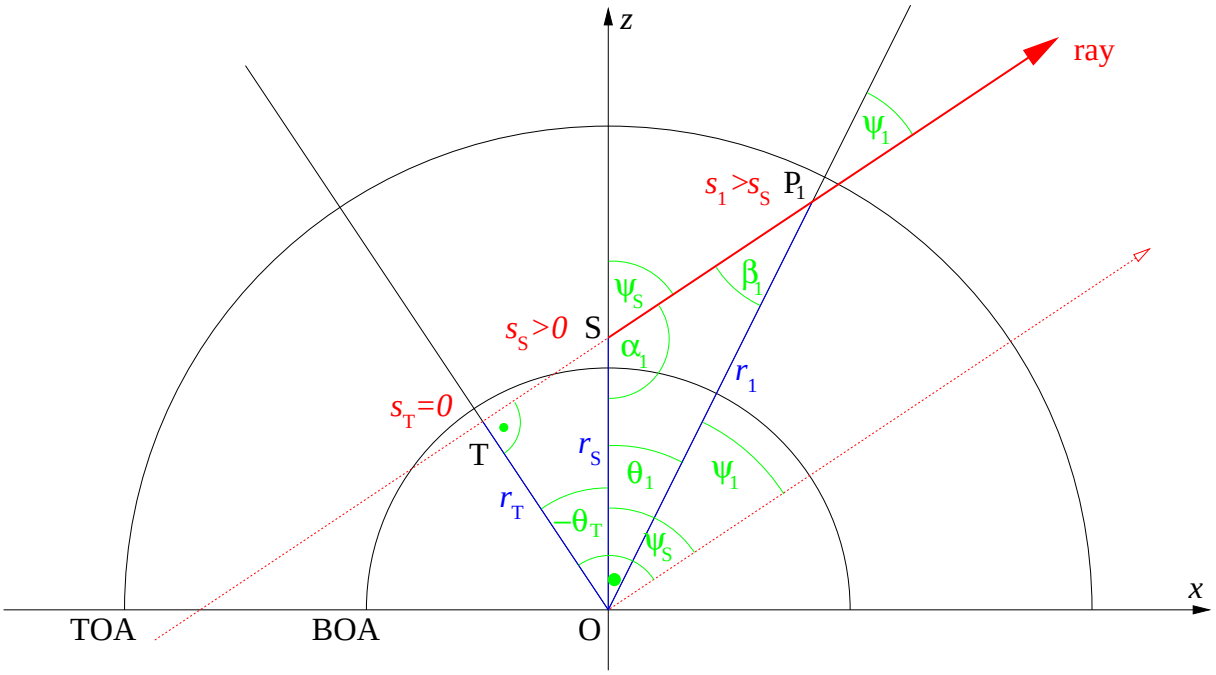

Figure A.1: Geometry of a sky-bound ray (without refraction)

The polar coordinate θ_T of the tangent point can be determined from the sum of angles of the triangle OST. For a ground-bound ray it is:

$$\theta_T = \pi - (\pi - \psi_S) - \frac{\pi}{2} = \psi_S - \frac{\pi}{2} \,. \tag{A.3}$$

The polar coordinate of the tangent point of a sky-bound ray is negative, see Section A.1. Therefore it can be calculated with the same formula as that of a ground-bound ray's:

$$\theta_T = -\left(\pi - \psi_S - \frac{\pi}{2}\right) = \psi_S - \frac{\pi}{2} \,. \tag{A.4}$$

Radius Levels and Number of Points

For sky-bound rays the ray point's radii are given by the starting radius level and all higher levels.

For ground-bound rays the ray point's radii are given by the starting radius level, then all levels down to the tangent points level (or the one below, if the tangent point lies between two levels) and then all levels above the tangent point's.

The number of points is trivially determined along with their levels.

Polar Coordinates

The polar coordinates of all individual points of a ray are given by formulae which can be derived from the right triangle OP_iT. For the three depicted points P_i ($i = 1, 2, 3$) the

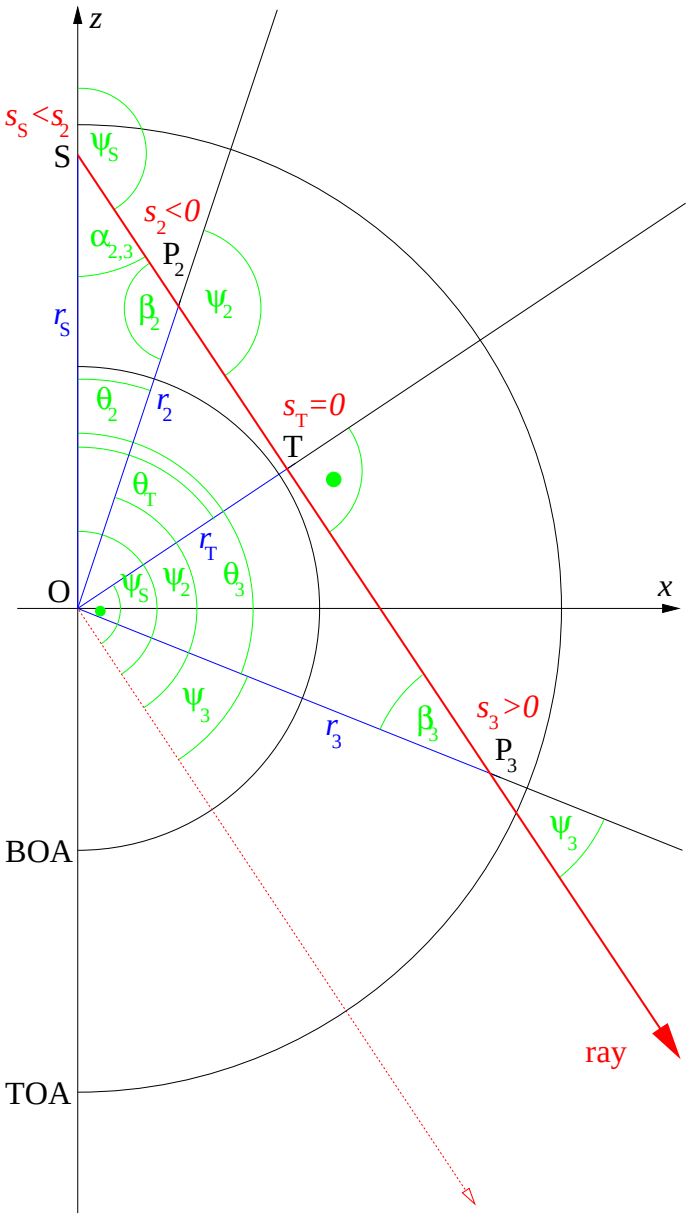

Figure A.2: Geometry of a ground-bound ray (without refraction)

individual formulae are:

$$r_1 = r_T \cos(\theta_1 - \theta_T) \qquad \text{(remember: } \theta_T < 0\text{)} \tag{A.5}$$

$$r_2 = r_T \cos(\theta_T - \theta_2) \tag{A.6}$$

$$r_3 = r_T \cos(\theta_3 - \theta_T) \tag{A.7}$$

Using the identity $\cos(\alpha) = \cos(-\alpha)$ (α arbitrary) all three terms reduce to a common form for all points on a ray:

$$r_i = r_T \cos(\theta_T - \theta_i) \qquad (i = 1, 2, 3) \tag{A.8}$$

Solving this equation yields the polar coordinate θ_i. Since the cosine cannot be inverted in its whole domain, (A.8) cannot be used directly and a "case sensitive" equation must be used:

$$\theta_i = \begin{cases} \theta_T + \arccos\left(\frac{r_i}{r_T}\right) & (i = 1, 3) \\ \theta_T - \arccos\left(\frac{r_i}{r_T}\right) & (i = 2) \end{cases} \tag{A.9}$$

The first equation holds, wherever the ray travels away from its tangent point, while the second equation applies, when the ray travels from its starting point toward the tangent point.

For practical applications, these formulae have the disadvantage that, when they are evaluated numerically, precautions have to be taken to assure that the argument to the $\arccos(.)$ does not leave its domain $[-1, 1]$ due to chance rounding errors.

Alternatively, a relationship between the radius and polar coordinates can be deduced from the following sine relationship of the triangle OSP_i:

$$\frac{\sin(\alpha_i)}{r_i} = \frac{\sin(\beta_i)}{r_S} \qquad (i = 1, 2, 3)\ , \tag{A.10}$$

where

$$\alpha_i = \pi - \psi_S \qquad \begin{cases} < \pi/2 & (i = 2, 3) \\ > \pi/2 & (i = 1) \end{cases} \tag{A.11}$$

$$\beta_i = \pi - \alpha_i - \theta_i = \psi_S - \theta_i \qquad \begin{cases} < \pi/2 & (i = 1, 3) \\ > \pi/2 & (i = 2)\ . \end{cases} \tag{A.12}$$

(A.10) can easily be solved for the radius coordinate r_i:

$$r_i = r_S \frac{\sin(\alpha)}{\sin(\beta)} = r_S \frac{\sin(\psi_S)}{\sin(\psi_S - \theta_i)} \qquad (i = 1, 2, 3)\ . \tag{A.13}$$

due to the limited range of the $\arcsin(.)$, the polar coordinate θ_i must be determined from (A.10) with a "case sensitive" formula:

$$\theta_i = \begin{cases} \psi_S - \arcsin\left(\frac{r_S}{r_i}\sin(\psi_S)\right) & (i = 1, 3) \\ \psi_S - \pi + \arcsin\left(\frac{r_S}{r_i}\sin(\psi_S)\right) & (i = 2)\ . \end{cases} \tag{A.14}$$

This formula is analogous to (A.9) in two aspects: Different formulae apply for the cases of the ray travelling toward the tangent point ($i = 2$) and travelling away from it ($i = 1, 2$). Also, during numerical evaluation, the argument of the $\arcsin(.)$ function may lie (slightly) outside of its domain $[-1, 1]$ due to limited machine precision.

Zenith Angles

From the different angles shown at the origin O in Figures A.1 and A.2 it becomes obvious that the zenith angle ψ_i of the ray at point i is the difference of the zenith angle ψ_S of the starting point and the polar coordinate θ_i of the point under consideration:

$$\psi_i = \psi_S - \theta_i \qquad (i = 1, 2, 3) \ . \tag{A.15}$$

Path Lengths

The ray path length Δs associated to each point is calculated from the ray path coordinates s of the point and its neighbours.

Let the *ray path coordinate* s_i be the distance of the point i to the tangent point T in the part of the ray travelling away from the tangent point and its negative in the other part of a sky-bound ray. Thus:

$$s_T \equiv 0 < s_S < s_1 \qquad \text{(sky-bound ray)} \tag{A.16}$$

$$s_S < s_2 < s_T \equiv 0 < s_3 \qquad \text{(ground-bound ray).} \tag{A.17}$$

The ray path coordinates s can be calculated from the radius coordinates r and either the zenith angles ψ or the polar coordinates θ. Considering the triangle OTP in Figures A.1 and A.2 leads to

$$s_1 = r_1 \cos(\psi_1) \tag{A.18}$$

$$s_2 = -r_2 \cos(\pi - \psi_2) = r_2 \cos(\psi_2) \tag{A.19}$$

$$s_3 = r_3 \cos(\psi_3) \ . \tag{A.20}$$

or, alternatively,

$$s_1 = r_1 \sin(\theta_1 - \theta_T) \tag{A.21}$$

$$s_2 = -r_2 \sin(\theta_T - \theta_2) = r_2 \sin(\theta_2 - \theta_T) \tag{A.22}$$

$$s_3 = r_3 \sin(\theta_3 - \theta_T) \ , \tag{A.23}$$

(A.18–A.20) and (A.21–A.23) can be written in the general forms

$$s_i = r_i \cos(\psi_i) \tag{A.24}$$

$$= r_i \sin(\theta_i - \theta_T) \quad (i = 1, 2, 3) \ . \tag{A.25}$$

The *ray path length* Δs_i associated with each point i is most easily determined from the ray path coordinates of its neighbours:

$$\Delta s_i \;=\; \frac{s_{i+1} - s_{i-1}}{2} \,. \tag{A.26}$$

For the first ($i = 0$) and last ($i = I$) point of a ray, only one neighbour is available. The following formulae ensure consistency, i.e., $\sum_{i=1}^{I} \Delta s_i = s_I - s_1$:

$$\Delta s_1 \;=\; s_2 - s_1 \tag{A.27}$$

$$\Delta s_I \;=\; s_I - s_{I-1} \tag{A.28}$$

Solar Rays

Since the sun can be assumed to be infinitely far away, a ray hits it, if the zenith angle ψ_S of its starting point equals the astronomical solar polar coordinate $\theta_\star$ of the sun at the starting point.

A.3 Refractive Spherical Ray Tracing

A.3.1 General Considerations

In a spherically symmetric atmosphere[1] with refractive index $n = n(r)$ the spherical formulation (4.19) of Snell's law holds:

$$n\, r\, \sin(\psi) = \text{const} \equiv c. \tag{A.29}$$

c is called *Snell's constant*. It is constant for all points of a ray, but, in general, varies from ray to ray.

Once Snell's constant has been determined from one point's radius r and zenith angle ψ, e.g., the starting point's, (A.29) provides a relationship between r and $\sin(\psi)$ of all points of this ray. Thus $\cos(\psi)$ and $\tan(\psi)$ are also known except for their signs. Again, the two different cases correspond to points where the ray is travelling upwards and downwards.

The curvature K, i.e., the inverse of the radius of curvature, at each point of a ray is [Kneizys et al., 1996, section 2.1.3]

$$K(r, \psi) = -\frac{\sin(\psi)}{n(r)} \frac{\mathrm{d}n(r)}{\mathrm{d}r} \,. \tag{A.30}$$

The ratio $R(r)$ of the radius coordinate r to the radius of curvature $(K(r, \pi/2))^{-1}$ of a tangent ray will prove to be a useful quantity in forthcoming formulae. It can be

[1] Formulae for the attenuation of the direct solar light with refraction can be found in Minin [1973], Edlén [1966], Peck and Reeder [1972], Kneizys et al. [1996].

interpreted as a measure of the influence of the refractive bending as compared to that of the spherical geometry:

$$R \equiv \frac{r}{(K(r,\pi/2))^{-1}} = -\frac{r}{n(r)}\frac{\mathrm{d}n(r)}{\mathrm{d}r} \,. \tag{A.31}$$

Taking the derivative of (A.29) w.r.t. the radius coordinate r yields an expression for the derivative of the zenith angle ψ w.r.t. r:

$$\frac{\mathrm{d}\psi}{\mathrm{d}r} = -\frac{\tan(\psi(r))}{r}\left(1+\frac{r}{n}\frac{\mathrm{d}n}{\mathrm{d}r}\right) \tag{A.32}$$

$$= \frac{\tan(\psi(r))}{r}(R-1). \tag{A.33}$$

A.3.2 Tangent Radius

At the tangent point with $\psi = \pi/2$, (A.29) becomes:

$$r_T\, n(r_T) = c \tag{A.34}$$

The tangent radius r_T is well defined from this equation for Earth's atmosphere[2].

A.3.3 Radius Levels

With known starting radius, starting zenith angle and tangent radius, the radii and a associated level indices $level$ of all points of the ray can be determined (as described in Section A.2.2). This implies knowledge of the total number $npts$ of points.

A.3.4 Zenith Angles

Using Snell's law (A.29), the zenith angles ψ of sky-bound and ground-bound points of a ray can be calculated with separate formulae:

$$\psi_i = \begin{cases} \pi - \arcsin\frac{c}{n(r_i)\,r_i} & \text{(sky-bound)} \\ \arcsin\frac{c}{n(r_i)\,r_i} & \text{(ground-bound)} \end{cases} \tag{A.35}$$

[2]Since the refractivity is proportional to the air density, see (4.20), it is in a good approximation of the form $a\,\exp(-r/b)$ with the atmospheric scale height b. Therefore, one can write $\frac{\mathrm{d}}{\mathrm{d}r}r\,n(r) = n(r) - r\frac{\mathrm{d}n}{\mathrm{d}r} = n(r)(1-r/b) < 0$, where the last inequality holds as Earth's radius is much larger than the atmospheric scale height. Thus $rn(r)$ is a monotonic function of r and (A.34) can be solved for r_T unambiguously.

A.3.5 Polar Coordinates and Path Lengths

Following Kneizys et al. [1996], the polar coordinates θ and path length coordinates s of the individual points have to be calculated by integration:

$$\theta_i = \theta_{i-1} + \int_{r_{i-1}}^{r_i} \frac{\mathrm{d}\theta}{\mathrm{d}r}\,\mathrm{d}r \tag{A.36}$$

$$s_i = s_{i-1} + \int_{r_{i-1}}^{r_i} \frac{\mathrm{d}s}{\mathrm{d}r}\,\mathrm{d}r \tag{A.37}$$

From Figure A.3, the following relationships between the infinitesimal quantities near ground-bound ray points can be derived:

$$\frac{-\mathrm{d}r}{\mathrm{d}s} = \cos(\pi-\psi) = -\cos\psi \tag{A.38}$$

$$\frac{r\mathrm{d}\theta}{-\mathrm{d}r} = \tan(\pi-\psi) = -\tan\psi \quad , \tag{A.39}$$

and for the sky-bound part of a ray one obtains:

$$\frac{\mathrm{d}r}{\mathrm{d}s} = \cos\psi \tag{A.40}$$

$$\frac{r\mathrm{d}\theta}{\mathrm{d}r} = \tan\psi \; . \tag{A.41}$$

In both cases the resulting integral kernels of (A.36, A.37) are the same:

$$\frac{\mathrm{d}s}{\mathrm{d}r} = \frac{1}{\cos\psi} \tag{A.42}$$

$$\frac{\mathrm{d}\theta}{\mathrm{d}r} = \frac{\tan\psi}{r} \tag{A.43}$$

The numerical integration of (A.37) is unstable due to the singularity $1/\cos\psi \rightarrow \infty \;\; (r \rightarrow r_T)$ at the tangent point. Therefore, the integration variable r has to be substituted by $x \equiv r\,\cos\psi$. This is exactly the path coordinate used in geometrical ray tracing, see (A.24). With (A.33) and (A.31) one obtains:

$$\frac{\mathrm{d}x}{\mathrm{d}r} = \cos\psi - r\sin\psi\frac{\mathrm{d}\psi}{\mathrm{d}r} \tag{A.44}$$

$$= \frac{\cos^2\psi - (R-1)\,\sin^2\psi}{\cos\psi} \tag{A.45}$$

$$= \frac{1 - R\,\sin^2\psi}{\cos\psi} \quad . \tag{A.46}$$

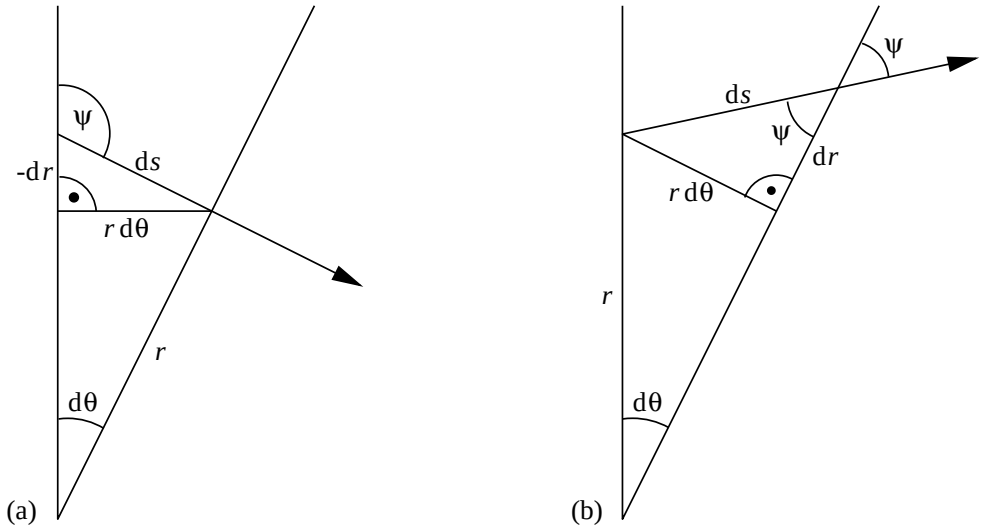

Figure A.3: Change of properties along a ray: (a) near ground-bound points, (b) near sky-bound points

With this expression and Snell's law (A.29), (A.36) and (A.37) can be replaced by

$$\frac{\mathrm{d}s}{\mathrm{d}x} = \frac{\mathrm{d}s}{\mathrm{d}r}\frac{\mathrm{d}r}{\mathrm{d}x} = \frac{1}{\cos\psi}\,\frac{\cos\psi}{1-R\sin^2\psi} = \frac{1}{1-R\sin^2\psi} \tag{A.47}$$

$$= \frac{1}{1-\frac{R}{n^2r^2}c^2} \tag{A.48}$$

$$\frac{\mathrm{d}\theta}{\mathrm{d}x} = \frac{\mathrm{d}\theta}{\mathrm{d}r}\frac{\mathrm{d}r}{\mathrm{d}x} = \frac{\tan\psi}{r}\,\frac{\cos\psi}{1-R\sin^2\psi} = \frac{\sin\psi}{r}\,\frac{1}{1-R\sin^2\psi} \tag{A.49}$$

$$= \frac{c}{n\,r^2}\,\frac{1}{1-\frac{R}{n^2r^2}c^2}\,, \tag{A.50}$$

and the following integral equations for the polar coordinate θ and the path coordinate s are obtained:

$$\theta_i = \theta_{i-1} + \int_{x_{i-1}}^{x_i} \frac{\mathrm{d}\theta}{\mathrm{d}x}\,\mathrm{d}x \tag{A.51}$$

$$= \theta_{i-1} + \int_{x_{i-1}}^{x_i} \frac{1}{1-\frac{R}{n^2r^2}c^2}\,\mathrm{d}x \tag{A.52}$$

$$s_i = s_{i-1} + \int_{x_{i-1}}^{x_i} \frac{\mathrm{d}s}{\mathrm{d}x}\,\mathrm{d}x \tag{A.53}$$

$$= s_{i-1} + \int_{x_{i-1}}^{x_i} \frac{c}{n\,r^2\left(1-\frac{R}{n^2r^2}c^2\right)}\,\mathrm{d}x \tag{A.54}$$

The same terms $n\,r^2$ and $\frac{R}{n^2r^2}$ are evaluated for all individual rays since they describe properties of the atmosphere rather than properties of a ray. In a numerical model, they

can therefore be evaluated once and then stored for subsequent frequent use in the ray tracing calculations.

Using (A.54), the ray path lengths Δs of the individual points can be computed like in Section A.2.2:

$$\Delta s_i = \frac{s_{i+1} - s_{i-1}}{2} , \tag{A.55}$$

for all but the first ($i = 0$) and last ($i = I$) point of a ray, for which

$$\Delta s_1 = s_2 - s_1 \tag{A.56}$$

$$\Delta s_I = s_I - s_{I-1} \tag{A.57}$$

is used to ensure consistency:

$$\sum_{i=1}^{I} \Delta s_i = s_I - s_1 . \tag{A.58}$$

A.4 Solar Coordinates

In the previous sections, expressions for the polar and radius coordinates of a ray were derived in the ray's own ray coordinate system. Owing to the definition of the ray coordinate system with vanishing azimuth coordinates (Section A.1), the problem could be treated in two dimensions. In contrast to this, the computations of the solar zenith and azimuth angles require three-dimensional considerations of the kind presented in this section.

A.4.1 Solar Coordinate System

If Earth's atmosphere is assumed to be spherically symmetrical, then its radiance field is rotationally symmetrical around the axis defined by Earth's and the sun's centres. Both symmetries are accounted for a coordinate system with origin at Earth's centre and the sun on the positive z-axis. The x- and y-axes can still be chosen arbitrarily. I shall call this coordinate system the *solar coordinate system*. The polar coordinate of a point in this coordinate system is identical to its solar zenith angle when refraction is neglected. It shall be called *astronomical solar zenith coordinate* $\theta_\star$. The transformation between the solar coordinate system and any ray coordinate system is a two-dimensional rotation around the origin.

A.4.2 Statement of the Problem

Given a ray with its point's coordinates α in the ray coordinate system and the solar zenith θ_1 and azimuth angles β_1 at the starting point, what are the solar coordinates θ_2 and β_2 at all other ray points? (See Figure A.4 for an illustration of the problem.)

A.4.3 Solution

The problem is solved in three steps:

1. transformation of all point's coordinates from the ray coordinate system into the solar coordinate system
2. identification of the solar zenith angle with the polar coordinate of each point
3. derivation of the solar azimuth angle from two point's coordinates for each point

Coordinate Transformation

Let $(\theta_1, \varphi_1, r_1)$ be the polar, azimuth and radius coordinate of the first point $\mathbf{r}_1$ of a ray in the solar coordinate system and $(\theta_2, \varphi_2, r_2)$ be these coordinates for another point $\mathbf{r}_2$ of the same ray. The angular coordinates are visualised in the top plot of Figure A.4.

Both radius coordinates are identical to those in the ray coordinate system, the polar coordinate of the first point is known, too: It is the astronomical solar zenith angle of the point. The azimuth coordinate of the first point can be chosen arbitrarily. The middle plot of Figure A.4 figure depicts two more angle which are known: The angle α between the two vectors $\mathbf{r}_1$ and $\mathbf{r}_2$ is the latter point's polar coordinate in the ray coordinate system.

The *astronomical solar azimuth angle* $\phi_\star$ is defined as the angle between the projections into a locally horizontal plane of the sun's position and the travelling direction of the ray. For instance, the angle β_1 in the middle plot of Figure A.4 is the astronomical solar azimuth angle at the starting point $\mathbf{r}_1$. It can be calculated as the angle between the projections of the z-axis and the vector $\mathbf{r}_2$ into a plane which is perpendicular to the starting point's vector $\mathbf{r}_1$.

The polar and azimuth coordinates θ_2 and φ_2 of any point $\mathbf{r}_2$ on the ray can be constructed from the angular coordinates of $\mathbf{r}_1$ with a series of rotations $D_{y/z}(\zeta)$ around the y- and z-axes. Here, the index y/z denotes the axis and the argument ζ gives the rotation angle:

$$\begin{aligned}
\mathbf{r}_2 &= D_z(\varphi_1) D_y(\theta_1) D_z(180^\circ - \beta) D_y(\alpha) D_z(-(180^\circ - \beta)) D_y(-\theta_1) D_z(-\varphi_1) \mathbf{r}_1 \\
&= D_z(\varphi_1) D_y(\theta_1) D_z(180^\circ - \beta) D_y(\alpha) \begin{pmatrix} 0 \\ 0 \\ 1 \end{pmatrix} \qquad \text{(A.59)}
\end{aligned}$$

$$\text{with} \quad D_y(\zeta) = \begin{pmatrix} \cos(\zeta) & 0 & \sin(\zeta) \\ 0 & 1 & 0 \\ -\sin(\zeta) & 0 & \cos(\zeta) \end{pmatrix}$$

$$D_z(\zeta) = \begin{pmatrix} \cos(\zeta) & -\sin(\zeta) & 0 \\ \sin(\zeta) & \cos(\zeta) & 0 \\ 0 & 0 & 1 \end{pmatrix}$$

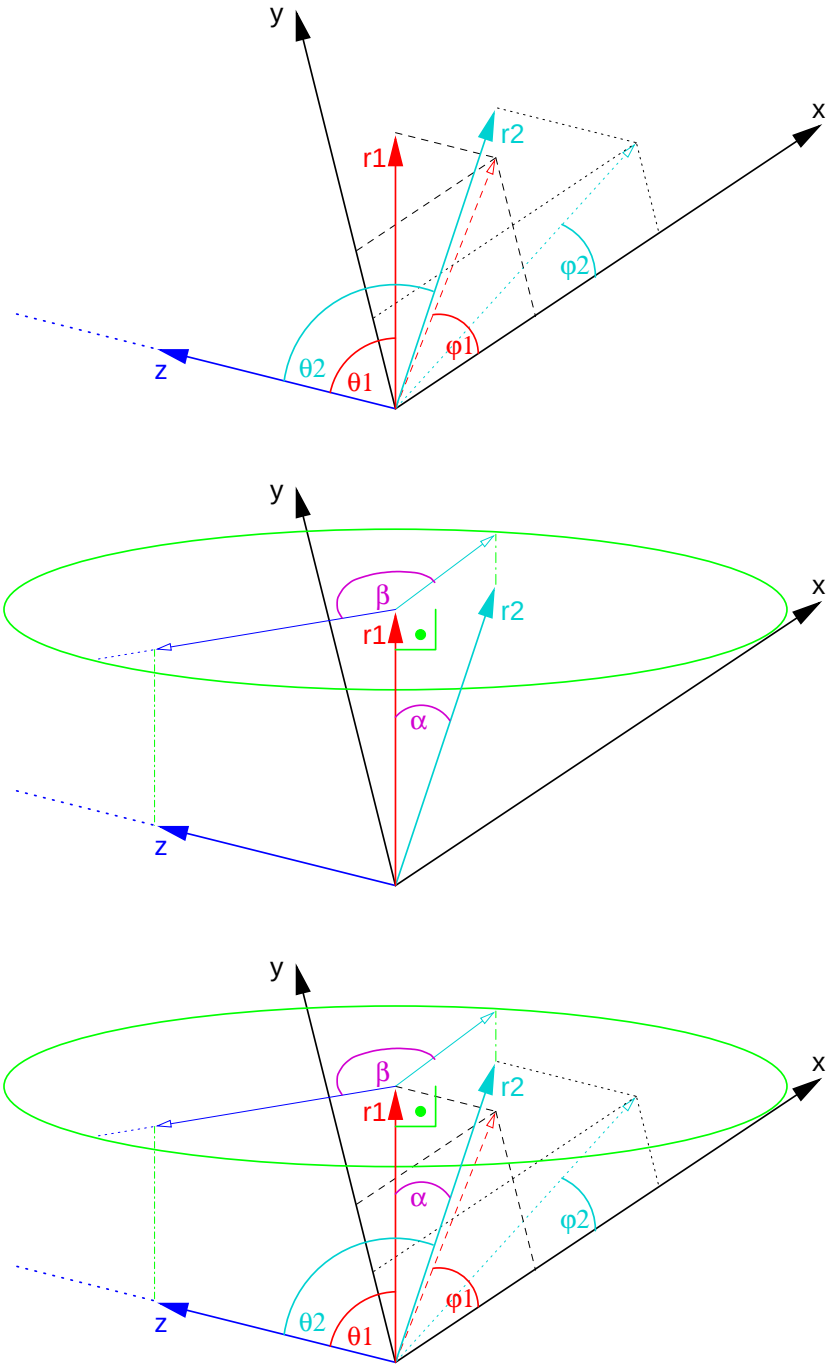

Figure A.4: Ray points in the solar coordinate system. The vectors are normalised to unit length. Top: Angular coordinates of two points. Middle: The angle α between the two points' vectors and the solar azimuth angle $\beta \equiv \beta_1$ at point $\mathbf{r}_1$. The plane perpendicular to $\mathbf{r}_1$ is visualised as green ellipse. The solar azimuth angle β_2 at point $\mathbf{r}_2$ exists in an analogous plane perpendicular to $\mathbf{r}_2$. Bottom: All angles in one plot.

The simplification in (A.59) results from the fact that the series of rotations $D_z(-(180^\circ - \beta))D_y(-\theta_1)D_z(-\varphi_1)$ is constructed to rotate the vector $\mathbf{r}_1$ on the z-axis. Evaluating the rotation matrices in (A.59) yields[3]:

$$\begin{aligned}
\mathbf{r}_2 &= \begin{pmatrix} -\sin(\alpha)\cos(\varphi_1)\cos(\theta_1)\cos(\beta) - \sin(\alpha)\sin(\varphi_1)\sin(\beta) + \cos(\varphi_1)\sin(\theta_1)\cos(\alpha) \\ -\sin(\alpha)\sin(\varphi_1)\cos(\theta_1)\cos(\beta) + \sin(\alpha)\cos(\varphi_1)\sin(\beta) + \sin(\varphi_1)\sin(\theta_1)\cos(\alpha) \\ \sin(\theta_1)\cos(\beta)\sin(\alpha) + \cos(\theta_1)\cos(\alpha) \end{pmatrix} \\
&= \begin{pmatrix} -\cos(\varphi_1)\cos(\theta_1)\cos(\beta) - \sin(\varphi_1)\sin(\beta) & -\cos(\varphi_1)\cos(\theta_1)\sin(\beta) + \sin(\varphi_1)\cos(\beta) & \cos(\varphi_1)\sin(\theta_1) \\ -\sin(\varphi_1)\cos(\theta_1)\cos(\beta) + \cos(\varphi_1)\sin(\beta) & -\sin(\varphi_1)\cos(\theta_1)\sin(\beta) - \cos(\varphi_1)\cos(\beta) & \sin(\varphi_1)\sin(\theta_1) \\ sin(\theta_1)\cos(\beta) & \sin(\theta_1)\sin(\beta) & \cos(\theta_1) \end{pmatrix} \begin{pmatrix} \sin(\alpha) \\ 0 \\ \cos(\alpha) \end{pmatrix} \\
&= \begin{pmatrix} -\cos(\varphi_1)\cos(\theta_1)\cos(\beta) - \sin(\varphi_1)\sin(\beta) & \cos(\varphi_1)\sin(\theta_1) \\ -\sin(\varphi_1)\cos(\theta_1)\cos(\beta) + \cos(\varphi_1)\sin(\beta) & \sin(\varphi_1)\sin(\theta_1) \\ \sin(\theta_1)\cos(\beta) & \cos(\theta_1) \end{pmatrix} \begin{pmatrix} \sin(\alpha) \\ \cos(\alpha) \end{pmatrix} \qquad \text{(A.60)}
\end{aligned}$$

The angular coordinates of vector $\mathbf{r}_2$ can be computed from its Cartesian coordinates (x_2, y_2, z_2) with standard formulae, e.g.:

$$\theta_2 = \begin{cases} \arctan\left(\frac{\sqrt{x_2^2+y_2^2}}{z_2}\right) & (z > 0) \\ \pi + \arctan\left(\frac{\sqrt{x_2^2+y_2^2}}{z_2}\right) & (z < 0) \\ \frac{\pi}{2} & (z = 0) \end{cases} \qquad \text{(A.61)}$$

$$\varphi_2 = \begin{cases} \arccos\left(\frac{x_2}{\sqrt{x_2^2+y_2^2}}\right) & (y > 0) \\ -\arccos\left(\frac{x_2}{\sqrt{x_2^2+y_2^2}}\right) & (y < 0) \\ 0 & (y = 0 \wedge x \geq 0) \\ \pi & (y = 0 \wedge x < 0) \end{cases} \qquad \text{(A.62)}$$

$$\text{(A.63)}$$

Solar Zenith Angle

The astronomical solar zenith angle $\theta_{\star i}$ of any point on a ray is given by its polar coordinate θ_i in the solar coordinate system.

***–¿ In purely geometrical ray tracing, $\theta_{\star i}$ is identical to the apparent solar zenith angle.

In a model with refractive bending the apparent solar zenith angle has to be determined iteratively. ¡–***

Solar Azimuth Angle

The astronomical solar azimuth angle $\phi_{\star i}$ of a point $\mathbf{r}_i$ is denoted β in the middle plot of Figure A.4. Being the angle between the projections of the z-axis and the vector $\mathbf{r}_2$

[3]This operation has been performed with the symbolic algebra program `Maple V`. Alternatively, `Mathematica`, `MuPad` or `Octave` can be used.

into a plane which is perpendicular to the vector $\mathbf{r}_i$, it can be calculated from $\mathbf{r}_i$ and a succeeding point $\mathbf{r}_2$ of the same ray:

$$\phi_{\star i} = \arcsin \frac{(\mathbf{p}_2 \bullet \mathbf{p}_z)}{|\mathbf{p}_2|\,|\mathbf{p}_z|} \tag{A.64}$$

$$\text{with:} \quad \mathbf{p}_2 = \mathbf{r}_2 - \frac{(\mathbf{r}_i \bullet \mathbf{r}_2)}{|\mathbf{r}_i|^2}\,\mathbf{r}_i \tag{A.65}$$

$$\mathbf{p}_z = (0,0,1)^T - \frac{\left(\mathbf{r}_i \bullet (0,0,1)^T\right)}{|\mathbf{r}_i|^2}\,\mathbf{r}_i\ , \tag{A.66}$$

where $(.\bullet.)$ denotes the inner product for vectors. The $|\mathbf{r}_i|^2$ terms can be ignored as the vectors $\mathbf{r}_i$ are normalised to unity, compare (A.60).

Appendix B

Detailed Weighting Functions

In this chapter weighting functions of the main retrieval target trace gases of SCIAMACHY are shown in plots exactly analogous to Figures 9.5–9.7 of Section 9.2.

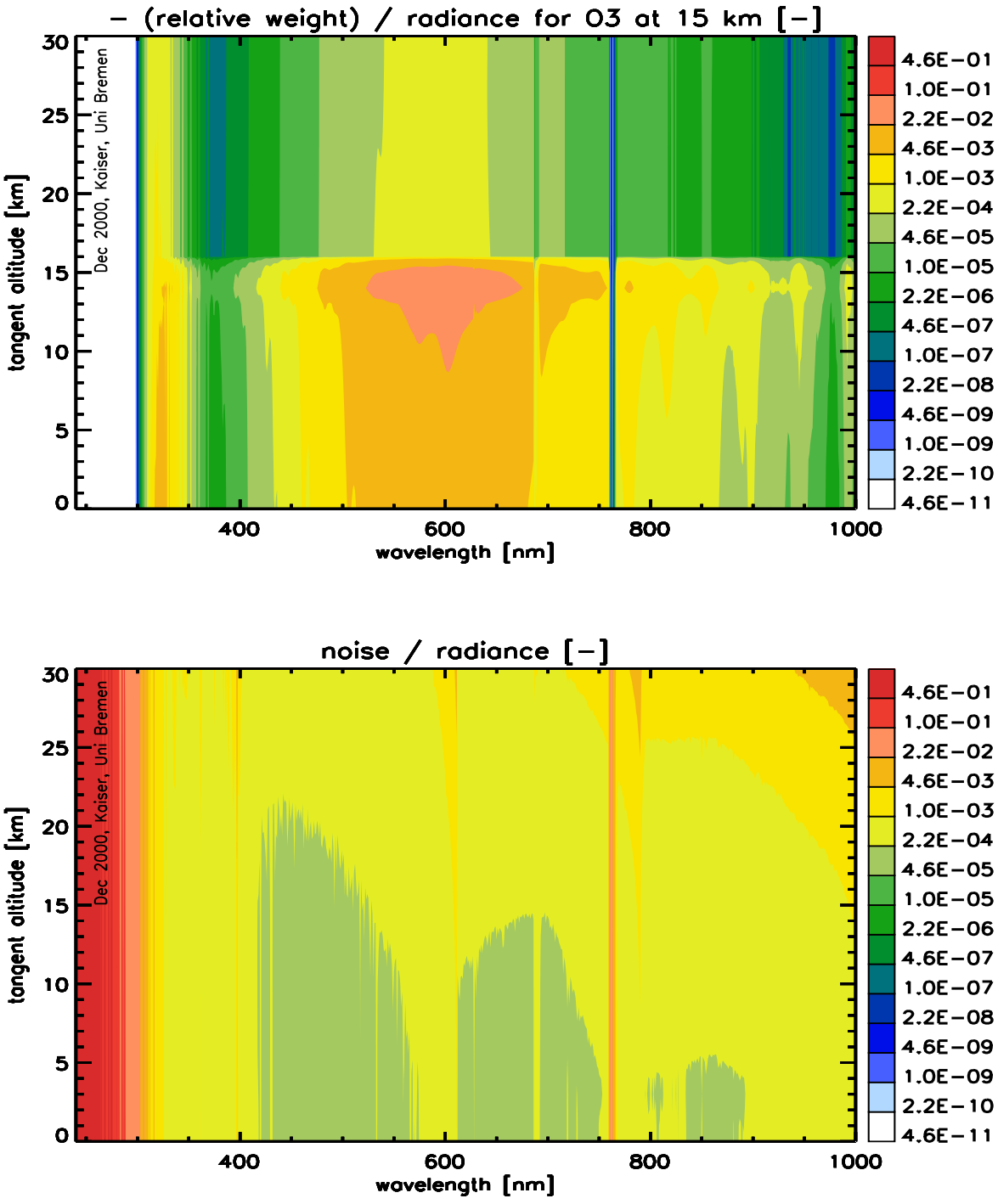

Figure B.1: Relative-relative weighting function of the 15 km-level of the O_3 profile (top) and SCIAMACHY's relative noise (bottom).

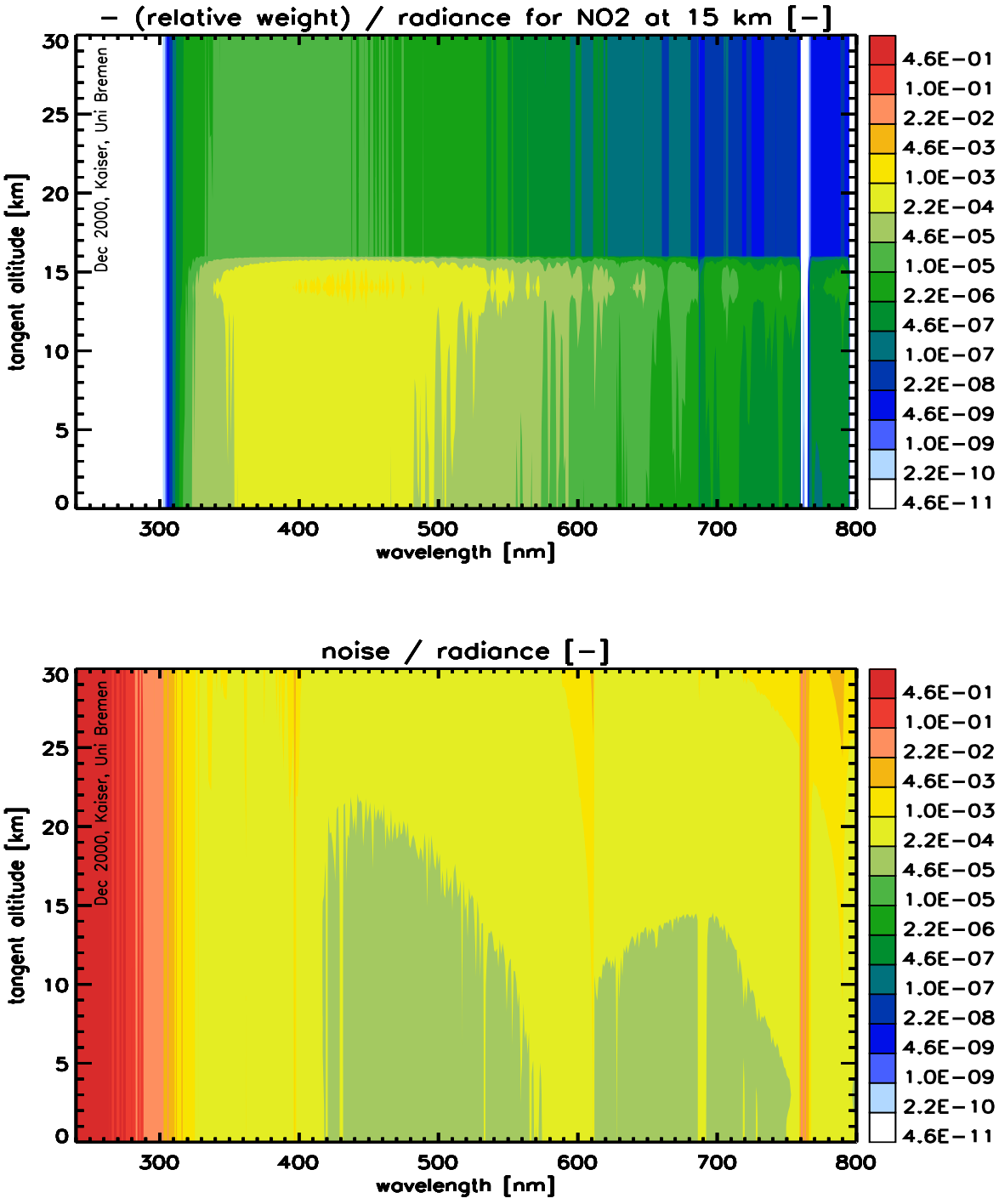

Figure B.2: Relative-relative weighting function of the 15 km-level of the NO_2 profile (top) and SCIAMACHY's relative noise (bottom).

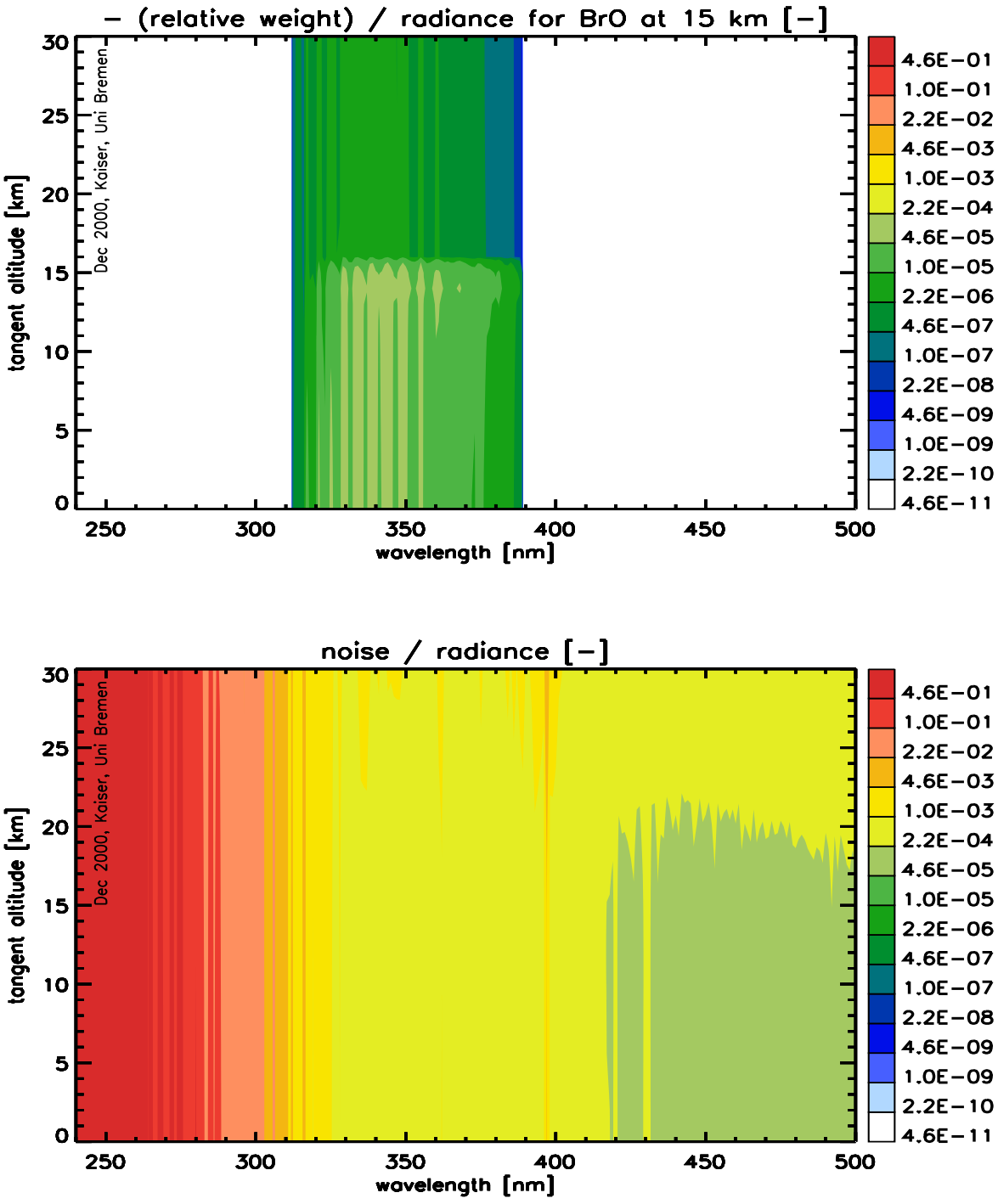

Figure B.3: Relative-relative weighting function of the 15 km-level of the BrO profile (top) and SCIAMACHY's relative noise (bottom).

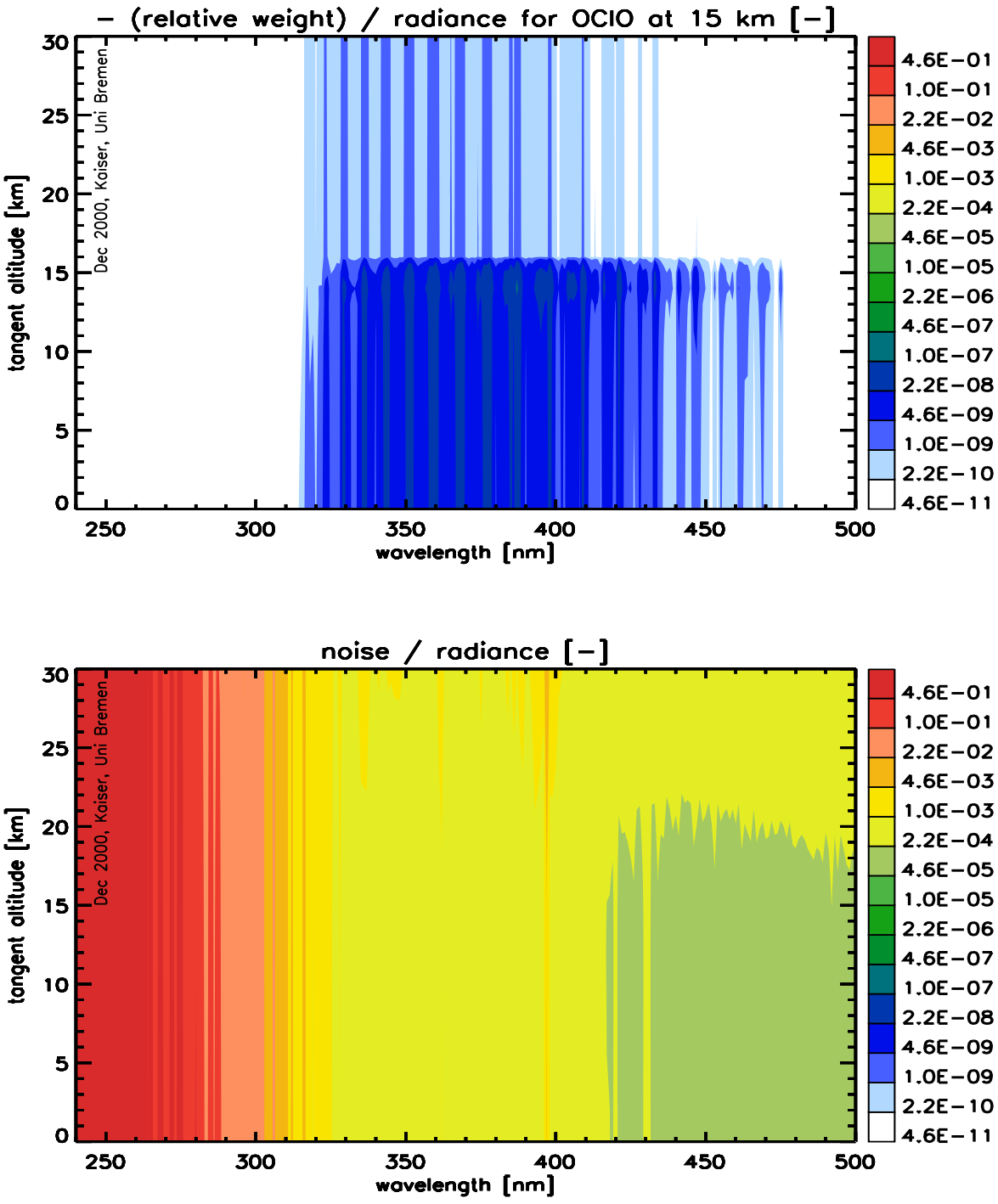

Figure B.4: Relative-relative weighting function of the 15 km-level of the OClO profile (top) and SCIAMACHY's relative noise (bottom).

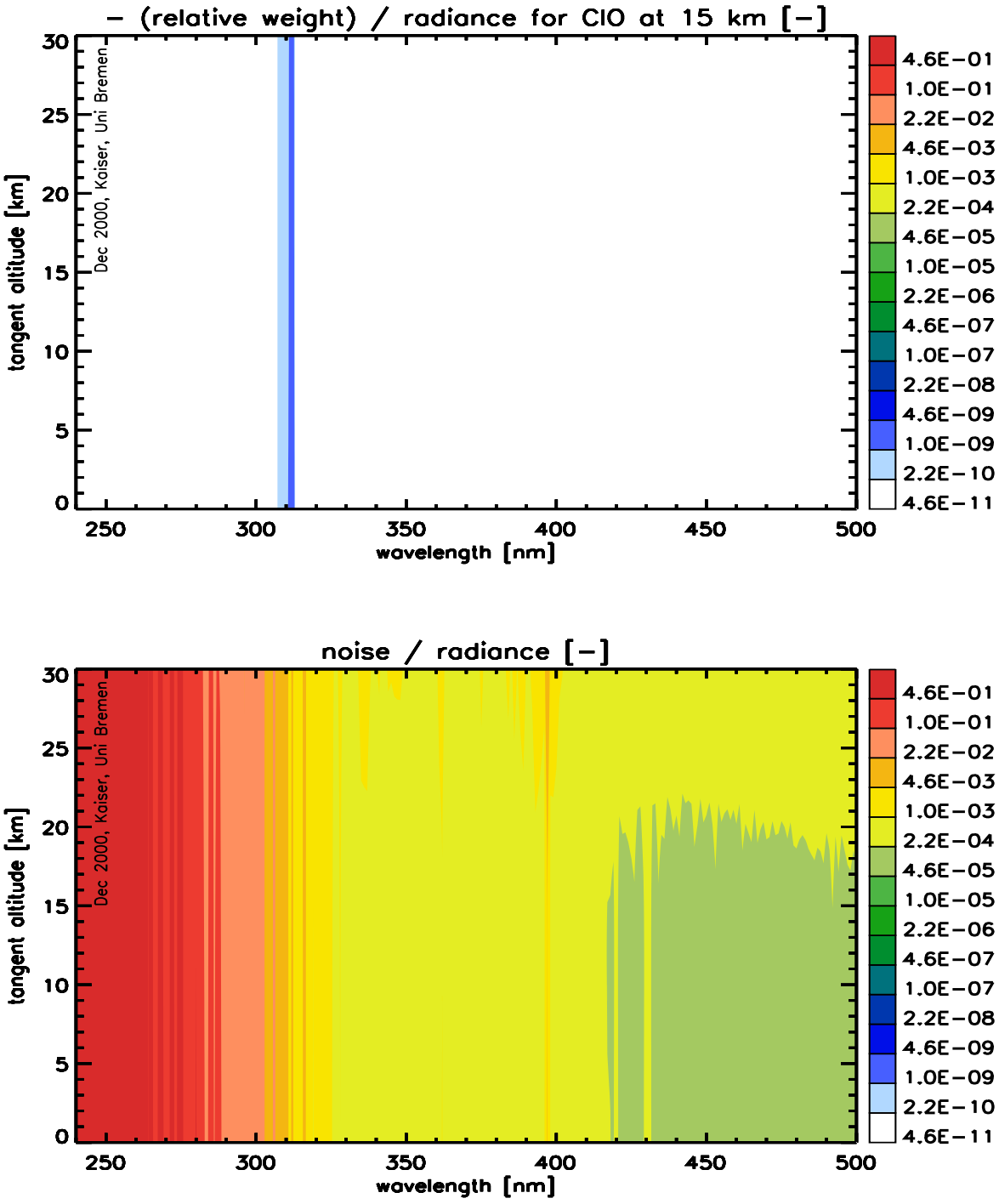

Figure B.5: Relative-relative weighting function of the 15 km-level of the ClO profile (top) and SCIAMACHY's relative noise (bottom).

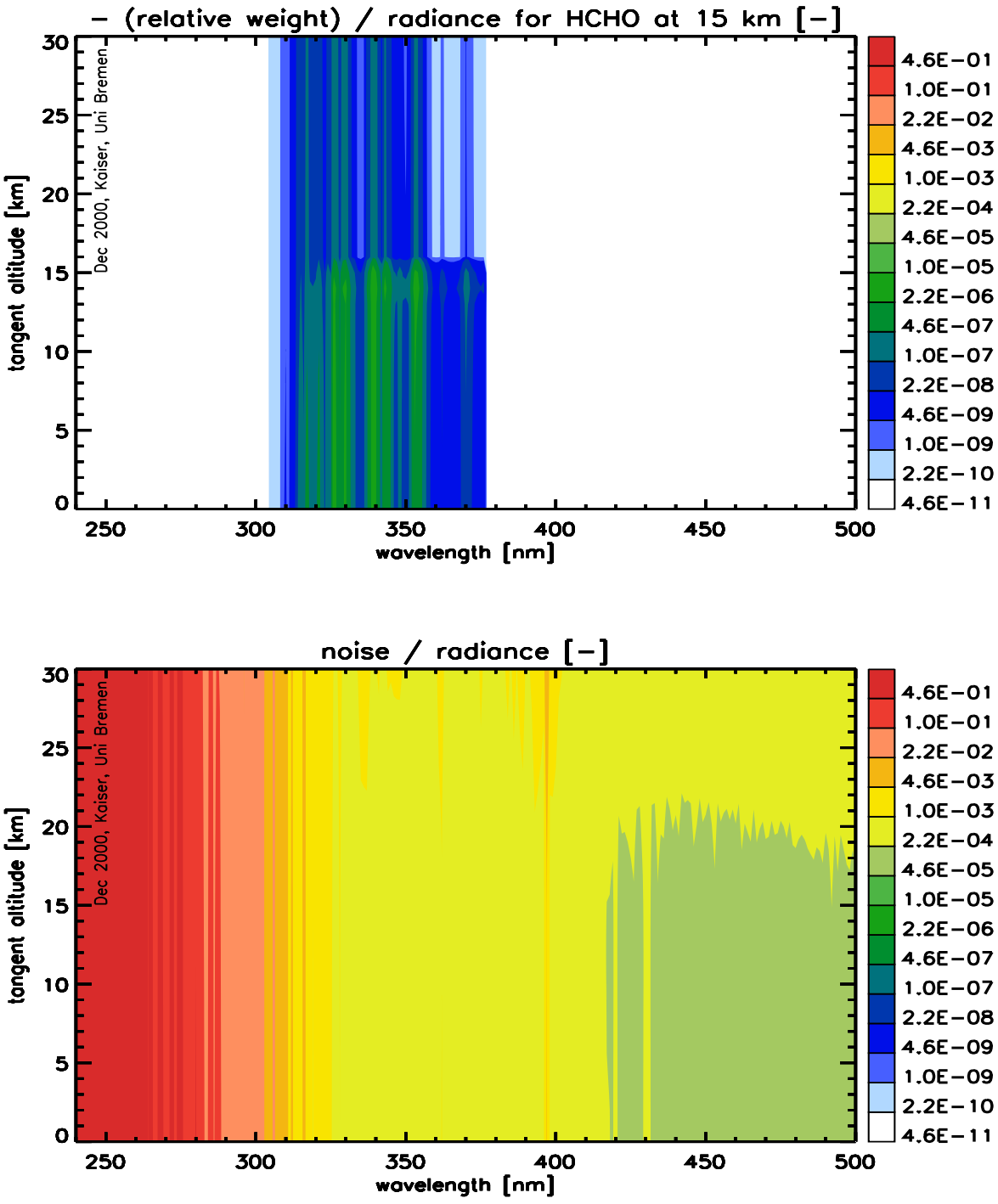

Figure B.6: Relative-relative weighting function of the 15 km-level of the HCHO profile (top) and SCIAMACHY's relative noise (bottom).

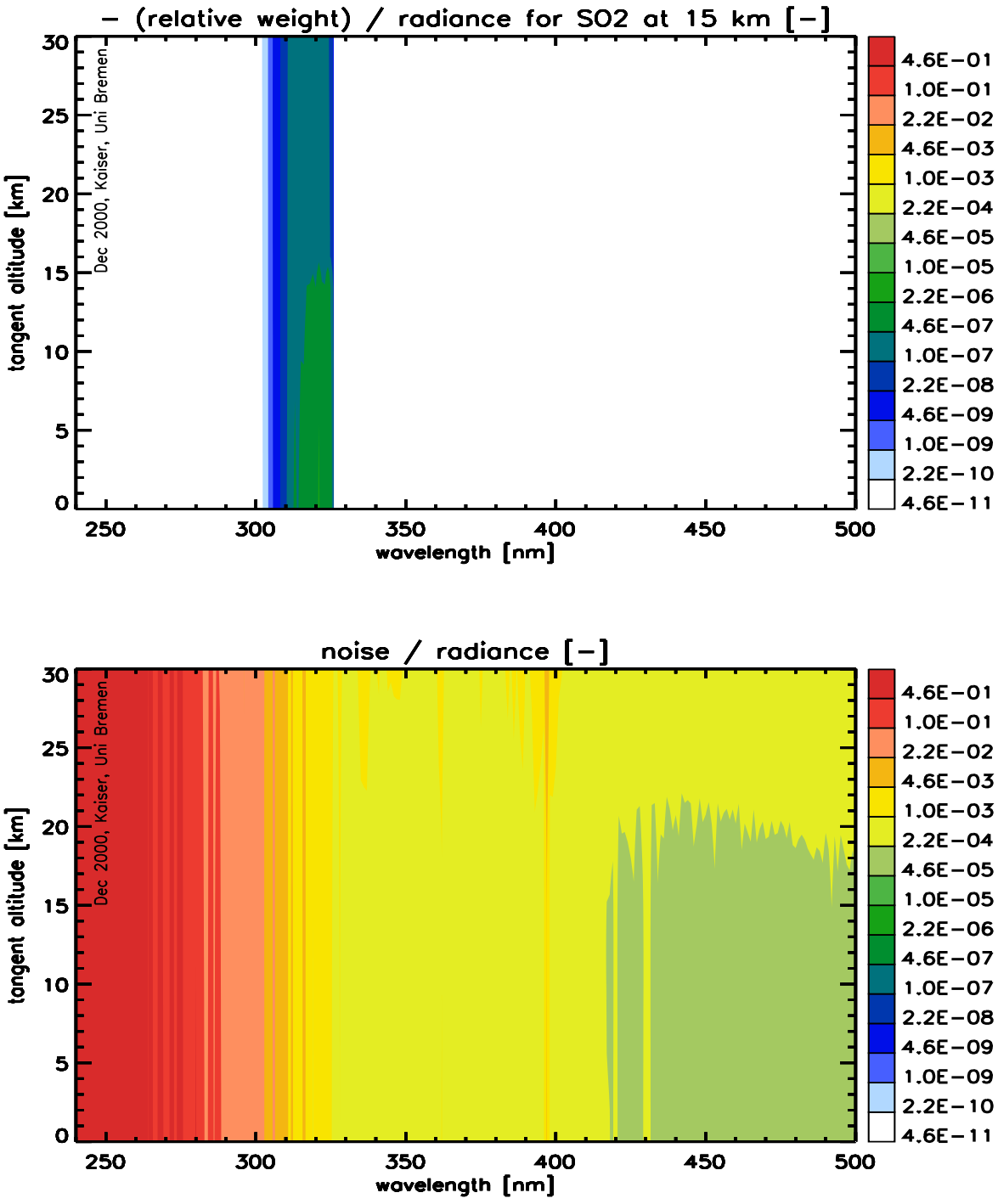

Figure B.7: Relative-relative weighting function of the 15 km-level of the SO_2 profile (top) and SCIAMACHY's relative noise (bottom).

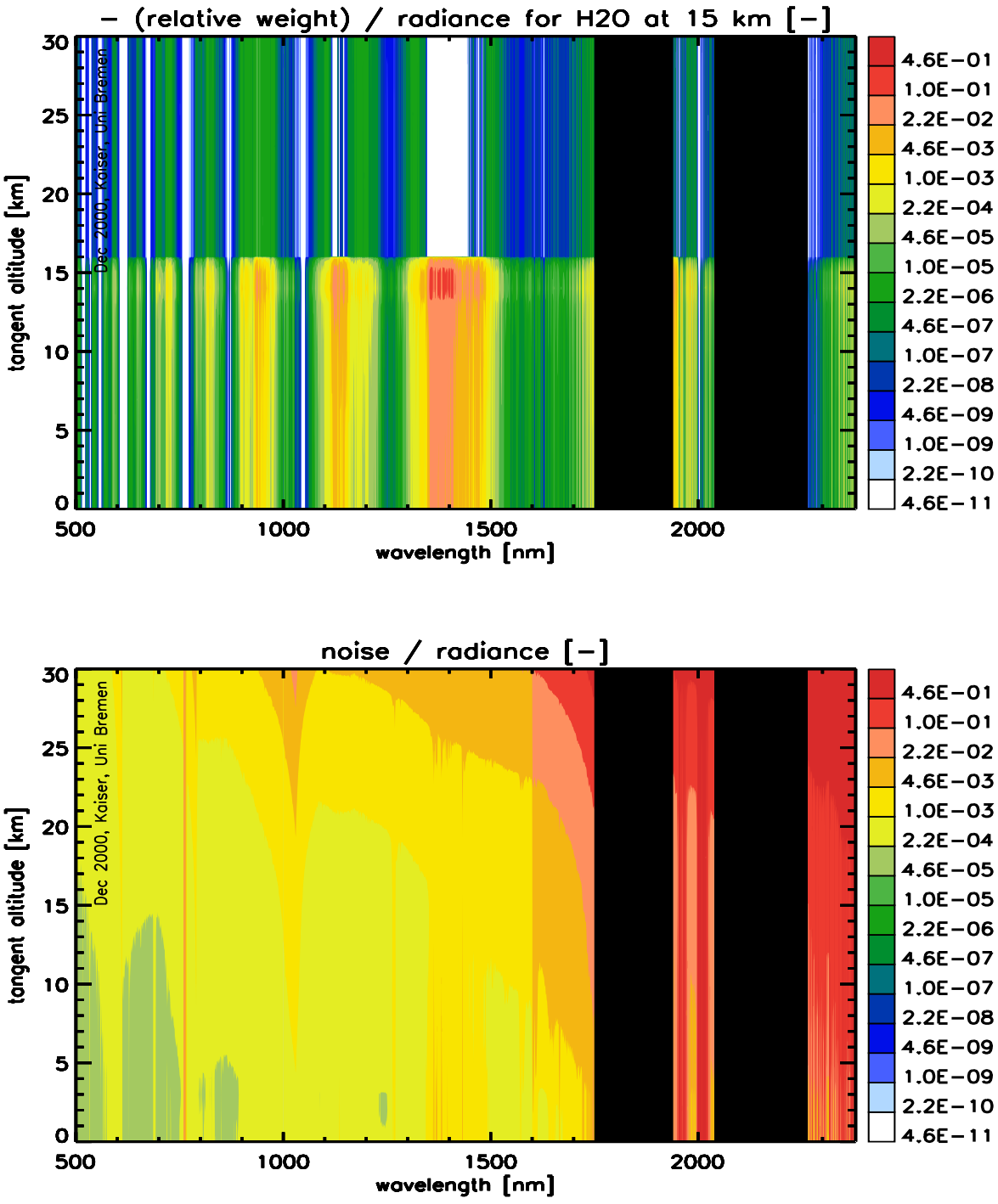

Figure B.8: Relative-relative weighting function of the 15 km-level of the H_2O profile (top) and SCIAMACHY's relative noise (bottom).

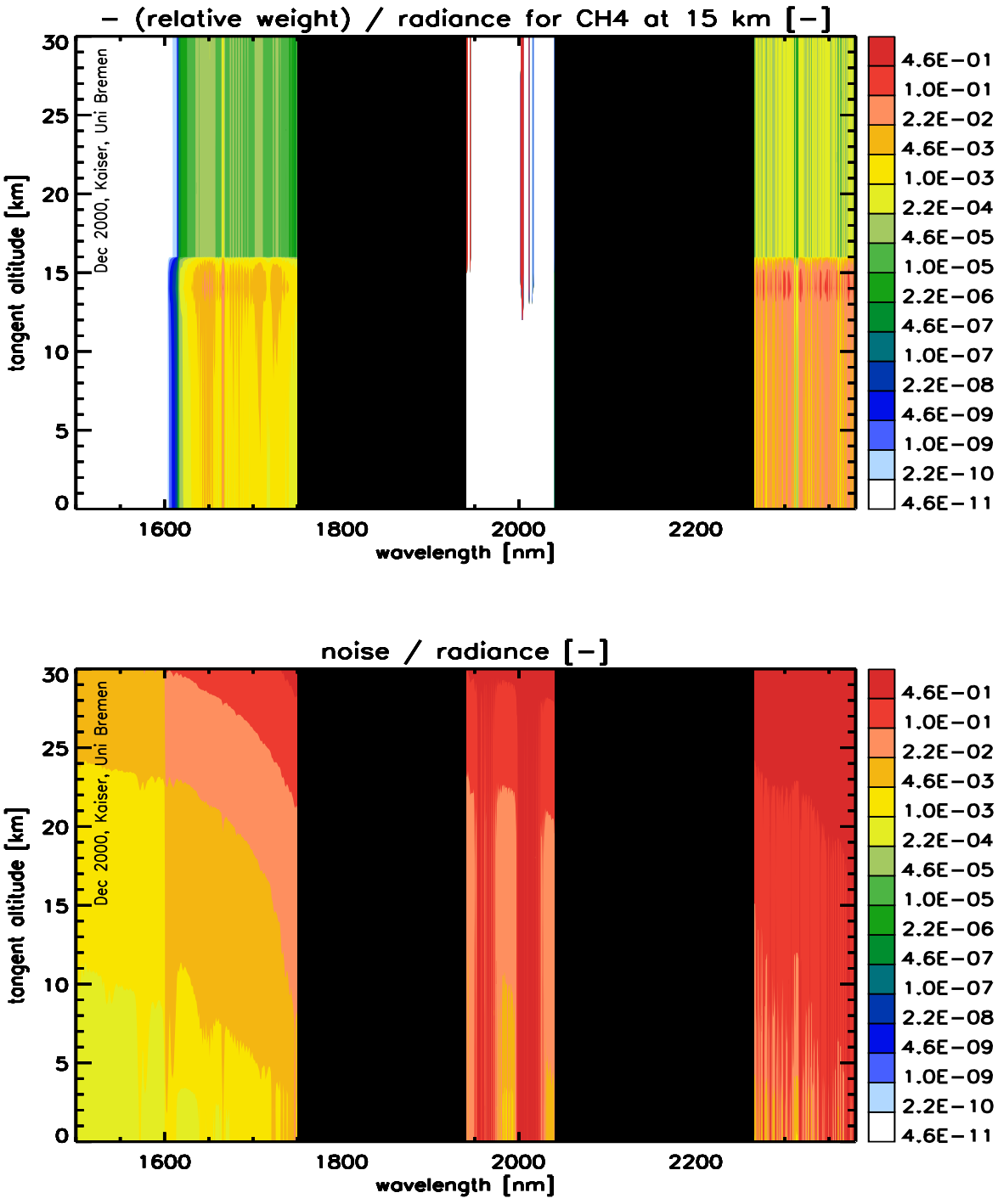

Figure B.9: Relative-relative weighting function of the 15 km-level of the CH_4 profile (top) and SCIAMACHY's relative noise (bottom).

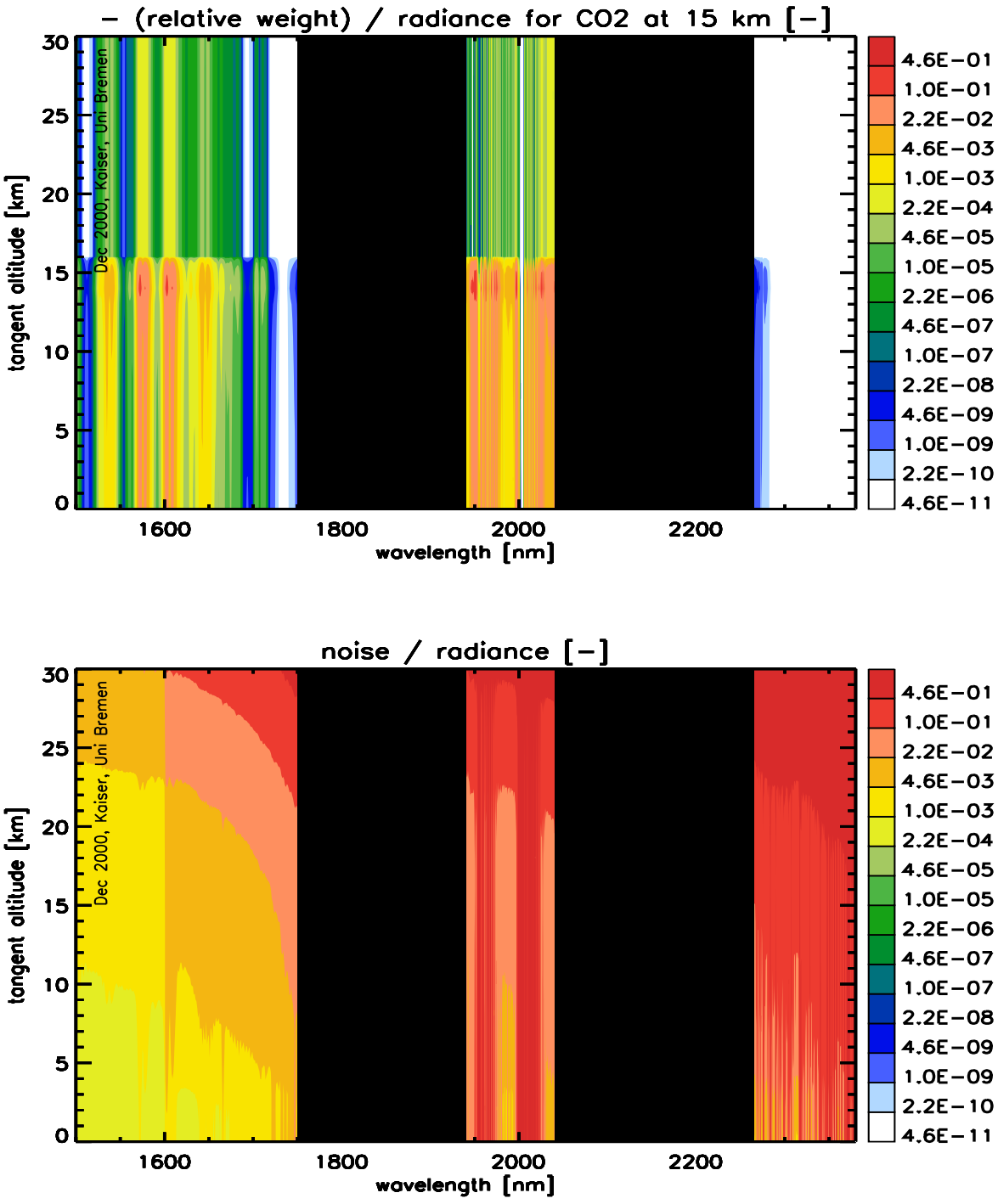

Figure B.10: Relative-relative weighting function of the 15 km-level of the CO_2 profile (top) and SCIAMACHY's relative noise (bottom).

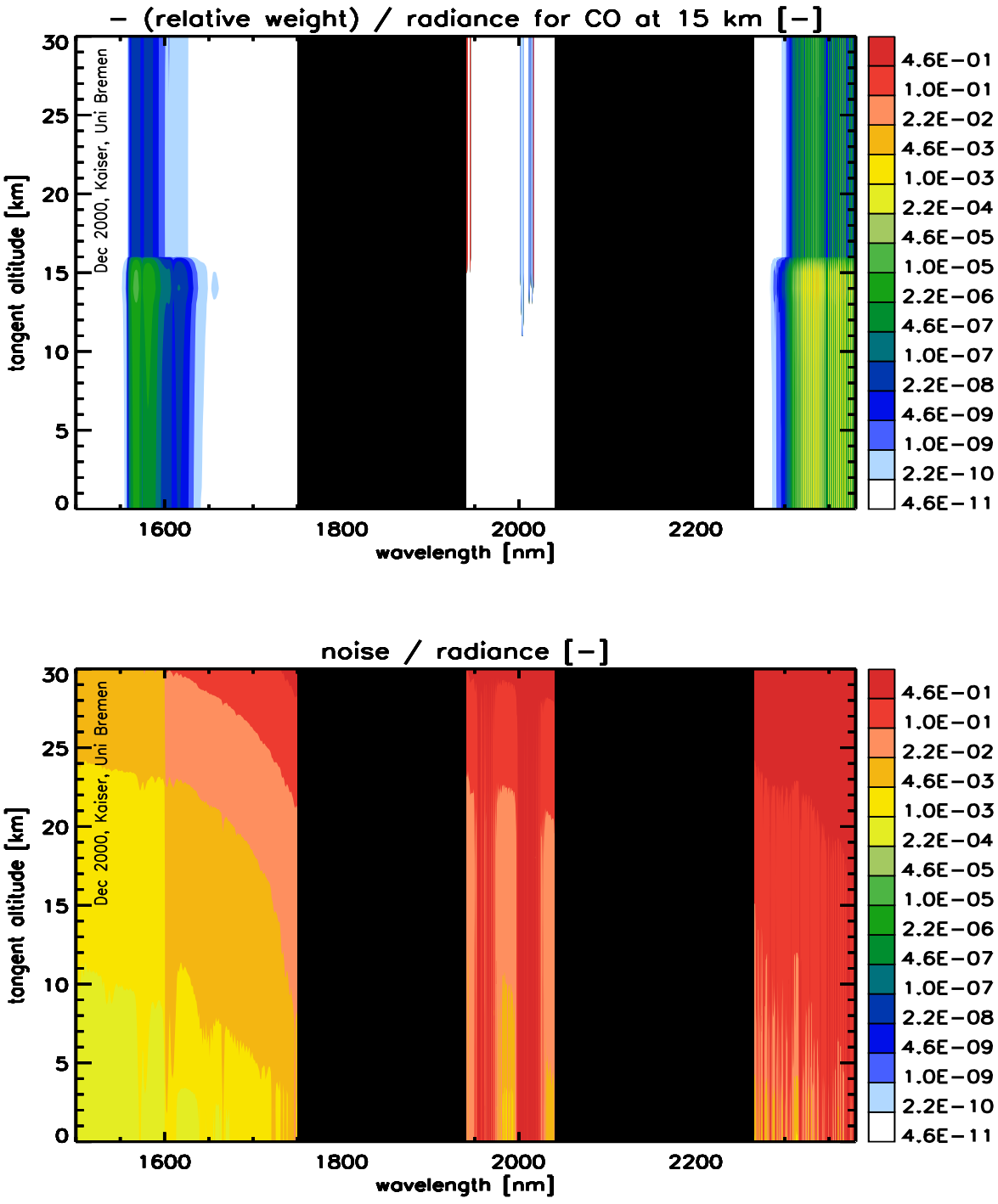

Figure B.11: Relative-relative weighting function of the 15 km-level of the CO profile (top) and SCIAMACHY's relative noise (bottom).

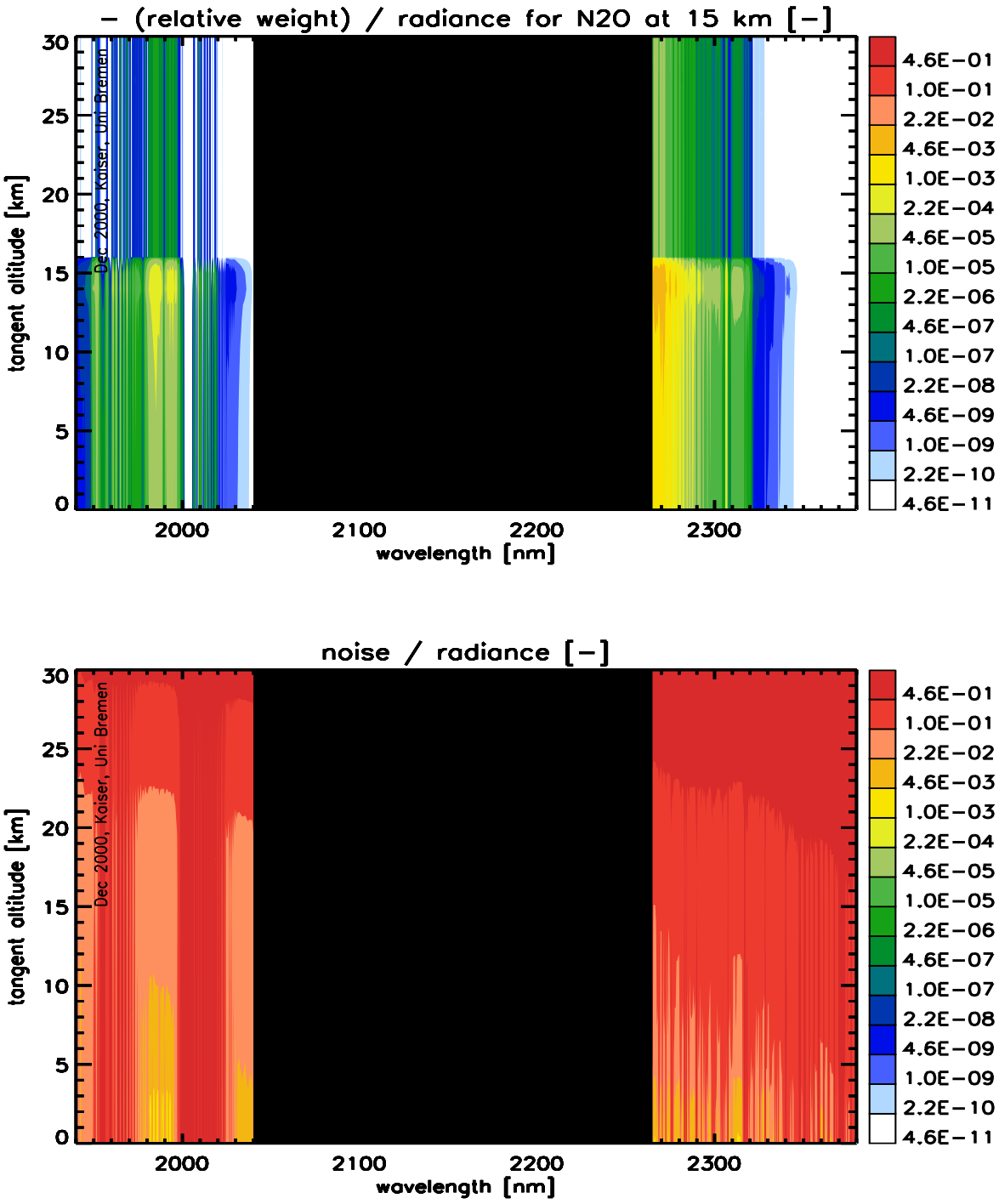

Figure B.12: Relative-relative weighting function of the 15 km-level of the N_2O profile (top) and SCIAMACHY's relative noise (bottom).

Appendix C

Curriculum Vitae

	Identification
name	Johannes W. Kaiser
date of birth	April 3, 1969
place of birth	Freiburg im Breisgau, Germany
	School Education
1975–79	*Grundschule*, Erftstadt and Bayreuth
1979–88	*Anne-Frank-Gymnasium*, Aachen
1988	degree: *Abitur* (grade: *1.6*)
	University Education
1988–89	mechanical engineering, *Technische Universität Berlin* (*TUB*)
1989–92	physics, TUB
1992–93	physics, *University of Canterbury* (*UC*), Christchurch, New Zealand
1993–96	physics, TUB
1996	degree: *Physik-Diplom* (grade: *sehr gut*)
1989–95	philosophy, *Freie Universität Berlin* and *Humboldt Universität Berlin*
	Practical Work, Cooperation and Employment
1988	3 months in the workshop of the *Kernforschungsanlage Jülich* (KFA)
1992	honours 3 project at the UC in cooperation with the *Department of Scientific and Industrial Research*, Lauder, New Zealand
1997–present	research scientist within the SCIAMACHY project at the *Institut für Fernerkundung*, Universität Bremen

Summer and Spring Schools

1996	*Numerische Lineare Algebra*, Hamburg-Harburg, Germany
1997	*Advanced Study Course on Tropospheric Chemistry and Space Observation*, Riom, France
1998	*Mathematische Methoden und Computeralgebra in der Physik*, Halle, Germany
2001	*Oxford/RAL Springschool on Quantitative Earth Observation*, Oxford, UK

Military Service

1987–96	*Ersatzdienst*, fire brigades in Aachen and Berlin

Appendix D

List of Publications

Printed Publications (first author):

Johannes W. Kaiser, Vladimir V. Rozanov, and John P. Burrows. Theoretical precisions for SCIAMACHY limb retrieval. *Advances in Space Research*, 2001. accepted.

Johannes W. Kaiser, K.-U. Eichmann, V.V. Rozanov, and J.B. Burrows. Precision estimates for SCIAMACHY limb retrievals. *Proc. IGARSS 2001*, IEEE, 2001.

Johannes W. Kaiser, Alexei V. Rozanov, Vladimir V. Rozanov, and John P. Burrows. Evaluation of approximative radiative transfer models intended for retrievals from limb measurements. In William L. Smith and Yuriy M. Timofeyev, editors, *IRS 2000: Current Problems in Atmospheric Radiation*, St.-Petersburg, Russia, 2001. St.-Petersburg State University, A. DEEPAK Publishing. accepted.

Johannes W. Kaiser, Vladimir V. Rozanov, and John P. Burrows. Stratospheric O_3 and NO_2 profile theoretical accuracies from SCIAMACHY limb measurements. In N.R.P. Harris, M. Guirlet, and G.T. Amanatidis, editors, *Stratospheric Ozone 1999: Proceedings of the Fifth European Workshop*, pages 779–782. European Commission. 2000. Air pollution research report 73.

Johannes W. Kaiser, Vladimir V. Rozanov, Michael Buchwitz, and John P. Burrows. Steps towards limb profile retrieval using a spherical radiative transfer model based on the single scattering approximation. In *Proceedings of ESAMS '99*, pages 771–777. Noordwijk, The Netherlands, 1999. ESA-ESTEC.

Johannes Kaiser, Michael Buchwitz, Heinrich Bovensmann, and John P. Burrows. SCIAMACHY on ENVISAT-1. In N.Chaumerliac, G. Mégie, N. Papineau, and G. Angeletti, editors, *Proceedings of the Advanced Study Course on Tropospheric Chemistry and Space Observation*, pages 255–256. European Commission, 1998. Air Pollution Research Report No. 65.

Johannes Kaiser. *Numerische Behandlung chemischer Ratennetzwerke für die Modellierung sauerstoffreicher stellarer Umgebungen*. Diplomarbeit, Technische Universität Berlin, Institut für Astronomie und Astrophysik, 1996.

Johannes Kaiser. *Profile Inversion for Retrieval of Vertical Distribution of Atmospheric Methane*. Fourth year project, University of Canterbury, Physics Department, Christchurch, New Zealand, 1992.

Printed Publications (co-author):

S. Noël, H. Bovensmann, J.P. Burrows, and J.W.Kaiser. SCIAMACHY – a hyperspectral sensor for global atmospheric studies. In *Proc. IGARSS 2001*, IEEE, 2001.

E. Kyrölä, T. Siiskonen, L. Oikarinen, H. Auvinen, G.W. Leppelmeier, A. Hauchecorne, J. Burrows, V. Rozanov, J. Kaiser, A. Rozanov, J. Stegman, G. Witt, D. Murtagh, E.J. Llewellyn, D.A. Degenstein, R.L. Gattinger, D. Flittner, R. Loughman, I. McDade, B. Solheim, C.S. Haley, W. Evans, K. Strong, E. Hilsenrath, and R. McPeters. Intercomparison of limb radiance measurements. In *Proceedings of SCIAMACHY validation group meeting*, May 2001. ESA-ESTEC. accepted.

R. Müller, H. Bovensmann, M. Bruns, J.P. Burrows, V. Eyring, J. Kaiser, A. Richter, J. Trentmann, and F. Wittrock. Interpretation of BrO slant column measurements using the model package SLACO. In *Proceedings of ESAMS '99*, Noordwijk, The Netherlands, 1999. ESA-ESTEC.

Oral and Poster Presentations at Conferences and Workshops:

International Geopscience and Remote Sensing Symposium (*IGARSS*) 2001, Sydney, Australia

Oxford/RAL Spring School in Quantitative Earth Observation 2001, Oxford, UK

International Radiation Symposium (*IRS*) 2000, St. Petersburg, Russia

Committee On Space Reasearch (*COSPAR*) Scientific Assembly 2000, Warsaw, Poland

European Geophysical Society (*EGS*) General Assembly 2000, Nice, France

American Geophysical Union (*AGU*) Fall Meeting 1999, San Francisco, CA, USA

European Symposium on Stratospheric Ozone 1999, St. Jean de Luz, France

International Workshop on Microwave Radiative Transfer Modelling in Bredbeck 1999, Bremen, Germany

European Symposium on Atmospheric Mearurements from Space (*ESAMS*) 1999, Noordwijk, The Netherlands

GOME & SCIAMACHY Data & Algorithm Scientific Working Sessions 1998, Frascati, Italy

Advanced Study Course on Tropospheric Chemistry and Space Observation 1997, Riom, France

Frühjahrestagung der Deutschen Physikalischen Gesellschaft (*DPG*) 1997, Regensburg, Germany

Appendix E

I Declare …

Hiermit erkläre ich, dass ich

1. diese Arbeit ohne unerlaubte fremde Hilfe angefertigt habe,
2. keine anderen als die von mir angegebenen Quellen und Hilfsmittel benutzt habe und
3. die den benutzten Werken wörtlich oder inhaltlich entnommenen Stellen als solche kenntlich gemacht habe.

Acknowledgements

Very many colleagues provided all sorts of help during my studies for this thesis. Most prominently, neither the SCIAMACHY project nor the large multi-facetted work group at the Institute of Environmental Physics in Bremen can be imagined without the visionary enthusiasm of **John Burrows**. His personal support and the contact to the different people in Bremen have been very stimulating for me.

Vladimir Rozanov and **Michael Buchwitz** have introduced me to the modelling of atmospheric radiative transfer and to many secrets of GOMETRAN. They have also been available for scientific advice again and again. **Heinrich Bovensmann** has splendidly performed in the indispensable job of coordinating and leading the activities of Bremen's SCIAMACHY group.

Liisa Oikarinen (FMI, Helsinki), **Richard Müller**, **Alexei Rozanov**, **Stefan Noël**, and **Ruud Hoogeveen** (SRON, Utrecht) have been congenial partners in my scientific work and provided important input data used in this thesis.

I have enjoyed many inspiring scientific discussions with **Stefan Bühler**, **Kai-Uwe Eichmann**, **Rüdiger de Beek**, **Ute Böttger** (DLR, Berlin), **Peter Spietz**, **Jerome Meyer**, **Klaus Bramstedt**, **Wolfgang von Hoyningen-Huene**, **Martin Freitag**, **Jacek Stegman** (MISU, Stockholm), and **Philippe Baron** (MISU, Stockholm). These have also proofread my thesis.

The solution of all those little every-day issues has sometime even been enjoyable owing to **Julian Meyer-Arnek**, **Folkard Wittrock**, **Manfred Wuttke**, **Jochen Skupin**, **Sabine Packeiser**, **Heidemarie Krug**, and **Heiko Schellhorn**.

I would not be anywhere near this lucky present without **Andrea Weiss** (EMPA, Zurich).

Thank you all!

Bibliography

C. Appenzeller, A. K. Weiss, and J. Staehelin. North Atlantic Oscillation modulates total ozone winter trends. *Geophys. Res. Let.*, 27:1131–1134, 2000.

B. Backus and L. Gilbert. Uniqueness in the inversion of inaccurate gross earth data. *Philosophical Transactions of the Royal Society of London*, 266:123–192, 1970.

George Backus and Freeman Gilbert. The resolving power of gross earth data. *Geophysical Journal of the Royal Astronomical Society*, 16:169–205, 1968.

M. Balluch and D.J. Lary. Refraction and atmospheric photochemistry. *JGR/A*, 102(D7): 8845–8854, 1997.

C.A. Barth, D.W. Rusch, R.J. Thomas, G.H. Mount, G.J. Rottman, G.E. Thomas, R.W. Sanders, and G.M. Lawrence. Solar mesosphere explorer: Scientific objectives and results. *GRL*, 10(4):237–240, 1983.

D.R. Bates and M. Nicolet. Atmospheric hydrogen. *Publ. Astron. Soc. Pac.*, 62, 1950.

E.R. Bates. Rayleigh scattering by air. *Planet. Space Sci.*, 32(6):785–790, 1984.

J.L. Bertaux, G. Megie, T. Widemann, E. Chassefiere, R. Pellinen, E. Kyrölä;, S. Korpela, and P. Simon. Monitoring of ozone trend by stellar occultations: The GOMOS instrument. *Adv. Space Res.*, 11(3):237–242, 1991.

BMU. *Aktuell: Schutz der Ozonschicht*. Bundesministerium für Umwelt, Naturschutz und Reaktorsicherheit, Berlin, Sep 2000.

K. Bogumil, J. Orphal, and J.P. Burrows. Reference spectra of atmospheric relevant trace gases measured with the SCIAMACHY PFM satellite spectrometer. In *Proceedings of Atmospheric Spectroscopy Applications 1999*, pages 133–136, UPRESA Q 6089, URF Sciences Exactes et Naturelle, BP 1039—51687 Reims Cedex 2—France, 1999. Groupe de Spectrométrie Moléculaire et Atmosphérique.

Konstanze Bogumil. *SCIAMACHY Calibration*. Dissertation, Universität Bremen, Institut für Umweltphysik, 2001. draft version.

H. Bovensmann, J.P. Burrows, M. Buchwitz, J. Frerick, S. Noël, V.V. Rozanov, K.V. Chance, and A.P.H.Goede. SCIAMACHY: Mission objectives and measurement modes. *Journal of the Atmospheric Sciences*, 56(2):127–150, 1999.

A.W. Brewer. Evidence for a world circulation provided by the measurements of helium and water vapor distributions in the stratosphere. *Q. J. R. Meteorol. Soc.*, 75:351–363, 1949.

Joachim Bublath. *Geheimnisse unseres Universums*. Droemer, München, 1999.

M. Buchwitz, V. V. Rozanov, and J. P. Burrows. Development of a correlated-k distribution band model scheme for the radiative transfer program GOMETRAN/SCIATRAN for retrieval of atmospheric constituents from SCIAMACHY/ENVISAT-1 data. In J. E. Russell, editor, *Satellite Remote Sensing of Clouds and the Atmosphere III*, volume 3495, pages 171–186, 1998. European Symposium on Remote Sensing, 21-24 Sept. 1998, Barcelona, Spain.

Michael Buchwitz. *Strahlungstransport- und Inversions-Algorithmen zur Ableitung atmosphärischer Spurengasinformationen aus Erdfernerkundungsmessungen in Nadirgeometrie im ultravioletten bis nahinfraroten Spektralbereich am Beispiel SCIAMACHY*. Doktorarbeit, Universität Bremen, FB 1, 28353 Bremen, Germany, 2000.

Michael Buchwitz, Vladimir V. Rozanov, and John P. Burrows. A correlated-*k* distribution scheme for overlapping gases suitable for retrieval of atmospheric constituents from moderate resolution radiance measurements in the visible/near-infrared spectral region. *JGR*, 2000. in press.

John P. Burrows, Mark Weber, Michael Buchwitz, Vladimir Rozanov, Annette Ladstätter-Weißmayer, Andreas Richter, Rüdiger DeBeek, Ricarda Hoogen, Klaus Bramstedt, Kai-Uwe Eichmann, and Michael Eisinger. The global ozone monitoring experiment (GOME): Mission concept and first scientific results. *J. Atmos. Sci.*, 56: 151–175, 1999.

J.P. Burrows. Current and future passive remote sensing techniques used to determine atmospheric constituents. In A.F. Bouwman, editor, *Approaches to Scaling of Trace Gas Fluxes in Ecosystems*, number 24 in Developments in Atmospheric Science. Elsevier Science B.V., 1999.

J.P. Burrows, A. Dehn, B. Deters, S. Himmelmann, A. Richter, S. Voigt, and J. Orphal. Atmospheric remote-sensing reference data from GOME: 1. temperature-dependent absorption cross sections of NO_2 in the 231–794 nm range. *JQSRT*, 60:1025–1031, 1998.

T.R. Caudill, D.E. Flittner, B.M. Herman, O. Torres, and R.D. McPeters. Evaluation of the pseudo-spherical approximation for backscattered ultraviolet radiances and ozone retrieval. *GJR*, 102(D3):3881–3890, 1997. limb.

S. Chandrasekhar. *Radiative Transfer*. Dover Publications, Inc., New York, 1960. originally published in 1950.

S. Chapman. A theory of upper atmospheric ozone. *Memoirs of the Roy. Meteo. Soc*, 3: 103–125, 1930.

W.P. Chu, M.P. McCormick, J. Lenoble, C. Brogniez, and P. Pruvost. SAGE II inversion algorithm. *JGR/A*, 94(D6):8339–8351, 1989.

Kinsell L. Coulson. *Polarization and Intensity of Light in the Atmosphere*. A. DEEPAK Publishing, 1988.

P.J. Crutzen. The influence of nitrogen oxides on the atmospheric ozone content. *Quart. J. Roy. Meteor. Soc.*, 103:320–327, 1970.

P.J. Crutzen. Ozone production rates in an oxygen-hydrogen-nitrogen oxide atmosphere. *JGR*, 76:7311–7327, 1971.

P.J. Crutzen. Estimates of possible future ozone reductions from continued use of fluoro-chloro-methanes ($CF_2Cl_2, CFCl_3$). *Geophys. Res. Let.*, 1:205–208, 1974.

Arne Dahlback and Knut Stamnes. A new spherical model for computing the radiation field available for photolysis and heating at twilight. *Planet. Space Sci.*, 39(5):671–683, 1991.

A. Dalgarno and D.A. Williams. Raman and rayleigh scattering of lyman α by molecular hydrogen. *Monthly notices of the Royal Astronomical Society*, 124:313–319, 1962.

Rüdiger de Beek. *Bestimmung von Ozonvertikalprofilen aus Messungen des Satelliteninstruments* GOME *im ultravioletten und sichtbaren Spektralbereich*. Dissertation, Universität Bremen, Institut für Fernerkundung, 1998.

J. de Vries and R. Hoogeveen. Optec 2 cold tests instrument performance evaluation report. Technical Report RP-SCIA-0000FO/207, SCIAMACHY Joint Team FS-TPD-SRON, Feb 1999.

G.M.B. Dobson. Observations of the amount of ozone in the earth's atmosphere and its relation to other geophysical conditions. *Proc. R. Soc. London*, 129:411, 1930. Ser. A.

Bengt Edlén. The refractive index of air. *Metrologia*, 2(2):71–80, 1966.

M. Endemann. MIPAS instrument concept and performance. In ESAMS ESAMS, pages 29–43.

Patrick Eriksson. *Microwave Radiometric Observations of the Middle Atmosphere: Simulations and Inversion*. Ph.d. thesis, School of Environmental Sciences, Chalmers University of Technology, S-41296 Göteborg, Sweden, 1999. Technical Report No. 355.

Definition of Observational Requirements for Support to a Future Earth Explorer Atmospheric Chemistry Mission. ESA, draft edition, June 2000. final report on ESA contract 1-3379/98/NL/GD.

ESAMS. *Proceedings of ESAMS '99*, Noordwijk, The Netherlands, 1999. ESA-ESTEC.

K. Franklin Evans. The spherical harmonics discrete ordinate method for three-dimensional atmospheric radiative transfer. *J. Atmos. Sci.*, 55:429–448, 1998.

D.W. Fahey, S.R. Kawa, E.L. Woodbridge, P. Tin, J.C. Wilson, H.H. Jonsson, J.E. Due, D. Baumgardner, S. Borrmann, D.W. Toohey, J.R. Avallone, M.H. Proffitt, J. Margitan, M. Loewenstein, J.R. Podolske, R. J. Salawitch, S.C. Wofsy, M.K.W. Ko, D. E. Anderson, M. R. Schoeberl, and K.R. Chan. In situ measurements constraining the role of sulphate aerosols in mid-latitude ozone depletion. *Nature*, 363:509–514, 1993.

Jürgen Falbe and Manfred Regitz, editors. *Römpp Chemie Lexikon*. Thieme, Stuttgart, New York, 9. edition, 1995. CD-ROM, version 1.0.

J. C. Farman, B. G. Gardiner, and J. D. Shanklin. Large losses of total ozone in Antarctica reveal seasonal $\mathrm{ClO_x/NO_x}$ interaction. *Nature*, 315:207–210, 1985.

D.E. Flittner, P.K. Barthia, and B.M. Herman. O_3 profiles retrieved from limb scatter measurements: Theory. *Geophys. Res. Let.*, 27(17):2601–2604, 2000.

J. Hampson. Photochemical behavior of the ozone layer. Technical Report TN 1627/64, Can. Armament Res. and Dev. Estab., Valcartier, Que. Canada, 1964.

Christine H. Hearn and Jeffrey A. Joenst. The near U.V. absorption spectrum of CS_2 and SO_2 at 300 K. *J.Q.S.R.T.*, 45(2):69–75, 1991.

B.M. Herman, A. Ben-David, and K-J. Thome. Numerical techique for solving the radiative transfer equation for a spherical shell atmosphere. *Applied Optics*, 33(9):1760 – 1770, 1994.

B.M. Herman, T. Caudill, D. Flittner, and K.N. Liou. Comments on "solar heating rates: The importance of spherical geometry". *J. Atmos. Sci.*, 52(3):380–382, 1995a.

B.M. Herman, T.R. Caudill, D.E. Flittner, K.J. Thome, and A. Ben-David. Comparision of gauss-seidel spherical polarized radiative transfer code with other radiative transfer codes. *Applied Optics*, 43(21):4563–4572, 1995b.

M. Hess, P. Koepke, and I. Schult. Optical properties of aerosols and clouds: The software package OPAC. *Bulletin of the American Meteorological Society*, 79(5):831–844, 1998. URL `http://ams.allenpress.com/amsonline`.

D. J. Hofmann and S. Solomon. Ozone destruction through heterogeneous chemistry following the eruption of El Chichoń. *J. Geophys. Res.*, 94:5029–5041, 1989.

J. R. Holton, P.H. Haynes, M. E. McIntyre, A.R. Douglass, R. B. Rood, and L. Pfister. Stratosphere-troposphere exchange. *Rev. Geophys.*, 33:403–439, 1995.

Ricarda Hoogen. Aerosol parametrization in GOMETRAN++. Technical report, *ife*, Universität Bremen, August 1995.

Ricarda Hoogen. *Inversion globaler Ozonvertikalverteilungen aus Messungen des Satelliteninstruments GOME*. Dissertation, Universität Bremen, Institut für Fernerkundung, 1998.

Ricarda Hoogen, Vladimir V. Rozanov, and John P. Burrows. Ozone profiles from GOME satellite data: Algorithm description and first validation. *JGR*, 104:8263–8280, 1999.

R. Hoogeveen. The ambient-performance test evaluation report. Technical Report RP-SCIA-0000FO/205, SCIAMACHY Joint Team FS-TPD-SRON, Jul 1999.

R. Hoogeveen and J. de Vries. Optec 5 cold tests instrument performance evaluation report. Technical Report RP-SCIA-0000FO/260, SCIAMACHY Joint Team FS-TPD-SRON, May 2000.

IPCC. *Climate Change 2001: Impacts, Adaptation, and Vulnerability*. WMO, Intergovernmental Panel on Climate Change, Working Group II, February 2001a. URL `http://www.ipcc.ch/pub/wg2SPMfinal.pdf`. Summary for Policymakers.

IPCC. *Climate Change 2001: Mitigation*. WMO, Intergovernmental Panel on Climate Change, Working Group III, March 2001b. URL `http://www.ipcc.ch/pub/wg3SPM.pdf`. Summary for Policymakers.

IPCC. *Climate Change 2001: The Scientific Basis*. WMO, Intergovernmental Panel on Climate Change, Working Group I, January 2001c. URL `http://www.ipcc.ch/pub/spm22-01.pdf`. Summary for Policymakers.

R.G. Isaacs, W.-C. Wang, R.D. Worsham, and S. Goldenberg. *Multiple Scattering Treatment for Use in the LOWTRAN and FASCODE Models*, 1986. AFGL-TR-86-0073, AD A 173990.

H. S. Johnston. Reduction of stratospheric ozone by nitrogen oxide catalysts from supersonic transport exhaust. *Science*, 173:517–522, 1971.

Johannes W. Kaiser, Alexei V. Rozanov, Vladimir V. Rozanov, and John P. Burrows. Evaluation of approximative radiative transfer models intended for retrievals from limb measurements. In William L. Smith and Yuriy M. Timofeyev, editors, *IRS 2000: Current Problems in Atmospheric Radiation*, St.-Petersburg, Russia, 2001a. St.-Petersburg State University, A. DEEPAK Publishing. accepted.

Johannes W. Kaiser, Vladimir V. Rozanov, Michael Buchwitz, and John P. Burrows. Steps towards limb profile retrieval using a spherical radiative transfer model based on the single scattering approximation. In ESAMS ESAMS, pages 771–777.

Johannes W. Kaiser, Vladimir V. Rozanov, and John P. Burrows. Stratospheric O_3 and NO_2 profile theoretical accuracies from SCIAMACHY limb measurements. In N.R.P. Harris, M. Guirlet, and G.T. Amanatidis, editors, *Stratospheric Ozone 1999: Proceedings of the Fifth European Workshop*, pages 779–782. European Commission, 2000. Air pollution research report 73.

Johannes W. Kaiser, Vladimir V. Rozanov, and John P. Burrows. Theoretical precisions for SCIAMACHY limb retrieval. *Advances in Space Research*, 2001b. accepted.

J.W. Kaiser, K.-U. Eichmann, V.V. Rozanov, and J.B. Burrows. Precision estimates for SCIAMACHY limb retrievals. In *2001 IEEE International Geoscience and Remote Sensing Proceedings*, 2001c.

Walter Kertz. *Einführung in die Geophysik I: Erdkörper*. BI Wissenschaftsverlag, Mannheim, Leipzig, Wien, Zürich, 1969.

L.V. King. On the complex anisotropic molecule in relation to the dispersion and scattering of light. *Proceedings of the Royal Society of London / A*, 104:333–357, 1923.

F.X. Kneizys, L.W. Abreu, G.P. Andrson, J.H. Chetwynd, E.P. Shettle, A. Berk, L.S. Bernstein, D.C. Robertson, P. Acharya, L.S. Rothman, J.E.A. Selby, W.O. Gallery, and S.A. Clough. The MODTRAN 2/3 report and LOWTRAN 7 model. Technical report, Phillips Laboratory, Hanscom AFB, 1996. contract F19628-91-C-0132 with Ontar Corp.

F.X. Kneizys, E.P. Shettle, W.O. Gallery, J.H. Chetwynd, Jr., L.W. Abreu, J.E.A. Selby, S.A. Clough, and R.W. Fenn. Atmospheric transmittance/radiance: Computer code lowtran 6. Technical Report project 7670, AFGL-TR-83-0187, Environmental Research Papers, No. 846, Optical Physics Division, Air Force Geophysics Laboratory, Air Force Systems Command, USAF, 1983. limb.

P.W. Kruse. The photon detection process. In R.J. Keyes, editor, *Optical and Infrared Detectors*, volume 19 of *Topics in Applied Physics*, pages 5–70. Springer-Verlag, second corrected and updated edition, 1980.

Thomas Kurosu. *Die Modellierung des Strahlungstransports in Wolken für atmosphärische Fernerkundung im ultravioletten und sichtbaren Spektralbereich*. Dissertation, Universität Bremen, 1997.

A. Kylling, K. Stamnes, and S.-C. Tsay. A reliable and efficient tweo-stream algorithm for spherical radiative transfer: Documentation of accuracy in realistic layered media. *Journal of Atmospheric Chemistry*, 21:115–150, 1995. limb.

Jacqueline Lenoble, editor. *Radiative Transfer in Scattering and Absorbing Atmospheres: Standard Computational Procedures*. A. DEEPAK Publishing, Hampton, Virginia USA, 1985.

Jacqueline Lenoble, editor. *Atmospheric Radiative Transfer*. A. DEEPAK Publishing, Hampton, Virginia USA, 1993.

E.J. Llewellyn et al. OSIRIS: An application of tomography for absorbed emissions in remote sensing. In G.A. Lampropoulos and R.A. Lessard, editors, *Applications of Photonic Technology*, volume 2, pages 627–632. Plenum, New York, 1997.

M.B. McElroy, R.J. Salawitch, S.C. Wofsy, and J.A. Logan. Reductions of antarctic ozone due to synergistic interactions of chlorine and bromine. *Nature*, 321:759–762, 1986.

Richard D. McPeters, Scott J. Janz, Ernest Hilsenrath, Tammy L. Brown, David E. Flittner, and Donald F. Heath. The retrieval of o_3 profiles from limb scatter measurements: Results from the Shuttle Ozone Limb Sounding Experiment. *Geophys. Res. Let.*, 27(17):2597–2600, 2000.

Richard Meller and Geert K. Moortgat. Temperature dependence of the absorption cross sections of formaldehyde between 223 and 323 K in the wavelength range 225–375 nm. *JGR*, 105(D6):7089–7101, 2000.

I.N. Minin. The optics of planetary atmospheres. *Izvestiya / Atmospheric and Oceanic Physics*, 9(8):829–836, 1973.

L.T. Molina and M.J. Molina. Production of Cl_2O_2 from the self-reaction of the ClO radical. *J. Phys. Chem.*, 91:433–436, 1987.

M. J. Molina and F. S. Rowland. Stratospheric sink for chlorofluoromethanes: clorine atom catalyzed destruction of ozone. *Nature*, 249:810–814, 1974.

G.K. Moortgat, W. Kippel, K.M. Möbus, W. Seiler, and P. Warneck. Laboratory measurements of photolysis parameters for formaldehyde. Technical Report FAA Rep. N. FAA-EE-80-47, Fed. Aviation Admin., Washington, D.C., 1980.

George H. Mount and David W. Rusch. Measurements of stratospheric NO_2 from the solar mesosphere explorer satellite, 1. an overview of the results. *JGR*, 89(D1):1327–1340, 1984.

R. Müller, H. Bovensmann, M. Bruns, J.P. Burrows, V. Eyring, J. Kaiser, A. Richter, J. Trentmann, and F. Wittrock. Interpretation of BrO slant column measurements using the model package SLACO. In ESAMS ESAMS, pages 617–619.

Richard Müller. *Entwicklung und Anwendung eines photochemischen schräge Säule Modell-Paketes zur Interpretation von DOAS-Daten atmosphärischer Spurengase*. Dissertation, Universität Bremen, Institut für Fernerkundung, 2001.

Stefan Noël. State parameter optimisation. Technical report, Institut für Fernerkundung, Universität Bremen, 1998. Version 2.0.

Stefan Noël. State parameter optimisation. Technical report, Institut für Fernerkundung, Universität Bremen, May 2000. Version 3.0 (preliminary).

L. Oikarinen. Monte carlo simulations of radiative transfer for limb scan measurements. In ESAMS ESAMS.

Liisa Oikarinen, Elina Sivhola, and Erkki Kyrölä. Multiple-scattering radiance in limb-viewing geometry. *JGR*, 104(D24):31261–31274, 1999.

Edson R. Peck and Kaye Reeder. Dispersion of air. *Journal of the Optical Society of America*, 62(8):958–962, 1972.

William H. Press, Saul A. Teukolsky, William T. Vetterling, and Brian P Flannery. *Numerical Recipes in C*. Cambridge University Press, 2. edition, 1992.

Andreas Richter. *Absorptionsspektoskopische Messungen Stratosphärischer Spurengase über Bremen, $53^\circ N$*. Dissertation, Universität Bremen, Institut für Umweltphysik, 1997.

J.P. Richter. *The Literary Works of Leonardo da Vinci*, volume I. Phaidon, London, 3. edition, 1970.

C.D. Rodgers. Retrieval of atmospheric temperature and composition from remote measurements of thermal radiation. *Reviews of Geophysics and Space Physics*, 14(4):609–624, 1976a.

C.D. Rodgers. The vertical resolution of remotely sounded temperature profiles with *a priori* statistics. *J. Atmos. Sci.*, 33:707–709, April 1976b.

Clive D. Rodgers. *Inverse Methods for Atmospheric Sounding: Theory and Practice*, volume 2 of *Series on Atmospheric, Oceanic and Planetary Physics*. World Scientific, Singapore, New Jersey, London, Hong Kong, 2000.

F.S. Rowland and M.J. Molina. Chlorofluoromethanes in the environment. *Rev. Geophys.*, 13:1–35, 1975.

Alexei V. Rozanov, Vladimir V. Rozanov, and John P. Burrows. A numerical radiative transfer model for a spherical planetary atmosphere: Combined differential–integral approach involving the picard iterative approximation. *JQSRT*, 2000. in press.

Vladimir Rozanov and Kai-Uwe Eichmann. Spherical geometry and refraction in gometran. Technical report, ife, 1997. limb.

Vladimir V. Rozanov, D. Diebel, R.J.D. Spurr, and J.P. Burrows. GOMETRAN: A radiative transfer model for the satellite project GOME, the plane parallel version. *JGR*, 102 (D14):16683–16695, 1997a.

Vladimir V. Rozanov, T. Kurosu, and J.P. Burrows. Retrieval of atmospheric constituents in the UV-visible: A new quasi-analytical approach for the calculation of weighting functions. *QSRT*, 60(2):277, 1997b.

David W. Rusch, George H. Mount, Charles A. Barth, Ronald J. Tomas, and Micheal T. Callan. Solar mesosphere explorer ultraviolet spectrometer: Measurements of ozone in the 1.0–0.1 mbar region. *JGR*, 89(D7):11,677–11,687, 1884. limb.

D.W. Rusch, G.H. Mount, C.A. Barth, G.J. Rottman, R.J. Thomas, G.E. Thomas, R.W. Sanders, G.M. Lawrence, and K.S. Eckman. Ozone densities in the lower mesosphere measured by a limb scanning ultraviolet spectrometer. *Geophysical Research Letters*, 10 (4):241–244, 1983.

George B. Rybicki and Alan P. Lightman. *Radiative Processes in Astrophysics*. John Wiley & Sons, 1979.

Silvia Schlieter. *Spurengasmessungen während der Nacht mittels Mondlichtspektroskopie im Vergleich mit Modellrechnungen*. Dissertation, Universität Bremen, Institut für Fernerkundung, 2001.

Erwin Sedlmayr. *Sternatmosphären*. Freie Universität Berlin, 1994. Vorlesung im WS 93/94.

D. T. Shindell, D. Rind, and P Lonergan. Increased polar stratospheric ozone losses and delayed eventual recovery owing to increasing greenhouse-gas concentrations. *Nature*, 392:589–592, 1998.

Frank H. Shu. *THE PHYSICAL UNIVERSE, An Introduction to Astronomy*. University Science Books, 1982.

F.G. Simon, W. Schneider, G.K. Moortgat, and J.P. Burrows. A study of the ClO absorption cross-section between 240 and 310 nm and the kinetics of the self-reaction at 300 k. *J. Photochem. Photobiol. A*, 55:1–23, 1990.

V.V. Sobolev. *Light Scattering in Planetary Atmospheres*. Pergamon Press, 1975.

S. Solomon, R. R. Garcia, F. S. Rowland, and D. Wuebbles. On the ozone depletion of Antarctic ozone. *Nature*, 321:755–758, 1986.

Susan Solomon. Stratospheric ozone depletion: a review of concepts and history. *Reviews of Geophysics*, 37(3):275–316, 1999.

SPARC. Assessment of trends in the vertical distribution of ozone. In N.R.P. Harris, R. Hudson, and C. Phillips, editors, *WMO Ozone Research and Monitoring Project Report Nr. 43*, 1998.

J. Staehelin, R. Kegel, and N.R.P. Harris. Trend analysis of the homogenized total ozone series of arosa (switzerland), 1926–1996. *JGR*, 103:8389–8399, 1998.

Knut Stamnes, S-Chee Tsay, Warren Wiscombe, and Kolf Jayaweera. Numerically stable algorithm for discrete-ordinate-method radiative transfer in multiple scattering and emitting layered media. *Applied Optics*, 27(12):2502–2508, 1988.

R.S. Stolarski and R.J. Cicerone. Stratospheric chlorine: A possible sink for ozone. *Can. J. Chem.*, 52:1610–1615, 1974.

R.S. Stolarski, A.J. Krueger, M.R. Schoeberl, R.D., McPeters, P.A. Newman, and J.C. Alpert. Nimbus 7 satellite measurements of the springtime Antarctic ozone decrease. *Nature*, 322:808–811, 1986.

J.W. Strutt. On the scattering of light by small particles. *The London, Edinburgh, and Dublin philosophical magazine and journal*, 41(102):447–454, 1871. by the later Lord Rayleigh.

Albert Tarantola. *Inverse Problem Theory: Methods for Data Fitting and Model Parameter Estimation*. Elsevier, Amsterdam, Oxford, New York, Tokyo, 1987.

G.E. Thomas, C.A. Barth, E.R. Hansen, C.W. Hord, G.M. Lawrence, G.H. Mount, G.J. Rottman, D.W. Rusch, A.I. Stewart, R.J. Thomas, J. London, P.L. Bailey, P.J. Crutzen, R.E. Dickenson, J.C. Gille, S.C. Liu, J.J. Noxon, and C.B.Farmer. Scientific objectives of the solar mesosphere explorer mission. *Pageoph*, 118:591–615, 1980.

Ronald J. Thomas, Charles A. Barth, David W. Rusch, and Ryan W. Sanders. Mesosphere explorer near-infrared spectrometer: Measurements of 1.27-μm radiances and the inference of mesospheric ozone. *JGRA*, 89(D6):9569–9580, 1984.

J.J. Tsou, Brian J. Connor, Alan Parrish, I. Stuart McDermid, and William P. Chu. Ground-based microwave monitoring of middle atmosphere ozone: Comparison to lidar and Stratospheric and Gas Experiment II satellite observations. *JGRA*, 100(D2): 3005–3016, 1995.

K.K. Tung, M.K.W. Ko, J.M. Rodriguez, and N.D. Sze. Are antarctic ozone variations a manifestation of dynamics or chemistry? *Nature*, 1986.

M. Vountas, V.V. Rozanov, and J.P. Burrows. Ring effect: Impact of rotational raman scattering on radiative transfer in earth's atmosphere. *J. Quant. Spectrosc. Radiat. Transfer*, 60(6):943–61, 1998.

Marco Vountas. *Background: Ring theory & Raman Routines within GT++*. iup, University of Bremen, Jan 1999a.

Marco Vountas. *Die Modellierung und Parametrisierung des Ring Effektes*. Dissertation, Universität Bremen, FB 1, 28353 Bremen, Germany, 1999b.

A. Wahner, A.R. Ravishankara, S.P. Sander, and R.R. Friedl. Absorption cross secion of BrO between 312 and 285 nm at 298 and 223 K. *Chemical Physics Letters*, 152(6): 507–512, 1988.

Andreas Wahner, Geoffrey S. Tyndall, and A.R. Ravishankara. Absorption cross sections for OClO as a function of temperature in the wavelength range 240–480 nm. *J. Phys. Chem.*, 91:2734–2738, 1987.

A. E. Waibel, T. Peter, K.S. Carslaw, H. Oelhaf, G. Wetzel, P.J. Crutzen, U. Pöschel, A. Tsias, E. Reimer, and H. Fischer. Arctic ozone loss due to denitrification. *Science*, 283:2064–2069, 1999.

Richard P. Wayne. *Chemistry of Atmospheres*. Clarendon Press, Oxford, second edition, 1991.

Andrea K. Weiss. *Anthropogenic and Dynamic Contributions to Ozone Trends of the Swiss Total Ozone, Umkehr and Balloon Sounding Series*. dissertation, ETH Zürich, 2000.

WMO. Scientific assessment of ozone depletion: 1994. World Meteorological Organization, Geneva, Switzerland, 1995. Rep. 37.

WMO. Scientific assessment of ozone depletion: 1998. World Meteorological Organization, Geneva, Switzerland, 1999a. Report 44.

WMO. Scientific assessment of ozone depletion:1998. World Meteorological Organization, Geneva, Switzerland, 1999b. Report 44.

Willian L. Wolfe and George J. Zissis, editors. *The Infrared Handbook*. Office of Naval Research, Department of the Navy, Washington, DC, USA, revised edition, 1989. third printing.

Carl Wunsch. *The Ocean Circulation Inverse Problem*. Cambridge University Press, 1996.

A.T. Young. Revised depolarization corrections for atmospherich extinction. *Applied Optics*, 19(20):3427–3428, 1980.

Index

I_j, 69
I_{diffuse}, 51
I_{direct}, 51
W^{aa}, 76
W^{ra}, 76
W^{rr}, 76
$\vec{\mathbf{r}}_s(.)$, 46
$\alpha(\vec{r})$, 44
δ_j^R, 69
δ_j^{S1}, 69
δ_j^{S2}, 69
$\overset{*}{T}$, 60
μ_{horizon}, 65
ρ, 40
$\sigma(\vec{r})$, 44
ξ, 39
n_i, 40
$npts$, 65
I_{D}, 60
A, 94
D, 93
K, 92
ClO-dimer, 11
$\phi_i(\vec{r}, \vec{\Omega}, \vec{\Omega}')$, 45
F(.), 91
f(.), 91
MS, 154
RS, 154
SS, 154
S, 154
pdf , 92
a priori, 90
Ångström parametrisation, 38

absolute method, 144
Absolute-absolute weighting functions, 76
absorption coefficient, 44
accumulated ray path lengths, 66
ACE study, 123
active radicals, 10
ADC, 83
aerosol absorption coefficient, 38
aerosol extinction coefficient, 38, 39
aerosol scattering coefficient, 38
aerosol scattering phase function, 38
AGU, 209
albedo, 39
analytical computation, 77
antarctic ozone hole, 4
astronomical solar azimuth angle, 189
astronomical solar zenith coordinate, 188
asymmetry factor, 38
averaging kernel matrix, 94
Avogadro's number, 32

backward ray tracing, 177
Bass-Paur-parametrisation, 34
bi-directional reflection distribution function, 39
Black Hole, 3
BOA, 177
Boltzmann's constant, 33
bottom of atmosphere, 177
BRAPHO, 99
BRDF, 39
Brewer-Dobson circulation, 9

Cabannes scattering, 32
catalytic, 9

CDIPI, 55
CFC, 9
CFC-11, 13
CFC-12, 13
Clouds, 40
clusters, 25
collected ray path lengths, 66
collisional quenching, 4, 8, 34
column, 9
column density, 9
contribution function, 93, 124
correlation matrix, 124
COSPAR, 209
covariance matrix, 92

denitrification, 11
denoxification, 10
density correction factor, 41
depolarisation factor, 32
descending node, 20
differential approach, 144
differential fit, 144
diffuse radiance, 51
direct radiance, 51
direct transmittance, 60
dispersion factor, 41
dispersion formula, 41
Dobson Units, 9
double scattering, 153
DPG, 210

effective aerosol phase function, 45
effective King correction factor, 33
effective phase function, 45
effictive aerosol scattering phase function, 39
EGS, 209
emission coefficient, 48
Envisat, 20
ESAMS, 210
expectation value, 92
extended midpoint rule, 65
extinction coefficient, 45
Extinktionskoeffizient, 45

flux, 48
FMI, 71
footprint, 14
forward function, 91
forward model, 91
forward model matrix, 92
FOV, 83
fractional volume abundance, 33
FWHM, 94, 115

Gaussian distribution, 92
Gaussian quadrature, 65
geometrical path coordinate, 45
global warming, 14
GOMETRAN, 52
GOMOS, 26
greenhouse effect, 14
greenhouse gases, 14
ground-bound, 177

halogens, 10
Hartley-Huggins bands, 4
Henyey-Greenstein, 38
HITRAN, 34
hyperspectral, 20, 21
hyperspectral advantage, 159
hyperspectral advantages, 116

IFOV, 25
IGARSS, 209
instantaneous field of view, 25, 83
integral form of the radiative transfer equation, 50
integro-differential form of the radiative transfer equation, 49
inverse problem, 90
irradiance, 48
IRS, 209

King factor, 32
Kyoto protocol, 17

Lambertian surface reflection, 39

level-0-to-1 data processor, 83
level 0, 83
level 1, 83
LFA, 60
LFS, 60
limb, 22
line of sight, 53
linear correlation coefficients, 93, 94
linearisation, 76
linearisation state, 95
local thermodynamic equilibrium, 34
location, 44
LORE, 26
LOS, 60
Loschmidt number, 32
LTE, 34

measurement response, 95
measurement vector, 91
mesosphere, 6
MISU, 144
moderately nonlinear, 95
MODTRAN, 52
molecular absorption cross section, 34
molecular scattering, 32
monochromatic radiative transfer modelling, 44
Monte Carlo, 55
Montreal Protocol, 13

nadir, 22
near-real-time, 173
neutral density, 33
NIR, 34
non-local, 51
Normal distribution, 92
numerical perturbation, 76

occultation, 22
Odd ozone, 8
ODIN, 26
OPTEC 5, 85
optical depth, 45, 47
optical length, 46
optical thickness, 47
optically thick, 47
optically thin, 47
optimal estimation, 90
optische Dichte, 45, 47
optische Dicke, 47
optische Tiefe, 45
orders of scattering model, 54
OSIRIS, 26
ozone layer, 4, 6
ozone shield, 6

partitioning, 10
phase functions, 44
photon noise, 84
PMD, 25
polar, 20
polar stratospheric clouds, 10
polarisation measurement devices, 25
probability density function, 92
PSC, 10
pseudo-spherical, 52

quadrature, 64
quasi-analytical, 28, 170
quasi-analytical computation, 77

radiance, 47
radiative forcing, 16
Raman scattering, 40
ray coordinate system, 177
ray path coordinate, 183
ray path length, 184
Rayleigh scattering, 32
Rayleigh scattering coefficient, 33
Rayleigh scattering cross section, 32
Rayleigh scattering phase function, 32, 33
readout noise, 84
reflected-then-scattered radiance, 62
reflection phase function, 40
reflection-then-scattering, 153
refractive index, 32, 40
refractivity, 41

Relative-absolute weighting functions, 76
Relative-relative weighting functions, 76
reservoir gases, 10
retrieved state, 93
RTE, 49
RTM, 169

S/N, 21
scattered-then-reflected radiance, 63
scattering coefficient, 44
SCIAMACHY, 20
second order of scattering, 62
Sellmeier form, 42
shift and squeeze, 84
shot noise, 84
signal to noise ratio, 88
single scattering albedo, 45
single-scattered radiance, 62
single-scattering approximation, 53
SIRO, 56
sky-bound, 177
SLACO, 99
SME, 26
smoothing error, 94
Snell's constant, 184
Snell's law, 41
Snell's law for spherical symmetry, 41
solar coordinate system, 188
Solar Mesosphere Explorer, 26
SOLSE, 26
source function, 48
specific radiance, 47
standard deviation, 92
state vector, 91
stratification, 4
stratopause, 6
stratosphere, 4, 6
stream approximation, 52
sun-normalised emission coefficient, 48
sun-normalised radiance, 48
sun-normalised source function, 48
sun-synchronous, 20
Super Nova, 3

tangent linear model, 95
terminator, 26
Thermal emission, 40
thermalisation, 34
throughput, 84
TOA, 177
tomographic, 27
top of atmosphere, 177
total ozone, 9
tropopause, 6
troposphere, 6
true absorption coefficient, 44
true state, 94
TUB, 206

UC, 206
UNCED, 17
United Nations Conference on Environment and Development, 17
UT/LS, 16
UV, 4, 34
UV-vis-NIR, 169

variance, 92
vertical resolution, 94, 115
vis, 34
volume mixing ratios, 9

weather, 6
weighting function matrix, 92, 95
weighting functions, 52, 75, 156
weighting functions, analytical computation, 156

FIN.